A rigorous multipolar framework for nanoparticles optical properties description : theory and experiments

Jérémy Rouxel

To cite this version:

Jérémy Rouxel. A rigorous multipolar framework for nanoparticles optical properties description : theory and experiments. Micro and nanotechnologies/Microelectronics. Université de Technologie de Troyes; Nanyang Technological University (Singapour), 2015. English. NNT : 2015TROY0013 . tel-03359603

HAL Id: tel-03359603
https://theses.hal.science/tel-03359603v1

Submitted on 30 Sep 2021

Thèse
de doctorat
de l'UTT

Jérémy ROUXEL

A Rigorous Multipolar Framework for Nanoparticles Optical Properties Description: Theory and Experiments

Spécialité :
Optique et Nanotechnologies

2015TROY0013

Année 2015

Thèse en cotutelle avec Nanyang Technological University - Singapour

NANYANG
TECHNOLOGICAL
UNIVERSITY

utt
université de technologie
Troyes

THESE

pour l'obtention du grade de

DOCTEUR de l'UNIVERSITE DE TECHNOLOGIE DE TROYES

Spécialité : OPTIQUE ET NANOTECHNOLOGIES

présentée et soutenue par

Jérémy ROUXEL

le 24 avril 2015

A Rigorous Multipolar Framework for Nanoparticles Optical Properties Description: Theory and Experiments

JURY

M. J. PLAIN	PROFESSEUR DES UNIVERSITES	Président
M. G. BACHELIER	MAITRE DE CONFERENCES - HDR	Examinateur
M. D. BARCHIESI	PROFESSEUR DES UNIVERSITES	Rapporteur
M. C. SUN	ASSOCIATE PROFESSOR	Rapporteur
M. J. ZYSS	PROFESSEUR EMERITE	Rapporteur

Personnalités invitées

Mme S. BRASSELET	DIRECTRICE DE RECHERCHE CNRS
M. S. MUKAMEL	PROFESSOR

Universite de Technologie de Troyes
Nanyang Technological University

Abstract

Doctor of Philosophy

A rigorous multipolar framework for nanoparticles optical properties description: theory and experiments

by Jeremy Rouxel

Using metallic nanoparticles with a threefold symmetry thorough the study, the impact of the symmetry on the nonlinear properties is investigated. Interpretations of polarization-resolved SHG experiments indicate the importance of multipolar resonances, in particular quadrupole and octupole, to explain the strong values of the nonlinear susceptibilities in such systems. A fully irreducible formalism is then developed to treat extended objects like nanoparticles. In this formalism, the nonlinear response tensor is a discrete set of values easily constrained by symmetries instead of a field. This formalism permits to describe simply linear and nonlinear optical response from nanoparticles. Finally, time-domain experiments are conducted with the aim to connect spatial and spectral properties. These experiments allow to interpret the spectra in terms of eigenmodes.

Key-Words : *nonlinear optics ; symmetries ; nanoparticles ; time-resolved spectroscopy*

Université de Technologie de Troyes
Nanyan Technological University

Résumé

Thèse de doctorat

Propriétés optiques nonlinéaires de nanoparticules métalliques

Jeremy Rouxel

Les propriétés optiques linéaires et non-linéaires de nanoparticules métalliques de tailles non-négligeables comparées à celles des longueurs d'onde excitatrices sont étudiées dans cette thèse. Les informations issues de la symétrie sont mises en avant afin de décrire des nanoparticules appartenant à des groupes ponctuels. Pour cela, un formalisme totalement irréductible est mis en place afin de prendre en compte l'extension spatiale des objets étudiés. Dans ce formalisme, le tenseur de réponse non-linéaire possède un nombre fini de valeurs significatives reliant les composantes multipolaires des champs incidents et sortants. Ce formalisme est alors appliqué analytiquement à l'étude de la réponse non-linéaire du second ordre de nano-étoiles d'or en interprétant des mesures de SHG résolue en polarisation. Finalement, des expériences de spectroscopies multidimensionnelles sont utilisées dans le but de connecter les propriétés spatiales et les propriétés spectrales de ces objets. L'introduction de modes propres définis par la symétrie des objets permet encore une fois de donner un sens physique aux comportements électroniques mis en jeu.

Mots-clefs : *Optique non-linéaire ; symétries ; nanoparticules ; spectroscopie résolue en temps*

Contents

Acknowledgments

First, I express my sincere gratitude to my supervisors Timothée Toury and Tan Howe-Siang. One could not simply wish for more friendly and accessible mentors who provide as much freedom to select topics of study.

I am also very grateful towards my jury members who used their time reading my manuscript and provided enlightening remarks on my work.

My PhD thesis would not have been such a breeze without the very nice atmosphere in the UTT and NTU laboratories. I learnt a lot from the warmful UTT professors during all my cursus and my thesis. The group members of my laboratory in Singapore, beyond their sympathy, helped me widen my horizon towards chemistry and biology. Many thanks to all of them.

Finally, I would like to thanks all my friends and family for their presence during those years.

General informations about notations

- Tensor fields of different ranks are indicated by an underline : $\underline{V}$ for rank 1 fields, $\underline{\underline{M}}$ for rank 2 fields and $\underline{\underline{\underline{T}}}$ for rank $\geqslant 3$ fields. Geometric vectors are indicated using an arrow over the symbol $\vec{n}$.
- The symbol $\otimes$ indicates a direct product. Irreducible tensor products are represented by a tensor product between curly brackets : $\{T \otimes U\}$.
- The fully contracted product is denoted by $\bullet$ while $\cdot$ represents a contraction over a single index.

Introduction

Introduction and general overview

The emergence of nanotechnologies together with the development of increasingly fast and reliable light sources has led to a new stage in the study of the optical phenomena in metals[1–4]. The ability to manufacture nanostructures such as nanoparticles[5–9], nanofilms[10], colloids[11] or nanowires[12] has a lot of promising applications in a multitude of fields. To cite a few of them, one could find ultrasensitive sensors[13, 14], photovoltaics[15], medical treatments[16] or photonics[17] among many others. An inclusive description on the behavior of nanoparticles of various shapes is still necessary in order to provide an improved ability to engineer the light-matter interaction. Moreover, metallic nano-objects have intriguing properties that are difficult to describe unlike bulk materials.

An early treatment of the scattering by a sphere has been rigorously solved in 1908 by G. Mie[18]. In this seminal paper, G. Mie uses an expansion in term of multipolar fields to solve the problem in spherical coordinates. Unfortunately, when the nanostructures are different from a sphere or a related shape, a fully analytical treatment is no longer possible and one has to rely on simplified models or numerical computations. Nevertheless, group theory and multipolar expansion can still provide a great deal of information. The main goal of this work is to describe the optical behavior of nanoparticles by a small number of significant coefficients and by taking account of the symmetries of the system. As a consequence, an irreducible frame has been developed focusing on the geometry and the shape of the nanoparticles.

Among the different optical techniques, non-linear optics provide a very sensitive and shape-specific set of experiments that have been used in this work. For example, polarization-resolved SHG experiment on single nanoparticles has been used to correlate the nature of the nonlinear optical response to their shapes. In this thesis, it has been chosen to focus on nanoparticles belonging to the group D_3 because this point group is the simplest of the non-trivial one. Its algebraic structure is easy to apprehend but still offer a step further to engineer the shape of the nanoparticles compared to, for example, nanorods. It is also possible to synthesize D_3 nanoparticles routinely in the laboratory using lithography or chemical synthesis.

This track of complexifying the shape of objects in order to engineer the nature of the light-matter interaction has already been followed by molecular physicists. With the aim to design optimized molecular nonlinear emitter, they showed that the introduction of molecules with more complex shape than the already well-used cylindrically symmetric ones permitted a whole new area of engineering. In particular, molecules belonging to discrete subgroup of the rotation group such as D_3 offered interesting behavior. Investigations showed that it was related to the relative weight of the multipolar component of the response tensor : molecules having only the octupolar part of the tensor non vanishing were indeed called octupolar molecules. The use of the irreducible tensor formalism allowed to settle the basic bricks to understand nonlinear interaction with those molecules but the multipolar nature of the problem was only present in the expansion of the response tensor. The fields emitted by the molecule were still almost purely dipolar since those molecules were much smaller than the wavelengths of radiation used, in the optical regime. In this work, we claim that the use of gold nanoparticles that resonate in the visible range offer again a new step in the development of optimized nonlinear emitter. Contrary to molecule, an understanding of their interaction with light necessitates the use of a fully multipolar formalism dealing with the fields and the response tensor in a uniform way. The non negligible size of nanoparticle compared to the exciting wavelength creates a response strongly sensitive to the shape. One can then tune the spatial extension, the shape and the symmetries of the object to obtain the desired optical response. The theoretical effort made to develop an appropriate formalism has to be assorted with a work on nanofabrication since efficient responses are easily altered by even slightly inappropriate shapes.

Figure 1 outlines the problematic of this thesis. A typical optical experiment on nanoparticles will possess an incoming electric field which role is to excite the system through its response tensor. As a reaction to the exciting field, an electric current is created that will in turn emit an outgoing electric field. An experimental apparatus is then in charge to detect the radiated field, most of the time in far field. In this thesis, both the incoming and outgoing are expanded over a multipolar basis and the response tensor relates those two expansions in a similar way that the T-matrix method does it[19]. However, the formalism of irreducible tensors provides a more physical angle of description of the response and allows to discuss links between geometry and optical properties using analytical modeling while the T-matrix method uses a less powerful basis for its definition and relies on numerical computations.

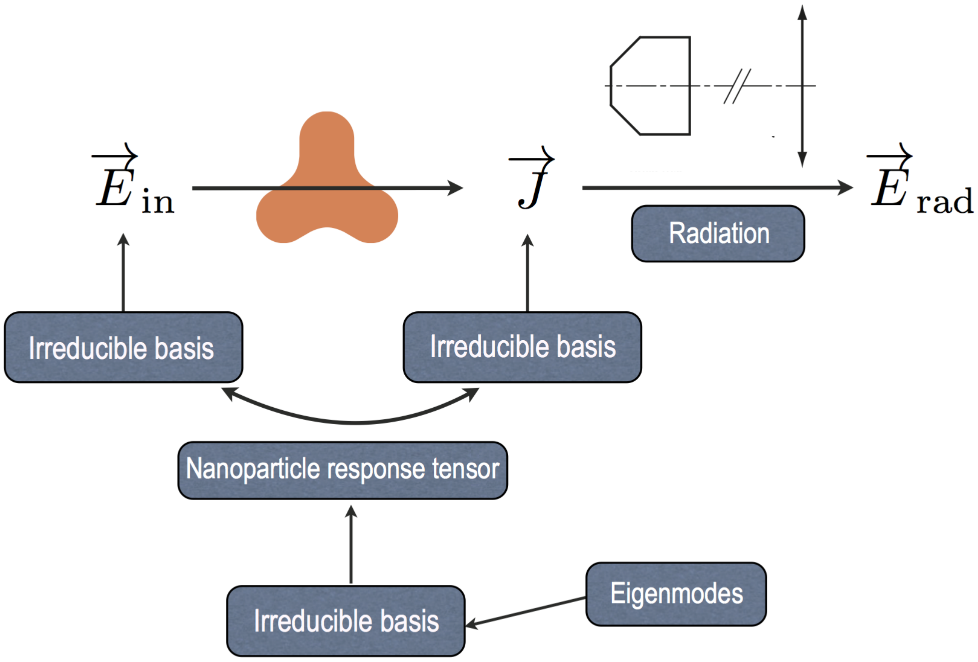

FIGURE 1: Outline of the general problem. The response tensor which relates the outgoing field to the incoming field is a cartesian tensor field. Instead of using this form linking two vector field, we expand both electromagnetic field on multipole fields. Thus, the response tensor becomes a irreducible tensor linking the multipolar components of the incoming and emitted electromagnetic fields. The propagation of each multipolar field through the experiment is then calculated in order to analyze the data.

Outline of this thesis

This thesis has been divided into three parts addressing different aspects of this work. The first part introduces quickly the key concepts used more extensively in the next two parts. In this part, those notions are also used to derive new results that appears to be a direct extension of already known results. For example, the derivation of multipolar point spread functions are used to discuss vector diffraction theory of electromagnetic waves but are also a pretext to furnish a first use of multipoles in this work. Moreover, multipolar PSFs are also side results of this that are used to interpret the experiment conducted by N. T. Nguyen[20] and interpreted in this part. The second part is the core of this thesis. It contains the presentation of the fully irreducible formalism for nonlinear optics which is the most fundamental results of this work. The next two chapters of this part are used to discuss developments of this theory and provide a possible structure for the methodology for its concrete usage. The third part will deal with time domain experiments achieved during this thesis. Preliminary results have been achieved on nanoparticles using pump probe spectroscopy. Moreover, photosynthetic complexes have been studied using two-dimensional electronic spectroscopy using the same experimental setup. Both topics are presented in this concluding part.

A more detailed summarization of the content of this thesis, chapter by chapter, is done in the following of this section :

The basic principles needed in this work encompassing topics in electromagnetism, non-linear optics, nanotechnologies and group representation theory, are introduced in **chapter 1** together with a quick overview of preliminary studies achieved in this field. The presentation of group theory also includes a short introduction to the expansion of tensors into irreducible parts, each part corresponding to an irreducible representation of the rotation group, also known as a multipole. Until recently, scientific interest about multipole in non-linear optics has been mainly focussed on so-called octupolar molecules which response tensor have a dominant octupolar irreducible component. These molecules offer great possibilities to engineer optical components but nanoparticles offer a whole new area of capabilities. Basic results about the nanoparticles under interest are then discussed to highlight their remarkable properties. Finally, the experimental process to achieve the fabrication of those nanoparticles and observation are given in the end of the chapter.

Chapter 2 introduces multipolar Point Spread Functions (PSF) that will be used in chapter 6 to link theoretical modeling with optical experiments. Firstly, vector diffraction theory is reviewed in the context of the focusing of an electric field by a perfect imaging system. It is shown that some results commonly accepted in the literature may be incomplete and an in-depth discussion about the validity of the description and of the useful approximations is given. From this solid starting point, multipolar electromagnetic fields are introduced and used to derive and display multipolar PSFs.

Chapter 3 pursues the discussion about the properties of D_{3h} nanoparticles and focuses on the interpretation of the SHG signal. A polarization resolved SHG experiment of single nanoparticles is described and its results are discussed. Those measurements have been conducted by N. T. Nguyen during her PhD thesis and the present work is rooted to a limited extent in the interpretation of her work. As a starting model, the nanoparticle can be considered as a set of dipoles located at its tips but, quickly, this description happens to be too simple since it takes into account the spatial extension partially. A multipolar approach can instead be introduced to provide more physical insight about the nature of the electromagnetic response. In this chapter, the introduction of multipoles is done using simple projections over the multipolar basis while more involved descriptions are proposed in the next chapters.

In **chapter 4**, an extensive presentation of a fully irreducible theory of the optical interaction of nanoparticles and light is given. In the irreducible formalism developed by J. Jerphagnon and J. Zyss, only the response tensor was split into its irreducible parts but the exciting and outgoing electromagnetic fields were still described in a cartesian fashion or as an irreducible local vector. The purpose of this chapter is to generalize this formalism in order to take in account the extension of the nanoparticle. The electromagnetic field can no longer be considered as a local vector and one needs to use an expansion in terms of vector multipolar fields. The viability of this formalism and its link with previous ones is firstly demonstrated in different fashions in linear optics. A nonlinear description is then introduced with the help of a new object, multipolar vector spherical harmonics, which are constructed from irreducible products of vector spherical harmonics.

Chapter 5 discusses the algebraic operations that can be achieved on multipolar fields to translate them. Before shortly exposing the demonstration of the translational addition theorem that effectively does the translation, its significance and its implications to interpret the spatial manipulation of multipoles is highlighted. This theorem, well-known in multiple sphere scattering, allows to write a multipole located somewhere in space as a sum of multipoles at one specific point. Gathering all the dipole over the nanoparticle, one can then consider the nanoparticle as one discrete set of multipole located at one specific point rather than a field of dipole all over the volume of the extended object. Indeed, when one starts to design nanoparticle to spatially engineer multipolar radiation, it is necessary to have a clear view on the spatial behavior of multipolar fields. Then, limiting cases of the translational addition theorem and examples are presented to conclude the chapter.

Chapter 6 uses the theory of the preceding chapter to derive a simple multipolar model for D_3 nanoparticles. The experiments of chapter 2 are discussed again briefly using the previous results. In the aim to link models with multiple dipoles and a multipolar description, translational addition theorems of multipolar fields are used according to the previous chapter. Then, the exciting electric field is also expanded in vector multipolar fields in order to reconstruct a possible response tensor for the nanoparticle under study. With this point of view, the experiment of chapter 3 can be used to investigate the irreducible response tensor components.

Chapter 7 opens the last part of this thesis that focuses more on temporal aspects of the nonlinear optical interaction. This chapter introduces the necessary concepts of ultrafast nonlinear spectroscopy to understand techniques used in the laboratory like pump-probe spectroscopy and two-dimensional electronic spectroscopy. Results of the latter techniques are used to inspect the frequency-frequency correlation function of Chlorophyll a according to the solvent.

Finally, **chapter 8** presents preliminaries results of ultrafast spectroscopies conducted on nanoparticles. A discussion in term of mode is presented to interpret ultrafast nonlinear signals. Experimental pitfalls are pointed out and further developments are proposed.

Personal contributions of the author

In order to simplify the exposition of this thesis' results, the personal contributions of the author are briefly presented in this section. Calculations presented in this thesis about multipolar Point Spread Functions, fully irreducible formalism and modeling of nanostars using translational addition theorem have been carried out by the author under the guidance of his PhD supervisors. Moreover, the fabrication of gold nanostars using e-beam lithography described in chapter 1 has also been done by the author together with an optimization of the fabrication parameters. The chemical synthesis of silver nanoprisms have been achieved with the help of Mikahil Moiseev in NTU that cordially showed his protocol.

Polarization resolved SHG experiments presented in chapter 3 have been done by Nguyen Thanh Ngoc in the group of Sophie Brasselet during her PhD thesis. She also contributed to the derivation of the fitting models in the cartesian domain but their final form, their extension to irreducible bases and the actual fits presented in this work have been achieved by the author. In order to use a suitable irreducible formalism, a compilation of known results in angular momentum theory has been used and adapted to the framework of this thesis.

About ultrafast spectroscopies of chlorophyll a and LHCII presented in the last part of this thesis, the author joined the experiments conducted by Kym Wells and actively participated in the experimental acquisition and modifications of the multidimensional spectroscopy setup. Those modifications included the addition of a new optical to extend the experiment ability to pump other wavelengths and the writing of the associated Labview programs. Moreover, an important contribution has been done in writing the Matlab and Mathematica codes to analyze the data using the CLS method. Those codes were writing by adapting known theoretical developments in nonlinear optics. Using the chemically synthesized nanoparticles as samples, the author also modified the setup to allow the use of a pump centered at 800 nm and 400 nm.

Part I

General frame of the study

Chapter 1

Irreducible tensors in nonlinear optics

In this chapter, we introduce the necessary theoretical background and concepts that will be used all along this thesis. After linking this work with existing researches, the basis used to describe multipolar fields is introduced together with simple illustrations.

1.1 Review of basic concepts in optics

In this work, we have chosen to use a classical point of view to describe the electromagnetic field and the matter under consideration. This is justified by the fact that a classical treatment is appropriate at room temperature and for typical sizes around 100 nm to 150 nm. However, the formalism that will be developed along this thesis is adaptable to a quantum approach. Then, one can rely on the Maxwell's classical theory of electromagnetism which is presented with much details in many textbook [21, 22].

In this theory, the light-matter interaction is contained in the polarization $\underline{P}$ that acts as a source in the wave equation for $\underline{E}$.

$$\Delta\underline{E} - \nabla(\nabla\cdot\underline{E}) - \frac{1}{c^2}\frac{\partial^2\underline{E}}{\partial t^2} = \frac{1}{\epsilon_0 c^2}\frac{\partial^2\underline{P}}{\partial t^2} \tag{1.1}$$

The vector potential $\underline{A}$ follows a similar wave equation but the source field is replaced by the current density $\underline{J}$. It is in general very difficult to relate the local polarization to the macroscopic electric field. However, when the fields are not too intense, one can assume that a power expansion in the electric field is a valid way to express the polarization[23–26]. Nonlinear optics is the domain that focusses in the nonlinear terms of this perturbative expansion. The object linking the n-th power of the macroscopic electric field to the nonlinear polarization are $n+1$ rank tensors called susceptibilities and written $\chi^{(n)}$. The polarization can then be written :

$$\begin{aligned} \underline{P}(\omega) &= \underline{P}^{(1)}(\omega) + \underline{P}^{(2)}(\omega) + \underline{P}^{(3)}(\omega) + ... \qquad (1.2)\\ &= \epsilon_0 \big(\underline{\underline{\chi}}^{(1)}(\omega;\omega_1) \cdot \underline{E}(\omega_1) + \underline{\underline{\underline{\chi}}}^{(2)}(\omega;\omega_1,\omega_2) \cdot \underline{E}(\omega_1) \otimes \underline{E}(\omega_2) \\ &\qquad + \underline{\underline{\underline{\underline{\chi}}}}^{(3)}(\omega;\omega_1,\omega_2,\omega_3) \cdot \underline{E}(\omega_1) \otimes \underline{E}(\omega_2) \otimes \underline{E}(\omega_3) + ... \big) \qquad (1.3) \end{aligned}$$

Those multilinear expressions can be expressed by a convolution product in time-domain using the properties of the Fourier transform. However, by assuming linearity, invariance by time translation and causality, convolution products can also appear naturally.

$$\underline{P}^{(1)}(t) = \int_0^{+\infty} \underline{\underline{R}}^{(1)}(t_1) \cdot \underline{E}(t-t_1) dt_1 \qquad (1.4)$$

$$\underline{P}^{(2)}(t) = \int_0^{+\infty} \underline{\underline{\underline{R}}}^{(2)}(t_2,t_1) \cdot \underline{E}(t-t_2) \otimes \underline{E}(t-t_1) dt_1 dt_2 \qquad (1.5)$$

Where the tensors $R^{(n)}$ are the Fourier transform of the tensor $\chi^{(n)}$. In this notations, the time t_n corresponds to temporal distance from time t to a time of interaction in the past. Even if this definition is a bit misleading because the symbol t is an absolute time while the t_i are time intervals, this notation is the one mainly used and we conform with it. At this stage, no spatial dependance has been taken into account which means that only homogeneous samples like colloids for example can be described in such a way. In the space-dependent case, the expression of the polarization in time and frequency spaces becomes :

$$\begin{aligned} \underline{P}^{(n)}(\vec{r},t) = \int d\vec{r}_n \int d\vec{r}_{n-1} \cdots \int d\vec{r}_1 \int_0^{\infty} dt_n \int_0^{\infty} dt_{n-1} \cdots \int_0^{\infty} dt_1 \, \underline{\underline{\underline{R}}}^{(n)}(\vec{r},\vec{r}_n \cdots \vec{r}_1, t_n \cdots t_1) \cdot \\ \underline{E}(\vec{r}_n, t-t_n) \underline{E}(\vec{r}_{n-1}, t-t_n-t_{n-1}) \cdots \underline{E}(\vec{r}_1, t-t_n-\cdots-t_1) \qquad (1.6) \end{aligned}$$

The previous definition corresponds to the convention used in figure 1.1 (a). All the time intervals t_i add up to express the time delay between the different pulses. This definition is convenient when one deals with short pulses and wants to use time ordering. However, when the electric fields are not time-limited, referencing all the pulses from time t as depicted in figure 1.1 (b) can be convenient. The following two equations correspond to this choice of time-domain variables with its Fourier transformed counterpart :

$$\underline{P}^{(n)}(\vec{r},t) = \int d\vec{r}_n \int d\vec{r}_{n-1} \cdots \int d\vec{r}_1 \int_0^\infty dt_n \int_0^\infty dt_{n-1} \cdots \int_0^\infty dt_1 \, \underline{\underline{\underline{R}}}^{(n)}(\vec{r},\vec{r}_n \cdots \vec{r}_1, t_n \cdots t_1) \cdot \\ \underline{E}(\vec{r}_n, t - t_n)\underline{E}(\vec{r}_{n-1}, t - t_{n-1}) \cdots \underline{E}(\vec{r}_1, t - t_1) \quad (1.7)$$

$$\underline{P}^{(n)}(\vec{r},\omega) = \frac{1}{(2\pi)^n} \int d\vec{r}_n \int d\vec{r}_{n-1} \cdots \int d\vec{r}_1 \int d\omega_n \int d\omega_{n-1} \cdots \int d\omega_1 \, \underline{\underline{\underline{\chi}}}^{(n)}(\vec{r},\vec{r}_n \cdots \vec{r}_1, \omega_n \cdots \omega_1) \cdot \\ \underline{E}(\vec{r}_n, \omega_n)\underline{E}(\vec{r}_{n-1}, \omega_{n-1}) \cdots \underline{E}(\vec{r}_1, \omega_1) \; e^{-i\omega_s t} \quad (1.8)$$

A graphical representation of the time integration variable is given in figure 1.1. The use of time intervals allows to write the nonlinear response as a convolution between the response tensor and the incoming electric fields.

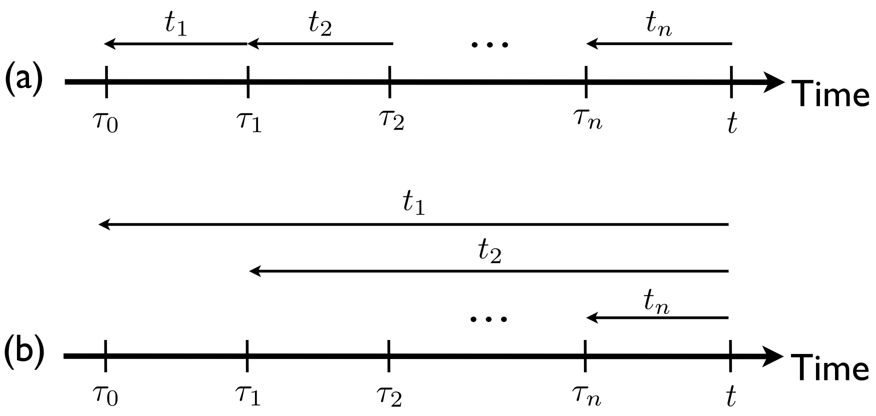

FIGURE 1.1: Time variable chosen in equation 1.6 : τ_i are absolute times while the t_i represent time intervals. In this diagram, the arrow direction from right to left corresponds, according to the definition, to a positive time interval.

No particular spatial dependance has been assumed in this expression and it is then necessary to integrate over all space. While describing a nanoparticle, this integration becomes bounded by the extension of the object. Thus, it can also be useful to consider relative space integration around each position $\vec{r}$ instead of the absolute positions $\vec{r}_i$ of equation 1.1.

1.2 Irreducible tensor for point objects

In this section, we will review some basics about group theory. The emphasis will be on the representation theory of the continuous Lie group SO(3) and its relationship with angular momentum theory. Many interesting books describe in details the application of group theory in physics and we refer to them for more details (Tinkham [27], Wigner [28], Hamermesh [29] for examples).

1.2.1 Introduction to group theory

1.2.1.1 Abstract group theory

We consider that the reader is already familiar with the basic properties of a group which is a set possessing an associative and invertible internal operation with a neutral element. Then, a representation of a group can directly be defined :

Definition 1.2.1. A group representation of the group G is an homomorphism Γ between G and $GL_n(K)$, the general linear group.

Thus, we associate to each abstract element in the group a matrix and the product of these matrices should follow the same rules than the group element themselves since the representation is an homomorphism. It is easier to work with group of matrices than with abstract elements of the original symmetry group and many informations can already be obtained from the representation. The homomorphisms Γ are not in general isomorphisms. When Γ is an isomorphim, the representation is said to be faithful : we assign a different matrix for each group element. On the other hand, we can assign the number 1, an element of $GL_1(\mathbb{R})$, to each group element to obtain the trivial representation. At an intermediate level, a matrix in the representation could represent a coset of the group.

A very important notion in group representation in the notion of irreducibility. Given some representations $\Gamma^{(i)}$ of the group G, it is easy to construct higher dimensional representations of the group. For example, for the group element A and B, we can construct :

$$\Gamma_{reducible}(A) = \begin{pmatrix} \Gamma^{(1)}(A) & 0 & 0 \\ 0 & \Gamma^{(2)}(A) & 0 \\ 0 & 0 & \ddots \end{pmatrix} \tag{1.9}$$

$$\Gamma_{reducible}(B) = \begin{pmatrix} \Gamma^{(1)}(B) & 0 & 0 \\ 0 & \Gamma^{(2)}(B) & 0 \\ 0 & 0 & \ddots \end{pmatrix} \tag{1.10}$$

Since the product of block diagonal matrices is reduced to the matrix product of the different blocks, these matrices are a representation of the group since they still satisfy the defining relation of an homomorphism.

$$\begin{pmatrix} \Gamma^{(1)}(A) & 0 & 0 \\ 0 & \Gamma^{(2)}(A) & 0 \\ 0 & 0 & \ddots \end{pmatrix} \begin{pmatrix} \Gamma^{(1)}(B) & 0 & 0 \\ 0 & \Gamma^{(2)}(B) & 0 \\ 0 & 0 & \ddots \end{pmatrix} =$$

$$\begin{pmatrix} \Gamma^{(1)}(A)\Gamma^{(1)}(B) & 0 & 0 \\ 0 & \Gamma^{(2)}(A)\Gamma^{(2)}(B) & 0 \\ 0 & 0 & \ddots \end{pmatrix} = \begin{pmatrix} \Gamma^{(1)}(AB) & 0 & 0 \\ 0 & \Gamma^{(2)}(AB) & 0 \\ 0 & 0 & \ddots \end{pmatrix} \quad (1.11)$$

However, since the matrices in the representation are all block diagonal in the same way, the representation can be thought of as a direct sum of lower dimensional ones and is then said to be reducible. We thus call a representation irreducible when it does not exist a transformation which bring all the matrices in an identical block diagonal form. The notion of irreducibility is central in group representation theory since any reducible representation can be written as the direct sum of the irreducible representations and since some powerful orthogonality theorems of great interest in physics exist for them : Irreducible representations can be recasted into unitary matrices ($U^\dagger = U^{-1}$) and they satisfy the following orthogonality relation :

$$\sum_R [\Gamma^{(i)}(R)]_{\mu\nu}[\Gamma^{(j)}(R)^*]_{\alpha\beta} = \frac{g}{l_i}\delta_{\mu\alpha}\delta_{\nu\beta}\delta_{ij} \quad (1.12)$$

With g the order of the symmetry group, l_i the dimension of the ith irreducible representation and R the different elements of the group under consideration. In equation 1.12, the summation over R implies that we are describing the orthogonality theorem for groups with a countable number of elements. However, this theorem can be extended to continuous groups by replacing the summation by an integration with a proper measure as we will see later. In physics, each eigenfunction can be associated to an irreducible representation. When computing matrix elements, one can then use the orthogonality theorem to infer vanishing elements without any explicit computation. We now turn our attention to the concept of character. As we have said before, the matrices of an irreducible representation can be recast into unitary matrices. However, this set of matrices is not unique since it is equivalent to an another set obtained through an unitary transformation. In order to have a description which is invariant to such transformation, one can use the invariance property of the trace through such transformation. In the context of group representation theory, the trace is called the character and is noted $\chi^{(i)}(R)$ for the trace of the matrix representing the element R in the i irreducible representation. Since all the matrices representing elements which belong to the same conjugacy class have the same trace (because they are related by unitary transformation), we can alternatively write $\chi^{(i)}(C_k)$ where C_k is the kth conjugacy class. The orthogonality theorem can also be expressed in term of characters of the irreducible representations :

$$\sum_k N_k \chi^{(i)}(C_k)\chi^{(j)}(C_k)^* = g\delta_{ij} \tag{1.13}$$

$$\sum_i \chi^{(i)}(C_k)\chi^{(i)}(C_l)^* = \frac{g}{N_k}\delta_{kl} \tag{1.14}$$

1.2.1.2 Angular momentum theory

In this section, we will introduce the concept of Lie groups, also called continuous groups, which are of great interest in physics. We will not enter deeply in the theory of Lie groups and will quickly focus on the angular momentum theory. The reader seeking for a more rigorous treatment can refer to the Gilmore's book for example [30].

Frequently, a physical system can exhibit a continuous symmetry, the most common example being the rotational invariance around an axis. In this case, many informations can be gained through the representation theory in a similar way with finite groups. However, the number of irreducible representations will be in general infinite. From a mathematical point of view, a Lie group is a group which also possesses the structure of a manifold. We recall that a manifold is a geometrical structure which is locally homeomorphic to $\mathbb{R}^n$, the nth dimensional cartesian space. For us, this means basically that it is possible to conduct differentiation over the Lie group. So, a Lie group can be thought of as a geometrical space in which two almost identical symmetry transformations are near, i.e. that the functions mapping the group operations on the manifold are differentiable. Examples of Lie groups are the group $GL_n(K)$ of $n \times n$ matrices of the field K, the special orthogonal groups $SO(n)$ of $n \times n$ real matrices with unit determinant and $SU(n)$ the group of $n \times n$ complex hermitian matrices with unit determinant. $SO(n)$ and $SU(n)$ will be studied later in this section since they physically describe the invariance by continuous rotations.

Another additional structure is the Lie algebra of a Lie group. Much information about a Lie group can be obtained by looking at the behavior of the symmetry operations around the identity. Thus, a vector space of infinitesimal transformation operators is constructed and is a Lie algebra :

Definition 1.2.2. A Lie algebra is a vector space endowed by a Lie bracket $[\bullet, \bullet]$ which is a bilinear, alternate operation satisfying the Jacobi identity.

The Lie algebra of the rotational group $SO(3)$, noted $\mathfrak{so}(3)$, is in fact well known by the physicists since it corresponds to the algebra of angular momentum operators. The main reason for the usefulness of the Lie algebra in physics is the following : any operation in the Lie group can be expressed as an exponential power series of the Lie algebra operators. As stressed in the previous section, symmetry operations provide a natural way to associate quantum numbers with eigenfuntions of the Hamiltonian. For a Lie group, since all symmetry operations can be expressed from Lie algebra operators, the "good" quantum numbers associated with a continuous symmetry are those associated with the finite number of operators in the Lie algebra.

The rotation group $SO(3)$ provides an excellent illustration of the Lie algebra of a Lie group. The rotation of a function $\psi(r)$ by an angle θ around an axis defined by the vector $\vec{n}$ can be expressed through an operator $R(\vec{n}, \theta)$. By the definition of the Lie group, this operator is orthogonal and can thus be written as the exponential of an Hermitian matrix.

$$R(\vec{n}, \theta) = e^{-iS(\vec{n},\theta)} \tag{1.15}$$

We now consider an infinitesimal translation θ in order to find the operators in the Lie algebra. Since the transformation is small, orders higher than one in the Taylor expansion of the exponential are neglected.

$$R(\vec{n}, \theta) = 1 - iS(\vec{n}, \theta) \tag{1.16}$$

Since the rotation is small, we can approximately say that the difference between the rotated and non rotated function is of first order in θ. We defined the angular momentum operators, vectors in the Lie algebra, in this way :

$$R(\vec{e}_x, \theta)\psi(\vec{r}) - \psi(\vec{r}) = -i\theta J_x \psi \tag{1.17}$$

Where we have chosen the rotation to be around the x axis. Of course, similar equations exist for any rotation axis. Using angular momentum operators, the finite rotation operator can then be recasted using infinitesimal angular momentum operators.

$$R(\vec{n}, \theta)\psi = e^{-i\theta(\vec{n}\cdot\vec{J})}\psi \tag{1.18}$$

Let us now work out the commutation properties of the angular momentum operators which will be the definition of the Lie algebra. Due to the non-commutativity of SO(3), making a rotation around x followed by another one around y and repeating this with the inverse rotations leads approximately to a rotation around the z axis :

$$R(\vec{e}_y,\theta')^{-1}\ R(\vec{e}_x,\theta)^{-1}\ R(\vec{e}_y,\theta')\ R(\vec{e}_x,\theta) \approx R(\vec{e}_z,\theta'\theta) \tag{1.19}$$

$$e^{i\theta' J_y}e^{i\theta J_x}e^{-i\theta' J_y}e^{-i\theta' J_x} \approx e^{i\theta\theta' J_z} \tag{1.20}$$

Expanding the exponentials up to second order in θ and θ', one can observe than the first order terms cancel each other out and that the $\theta\theta'$ terms have to obey the following commutation relation :

$$J_xJ_y - J_yJ_x = iJ_z \tag{1.21}$$

In a more compact form, the commutation relations between angular momentum operators can be written :

$$[J_i, J_j] = i\epsilon_{ijk}J_k \tag{1.22}$$

Where ϵ_{ijk} is the Levi-Civita symbol and i, j and k represent the cartesian coordinates. Equation 1.22 defines the Lie algebra $\mathfrak{so}(3)$ of the group $SO(3)$ and the angular momentum operators constitutes a good set to define quantum numbers. If one has started from the Lie algebra as a definition, he could have constructed finite rotations. However, a Lie group has a unique Lie algebra but a Lie algebra can construct many Lie groups by exponentiation. For example, the Lie group $SU(2)$ of complex 2×2 hermitian matrices possesses the same Lie algebra.

At this stage, we can give a short presentation of the representations of $SO(3)$ and $SU(2)$. The usual method is firstly to prove the existence of an homomorphism between these two Lie groups. More precisely, to each element on $SO(3)$ it is possible to associate two elements in $SU(2)$. Secondly, it is possible to work out the irreducible representations of $SU(2)$ and then to obtain those of $SO(3)$. The irreducible representations of $SO(3)$ are called the Wigner matrices $D^{(j)}(\alpha, \beta, \gamma)$ where α, β and γ are the Euler angles defined in figure 1.2 in the $z - y' - z'$ convention and are $(2j+1)\times(2j+1)$ hermitian matrices. This is the convention (A) used by Varshalovich [31] and it is different from the one used by Mathematica which follows an $z - x' - z'$ convention with the Wigner matrix defined as $D^{(j)}(\phi, \theta, \psi)$. The two conventions describe an equivalent rotation when :

$$\phi = \alpha + \frac{\pi}{2} \qquad \beta = \theta \qquad \gamma = \psi - \frac{\pi}{2} \tag{1.23}$$

In the case of $SO(3)$, the number of irreducible representations is infinite : j is a positive integer number. In $SU(2)$, half-integer representations also exist and they correspond to spin degrees of freedom. When the space under interest in the usual geometrical space, the function which subtends the irreducible representations are the well known spherical

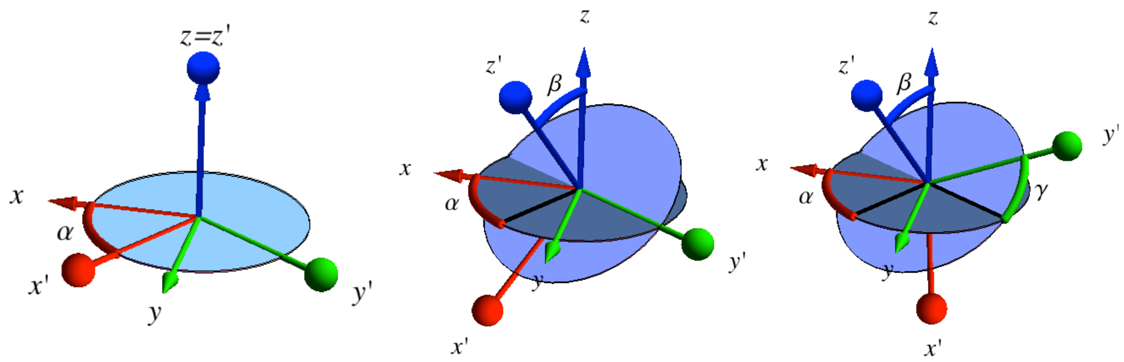

FIGURE 1.2: Successive rotations α, β and γ in the $z-y-z$ convention used thorough this manuscript. Many conventions using either the x axis or the y axis for the second rotation, making rotation from initial or new axis and using rotation α and β starting from the x or the y components. In this thesis, we use rotation in the $z-y-z$ convention, from new axis with angles α and β starting from x. Those graphs have been obtained using the Mathematica notebook on Euler angles written by Strauch [32].

harmonics defined by :

$$Y_{lm}(\theta,\varphi) = \sqrt{\frac{2l+1}{4\pi}}\sqrt{\frac{(l-m)!}{(l+m)!}}P_l^m(\cos\theta)e^{im\varphi} \tag{1.24}$$

Where the P_l^m are the associated Legendre polynomials. We have replaced the letter j usually reserved to abstract angular momentum by the letter l which is customary when using spherical harmonics representation. The rotation of a spherical harmonics is thus expressed using the corresponding Wigner matrix.

$$R(\theta,\varphi,\psi)\ Y_{lm} = \sum_{m'=-l}^{l} D^{(l)}_{m'm}(\theta,\varphi,\psi)\ Y_{lm'} \tag{1.25}$$

These functions are labelled according to their eigenvalues in the Lie algebra of $SO(3)$. In the context of geometrical angular momentum, the operators J are denoted L and called orbital angular momentum.

One subject of great interest in physics is the coupling of angular momenta. The problem is the following : one has two distinct systems with angular momenta L_1 and L_2 and want to consider the angular momentum of the whole system $L = L_1 + L_2$. A basis to describe the angular momentum L could be constituted of the direct products of $2l_1+1$ functions of L_1 and the $2l_2+1$ functions of L_2. However, this representations will not be reducible in general and one has to reduce it to be able to use efficiently angular momentum theory in the product space. Using bracket notation or directly spherical harmonics, one can define coefficients which do the reduction for us :

$$|lml_1l_2\rangle = \sum_{m_1m_2} C^{lm}_{l_1m_1,l_2m_2} |l_1m_1\rangle \otimes |l_2m_2\rangle \tag{1.26}$$

$$Y^{lm}_{l_1l_2}(\theta,\varphi,\theta',\varphi') = \sum_{m_1m_2} C^{lm}_{l_1m_1,l_2m_2} Y_{l_1m1} \otimes Y_{l_2m_2} \tag{1.27}$$

The coefficients $C^{lm}_{l_1m_1,l_2m_2}$ are called the Clebsch-Gordan coefficients and their values has been calculated and tabulated. It is also useful to define $3j$ symbols that are only an alternative definition to the Clebsch-Gordan coefficients and are easier to handle in calculations.

$$\begin{pmatrix} l_1 & l_2 & l \\ m_1 & m_2 & -m \end{pmatrix} = (-1)^{l_1-l_2+m} \frac{1}{\sqrt{2l+1}} C^{lm}_{l_1m_1l_2m_2} \tag{1.28}$$

$3j$ symbols are invariants by even permutations of columns and change by a phase $(-1)^{l_1+l_2+l}$ through odd permutations or by inverting signs in the second row. Finally, we define the $6j$ symbols which correspond to the recoupling of three angular momenta. When coupling 3 irreducible representations of SO(3) of order J_1, J_2 and J_3, one can operate the coupling in three different ways :

$$1)\ \ J_1 + J_2 = J_{12} \qquad \text{then} \qquad J_{12} + J_3 = J \tag{1.29}$$

$$2)\ \ J_2 + J_3 = J_{23} \qquad \text{then} \qquad J_{23} + J_1 = J \tag{1.30}$$

$$3)\ \ J_1 + J_3 = J_{13} \qquad \text{then} \qquad J_{13} + J_2 = J \tag{1.31}$$

Those three coupling schemes lead to the same set of states up to an unitary transformation. The coefficients of this transformation are related to the $6j$ symbols by a normalization and a phase factor chosen to make them more symmetric. For example, if the coefficients relating the coupling scheme 1 to the scheme 2 are $U(J_1J_2JJ_3; J_{12} \rightarrow J_{23})$, the corresponding $6j$ are defined by :

$$U(J_1J_2JJ_3; J_{12} \rightarrow J_{23}) = (-1)^{J_1+J_2+J_3+J} \sqrt{(2J_{12}+1)(2J_{23}+1)} \begin{Bmatrix} J_1 & J_2 & J_{12} \\ J_3 & J & J_{23} \end{Bmatrix} \tag{1.32}$$

In this thesis, the $6j$ will be appear while using the translational addition theorem in chapter 5 for vector spherical harmonics.

1.2.1.3 Definition of irreducible tensor

This section will be dedicated to the irreducible tensor formalism. Tensors are often used in science to describe some physical properties in a vector space. For example, the tensor giving the second order polarization $\chi^{(2)}$ is related to the polarization by :

$$P^i(\omega_1+\omega_2) = \chi^{(2)}(\omega_1,\omega_2)^i_{jk} \cdot E^j(\omega_1) \otimes E^k(\omega_2) \tag{1.33}$$

Tensors possess some constraints over their components according to the geometrical symmetries of the system they describe. Since all the finite groups of symmetry are subgroups of the rotation group $SO(3)$, it is interesting to recast tensors into an irreducible form, i.e. a tensor which behave like an irreducible representation under rotation. For instance, one can show that, by the simple following change of basis, cartesian vectors can be rotated using the $J=1$ irreducible representation of $SO(3)$[1].

$$\vec{e}_{\pm 1} = \mp \frac{1}{\sqrt{2}}\left(\vec{e}_x \pm i\vec{e}_y\right) \qquad \vec{e}_0 = \vec{e}_z \tag{1.35}$$

However, the irreducible decomposition of a cartesian tensor will not be, in general, that straightforward. A rank n cartesian tensor T is written as the direct sum of its irreducible part :

$$T = \sum_{\oplus \tau, J} T^{(\tau)J} \tag{1.36}$$

The so-called seniority index τ corresponds to the possibility, for a cartesian tensor, to be reduced in more than one irreducible part of the same weight J. The irreducible parts of a tensor describing physical properties contain straightforward information about the influence of the symmetry on physical properties[33]. They are also convenient to deal with when one wants to make reference-frame transformations and orientational averaging. The reduction of a cartesian tensor into its irreducible parts is done in two steps. Firstly, a change of basis 1.35 is done for each of the ranks of the cartesian tensor. The resulting tensor is in general not irreducible and is then reduced using $3n-j$

---

[1] This change of basis using a complex coefficient for the $\vec{e}_y$ components is more tricky that it looks. As one can see in equation 1.40, the metric tensor is no longer diagonal and is now equal to :

$$g = \begin{pmatrix} 0 & 0 & -1 \\ 0 & 1 & 0 \\ -1 & 0 & 0 \end{pmatrix} \tag{1.34}$$

This implies that covariant and contravariant vectors are no longer equivalents and one needs to take care of this in calculations. In this work, the notation does not always distinguish the two since the context is in general clear enough to know the nature of the vector.

symbols. This reduction scheme as well as tables for the reduction of $n \leq 3$ cartesian tensors can be found in Jerphagnon's article [34]. For instance,the second rank tensor α can be represented as the direct sum of three irreducible tensors :

$$\alpha = \alpha^0 \oplus \alpha^1 \oplus \alpha^2 \tag{1.37}$$

- the trace α^0 with one component α^{00} ;
- the antisymmetric part α^1 with three components $\alpha^{1,\pm1}$ and α^{10};
- the traceless symmetric part α^2 with five components $\alpha^{2,\pm2}$, $\alpha^{2,\pm1}$ and α^{20}.

Each of these components can be related to the cartesian ones using the mentioned tables. As in angular momentum theory, each irreducible tensor part of weight J has $2J+1$ components and a rotation of a weight J irreducible tensor is accomplished with the help of the Wigner D matrix.

$$R_{(\theta,\varphi,\psi)}[T^J]^M = \sum_{M'=-J}^{J} \mathcal{D}^J(\theta,\varphi,\psi)_{M'M} T^{JM'} \tag{1.38}$$

This equation can be considered as the definition of an irreducible tensor of weight J. Of course, one can also make a definition starting from the infinitesimal rotation :

$$[J^\mu, T^{JM}] = \sqrt{J(J+1)} C^{JM+\mu}_{JM1\mu} T^{JM+\mu} \tag{1.39}$$

The commutation properties of irreducible tensors are thus the same than those with spherical harmonics. The reduction of a tensor into its irreducible parts is interesting by itself for physical applications since a norm can be defined which allows to interpret and compare the magnitude of different effects.

$$||T^J||^2 = \sum_M (-1)^M T^{JM}\ T^{J,-M} \tag{1.40}$$

The norm of the different irreducible parts help measuring the degree of anisotropy of a given effect. Moreover, if the geometry of the system is symmetric under some point groups, the simplifications induced in the tensor will be easier to handle in the spherical formalisms in most cases. However, for this study, we will need to make some algebra between different tensors and thus need to have a definition for direct product and contracted product. We can not take the cartesian product of the two irreducible spaces as a direct product since the result would not be irreducible. Thus, we define the irreducible tensor product as :

$$\{T^{j_1} \otimes U^{j_2}\}^{JM} = \sum_{m_1,m_2} C^{JM}_{j_1m_1,j_2m_2} T^{j_1m_1}\, U^{j_2m_2} \tag{1.41}$$

The produced tensor is an irreducible tensor of weigh J. The fully contracted product between tensor of same ranks is easy to define :

$$T^J \cdot U^J = \sum_M (-1)^M T^{JM}\, U^{J,-M} \tag{1.42}$$

1.2.2 Multipolar molecules for nonlinear optics

The field of organic nonlinear optics experienced a revival in the past 20 years thanks to the use of irreducible tensors. The objective was to synthesize nonlinear molecular units with a high hyperpolarizability β that can be used to develop a material with a high $\chi^{(2)}$ in the macroscopic frame. While the attention was previously directed toward polar nonlinear molecules having only a non-vanishing dipolar response tensor part, group theory help designing new multipolar molecules that are not dominated by a single dipolar component of their irreducible parts [35–37]. Those molecules no longer have $C_{\infty\nu}$ as a symmetry group but rather belong to C_{3h} or D_{3h}. A large family of multipolar molecules has been introduced since then but then schematically represented by the molecules (b) and (c) in figure 1.3.

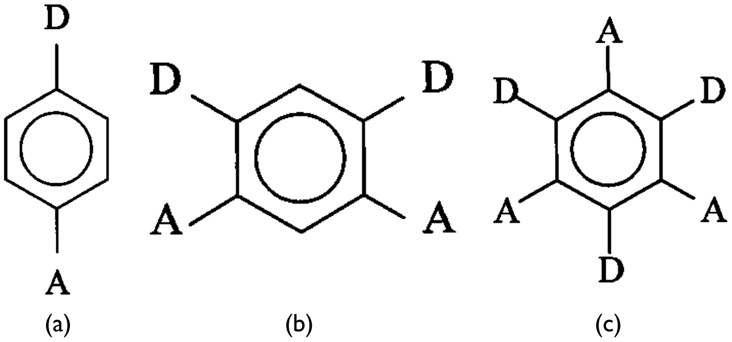

Figure 1.3: Schematic representation of non-centrosymmetric molecules investigated by Brasselet and Zyss [36]. (a) Dipolar molecule. (b) Multipolar molecule. (c) Octupolar molecule.

Under Kleinman symmetry, only the irreducible tensors $\beta^{J=1}$ and $\beta^{J=3}$ do not vanish and the total hyperpolarizability can be written :

$$\beta = \beta^{J=1} \oplus \beta^{J=3} \tag{1.43}$$

As said in the previous section, the $J = 1$-components are a signature of the dipolar nature of the molecule while the $J = 3$-components correspond to a nonlinear octupolar anisotropy. Because of the invariance of the norm of an irreducible tensor under rotations, the nonlinear anisotropy ρ of such molecules has been defined in this field by the ratio of the octupolar part's norm over the dipolar one :

$$\rho = \frac{||\beta^{J=3}||}{||\beta^{J=1}||} \tag{1.44}$$

This ratio, that vary from 0 to $+\infty$ for a dipolar and an octupolar molecule respectively, can be used to relate the weight that the symmetry has on the efficiency of the quadratic nonlinear response. In a fully irreducible tensorial formalism, the polarization is expressed as the fully contracted product of the hyperpolarizability and the incoming electric field. However, since the molecules studied were very small, the extended nature of the electric field did not have to be taken into account and only the local polarization vector nature has to be reduced instead of the full vectorial field. Since a fully contracted product gives a scalar as result, one need to contract the hyperpolarizability with a tensor of the same rank. The reading tensor F is defined in this aim by $F = e^{2\omega} \otimes E^{\omega} \otimes E^{\omega}$. The polarization is then :

$$P^{2\omega} = \beta \cdot F \tag{1.45}$$

The vector $e^{2\omega}$ corresponds to the direction of the detector since, by the contracted product, the polarization will be calculated along this direction. One can experimentally choose a combination of polarizations for the incoming fields and a specific direction for a polarizer before the detector in order to have different surviving components in the reading tensor F and then measuring different components of the hyperpolarizability.

As mentioned before, those results are obtained under the simplification of the Kleinman symmetry for the hyperpolarizability. The Kleinman symmetry is valid only when non-resonant processes are involved which is not a problem in this case since such a process is better avoided to not damage the system. However, this matter of fact is also a limitation of those molecules since mostly off-resonant hyperpolarizabilities are considered. Using much more robust metallic nanoparticles, one can expect to work closer to the resonance and then achieve higher efficiencies.

1.3 Multipolar radiation

1.3.1 Spherical expansion of vector potential Green's function

Because of the gauge invariance of the Maxwell equation, the electric field can be expressed in term of the vector potential $\underline{A}$ and the scalar potential Φ. In the Lorentz gauge, the scalar and the vector potentials satisfy two inhomogeneous wave equations :

$$\Delta\Phi - \frac{1}{c^2}\frac{\partial^2\Phi}{\partial t^2} = -\frac{\rho}{\epsilon_0} \tag{1.46}$$

$$\Delta\underline{A} - \frac{1}{c^2}\frac{\partial^2\underline{A}}{\partial t^2} = -\mu_0\underline{J} \tag{1.47}$$

The scalar potential is of no use now since no static charges are considered now. In the case of an harmonic time dependence, the inhomogeneous wave equation becomes the Helmholtz equation :

$$\Delta\underline{A} + k^2\underline{A} = -\mu_0\underline{J} \tag{1.48}$$

This Helmholtz equation can be solved in term of the Green function. The vector potential $\underline{A}(\vec{r})$ caused by a current distribution $\underline{J}(\vec{r'})$ is then given by the following integral form :

$$\underline{A}(\vec{r}) = \frac{\mu_0}{4\pi}\int \underline{J}(\vec{r'})\frac{e^{ik|\vec{r}-\vec{r'}|}}{|\vec{r}-\vec{r'}|}d^3r' \tag{1.49}$$

In order to express the vector potential in terms of multipoles, one can expand the Green function into spherical harmonics. This expansion is defined over all space using the following form :

$$\frac{e^{ik|\vec{r}-\vec{r'}|}}{4\pi|\vec{r}-\vec{r'}|} = ik\sum_{lm} j_l(kr_<)Y^*_{lm}(\theta_<,\phi_<)h^{(1)}_l(kr_>)Y_{lm}(\theta_>,\phi_>) \tag{1.50}$$

Where $r_<$ corresponds of the vector having the smallest norm between r and r' while $r_>$ corresponds to the biggest one. Thus, at fixed $|r|$, the expression of the spherical of the expansion varies when the expansion is considered inside the sphere of radius $|r|$ or outside.

Inserting that expansion into the integral form of the vector potential, one can get the following multipolar expansion :

$$\underline{A}(\vec{r}) = ik\mu_0\sum_{lm}\vec{J}_{lm}(r)h^{(1)}_l(kr)Y_{lm}(\theta,\phi) + \vec{\tilde{J}}_{lm}(r)j_l(kr)Y_{lm}(\theta,\phi) \tag{1.51}$$

Where the multipolar coefficients $\vec{J}_{lm}(r)$ and $\vec{\tilde{J}}_{lm}(r)$ are defined by :

$$\vec{J}_{lm}(r) = \int_0^r \underline{J}(\vec{r'}) j_l(kr') Y^*_{lm}(\theta', \phi') d^3r' \tag{1.52}$$

$$\vec{\tilde{J}}_{lm}(r) = \int_r^{+\infty} \underline{J}(\vec{r'}) h_l^{(1)}(kr') Y^*_{lm}(\theta', \phi') d^3r' \tag{1.53}$$

The multipolar expansion can be greatly simplified by considering only sources that have a finite extension in space and evaluating the fields outside a sphere containing those sources. The coefficients $\vec{\tilde{J}}_{lm}(r)$ are then zero because the current density is vanishing over the r' values. Moreover, the coefficients $\vec{J}_{lm}(r)$ does not depend on r anymore and the integral can be conducted over all space for simplification. Then, one gets the following multipolar expansion for the vector potential :

$$\underline{A}(\vec{r}) = ik\mu_0 \sum_{lm} \vec{J}_{lm} h_l^{(1)}(kr) Y_{lm}(\theta, \phi) \tag{1.54}$$

Where the coefficients $\vec{J}_{lm}$ have been defined as :

$$\vec{J}_{lm} = \int \underline{J}(\vec{r'}) j_l(kr') Y^*_{lm}(\theta', \phi') d^3r' \tag{1.55}$$

In the long wavelength limit and in the far field region, each term can be associated with the usual multipoles of electrostatic : $l = 0$ to the dipole, $l = 1$ to the quadrupole,... The radiation space can be split into three zones : the near zone, the induction zone and the far zone. In the near and far zones, simplifications can be made to avoid the use of the spherical formalism. Anyway, the spherical expansion of the vector potential is valid everywhere and no approximation has been made so far.

1.3.2 Dipolar and quadrupolar radiation

We are now going to show how one can associate each term of the above spherical expansion to the usual multipolar radiations. Let us consider the first term $l = 0$ of the expansion. Assuming that only J_{00} in equation 1.54 is non-zero and using in expression in terms of $\underline{J}(\vec{r'})$, one is lead to the following expression :

$$\underline{A}(\vec{r}) = ik\mu_0 h_0^{(1)} Y_{00}(\theta, \phi) \iiint \underline{J}(r') j_0(kr') Y_{00}(\theta', \phi')^* d^3r' \tag{1.56}$$

Using the explicit expression for the spherical harmonic Y_{00} and spherical Hankel function $h_0^{(1)}$ (see appendix A for the properties of the spherical Bessel-like function used in this chapter), the previous equation becomes :

$$\underline{A}(\vec{r}) = \frac{\mu_0}{4\pi}\frac{e^{ikr}}{r}\iiint \underline{J}(r')j_0(kr')d^3r' \tag{1.57}$$

As pointed out, this relationship is true for any size of the radiating object and the wavelength. We now make the approximation that the object is small compared to the wavelength. This approximation is illustrative but will not be valid in the case of nanoparticles of non negligible size. This means that $\underline{J}(\vec{r}')$ is non-zero only for small values of kr'. In the small argument limit, the spherical Bessel function simply tends towards 1 at first order which give us the following expression for the vector potential :

$$\underline{A}(\vec{r}) \underset{kr'\ll 1}{\longrightarrow} \frac{\mu_0}{4\pi}\frac{e^{ikr}}{r}\iiint \underline{J}(r')d^3r' \tag{1.58}$$

Integrating by part and then using the charge conservation law ($\nabla \cdot \underline{J}(r') = i\omega\rho(r')$), one can show the following identity :

$$\iiint \underline{J}(r')d^3r' = -\iiint \Big(\nabla \cdot \underline{J}(r')\Big)\vec{r}'d^3r' = -i\omega\iiint \vec{r}'\rho(r')d^3r' = -i\omega\vec{\mu} \tag{1.59}$$

The last equality is the definition of the dipole moment of electrostatics $\vec{\mu}$. Finally, the electric dipolar vector potential is :

$$\underline{A}(\vec{r}) = -\frac{\omega\mu_0}{4\pi}\frac{e^{ikr}}{r}\vec{\mu} \tag{1.60}$$

This equation is exactly the one which define a pure dipolar vector potential as one can find in Jackson's book [21]. We now turn our attention to the next order. Thus, we keep only the $l = 1$ terms in equation 1.54 which correspond to the electric quadrupolar and magnetic dipolar radiations and contain three values of $m = -1, 0, 1$.

$$\underline{A}(\vec{r}) = ik\mu_0 h_1^{(1)}(kr)\sum_m Y_{1m}(\theta,\phi)\iiint \underline{J}(r')j_1(kr')Y_{1m}(\theta',\phi')^* d^3r' \tag{1.61}$$

The sum over m of a spherical harmonics product is related to Legendre polynomials :

$$\sum_m Y_{1m}(\theta,\phi)Y_{1m}(\theta',\phi')^* = \frac{3}{4\pi}P_1\Big(\frac{\vec{r}\cdot\vec{r}'}{rr'}\Big) \tag{1.62}$$

$$\underline{A}(\vec{r}) = \frac{3i}{4\pi}k\mu_0 h_1^{(1)}(kr)\iiint \underline{J}(r')j_1(kr')P_1\Big(\frac{\vec{r}\cdot\vec{r}'}{rr'}\Big)d^3r' \tag{1.63}$$

Since the first Legendre polynomial is $P_1(x) = x$, the previous equation can be drastically simplified.

$$\underline{A}(\vec{r}) = \frac{3i}{4\pi} k\mu_0 \frac{h_1^{(1)}(kr)}{r} \iiint \underline{J}(r') \frac{j_1(kr')}{r'} \vec{r} \cdot \vec{r}' d^3r' \tag{1.64}$$

We can again use the long wavelength limit of the spherical Hankel and Bessel function to obtain the solution for a source which is very small compared to the wavelength :

$$\underline{A}(\vec{r}) = \frac{\mu_0}{2\pi} \frac{e^{ikr}}{r} \Big(\frac{1}{r} - ik \Big) \iiint \underline{J}(r') \big(\vec{n} \cdot \vec{r}' \big) d^3r' \tag{1.65}$$

We defined the unit vector $\vec{n} = \vec{r}/|r|$. The magnetic dipolar and electric quadrupolar radiations are mixed in this equation. If one want to extract them, it is necessary to separate the antisymmetric part (magnetic dipolar) and the symmetric part (electric quadrupolar) of the matrix $\underline{J}(r')(\vec{n} \cdot \vec{r}')$.

This section has allowed us to familiarize with the spherical expansion of the vector potential Green's function. Before discussing vector multipole fields, it is however necessary to introduce the wavenumber dependence of the multipolar basis to describe electromagnetic radiation.

1.3.3 Multipolar expansion of the current density

In section 1.3.1, the spherical expansion of the Green's function of the Helmholtz equation has been discussed. It is important to observe that the Helmholtz equation is obtained for a fixed wavenumber k and that the time-domain variations of the vector potential are obtained by Fourier transform.

In this context, the expansion coefficients of the vector potential were obtained by projecting the current density over the scalar multipolar basis :

$$\vec{J}_{lm}(k) = \int \underline{J} \; \psi_{klm} d^3r' \tag{1.66}$$

Where the dependence of the projection on the wavenumber has been emphasized. Doing this projection for all wavenumbers is in fact a spherical Bessel transform that can be defined for an abstract scalar function in the following way :

$$f(r, \theta, \varphi) = \sum_{lm} \int_k f_{klm} \psi_{klm} dk \tag{1.67}$$

$$\psi_{klm} = \sqrt{\frac{2}{\pi}} k \; j_l(kr) Y_{lm}(\theta, \varphi) \tag{1.68}$$

$$\tilde{\psi}_{klm} = \sqrt{\frac{2}{\pi}}k\ h_l^{(1)}(kr)Y_{lm}(\theta,\varphi) \tag{1.69}$$

The additional $\sqrt{2/\pi}\ k$ factor has been added to ensure the orthogonality of the scalar multipolar basis for different wavenumbers using the following property of the spherical Bessel functions :

$$\int_r j_l(kr)j_l(k'r)r^2dr = \frac{\pi}{2k^2}\delta(k-k') \tag{1.70}$$

The basis function $\tilde{\psi}_{klm}$ has also been introduced. It is not needed at this point for the considered current density because this field is regular but if one would have to consider expansion of diverging field, those elements have to be used. When dealing with the vector potential or electromagnetic fields, the diverging basis elements are to be used according to section 1.3.1 When one consider the Helmholtz equation with a fixed k, only the projection of current density on this k subspace contributes to the radiation. Thus, if one is observing only a few frequencies, only the corresponding parts of the current density has to be taken into account.

Due to this choice of normalization, the spherical expansion of the Green's function and the vector potential can now be written :

$$G(r-r') = \frac{e^{ik|r-r'|}}{4\pi|r-r'|} = \frac{i\pi}{2k}\sum_{lm}\tilde{\psi}_{klm}(r,\theta,\varphi)\psi_{klm}(r',\theta',\varphi') \tag{1.71}$$

$$\underline{A} = \frac{i\pi}{2k}\mu_0\sum_{lm}\tilde{\psi}_{klm}(kr)\int_{r'}\underline{J}(\vec{r}')\psi^*_{klm}(\vec{r}')d^3r' \tag{1.72}$$

Using the spherical Bessel transform of the current density, one gets :

$$A = \frac{i\pi}{2k}\mu_0\sum_{lm}\vec{J}_{klm}\tilde{\psi}_{klm}(\vec{r}) \tag{1.73}$$

Where $\vec{J}_{klm}$ are the components of the spherical Bessel transform of the current density. The basis ψ_{klm} is a convenient multipolar basis to deal with scalar fields. However, the quantities described in electromagnetism are mostly vector fields. Here, each of the components of the current density is expanded over the scalar multipolar basis but the irreducibility of the expansion is not conserved because the vectorial nature of the current density has not been taken into account.

Thus, it is necessary to introduce a vector multipolar basis that would allow to expand vector fields while obtaining irreducible components.

1.3.4 Definition of the vector spherical harmonics

A naive method to construct a vector basis of spherical harmonics could be to simply couple each scalar spherical harmonics with the cartesian basis vector e_x, e_y and e_z. However, this construction will not be consistent with the irreducible tensor formalism since we will not form irreducible tensors in this way. To solve this problem, we use the irreducible tensor product of spherical harmonics with spherical basis vectors [31]. We recall here the convention used in this report for the spherical basis vector :

$$\begin{aligned}\vec{e}_1 &= -\frac{1}{\sqrt{2}}(\vec{e}_x + i\vec{e}_y) && (1.74)\\ \vec{e}_0 &= e_z && (1.75)\\ \vec{e}_{-1} &= \frac{1}{\sqrt{2}}(\vec{e}_x - i\vec{e}_y) && (1.76)\end{aligned}$$

This simple orthogonal transformation offers an irreducible basis vectors. We now define vector spherical harmonics (VSH) as the irreducible tensor product between this basis and scalar spherical harmonics :

$$\underline{Y}_l^{JM} = \{Y^l \otimes \underline{e}^{S=1}\}^{JM} = \sum_{m\sigma} C_{lm1\sigma}^{JM} Y_{lm}\ \underline{e}_\sigma \tag{1.77}$$

We can also easily extend this definition to tensor spherical harmonics. These functions will be eigenfunctions of an angular momentum operator J, direct sum of an orbital angular momentum L and a spin angular momentum in the tensor spherical basis. Tensor spherical harmonics are written Y_{ls}^{JM} and obey the following identities :

$$\begin{aligned}J^2 Y_{ls}^{JM} &= j(j+1)Y_{ls}^{JM} && (1.78)\\ S^2 Y_{ls}^{JM} &= s(s+1)Y_{ls}^{JM} && (1.79)\\ L^2 Y_{ls}^{JM} &= l(l+1)Y_{ls}^{JM} && (1.80)\\ J_z Y_{ls}^{JM} &= MY_{ls}^{JM} && (1.81)\end{aligned}$$

The tensor equivalent of the equation 1.77 is

$$Y_{ls}^{JM} = \{Y^l \otimes e^{S=s}\}^{JM} = \sum_{m\sigma} C_{lms\sigma}^{JM} Y_{lm}\ e_\sigma^s \tag{1.82}$$

Of course, tensor spherical harmonics reduce to scalar ones when $s = 0$ and to vector ones when $s = 1$. A fundamental relationship which allows to find many properties of the VSH algebra is :

$$2iL \wedge \underline{Y}_{l1}^{JM} = \Big(J(J+1) - l(l+1) - 2\Big)\underline{Y}_{l1}^{JM} \tag{1.83}$$

Using mainly VSH, we will usually omit the subscript $s = 1$ in $\underline{Y}_{l1}^{JM}$. The selection rules of the Clebsch-Gordan coefficients show that J and l are not independent : $l = J-1,\ J$ or, $l+1$. We find that for each irreducible rank J, we need three independent vectors $\underline{Y}_{J-1}^{JM}$, $\underline{Y}_{J}^{JM}$ et $\underline{Y}_{J+1}^{JM}$ in accordance to the dimension of the three dimensional euclidean space. The VSH defined by Jackson [21] in the multipolar expansion of the electromagnetic field are equivalent to Y_l^{lm} :

$$\underline{Y}_l^{lm} = \underline{X}_{lm} = \frac{1}{\sqrt{l(l+1)}}\underline{L}Y_{lm} \tag{1.84}$$

More equivalences between the different notations and conventions used to express the vector spherical harmonics are given in appendix B.

1.3.5 Vector multipole fields expansion

In the previous section, we expanded the vector potential over a scalar basis and the coefficients $\vec{J}_{klm}$ contained the vectorial nature of the field. However, in this formalism, different orders of multipolar radiation come mixed and the algebra involved to separate them becomes more and more tricky as the orders grow. This algebra is in fact closely related to an irreducible tensors decomposition and to avoid doing it, we can directly use a vector irreducible tensor formalism, i.e. vector multipole fields.

Let us start by writing the vector $\vec{J}_{klm}$ over the irreducible basis : $\underline{J}_{klm} = \sum_\sigma J^\sigma_{klm}\underline{e}_\sigma$. Inserting it in equation 1.54, we get terms like $Y_{lm}\ \underline{e}_\sigma$ that we can express as a sum of vector spherical harmonics. To get this sum, we simply use the definition of vector spherical harmonics and introduce orthogonality relationships between Clebsch-Gordan coefficients.

$$\underline{Y}_{l1}^{J'M'} = \sum_{m\sigma} C_{lm1\sigma}^{J'M'} Y_{lm}\underline{e}_\sigma \tag{1.85}$$

$$\sum_{JM} \underline{Y}_{l1}^{JM} \left(\sum_{m\sigma} C_{lm1\sigma}^{JM} C_{lm1\sigma}^{J'M'} \right) = \sum_{m\sigma} C_{lm1\sigma}^{J'M'} Y_{lm}\ \underline{e}_\sigma \tag{1.86}$$

Rearranging the left-hand side sum and identifying the terms of equal orders, we find :

$$Y_{lm}\underline{e}_\sigma = \sum_{JM} \underline{Y}_{l1}^{JM} C_{lm1\sigma}^{JM} \tag{1.87}$$

We can now expand the vector potential over vector spherical harmonics :

$$\begin{aligned}
\underline{A}(\vec{r}) &= \frac{i\pi}{2k}\mu_0 \sum_{lm} h_l^{(1)}(kr) \sum_{\sigma} J^{\sigma}_{klm} Y_{lm} \underline{e}_{\sigma} && (1.88)\\
&= \frac{i\pi}{2k}\mu_0 \sum_{JlM} h_l^{(1)}(kr) \Big(\sum_{m\sigma} J^{\sigma}_{klm} C^{JM}_{lm1\sigma} \Big) \underline{Y}^{JM}_{l1} && (1.89)\\
&= \frac{i\pi}{2k}\mu_0 \sum_{JlM} h_l^{(1)}(kr) J_k^{lJM} \underline{Y}^{JM}_{l1}(\theta,\phi) && (1.90)
\end{aligned}$$

The coefficients J_k^{lJM} of the vector multipole fields expansion are related to the scalar ones by the following transformation :

$$J_k^{lJM} = \sum_{m\sigma} J^{\sigma}_{klm} C^{JM}_{lm1\sigma} \qquad (1.91)$$

$$J^{\sigma}_{klm} = \sum_{J'M'} C^{J'M'}_{lm1\sigma} J_k^{l'J'M'} \qquad (1.92)$$

We want our formalism to be self-consistent and to avoid the use of the scalar expansion coefficients. Thus, we need to express the coefficients J_k^{lJM} directly in the vector basis. Starting with equation 1.91 and using the definition of J^{σ}_{klm} given in equation 1.55, we find :

$$\begin{aligned}
J_k^{lJM} &= \sqrt{\frac{2}{\pi}}k \int j_l(kr') \Big(\sum_{m\sigma} C^{JM}_{lm1\sigma} \big[\underline{J}(\vec{r}')\big]_{\sigma} Y^*_{lm}(\theta',\phi') \Big) d^3r' && (1.93)\\
&= \sqrt{\frac{2}{\pi}}k \int j_l(kr') \sum_{\sigma} \big[\underline{J}(\vec{r}')\big]_{\sigma} \sum_{m} C^{JM}_{lm1\sigma} Y^*_{lm}(\theta',\phi') d^3r' && (1.94)\\
&= \sqrt{\frac{2}{\pi}}k \int j_l(kr') \sum_{\sigma} \big[\underline{J}(\vec{r}')\big]_{\sigma} \big[\underline{Y}^{JM}_{l}(\theta',\phi')^*\big]_{\sigma} d^3r' && (1.95)\\
&= \int \underline{J}(r') \cdot \underline{\Psi}^{JM}_{l}(k)(r',\theta',\phi')^* d^3r' && (1.96)
\end{aligned}$$

This last equation shows that we can project the current density in a straightforward fashion on the vector spherical basis without relying on the scalar basis. Moreover, the basis of vector multipole fields defined for the expansion is :

$$\begin{aligned}
\underline{\Psi}^{JM}_{l}(k) &= \sqrt{\frac{2}{\pi}} k j_l(kr) \underline{Y}^{JM}_{l}(\theta,\phi) && (1.97)\\
\underline{\widetilde{\Psi}}^{JM}_{l}(k) &= \sqrt{\frac{2}{\pi}} k h_l^{(1)}(kr) \underline{Y}^{JM}_{l}(\theta,\phi) && (1.98)
\end{aligned}$$

The two basis elements correspond to the regular and irregular solutions of the Helmholtz equation. When the expansion is carried over fields regular at the origin, typically sources, one has to use the j_l while $h_l^{(1)}$ has to be use for fields corresponding to a radiation like the electric field or the vector potential. The k-dependence of the vector multipolar basis will be noted between parenthesis or as a subscript according to what make the equation the simplest to read. When no confusion is possible, the k-dependence will be omitted from the notation.

As a conclusion of this section, we have shown how we can expand the vector potential into vector spherical harmonics and how the coefficients of the vector expansion are related to those of the scalar one. However, this basis is not the most convenient one since we can choose another basis equivalent by an unitary transformation which much more powerful algebraic properties and physical insights.

1.3.6 Electromagnetic multipole fields

In this section, we want to define a basis for the fields expansion that has more physical meaning but conserves the irreducibility of the vector multipolar basis. In order to conserve those algebraic properties, we can only perform an unitary transformation inside each irreducible subspace. Thus, the best choice of combination of vector multipole fields to describe electromagnetic fields is the following :

$$\underline{\Psi}_m^{JM} = \underline{\Psi}_J^{JM} \tag{1.99}$$

$$\underline{\Psi}_e^{JM} = \sqrt{\frac{J+1}{2J+1}}\underline{\Psi}_{J-1}^{JM} - \sqrt{\frac{J}{2J+1}}\underline{\Psi}_{J+1}^{JM} \tag{1.100}$$

$$\underline{\Psi}_l^{JM} = \sqrt{\frac{J}{2J+1}}\underline{\Psi}_{J-1}^{JM} + \sqrt{\frac{J+1}{2J+1}}\underline{\Psi}_{J+1}^{JM} \tag{1.101}$$

Here, the m, e and l indices stand respectively for magnetic, electric and longitudinal for a reason that will become clear later in the end of this section. Those basis vectors will be called electromagnetic multipole fields (EMF). The angular part of the EMF are the combinations of vector spherical harmonics just given above. The radial parts are the corresponding combination of spherical functions associated to different physical behavior : spherical Bessel functions when discussing the current distribution expansion and spherical Hankel functions of the first kind when discussing fields. This comes from the Green tensor's expansion 1.3.6. Again, the diverging basis components will denoted using a tilde.

The two first EMF $\underline{\Psi}_m^{10}$ and $\underline{\Psi}_e^{10}$ are represented in figure 1.4 and can intuitively be associated with the well-known electric and magnetic dipolar currents.

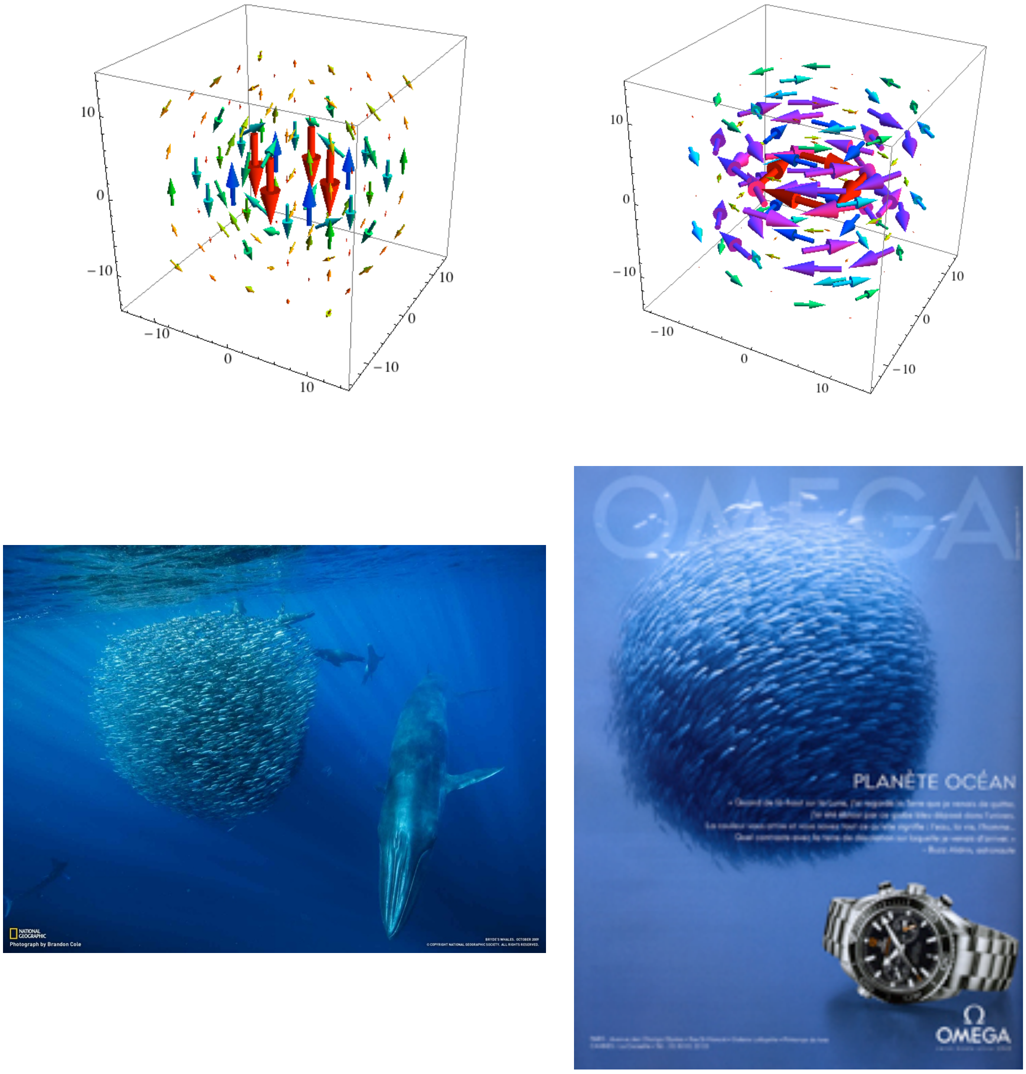

FIGURE 1.4: Graphical representation of some electromagnetic multipole fields. The electromagnetic multipole fields $\underline{\Psi}_e^{10}$ and $\underline{\Psi}_m^{10}$ are respectively represented in the top left and top right position. Pictures in the bottom represent a quasi $\underline{\Psi}_m^{10}$ of fish shoals taken from an Omega advertisement (bottom right) and a National Geographic image (bottom left).

The definition for the EMF proposed in the previous equations is particularly suitable for electromagnetic problems due to the way they behave under transformations by differential operators, such as :

$$\nabla \wedge \underline{\Psi}_e^{JM} = -ik\underline{\Psi}_m^{JM} \qquad \nabla \cdot \underline{\Psi}_e^{JM} = 0 \tag{1.102}$$

$$\nabla \wedge \underline{\Psi}_m^{JM} = ik\underline{\Psi}_e^{JM} \qquad \nabla \cdot \underline{\Psi}_m^{JM} = 0 \tag{1.103}$$

$$\nabla \wedge \underline{\Psi}_l^{JM} = 0 \qquad \nabla \cdot \underline{\Psi}_l^{JM} = -k\Psi_{JM} \tag{1.104}$$

Those results can be proven using the definition of the electromagnetic multipole fields, and the curl and divergence of vector multipole fields :

$$\begin{aligned}
\nabla \wedge \underline{\Psi}_{J+1}^{JM} &= ik\sqrt{\frac{J}{2J+1}}\underline{\Psi}_{J}^{JM} && (1.105)\\
\nabla \wedge \underline{\Psi}_{J}^{JM} &= ik\sqrt{\frac{J+1}{2J+1}}\underline{\Psi}_{J-1}^{JM} - ik\sqrt{\frac{J}{2J+1}}\underline{\Psi}_{J+1}^{JM} && (1.106)\\
\nabla \wedge \underline{\Psi}_{J-1}^{JM} &= -ik\sqrt{\frac{J+1}{2J+1}}\underline{\Psi}_{J}^{JM} && (1.107)
\end{aligned}$$

$$\begin{aligned}
\nabla \cdot \underline{\Psi}_{J+1}^{JM} &= -k\sqrt{\frac{J+1}{2J+1}}\Psi_{JM} && (1.108)\\
\nabla \cdot \underline{\Psi}_{J}^{JM} &= 0 && (1.109)\\
\nabla \cdot \underline{\Psi}_{J-1}^{JM} &= -k\sqrt{\frac{J}{2J+1}}\Psi_{JM} && (1.110)
\end{aligned}$$

Of course, the basis vectors form an orthonormal basis according to the following scalar product :

$$\int \underline{\Psi}_{i}^{JM*}(k) \cdot \underline{\Psi}_{i'}^{J'M'}(k')d^3r = \delta_{ii'}\delta_{JJ'}\delta_{MM'}\delta(k-k') \qquad (1.111)$$

With a simple dimensional analysis, one can see that the EMF vectors are without dimensions and then a correct definition of the projections need to be done. We define the projection of the electric current density over the multipolar basis as :

$$J_k^{iJM} = \frac{\int \underline{\Psi}_{i}^{JM*}(k) \cdot \underline{J}d^3r}{\int \underline{\Psi}_{i}^{JM*} \cdot \underline{\Psi}_{i}^{JM}d^3r} \qquad (1.112)$$

Where i stands for e, m or l. The denominator ensures the correctness of the coefficient dimension which is the same as that of an electric current multiplied by a length, i.e. $CL^{-1}T^{-1}$. The extra length dimension comes from the k factor in the normalization of the vector basis. Now, we can expand the electric current density into EMFs and calculate in an easy way the radiated electromagnetic field. Again, we start with the integral expression of the vector potential . So, the part of $\underline{J}$ that radiates with the wavenumber k is expressed as :

$$\underline{J}(k) = \sum_{JM} J_k^{eJM}\underline{\Psi}_{e}^{JM}(k) + J_k^{mJM}\underline{\Psi}_{m}^{JM}(k) + J_k^{lJM}\underline{\Psi}_{l}^{JM}(k) \qquad (1.113)$$

$$\underline{A} = \mu_0 ik \sum_{iJM} \underline{\Psi}_{i}^{JM} \int \underline{\Psi}_{i}^{JM*} \cdot \Big(\sum_{i'J'M'} J_{i'}^{J'M'}\underline{\Psi}_{i'}^{J'M'}\Big) d^3r \qquad (1.114)$$

Thanks to the orthogonality equation 1.111, we obtain directly the vector potential and the magnetic and electric fields using the curl of the basis vectors :

$$\underline{A} = \mu_0 \frac{i\pi}{2k} \sum_{JM} J_e^{JM} \underline{\Psi}_e^{JM} + J_m^{JM} \underline{\Psi}_m^{JM} + J_l^{JM} \underline{\Psi}_l^{JM} \tag{1.115}$$

$$\underline{H} = -\frac{\pi}{2} \sum_{JM} (-) J_e^{JM} \underline{\Psi}_m^{JM} + J_m^{JM} \underline{\Psi}_e^{JM} \tag{1.116}$$

$$\underline{E} = \frac{\pi}{2} ikZ_0 \sum_{JM} J_e^{JM} \underline{\Psi}_e^{JM} + J_m^{JM} \underline{\Psi}_m^{JM} \tag{1.117}$$

Where Z_0 is the vacuum impedance $\sqrt{\mu_0/\epsilon_0}$. Some remarks can be made about this multipolar expansion the electromagnetic fields. First, thanks to the orthogonality properties of the EMF, once the multipolar expansion of the current density is known, the electric and magnetic fields can be calculated easily outside and inside the charge distribution algebraically. In order to compute the fields inside the charge distribution, one just needs to take care of the radial part of the EMFs by using the regular ones.

Moreover, one can observe that the so-called longitudinal coefficients do not contribute to the electric and magnetic fields but only to the vector potential. Thus, they correspond to a non-radiating part of the electric field and to a pure near-field effect. This also means that, from far-field measurements, one will only be able to determine the electric and magnetic coefficients of the electric density expansion. Finally, in this choice of basis, the electric field has exactly the same angular behavior as its sources if one does not consider the non-radiating part.

We now turn our attention to a limit case of the electric and magnetic multipole coefficients. Using the section 9.10 of Jackson's book [21], it is possible to obtain the following expressions for the multipole coefficients :

$$J_e^{JM} = \frac{i}{\sqrt{J(J+1)}} \int Y_{JM}^* \Big(c\rho \frac{\partial}{\partial r}(r j_J(kr)) + ik(\underline{r}\cdot\underline{J}) j_J(kr) - ik\nabla\cdot(\underline{r}\wedge\underline{M}) j_J(kr)) \Big) d^3r \tag{1.118}$$

$$J_m^{JM} = \frac{-i}{\sqrt{J(J+1)}} \int Y_{JM}^* \Big(\nabla\cdot(\underline{r}\wedge\underline{J} - j_J(kr) + \nabla\cdot\underline{M} \frac{\partial}{\partial r}(r j_J(kr)) - k^2(\underline{r}\cdot\underline{M}) j_J(kr) \Big) d^3r \tag{1.119}$$

Where $\underline{J}$ and $\underline{M}$ are the current density and the magnetization respectively. As one can see, those expressions are quite complicated ! The reason is that the current density or equivalently, the charge density are not treated with an irreducible point of view and make the computation much more cumbersome. However, we show this result here in order to make a connection with usual descriptions. Still following Jackson, we can take the small argument approximation of the spherical Bessel function to obtain much simpler expressions. This corresponds to source scale very small compared to the wavelength. Moreover, we neglect magnetization to make it even simpler.

$$J_e^{JM} \underset{kr\ll 1}{\longrightarrow} \frac{ick^J}{(2J+1)!!}\sqrt{\frac{J+1}{J}}\int r^J \rho Y_{JM}^* d^3r \tag{1.120}$$

$$J_m^{JM} \underset{kr\ll 1}{\longrightarrow} \frac{ik^J}{(2J+1)!!}\sqrt{\frac{1}{J(J+1)}}\int r^J \nabla\cdot(\underline{r}\wedge\underline{J})Y_{JM}^* d^3r \tag{1.121}$$

Where *tvecJ* and $\underline{M}$ are respectively the current density and the magnetization. We see with those expressions that the electric multipole coefficients have a similar expression in the long wavelength limit as the multipoles from the electrostatics. Similarly, the magnetic coefficients are related to magnetic moments.

1.3.7 Mie theory

In 1908, Gustav Mie wrote an important paper on how to calculate light scattering by a spherical particle [18]. Early computation were already done by Lorenz in 1890 but were not recognized at the time, probably due to the danish language used in his article [38]. In his theory, Mie's vector basis for the incident, the scattered and the internal electric fields expansion is equivalent to the vector multipolar fields that we use here. The link between is basis vectors M and N is discussed in appendix B :

$$\underline{E}_{\text{inc}} = \frac{k_m}{\omega^2\epsilon_m\mu}\sum_{JM} A_{JM}\underline{M}^{JM} + B_{JM}\underline{N}^{JM} \tag{1.122}$$

$$\underline{E}_{\text{scat}} = \frac{k_m}{\omega^2\epsilon_m\mu}\sum_{JM} A_{JM}a_J\underline{M}^{JM} + B_{JM}b_J\underline{N}^{JM} \tag{1.123}$$

$$\underline{E}_{\text{int}} = \frac{k_m}{\omega^2\epsilon_m\mu}\sum_{JM} A_{JM}c_J\underline{M}^{JM} + B_{JM}d_J\underline{N}^{JM} \tag{1.124}$$

Where k_m and ϵ_m are the wavenumber and the permittivity in the medium surrounding the sphere. Similar equations hold for the magnetic field. The coefficients A_{JM} and B_{JM} are determined by the choice of the incident electric field. For a plane wave polarized along x, those coefficients are :

$$A_{J\pm 1} = \sqrt{\pi(2J+1)}i^J \tag{1.125}$$

$$B_{J\pm 1} = \pm\sqrt{\pi(2J+1)}i^{J+1} \tag{1.126}$$

The calculation of the coefficients a_J and b_J allows to know the scattered field outside of the spherical particle. They are calculated using the continuity of the tangential components of the fields as a boundary condition between the sphere and the surrounding medium[39]. Using the basing functions defined by Mie instead of the one used in this work, one obtains the well known Mie coefficients :

$$a_J = \frac{\mu_m m^2 j_J(mx)[xj_J(x)]' - \mu j_J(x)[mxj_J(mx)]'}{\mu_m m^2 j_J(mx)[xh_J^{(1)}(x)]' - \mu h_J^{(1)}(x)[mxj_J(mx)]'} \tag{1.127}$$

$$b_J = \frac{\mu j_J(mx)[xh_J^{(1)}(x)]' - \mu_m h_J^{(1)}(x)[mxj_J(mx)]'}{\mu j_J(mx)[xj_J(x)]' - \mu_m j_J(x)[mxj_J(mx)]'} \tag{1.128}$$

With $x = ka$ and $m = n/n_m$. Once the electric fields are completely known, one can calculate, as displayed in figure 1.5, the extinction cross-section using a proper model for the wavelength-dependent permittivity [40] that can be measured experimentally.

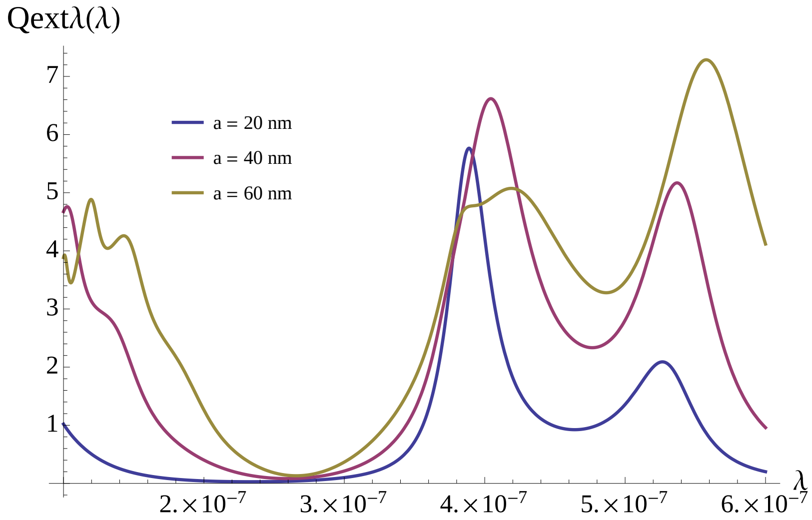

FIGURE 1.5: Extinction cross section of spherical gold nanoparticle in an homogeneous solution of water ($n_m = 1.33$).

Many extensions of Mie's theory have been developed especially since the advent of computers. To cite a few of them, the interested reader can find topics on nonspherical particles like oblates or prolates [41], coated spheres [39], scattering of a gaussian beams [42], multiple spheres scattering[43–47] and many others [48].

The vector multipole fields help solving analytically the problem of scattering by a sphere. In this work, they will be used to focus on non-spherical nanoparticles in non-linear optics problems.

1.4 An illustration : designing apolar nanoparticles

SERS has widely been used to inspect molecular modes in the visible spectrum. This technic advantage is to overcome the low signal provided by traditional Raman scattering. In SERS, the molecule is adsorbed at a metal surface which will enhance dramatically Raman signal. On the other hand, SEIRA is analogous to SERS by being its infrared counterpart. Like Raman spectroscopy and infrared spectroscopy are complementary to characterize molecules, SERS and SEIRA provide each other complementary informations.

In the aim of providing nanostructures suitable for those two techniques, it is necessary to comply with the following two constraints : the structure needs to be apolar since polarization management is non-desirable for sensing applications and the it is also necessary that the substrate resonates efficiently both in visible for SERS and in IR for SEIRA. The first constraint is discussed in this section while the second one is discussed in appendix D. Those works have been a part of the european project *Nanoantenna*.

1.4.1 Fabrication process

In this section, we briefly describe the nanoparticles fabrication process using e-beam lithography (EBL) on glass. EBL is a well-known technique [49] that allows the fabrication of high quality patterns of nanoparticle on a substrate. It is a necessary step to study the nanoparticles behavior and the process is described briefly here :

- Sample preparation : As a substrate, we use a glass microscope slide. To clean the substrate, we sonicate it for 5 minutes in water, 5 minutes in IPA, 5 minutes in acetone and finally for 5 minutes in IPA. A thin layer of PMMA (about 100 nm) is spin coated onto the substrate (Spin coating parameters : Speed = 4000 RPM/s, Acceleration = 3000 RPM/s and the time of centrifugation is 30s). The film is then baked for 15 minutes at 170 C. To complete the sample preparation, a very thin layer of aluminium is evaporated onto the surface in order to ensure a good conduction during the lithography.
- Lithography : After achieving a good setting of the Scanning Electron Microscope (SEM), the lithography is completed according to the patterns previously defined with the software. Lithography parameters on Hitachi SEM : Voltage = 30 kV, current = 10 pA. The Area or Line dose parameter is optimized for each different desired shape.

- The aluminium is removed by dipping the sample for 50 seconds in a KOH solution and then rinsed with water for 15 seconds.

- The development of the insolated parts is accomplished by dipping the sample for 1 minute in MIBK:IPA 1:3. The sample is then rinsed in IPA.

- A 50nm-thick gold layer is evaporated on the surface of the substrate.

- The lift off is accomplished by dipping the sample for more than 20 minutes and no more than a couple of hours in acetone. Then, by shaking softly the solution the PMMA and unwanted gold is removed. Finally, the sample is rinsed in IPA and dried.

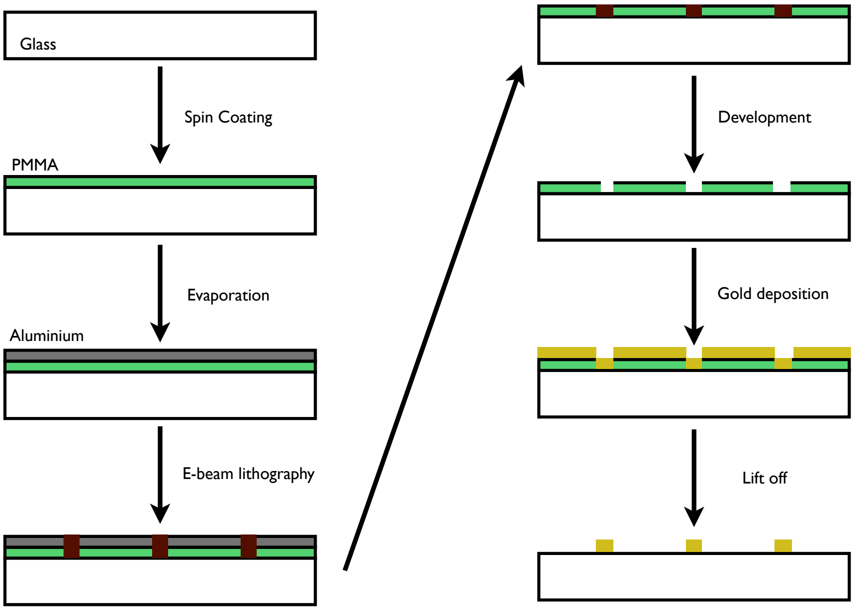

FIGURE 1.6: Nanolithography process.

In addition to this process, the cleaning procedure can be replaced by a surface functionalization since the nanoparticles can easily be removed from the substrate during the lift-off. Chromium is an efficient bonding material which is often used. However, the chromium has a strong effect on the optical response and can not be used in gold plasmonics.

1.4.2 Apolar metallic nanoparticles

In this section, we suggest a model to demonstrate why nanostructures with C_n symmetry ($n \geqslant 3$) exhibit an apolar behavior in linear optic. In this model, we assume that the linear optical response of the nanoparticle can be described using a linear polarizability

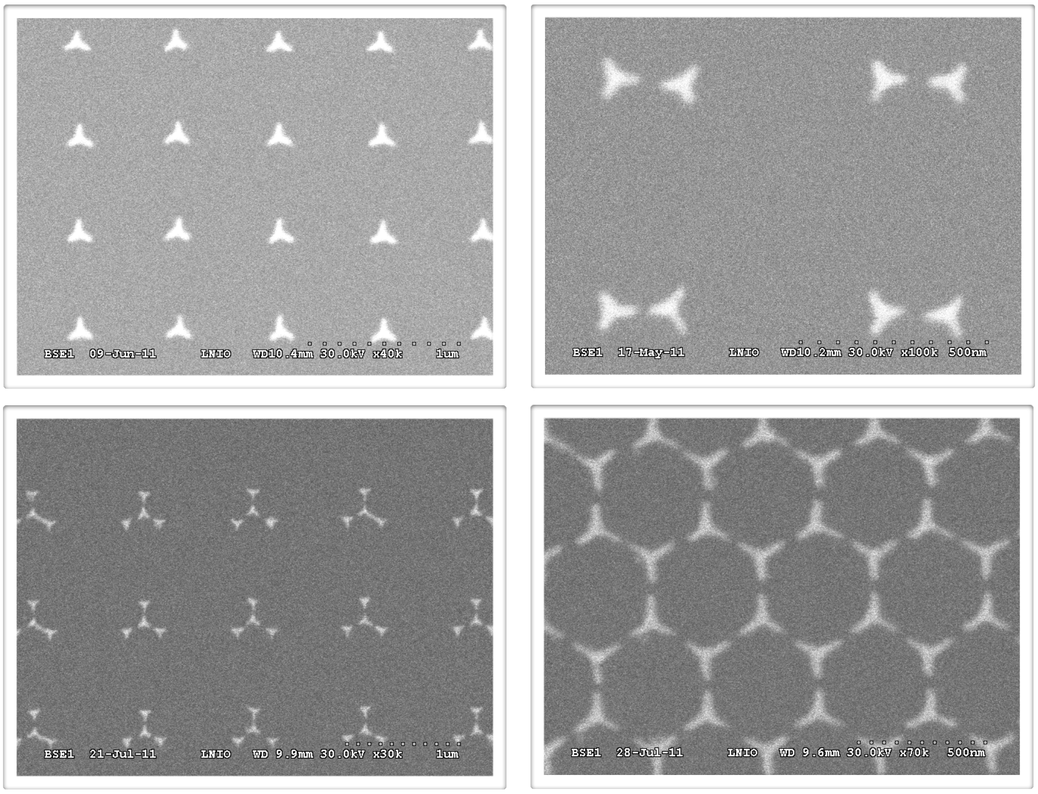

Figure 1.7: Nanolithography process.

α which is similar to giving it a molecule-like behavior. It is a crude approximation to neglect the spatial extension of the nanoparticle but it offers a simple application of irreducible tensors and spatial extension issues will be dealt with later in this thesis. Thus, the polarization that is detected in far-field is linearly related to the incident electric field via a second-rank polarizability tensor α and have the intrinsic relationship $\mathbf{P} = \underline{\underline{\alpha}} \bullet \mathbf{E}$. Although the response of the particle is a near-field phenomenon, far-field observation and response homogeneity allow us to define a linear relationship. The second rank tensor α can be represented as a direct sum of three irreducible tensors according to equation 1.37 :

$$\alpha = \alpha^0 \oplus \alpha^1 \oplus \alpha^2 \tag{1.129}$$

The components of the irreducible polarization are obtained by fully contracting the irreducible polarizabilities. To select a component of the polarization, the reading vector $\hat{e}$ is used the same way it was for nonlinear organic molecules. The components in the spherical basis of the polarization are thus given by taking the following reading tensor $\hat{e} = e_\mu$.

$$P^\mu = \alpha^0 \bullet \{E \otimes e_\mu\}^0 + \alpha^1 \bullet \{E \otimes e_\mu\}^1 + \alpha^2 \bullet \{E \otimes e_\mu\}^2 \tag{1.130}$$

The nanoparticle's C_3 symmetry axis is oriented along the direction z as depicted in figure 1.8 in order to use easily the Wigner $\mathcal{D}$ matrices.

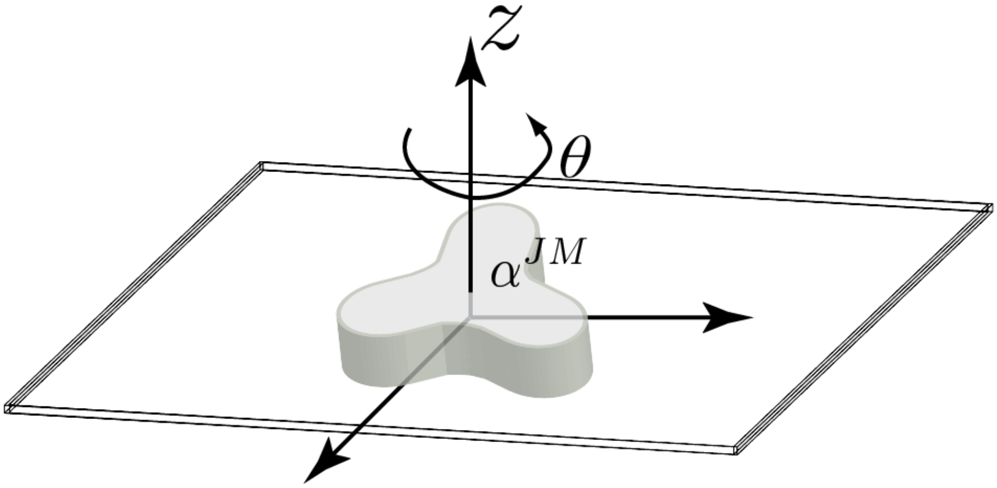

FIGURE 1.8: Geometry of the nanoparticles and the local frame associated.

Let's now consider a particle with C_n symmetry ($n \geqslant 3$). In this case, each component has to obey the following equation : $\alpha^{JM} = \mathrm{e}^{2\pi i \frac{M}{n}} \alpha^{JM}$. This relationship can be verified only if M is a multiple of 3. So, only the components α^{00}, α^{10} and α^{20} of α do not vanish. They are connected to a cylindrically symmetric behavior. Since all these components are invariant by rotation around the z axis, the response of the particle is polarization independent when considering normal incidence :

$$\alpha = \alpha^{00} \oplus \alpha^{10} \oplus \alpha^{20} \tag{1.131}$$

Furthermore, α^{10} is also zero for a particle belonging to a $C_{n\nu}$ or D_{nh} group since it corresponds to the antisymmetric part of the tensor which vanishes under reflection symmetries. A surviving α^{10} component would lead to a polarization rotation and would appear in the C_n group. Using equation 1.130, the response to a normally incident electric field is easily deduced by using the numerical values of the Clebsch-Gordan symbols and $e_\mu = (-1)^\mu \, e^{-\mu}$:

$$P^1 = -E^1(\frac{1}{\sqrt{3}}\alpha^{00} - \frac{1}{\sqrt{2}}\alpha^{10} + \frac{1}{\sqrt{6}}\alpha^{20}) \tag{1.132}$$

$$P^0 = 0 \tag{1.133}$$

$$P^{-1} = -E^{-1}(\frac{1}{\sqrt{3}}\alpha^{00} + \frac{1}{\sqrt{2}}\alpha^{10} + \frac{1}{\sqrt{6}}\alpha^{20}) \tag{1.134}$$

The polarization field is then parallel to the incident electric field when $\alpha^{10} = 0$ and their magnitude are related by :

$$||P|| = ||E|| \left[\left(\frac{1}{\sqrt{3}} \, \alpha^{00} + \frac{1}{\sqrt{6}} \alpha^{20} \right)^2 - \frac{1}{2} \, \left(\alpha^{10} \right)^2 \right] \tag{1.135}$$

To resume, we have shown that a particle belonging to a C_n ($n \geqslant 3$) group has an apolar polarization response. Moreover, if the particle belongs to $C_{n\nu}$ or D_{nh} groups, the polarization is parallel to the incoming electric field.

Chapter 2

Multipolar Point Spread Functions

Recently, spectroscopy and microscopy of single molecules or nanoparticles have seen an important development. It is now very common to investigate single nanoparticle by exciting it and collecting its signal through the objective of a confocal microscope. In particular, nanoparticles emit a signal which offer a richer physics since the dipolar approximation for the emitted field can not be used anymore due to their non-negligible spatial extension. Thus, a precise description of the image field is essential to deduce some information from the measured signal.

An early treatment by Richards and Wolf [50, 51] on the structure of the image field of a source located at infinity on the axis of the objective has given the theoretical basis of a vectorial description of the problem. This work has been extended by Enderlein [52] in order to obtain the analytical expression of a dipole emitter located at the focal point of the objective. However, it is necessary to develop the theory further to deal with multipolar emitters that appear for non-punctual radiating objects.

We start by reviewing the derivation of the PSF (Point Spread Function) for a dipolar emitter. The emphasis is put on the validity of the paraxial approximation which is sometimes used inappropriately in the literature. Then, we offer an alternative derivation within the frame of a more general multipolar formalism using vector spherical harmonics. The next section presents the analytical expressions of the image field for quadrupole and octupole in a ”ready to use” format. Their paraxial approximations are also given. Moreover, it has been noticed that a projection of the image field along a specific direction with a polarizer provides a better signature of its multipolar behavior. For each multipolar order presented, polar graphs are then represented. Finally, a way to obtain the electric field structure for orders higher than the octupole is given in the last section.

In the next chapter, the dipolar PSF will be used to calculate the electric field measured on an square-law detector from a single nanoparticle through an imaging system. In chapter 6, multipolar PSFs will be used since the nanoparticle will be described as a collection of multipoles rather than various dipoles.

2.1 Vector Diffraction Theory

In this section, the problem of diffraction of a vector electric wave by a convergent lens is tackled. This topic has been covered by Wolf [50] using the angular spectrum representation of the fields. In this paper, the integral representation of the electric field will be retrieved using a Green function formalism. This derivation will allow to have a better control on the approximations and also to deal with different lens geometries. The starting point is the integral formulation expressing the electric field in a source-free region enclosed by a surface S which has been developed by Stratton and Chu[53], Bouwkamp [41] and Visser and Wiersma [54–56] :

$$\underline{E} = \iint_S -ik'G\underline{E}_S - \nabla G \wedge (\vec{n} \wedge \underline{E}_S)dS \tag{2.1}$$

Where $\underline{E}_S$ is the electric field on the surface S, $\vec{n}$ is the inward normal vector on S and G is the Green function defined by :

$$G = \frac{e^{ik'||\overrightarrow{PF}+\vec{r}||}}{4\pi||\overrightarrow{PF}+\vec{r}||} \qquad \nabla G = \left(\frac{1}{||\overrightarrow{PF}+\vec{r}||} - ik'\right)\frac{e^{ik'||\overrightarrow{PF}+\vec{r}||}}{4\pi||\overrightarrow{PF}+\vec{r}||}\vec{e}_{rs} \tag{2.2}$$

Where $\vec{e}_{rs}$ is the unit vector in the direction of $||\overrightarrow{PF}+\vec{r}||$. We first choose the surface S shown in figure 2.1 as the integration limit in equation 2.1. Even if the integration is over the whole closed surface S, one just needs to integrate on the reference sphere spawned by the lens because the electric field contribution on the rest of the surface is negligible.

It is necessary to do some approximations to make the integral tractable. At this stage, the focused electric field is expressed in spherical coordinates $\vec{r} = (r, \theta, \varphi)$ and the integral is carried over the reference sphere also expressed in spherical coordinates (θ', ϕ). Since the focused electric field becomes negligible when r is bigger than a decade of λ and that the tube lens of an imaging system is of the order of hundreds of millimeter, one

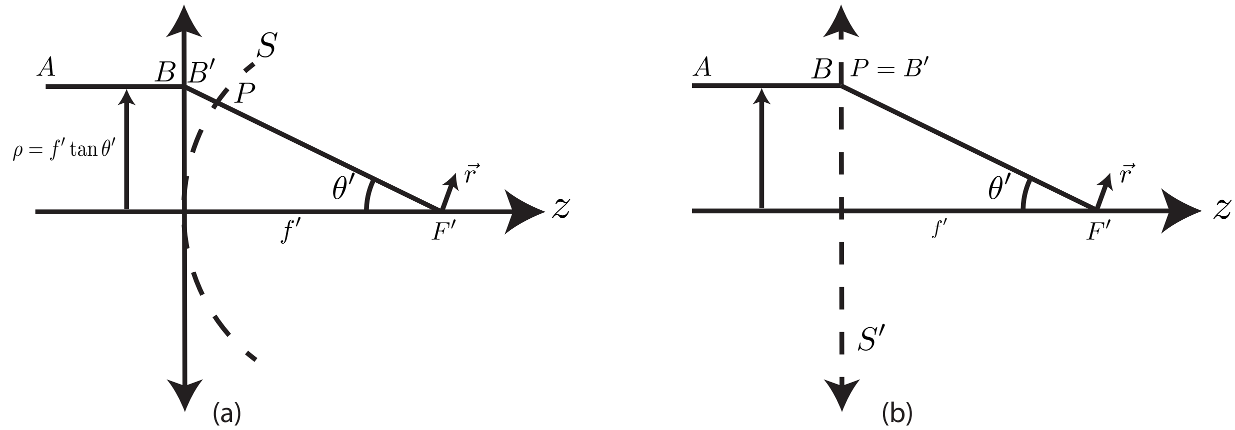

FIGURE 2.1: Geometries considered to describe the focusing of an electric field by an aplanetic lens. (a) First geometry considered using the reference sphere S as a boundaries. (b) Second geometry considered using directly the surface of the lens as the diffracting surface. As expected, both boundaries give the same diffraction integral.

can use a first order expansion for $||\overrightarrow{PF} + \vec{r}||$ [57].

$$||\overrightarrow{PF} + \vec{r}|| = f'\Big(1 + \frac{\overrightarrow{PF} \cdot \vec{r}}{f'^2}\Big) = f'\Big(1 + \frac{r}{f'}\cos\epsilon\Big) \tag{2.3}$$

Where :

$$\cos\epsilon = \sin\theta \sin\theta' \cos(\varphi - \phi) + \cos\theta \cos\theta' \tag{2.4}$$

Using this approximation, one obtains the following expression for the Green function :

$$G = \frac{e^{ik'f'}}{4\pi f'} e^{ik'r\cos\epsilon} \tag{2.5}$$

The double cross product can also be simplified :

$$\begin{aligned} \vec{e}_{rs} \wedge (\vec{n} \wedge \underline{E}_S) &= \frac{1}{f'}\big(f'\vec{n} \wedge (\vec{n} \wedge \underline{E}_S) + \vec{r} \wedge (\vec{n} \wedge \underline{E}_S)\big) & (2.6) \\ &= -\underline{E}_S & (2.7) \end{aligned}$$

Inserting those approximations in the equation 2.1, one obtains an integral equation similar to the angular spectrum representation used by Wolf [50].

$$\underline{E}(\vec{r}) = -2ik'\frac{e^{ik'f'}}{4\pi f'} \iint_S e^{ik'r\cos\epsilon} \underline{E}_S \sin\theta' d\theta' d\phi \tag{2.8}$$

One now needs to obtain an expression for $\underline{E}_S$ on the reference sphere. The lens is considered as a phase transformation object. Using the Malus-Dupin theorem, the optical path $ABB'PF'$ is the same for every rays going through the lens as depicted in the figure 2.1. The phase shift induced by the lens is $\delta(\rho) = [BB'] = K - [B'P]$. $[B'P]$ is equal to the length from the surface of the lens to the one of the reference sphere which gives $\delta(\rho) = K - \sqrt{\rho^2 + f'^2}$. K is found by using the condition $\delta(R) = 0$ which leads to the final expression of the phase shift function :

$$\delta(\rho) = \sqrt{R^2 + f'^2} - \sqrt{\rho^2 + f'^2} \tag{2.9}$$

Moreover, one needs to include the phase shift induced by the propagation from B' to S which is $e^{ik'f'\left(1/\cos\theta'-1\right)}$ together with a coefficient $A(\theta')$ which accounts for the conservation of energy. The energy conservation is assured by the intensity law. More precisely, the surface intensity of the electric field coming from an annulus of area δS_1 directed along the vector e_1 is preserved at the interface of the lens. If the amplitudes are A_1 for the incoming field and A_2 for the refracted field, we have :

$$|A_1|^2 dS_1 = |A_2|^2 dS_2 \tag{2.10}$$

According to the figure 2.2, the surface elements dS_1 and dS_2 can be expressed in their corresponding frame of coordinates : $dS_1 = \rho d\rho d\phi$ and $dS_2 = f'^2 \sin\theta' d\theta' d\phi$. Using that a point ρ in the cylindrical system of coordinates can be expressed as $\rho = f' \tan\theta'$, one obtains $A_1 = A_2 \cos^{3/2}\theta'$. Then, the function $A(\theta')$ dealing with the conservation of energy is :

$$A(\theta') = \cos^{-3/2}\theta' \tag{2.11}$$

Finally, the electric field $\underline{E}_S$ used as a boundary on the surface S can be expressed as :

$$\begin{aligned} \underline{E}_S &= \underline{E}_{\text{inc}}(\rho, \phi) e^{-ik'\sqrt{r^2+f'^2}} e^{ik'f'\left(\frac{1}{\cos\theta'}-1\right)} \frac{H(R-r)}{\cos^{\frac{3}{2}}\theta'} && (2.12) \\ \underline{E}_S &= \underline{E}_{\text{inc}}(f' \tan\theta', \phi) \frac{H(R-r)}{\cos^{\frac{3}{2}}\theta'} && (2.13) \end{aligned}$$

Where $H(R-r)$ is the Heaviside function which takes into account the finite size of the lens. The final expression for the diffraction integral by a lens is :

$$\underline{E}(r, \theta, \varphi) = -ik \frac{e^{ik'f'}}{2\pi f'} \int_{\theta'=0}^{\theta_m} \int_{\phi=0}^{2\pi} e^{ik'r\cos\epsilon} \underline{E}_{\text{inc}}(f' \tan\theta', \phi) \frac{\sin\theta'}{\cos^{3/2}\theta'} d\theta' d\phi \tag{2.14}$$

This expression is not exactly equivalent to the one obtained by Wolf [51] since the intensity conservation coefficient is not the same. However, one can check easily that the intensity of the total field is conserved over the surface of the lens.

So far, the reference sphere S was used as our boundaries for the equation 2.8. It is also possible to use the surface of the lens S' as our boundaries and to obtain the same result as in equation 2.14. Using the same approximation as previously in the new geometry leads to the following expression for $||\overrightarrow{PF}+\vec{r}||$:

$$||\overrightarrow{PF}+\vec{r}|| = \frac{f'}{\cos\theta'} + r\cos\epsilon \tag{2.15}$$

The surface element of integration dS' can be converted from the cylindrical to the spherical coordinates :

$$dS' = \rho d\rho d\phi = f'^2 \frac{\sin\theta'}{\cos^3\theta'} d\theta' d\phi \tag{2.16}$$

The conservation of energy now gives $A_2 = \sqrt{\cos\theta'}A_1$. Inserting equations 2.15 and 2.16 in the integral expression of the electric field 2.1 permits to obtain also the same result as in equation 2.14 :

$$\underline{E}(r,\theta,\varphi) = -ik'\frac{e^{ik'f'}}{2\pi}\int_{\theta'=0}^{\theta_m}\int_{\phi=0}^{2\pi}\frac{\cos\theta'}{f'}e^{ik'r\cos\epsilon}\underline{E}_{\mathrm{inc}}(f'\tan\theta',\phi)\sqrt{\cos\theta'}\frac{\sin\theta'}{\cos^3\theta'}d\theta' d\phi \tag{2.17}$$

Using either surfaces S or S' lead to a final equation 2.14 that is similar but not equivalent to the one used in most references [52, 58]. However, the consistency of the result with different geometries is convincing of the correctness of the previous derivation.

2.2 Dipolar Point Spread Function

2.2.1 Cartesian derivation

In the previous section, the focusing of an incoming electromagnetic wave by an aplanatic lens has been considered and an integral equation 2.14 has been obtained. This section will deal with the problem of imaging a dipolar source localized at the focus of a perfect objective.

To go further in the analytical development of the diffraction integral, one has to express the field $\underline{E}_{\mathrm{inc}}$ in the same vector basis. As shown in figure 2.2, this is done by splitting the incoming electric field into TE and TM components. The TE part is not changed by the refraction while the TM part is refracted as in the following equation :

$$\underline{E}_S = \left((\underline{E}_{inc}\cdot\vec{n}_\phi)\vec{n}_\phi + (\underline{E}_{inc}\cdot\vec{n}_\rho)\vec{n}_\theta\right)\sqrt{\frac{n_1}{n_2}\frac{1}{\cos^{\frac{3}{2}}\theta'}} \tag{2.18}$$

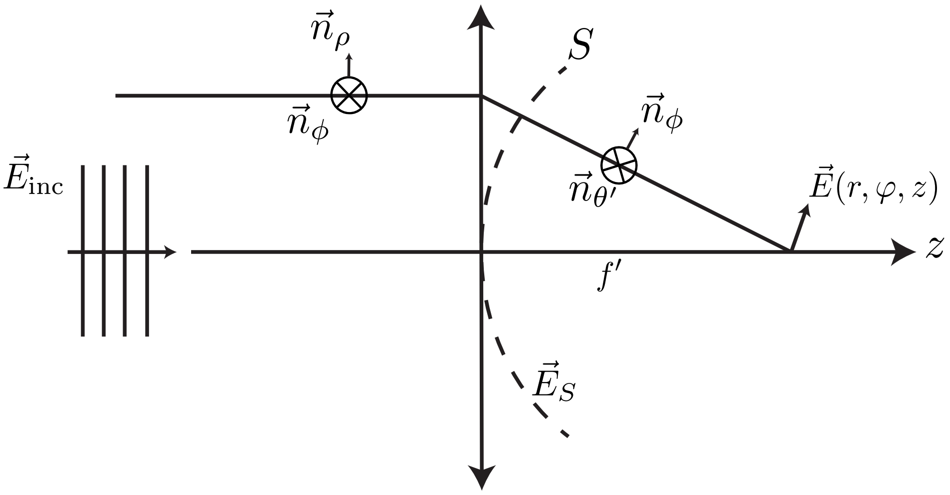

FIGURE 2.2: The incoming electric field $\underline{E}_{\text{inc}}$ is splitted into its TE (along $\vec{n}_\phi$) and TM (along $\vec{n}_\rho$) parts. The field refracted on the lens is thus the projection of these parts along the new coordinates $\vec{n}_\theta$ and $\vec{n}_\phi$. Finally, one can use the integral 2.14 to calculate the focused field $\underline{E}(r,\theta,\varphi)$ in the image space.

From now, cylindrical coordinates (r,φ,z) in the image space will be used for the focused electric field. The origin of the coordinates frame is positionned at the focal point in the image space. The reference sphere in the object space has coordinates (θ,ϕ) and the one in the image space has (θ',ϕ). Using those systems of coordinates, the focused can be expressed in the following manner :

$$\underline{E}(r,\varphi,z) = \frac{-ik'e^{ik'f}}{2\pi f'} \int_0^{\theta_m} \int_0^{2\pi} \underline{E}_S(\theta',\phi) e^{ik'z\cos\theta'} e^{ik'r\sin\theta'\cos(\varphi-\phi)} \sin\theta' d\phi d\theta' \tag{2.19}$$

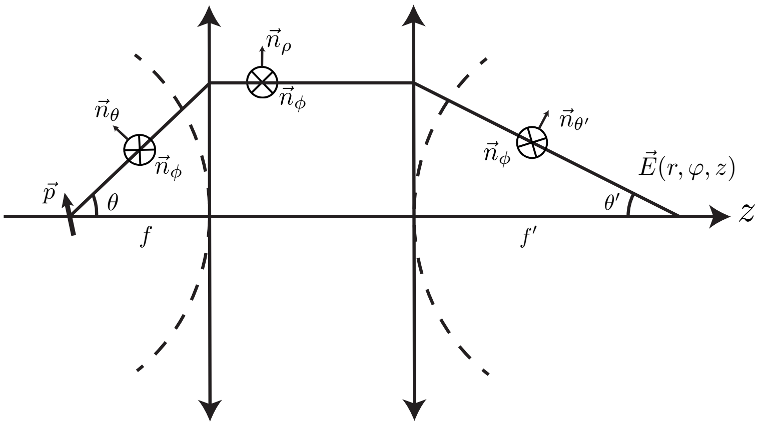

FIGURE 2.3: Schematic of a perfect imaging system. This configuration is used throughout the analytical derivation of multipolar. In this case, $\vec{p}$ represents a cartesian dipole but an irreducible dipole and higher multipolar sources are also used.

We now consider the configuration of figure 2.3 where a dipole radiation is collimated and then focused by a second lens. However, we now have two lens with focal length

f on the left and f' on the right. We denote $\underline{E}_0$, $\underline{E}_1$ and $\underline{E}_2$ the electric fields with amplitude A_0, A_1 and A_2. The intensity law now states that :

$$|A_0|^2 \; dS_0 = |A_1|^2 \; dS_1 = |A_2|^2 \; dS_2 \tag{2.20}$$

$$A_2 = A_0 \sqrt{\frac{n}{n'}} \frac{\cos^{\frac{3}{2}} \theta}{\cos^{\frac{3}{2}} \theta'} \tag{2.21}$$

There is no need to do the projection twice since the rays are parallel between the lens. We can thus directly make the projection from the left on the first lens to the right of the second lens as shown in figure 2.3. The focused electric field is now :

$$\underline{E}(r,\varphi,z) = -\frac{ik'}{2\pi}\frac{f}{f'}e^{i(k'f'-kf)} \int_0^{\theta_m} \int_0^{2\pi} \underline{E}_S(\theta,\phi) e^{ik'z\cos\theta'} e^{ik'r\frac{f}{f'}\sin\theta'\cos(\varphi-\phi)} \sin\theta d\phi d\theta \tag{2.22}$$

We can explicitly show the dependence in the incoming electric field :

$$\underline{E}(r,\varphi,z) = -\frac{ik'}{2\pi}\frac{f}{f'}e^{i(k'f'-kf)} \sqrt{\frac{n}{n'}} \int_0^{\theta_m} \int_0^{2\pi} \left(\frac{\cos\theta}{\cos\theta'}\right)^{\frac{3}{2}} \left[(\underline{E}_{\text{inc}} \cdot \vec{n}_\phi)\vec{n}_\phi + (\underline{E}_{\text{inc}} \cdot \vec{n}_\rho)\vec{n}_{\theta'} \right] e^{ik'z\cos\theta'} e^{ik'r\frac{f}{f'}\sin\theta\cos(\varphi-\phi)} \sin\theta d\phi d\theta \tag{2.23}$$

At this stage, one can use an exact multipolar expression of the incoming field or some approximations related to the dipolar order. Firstly, we are going to use a dipolar specific derivation following the letter of Enderlein [52]. Then, the electric field can be written as

$$\underline{E}(r,\varphi,z) = -\frac{ik'}{2\pi}\frac{f}{f'}e^{i(k'f'-kf)} \sqrt{\frac{n}{n'}} \int_0^{\theta_m} \int_0^{2\pi} \left(\frac{\cos\theta}{\cos\theta'}\right)^{\frac{3}{2}} \left[(\vec{p} \cdot \vec{n}_\phi)\vec{n}_\phi + (\vec{p} \cdot \vec{n}_\rho)\vec{n}_{\theta'} \right] e^{ik'z\cos\theta'} e^{ik'r\frac{f}{f'}\sin\theta\cos(\varphi-\phi)} \sin\theta d\phi d\theta \tag{2.24}$$

In this equation, $\vec{p}$ is the dipole moment vector. At this stage, the scalar product can be calculated by expressing $\vec{n}_\phi$, $\vec{n}_\rho$ and $\vec{n}_\theta$ explicitly in cartesian coordinates. This calculation would lead exactly to the results provided in the Enderlein's letter and this article will rather focus on a derivation using vector spherical harmonics. We are first recovering the known dipolar result for the PSF in the next section in a way that can be generalized in a easy way for the higher order multipoles.

2.2.2 Spherical derivation

To obtain the electric dipole propagation tensor, we now need to replace $\underline{E}_{\text{inc}}$ by the far-field dipolar radiation. In term of vector multipole fields, the irreducible electric dipolar radiation is :

$$\underline{E}_{\text{inc}}(r,\theta,\phi) = Z_0 \sum_m J_e^{1M} \nabla \wedge \underline{\Psi}_1^{1m}(r,\theta,\phi) \tag{2.25}$$

Using the far-field approximation and the long wavelength limit, the electric field can be simplified :

$$\underline{E}_{\text{inc}}(r,\theta,\phi) = Z_0 \frac{\sqrt{2}}{3}\; i\; c\; k^2 \frac{e^{ikr}}{r}(\mu_1 \underline{Y}_1^{11} \wedge \vec{n} + \mu_0 \underline{Y}_1^{10} \wedge \vec{n} + \mu_{-1} \underline{Y}_1^{1-1} \wedge \vec{n}) \tag{2.26}$$

Where the asymptotic expression of the spherical Hankel function of the first kind has been used (see appendix A). In order to obtain a result comparable to those of the precedent section, we now switch from irreducible coordinates to cartesian coordinates. To handle this, we first recast the sum in equation 2.26 in a matrix form arranging the dipole components into a vector and we then use the passage matrix between the irreducible and cartesian coordinates systems. Finally, the cartesian electric field can be written as :

$$\underline{E}_{\text{inc}}(r,\theta,\phi) = \frac{\omega^2}{\epsilon_0 c^2} \frac{e^{ikr}}{4\pi r} \underline{\underline{G}}^{\text{dip,cart}}(\theta,\phi) \cdot \vec{p} \tag{2.27}$$

$$\underline{\underline{G}}^{\text{dip,cart}}(\theta,\phi) = \begin{pmatrix} 1-\cos^2\phi\sin^2\theta & -\sin\phi\cos\phi\sin^2\theta & -\cos\phi\sin\theta\cos\theta \\ -\sin\phi\cos\phi\sin^2\theta & 1+\cos^2\phi\sin^2\theta & -\sin\phi\sin\theta\cos\theta \\ -\cos\phi\sin\theta\cos\theta & -\sin\phi\sin\theta\cos\theta & \sin^2\theta \end{pmatrix} \tag{2.28}$$

The vector $\vec{p} = (p_x, p_y, p_z)$ is the usual dipole moment. It is obtained from the irreducible electric dipole by the following change of coordinates :

$$\begin{pmatrix} p_x \\ p_y \\ p_z \end{pmatrix} = M_{\text{cart}\leftarrow\text{irr}} \begin{pmatrix} \mu_1 \\ \mu_0 \\ \mu_{-1} \end{pmatrix} \qquad \text{with} \qquad M_{\text{cart}\leftarrow\text{irr}} = \begin{pmatrix} -\frac{1}{\sqrt{2}} & 0 & \frac{1}{\sqrt{2}} \\ -\frac{i}{\sqrt{2}} & 0 & -\frac{i}{\sqrt{2}} \\ 0 & 1 & 0 \end{pmatrix} \tag{2.29}$$

Once the incoming electric field has been recasted in a suitable form, we can calculate its projection on the imaging system. Since the dipole is supposed to be placed at the focal point in the object space, the r variable of the electric field is equal to f and then $\underline{E}_S$ depends only on θ and ϕ. The electric field $\underline{E}_\infty^{(x)}$ on the lens created by a dipole oriented along x ($\vec{p} = p_x \vec{n}_x$) is calculated using equation 2.18. To make the calculation, we first give the expression of the vectors $\vec{n}_\phi$, $\vec{n}_\theta$ and $\vec{n}_{\theta'}$.

$$\vec{n}_\phi = \begin{pmatrix} -\sin\phi \\ \cos\phi \\ 0 \end{pmatrix} \qquad \vec{n}_\theta = \begin{pmatrix} \cos\phi\cos\theta \\ \sin\phi\cos\theta \\ -\sin\theta \end{pmatrix} \qquad \vec{n}_{\theta'} = \begin{pmatrix} \cos\phi\cos\theta' \\ \sin\phi\cos\theta' \\ \sin\theta' \end{pmatrix} \tag{2.30}$$

From figure 2.3, θ and θ' are not independent :

$$f\tan\theta = f'\tan\theta' \tag{2.31}$$

$$\sin\theta' = \frac{\frac{f}{f'}\tan\theta}{\sqrt{1+\left(\frac{f}{f'}\right)^2\tan^2\theta}} \qquad \cos\theta' = \frac{1}{\sqrt{1+\left(\frac{f}{f'}\right)^2\tan^2\theta}} \tag{2.32}$$

$$\begin{aligned}\underline{E}^{(x)}_\infty(\theta,\phi) = \frac{\omega^2}{\epsilon_0\ c^2}p_x\frac{e^{ikf}}{4\pi f}\sqrt{\frac{n}{n'}}\left(\frac{\cos\theta}{\cos\theta'}\right)^{\frac{3}{2}}\Bigg[&\begin{pmatrix} 1-\cos^2\phi\sin^2\theta \\ -\cos\phi\sin\phi\sin^2\theta \\ -\cos\phi\sin\theta\cos\theta \end{pmatrix}\cdot\begin{pmatrix} -\sin\phi \\ \cos\phi \\ 0 \end{pmatrix}\begin{pmatrix} -\sin\phi \\ \cos\phi \\ 0 \end{pmatrix} + \\ &\begin{pmatrix} 1-\cos^2\phi\sin^2\theta \\ -\cos\phi\sin\phi\sin^2\theta \\ -\cos\phi\sin\theta\cos\theta \end{pmatrix}\cdot\begin{pmatrix} \cos\phi\cos\theta \\ \sin\phi\cos\theta \\ -\sin\theta \end{pmatrix}\begin{pmatrix} \cos\phi\cos\theta' \\ \sin\phi\cos\theta' \\ \sin\theta' \end{pmatrix}\Bigg]\end{aligned} \tag{2.33}$$

$$\underline{E}^{(x)}_\infty(\theta,\phi) = \frac{\omega^2}{\epsilon_0\ c^2}p_x\frac{e^{ikf}}{4\pi f}\sqrt{\frac{n}{n'}}\left(\frac{\cos\theta}{\cos\theta'}\right)^{\frac{3}{2}}\begin{pmatrix} 1+\cos\theta\cos\theta' - (1-\cos\theta\cos\theta')\cos 2\phi \\ (\cos\theta\cos\theta'-1)\sin 2\phi \\ 2\cos\theta\sin\theta'\cos\phi \end{pmatrix} \tag{2.34}$$

Similar expressions hold for a dipole oriented along y and one oriented along z. Finally, we can calculate the focused field using equation 2.23 and using some identities of the integrals involved :

$$\int_0^{2\pi} \cos n\phi e^{ix\cos(\varphi-\phi)}\ d\phi = 2\pi\ i^n \mathrm{J}_n(x)\ \cos n\varphi \tag{2.35}$$

$$\int_0^{2\pi} \sin n\phi e^{ix\cos(\varphi-\phi)}\ d\phi = 2\pi\ i^n \mathrm{J}_n(x)\ \sin n\varphi \tag{2.36}$$

$$\underline{E}^{(x)}(r,\varphi,z) = i\frac{k'\omega^2}{\epsilon_0 c^2}\, p_x \frac{f'}{f}\frac{e^{i(kf-k'f')}}{8\pi}\sqrt{\frac{n}{n'}}\int_0^{\theta_m}\left(\frac{\cos\theta}{\cos\theta'}\right)^{\frac{3}{2}}\sin\theta\;\times$$

$$\times\begin{pmatrix} (1+\cos\theta\cos\theta')\mathrm{J}_0(k'r\frac{f}{f'}\sin\theta) + (1-\cos\theta\cos\theta')\mathrm{J}_2(k'r\frac{f}{f'}\sin\theta)\cos 2\varphi \\ (1-\cos\theta\cos\theta')\mathrm{J}_2(k'r\frac{f}{f'}\sin\theta)\sin 2\varphi \\ 2i\cos\theta\sin\theta'\mathrm{J}_1(k'r\frac{f}{f'}\sin\theta)\sin\varphi \end{pmatrix} e^{ik'z\cos\theta'}\,d\theta \tag{2.37}$$

We can also calculate the field for dipole along y and z in the same way but it is more convenient to put the result in a matrix form and to define some functions. The cartesian dipole propagation tensor will be written $G_c^{\text{dip}}(\vec{r},\vec{r}_0)$ and it relates a radiation dipole located at $\vec{r}_0$ in the object space to the focused electric field at the point $\vec{r}$ in the image space. We have calculated the case of a dipole located at the focus of the object space, i.e. $\vec{r}_0 = 0$.

$$\underline{E}(\vec{r}) = K\underline{\underline{G}}^{\text{dip}}(\vec{r},0)\cdot\vec{p} \tag{2.38}$$

$$K_1 = i\frac{k'\omega^2}{\epsilon_0 c^2}\,\frac{f'}{f}\frac{e^{i(kf-k'f')}}{8\pi}\sqrt{\frac{n}{n'}} \tag{2.39}$$

$$\underline{\underline{G}}_c^{\text{dip}}(\vec{r},\vec{r}_0=0) = K_1\begin{pmatrix} g_{d1}(r,z)+g_{d3}(r,z)\cos(2\varphi) & g_{d3}(r,z)\sin(2\varphi) & -2ig_{d2}(r,z)\cos(\varphi) \\ g_{d3}(r,z)\sin(2\varphi) & g_{d1}(r,z)-g_{d3}(r,z)\cos(2\varphi) & -2ig_{d2}(r,z)\sin(\varphi) \\ 2ig_{d4}(r,z)\cos(\varphi) & 2ig_{d4}(r,z)\sin(\varphi) & -2g_{d5}(r,z) \end{pmatrix} \tag{2.40}$$

For conciseness, the definition of the functions g_{di} can be found in appendix C where we have omitted the argument of the Bessel functions which is always $k'r\frac{f}{f'}\sin\theta$. We have also introduced the angle θ_m related to the numerical aperture NA by $\theta_m = \arcsin(NA/n')$. The tensor G^{dip} in equation 2.38 allows one to obtain the exact expression of the electric field in every point of the image space radiated by an electric dipole $\vec{p}$. The intensity of the imaged electric is represented in figure 2.5 for each cartesian dipole orientation. The numerical values used to compute the PSF are $M = 60$, $NA = 1.15$ and $\lambda' = 600$ nm. One can see that the intensity for a dipole oriented along the z axis is, as one can expect intuitively, lower than for the two other directions and can usually be neglected. Moreover, one can observe the ellipticity of the PSF for the x and y dipolar components. This feature is a sign that we do not use a natural representation for the dipole which would be described in a better way using, indeed, the irreducible basis. This more convenient representation for the dipole will in fact become necessary when higher multipolar orders will be under investigations because higher order cartesian multipoles are higher rank tensors and would involve higher rank propagation tensors. Instead of using tensor algebra, it is more convenient to deal with irreducible coordinates and the multipolar propagation tensor are $3 \times (2J+1)$ matrices.

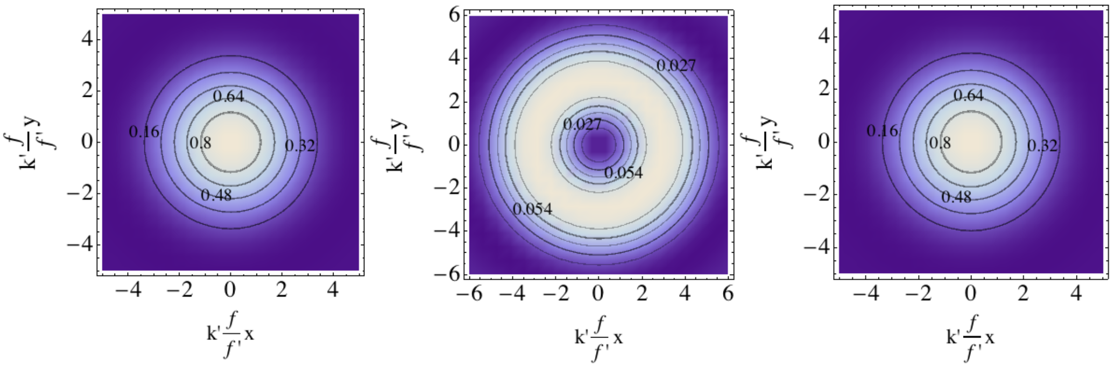

FIGURE 2.4: Contour plots of the intensity in the image plane of the field radiated by an irreducible electric dipole of components μ_{-1}, μ_0 and μ_1 from left to right.

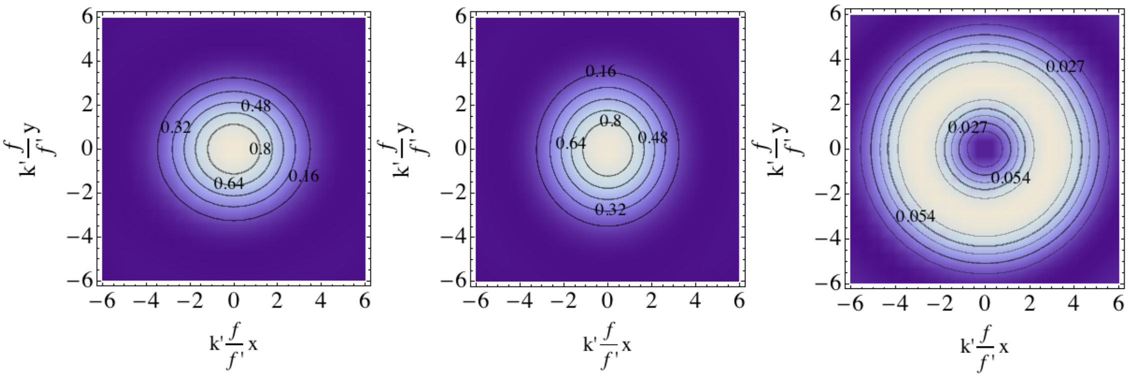

FIGURE 2.5: Contour plots of the intensity in the image plane of the field radiated by a cartesian electric dipole of components p_x, p_y and p_z from left to right.

We then introduce the spherical dipole propagation tensor $G_s^{\text{dip}}(\vec{r}, \vec{r}_0)$ related to the cartesian one by $G_s^{\text{dip}}(\vec{r}, \vec{r}_0) = M^{-1}_{\text{cart}\leftarrow\text{irr}} G_c^{\text{dip}}(\vec{r}, \vec{r}_0) M_{\text{cart}\leftarrow\text{irr}}$.

$$\underline{\underline{G}}_s^{\text{dip}}(\vec{r}, \vec{r}_0 = 0) = K_1 \begin{pmatrix} g_{d1}(r,z) & i\sqrt{2} g_{d2}(r,z) e^{-i\varphi} & -g_{d3}(r,z) e^{-2i\varphi} \\ -i\sqrt{2} g_{d4}(r,z) e^{i\varphi} & -2 g_{d5}(r,z) & i\sqrt{2} g_{d4}(r,z) e^{-i\varphi} \\ -g_{d3}(r,z) e^{2i\varphi} & -i\sqrt{2} g_{d2}(r,z) e^{i\varphi} & g_{d1}(r,z) \end{pmatrix} \tag{2.41}$$

From now, we will omit the argument $\vec{r}_0 = 0$ of the propagation tensors since we consider only object located approximately at the focal point. In this equation, one can see that both the μ_1 and μ_{-1} components have exactly the same intensity. At this point, we also point out that we have been interested only in the electric radiation so far. The magnetic radiation could be handled out using $\underline{\Psi}_m^{JM}$ instead of $\underline{\Psi}_e^{JM}$ at the beginning of the derivation. This choice would lead to the same PSFs with a different constant and can be found in the supplementary material.

2.2.3 Approximations

The exact expression of the imaged electric field involves different oscillating integrals which need to be evaluated numerically when one wants to display or quantify them. However, approximations can be done in order to make their expression much simpler.

First, in a magnifying optical system, the focal length f' will be much bigger than f. Then, one can simply use this simplification in equation 2.32 : $\sin\theta' \to 0$ and $\cos\theta' \to 1$. In this approximation, the E_z component of the electric field (or equivalently the E_0 one) will vanish and the electric field is then polarized orthogonally to the optical axis. The $\cos^{\frac{3}{2}}\theta$ that appears because of the energy conservation is different to what is generally employed in the literature [58]. This small difference will be crucial shortly when discussing the validity of the paraxial approximation. The expression of the cartesian and spherical tensors are respectively :

$$\underline{\underline{G}}_c^{\text{dip}}(\vec{r}) = K_1 \int_0^{\theta_m} \sin\theta\cos^{\frac{3}{2}}\theta e^{ik'z} \begin{pmatrix} (1+\cos\theta)J_0 + (1-\cos\theta)J_2\cos 2\varphi & (1-\cos\theta)J_2\sin 2\varphi & -2i\sin\theta J_1\cos\varphi \\ (1-\cos\theta)J_2\sin 2\varphi & (1+\cos\theta)J_0 - (1-\cos\theta)J_2\cos 2\varphi & -2i\sin\theta J_1\sin\varphi \\ 0 & 0 & 0 \end{pmatrix} d\theta \tag{2.42}$$

$$\underline{\underline{G}}_s^{\text{dip}}(\vec{r}) = K_1 \int_0^{\theta_m} \sin\theta\cos^{\frac{3}{2}}\theta e^{ik'z} \begin{pmatrix} (1+\cos\theta)J_0 & i\sqrt{2}\sin\theta J_1 & -(1-\cos\theta)J_2 e^{-2i\varphi} \\ 0 & 0 & 0 \\ -(1-\cos\theta)J_2 e^{2i\varphi} & -i\sqrt{2}\sin\theta J_1 & (1+\cos\theta)J_0 \end{pmatrix} d\theta \tag{2.43}$$

Since the argument $k'r\frac{f}{f'}\sin\theta$ of the Bessel function is small , the function J_0 gives a much higher contribution and the approximation can be extended further by neglecting the terms involving J_1 and J_2. However, by doing so, some features of the PSF are lost like the ellipticity of the cartesian one. In this case, the propagation tensors are diagonal matrices and only the function g_{d1} is enough to describe the propagation tensor :

$$\underline{\underline{G}}_c^{\mathrm{dip}}(\vec{r}) = K_1 \int_0^{\theta_m} \sin\theta \cos^{\frac{3}{2}}\theta(1+\cos\theta) J_0 e^{ik'z} \begin{pmatrix} 1 & 0 & 0 \\ 0 & 1 & 0 \\ 0 & 0 & 0 \end{pmatrix} d\theta \tag{2.44}$$

$$\underline{\underline{G}}_s^{\mathrm{dip}}(\vec{r}) = K_1 \int_0^{\theta_m} \sin\theta \cos^{\frac{3}{2}}\theta(1+\cos\theta) J_0 e^{ik'z} \begin{pmatrix} 1 & 0 & 0 \\ 0 & 0 & 0 \\ 0 & 0 & 1 \end{pmatrix} d\theta \tag{2.45}$$

Furthermore, one could invoke the paraxial approximation to simplify even more the expression of the dipolar propagation tensor. This approximation is valid when one uses a low numerical aperture and integrates only upon small values of the collection angle. The integrals then turn out to be analytical. Using the following integral, one can calculate the paraxial propagation tensors :

$$\int_0^{X_m} X^{n+1} J_n(X) dX = X_m^{n+1} J_{n+1}(X_m) \tag{2.46}$$

$$\underline{\underline{G}}_c^{\mathrm{dip}}(\vec{r}) = 2K e^{ik'z} \theta_m^2 \frac{J_1(\frac{k'rf}{f'}\theta_m)}{k'r\frac{f}{f'}\theta_m} \begin{pmatrix} 1 & 0 & 0 \\ 0 & 1 & 0 \\ 0 & 0 & 0 \end{pmatrix} \tag{2.47}$$

Some authors propose that the paraxial approximation is valid even for high numerical apertures when comparing numerical results. However, we believe it is not the case and, when the correct expression of the propagation tensor is used, it leads to non-negligible discrepancies as can be observed in the figure 2.6. The reason of the difference is the following : when using the paraxial approximation one usually apply it also on the boundaries of the angular spectrum integral and so $NA = n\theta_m$. Then, if one integrates up to NA/n even using the non approximated integrand, the integration is not carried over the whole angle of collection and the rays far from the paraxial approximation are just discarded. The paraxial approximation result gives almost the same result because the paraxial rays are not used also in the ”exact” expression. Finally, one has to carefully express the boundaries of the integral in order to take in account all the rays.

The evolution of the relative error of the full width at half maximum (FWHM) of the approximated paraxial PSF is represented as a function of the numerical aperture in figure 2.8. One can observe that the error increases drastically as the numerical aperture increases. Thus, with the standard parameters used in this section, the relative error is 14% at $NA = 1.1$ and 28% at $NA = 1.4$. In fact, as NA will be closer and closer from its

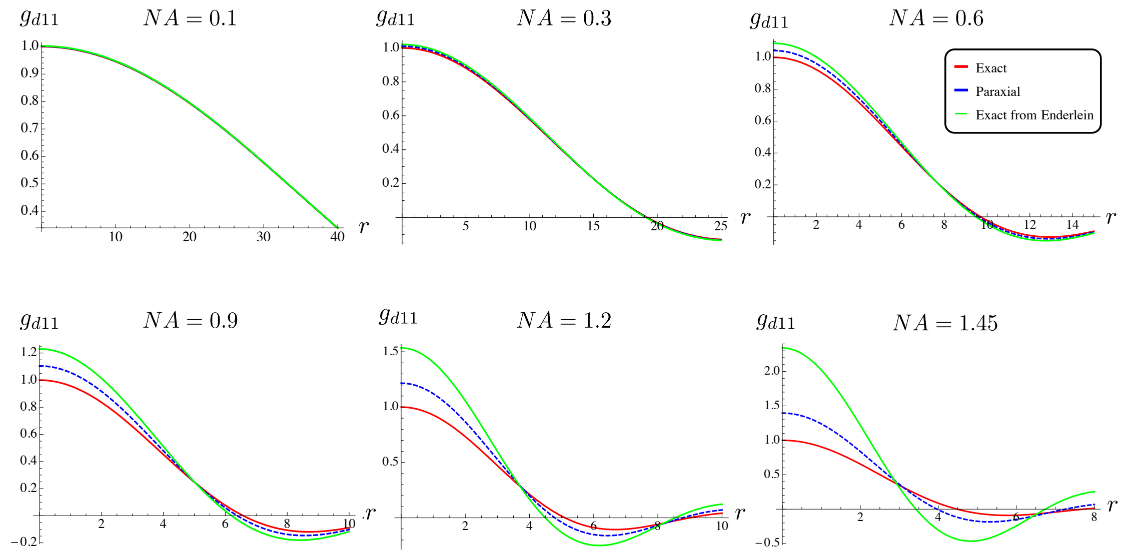

FIGURE 2.6: The exact function $g_{d1}(r, z = 0)$ is plotted in red and compared to the approximated functions. Comparisons between the exact function (red), the correctly approximated function using the paraxial approximation (blue) and the approximated one from Enderlein's paper [52] (green) are displayed for different values of the numerical aperture . As one can see, the paraxial approximation is valid for small NA but some discrepancies appear for bigger NA as expected. As NA increases, the discrepancies between the function from reference [52] and the exact one become larger.

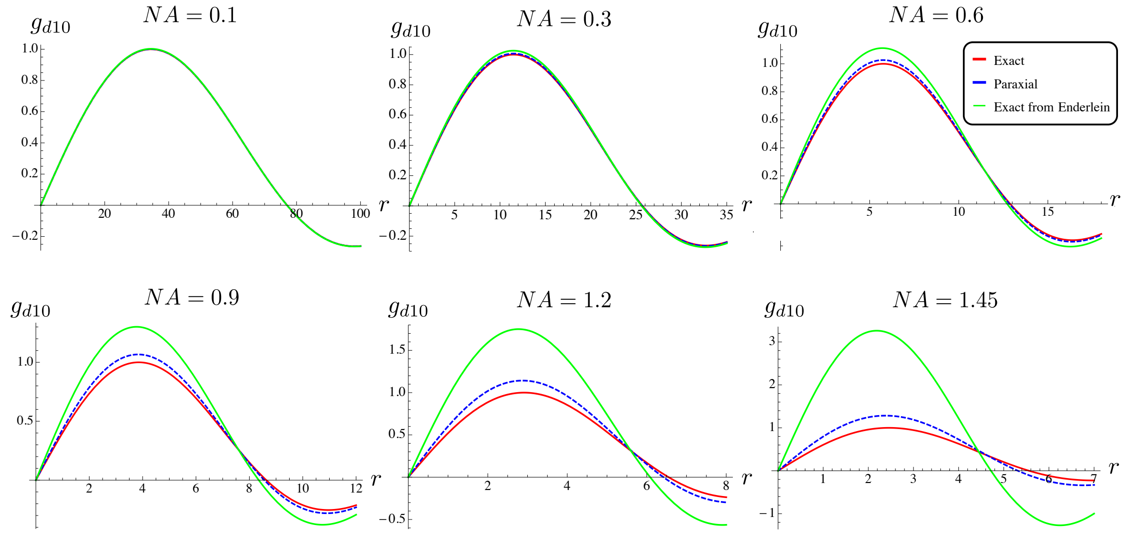

FIGURE 2.7: The exact function $g_{d2}(r, z = 0)$ is plotted in red and compared to the approximated functions as in figure 2.6.

maximum value n', the error will be larger and larger. Then, the paraxial approximation can not be used when one wants to use high NA objectives.

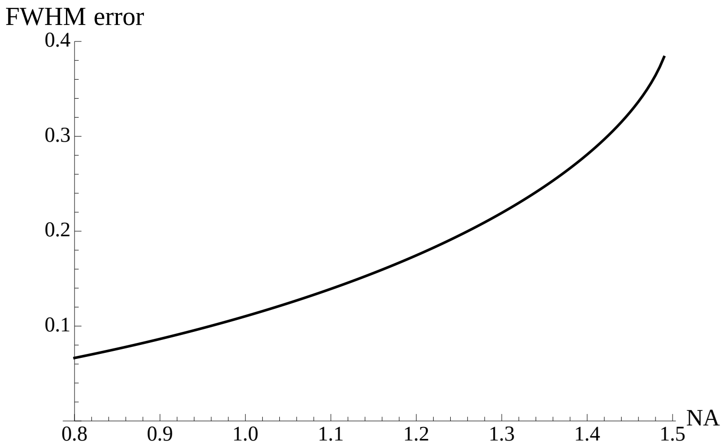

FIGURE 2.8: Relative error made on the FWHM when one uses the paraxial approximation instead of the exact function. The relative error is about 28% for objectives having a numerical aperture of 1.4 which is almost the theoretical maximum in oil immersion objective.

2.3 First higher multipolar orders

In this section, the quadrupolar and octupolar electric propagation tensor will be calculated following the notation and method of the previous section. For higher order multipoles, the cartesian basis becomes very inconvenient since one has to deal with higher rank tensors containing a lot of redundant information. The irreducible form of the multipoles are then used and are written J_e^{JM} where M can take value from $-J$ to J. The image electric field can be described in a cartesian or an irreducible basis since those 2 basis are equivalent through an unitary transformation $M_{\text{cart}\leftarrow\text{irr}}$ when $J = 1$. The choice has been to use the irreducible basis because it leads to more compact expressions.

2.3.1 Quadrupole

The result of the calculation of the quadrupolar PSFs is given directly in equation 2.48. The quadrupolar PSF is obtained by inserting $\underline{\Psi}_e^{2M}$ in equation 2.23. The definition of the function g_{qi} can be found in appendix C.

$$\underline{\underline{G}}_s^{\text{quad}} = K_2 \begin{pmatrix} -g_{q1}(r,z)e^{i\varphi} & -ig_{q4}(r,z) & \sqrt{6}g_{q7}(r,z)e^{-i\varphi} & ig_{q5}(r,z)e^{-2i\varphi} & -g_{q2}(r,z)e^{-3i\varphi} \\ i\sqrt{2}g_{q3}(r,z)e^{2i\varphi} & -\sqrt{2}g_{q6}(r,z)e^{i\varphi} & i\sqrt{3}g_{q8}(r,z) & \sqrt{2}g_{q6}(r,z)e^{-i\varphi} & i\sqrt{2}g_{q3}(r,z)e^{-2i\varphi} \\ -g_{q2}(r,z)e^{3i\varphi} & ig_{q5}(r,z)e^{2i\varphi} & -\sqrt{6}g_{q7}(r,z)e^{i\varphi} & -ig_{q4}(r,z) & g_{q1}(r,z)e^{-i\varphi} \end{pmatrix} \tag{2.48}$$

Where the coefficient $K_2 = -iK_1$. In general, the coefficient corresponding to the multipole of order J will be $K_J = -(-i)^{J+1}K_1$ due to the factor $(-i)^{J+1}$ in the asymptotic limit of $h_J^{(1)}$. The intensity in the image plane from unit quadrupoles are displayed in figure 2.10. As one can see, the appearance of the density plots is qualitatively the same as the one for the dipolar PSF. This comes from the fact that all those functions are rotationally invariant around z up to a phase factor due to the choice of an irreducible basis function. Moreover, the radial functions appearing in the expression are integral of Bessel function J_n that have all the same qualitative behavior except J_0. Then, those density maps offer incomplete informations about the multipole being measured. However, one can instead consider cartesian components of the quadrupolar current density as displayed in figure 2.9 since they do have different qualitative behavior. Using cartesian components, the quadrupole is now a traceless symmetric matrix which components are obtaining from linear combinations of the irreducible ones :

$$\begin{aligned}
Q_{xy} &\propto Q_2 - Q_{-2} && (2.49)\\
Q_{xz} &\propto Q_1 - Q_{-1} && (2.50)\\
Q_{yz} &\propto Q_1 + Q_{-1} && (2.51)\\
Q_{xx} &\propto \sqrt{\frac{3}{2}}(Q_2 + Q_{-2}) - Q_0 && (2.52)\\
Q_{yy} &\propto -\sqrt{\frac{3}{2}}(Q_2 + Q_{-2}) - Q_0 && (2.53)\\
Q_{zz} &\propto 2Q_0 && (2.54)
\end{aligned}$$

Where we haven't stated the proportionality coefficient since it differs from convention to another [21, 34]. The two components Q_{xx} and Q_{yy} look similar because Q_{zz} is small compared to them in our standard configuration.

One can also rely on other techniques such as defocus imaging that increases the degree of informations achievable or use quantitative measurements of the radial functions if the experiment offers this precision. The first option is much more feasible. Once again, using the fact that $f' \gg f$, one can simplify the expression of the tensor greatly :

$$\underline{\underline{G}}_s^{\text{quad}} = K_2 \int_0^{\theta_m} \sin\theta \cos^{\frac{3}{2}}\theta e^{ik'z}$$
$$\begin{pmatrix} (G_s^{\text{quad}})_{12} e^{i\varphi} & (G_s^{\text{quad}})_{11} & (G_s^{\text{quad}})_{10} e^{-i\varphi} & (G_s^{\text{quad}})_{1-1} e^{-2i\varphi} & (G_s^{\text{quad}})_{1-2} e^{-3i\varphi} \\ 0 & 0 & 0 & 0 & 0 \\ (G_s^{\text{quad}})_{-12} e^{3i\varphi} & (G_s^{\text{quad}})_{-11} e^{2i\varphi} & (G_s^{\text{quad}})_{-10} e^{i\varphi} & (G_s^{\text{quad}})_{-1-1} & (G_s^{\text{quad}})_{-1-2} e^{-i\varphi} \end{pmatrix} d\theta \tag{2.55}$$

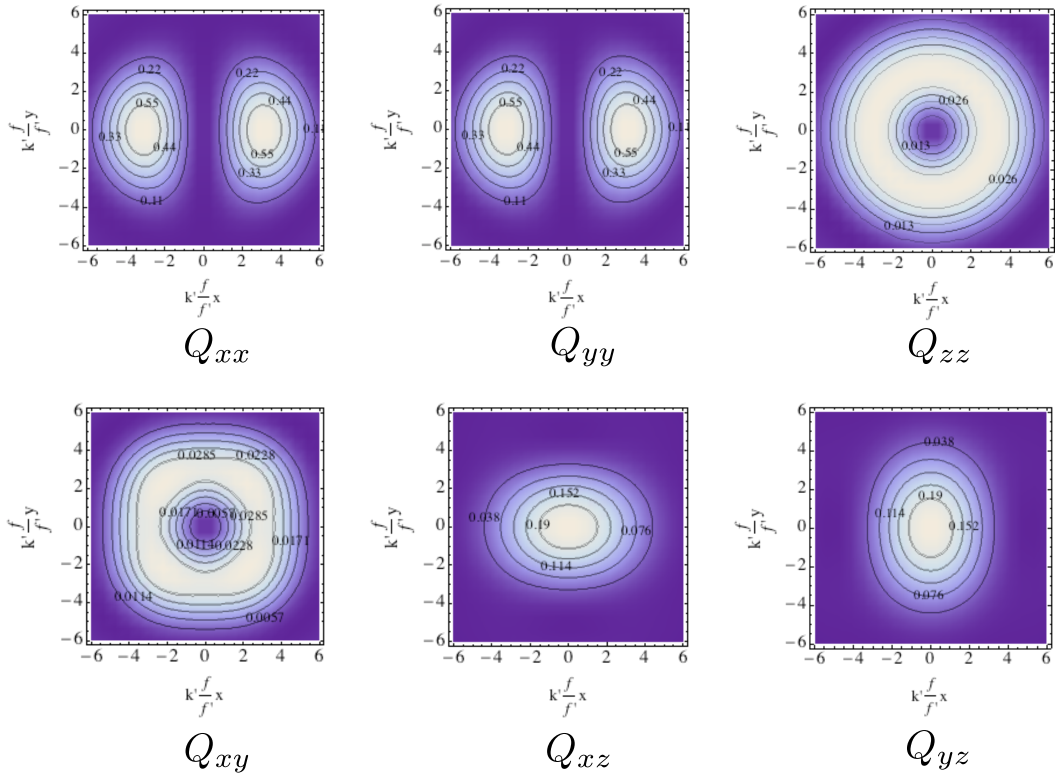

Q_{xx} Q_{yy} Q_{zz}

Q_{xy} Q_{xz} Q_{yz}

FIGURE 2.9: Contour plots of the intensity in the image plane of the field radiated by a cartesian electric quadrupole.

$$\begin{aligned}
(G_s^{\text{quad}})_{12} &= -2(1+\cos\theta)\sin\theta J_1 = (G_s^{\text{quad}})_{-1-2} && (2.56)\\
(G_s^{\text{quad}})_{-12} &= 2(1-\cos\theta)\sin\theta J_3 = (G_s^{\text{quad}})_{1-2} && (2.57)\\
(G_s^{\text{quad}})_{11} &= 2i(\cos\theta+\cos 2\theta)J_0 = -(G_s^{\text{quad}})_{-1-1} && (2.58)\\
(G_s^{\text{quad}})_{-11} &= 2i(\cos\theta-\cos 2\theta)J_2 = -(G_s^{\text{quad}})_{-1-1} && (2.59)\\
(G_s^{\text{quad}})_{10} &= -\sqrt{6}\sin 2\theta J_1 = (G_s^{\text{quad}})_{-10} && (2.60)
\end{aligned}$$

The paraxial approximation of the quadrupolar spherical propagation tensor is the following :

$$\underline{\underline{G}}_s^{\text{quad}} = 2K_2 \frac{ik'z}{k'r\frac{f}{f'}} \begin{pmatrix} -2\theta_m^2 J_2 e^{i\varphi} & 2i\theta_m J_1 & -\sqrt{6}\theta_m^2 J_2 e^{-i\varphi} & 0 & 0 \\ 0 & 0 & 0 & 0 & 0 \\ 0 & 0 & -\sqrt{6}\theta_m^2 J_2 e^{i\varphi} & -2i\theta_m J_1 & -2\theta_m^2 J_2 e^{-i\varphi} \end{pmatrix} \tag{2.61}$$

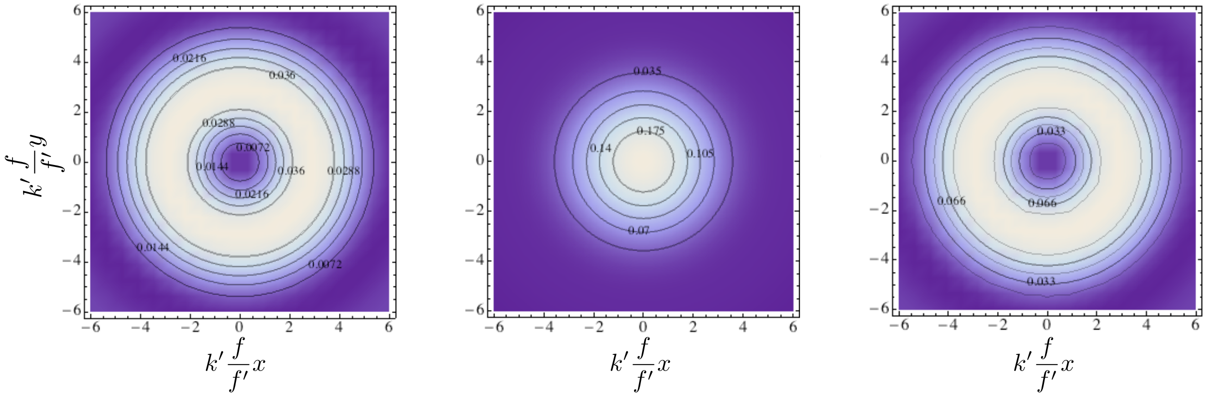

$Q_2,\ Q_{-2}$ $Q_1,\ Q_{-1}$ Q_0

FIGURE 2.10: Contour plots of the intensity in the image plane of the field radiated by an irreducible electric quadrupole of components $Q_{\pm2}, Q_{\pm1}$ and Q_0 from left to right.

2.3.2 Octupole

This section follows exactly the previous one by dealing with the octupolar order this time. The field from an unit radiating octupole is obtained from $\underline{\Psi}_e^{3M}$ and inserted in equation 2.23.

$$\underline{\underline{G}}_s^{\text{oct}} =$$

$$\begin{pmatrix} g_{o1}e^{2i\varphi} & \frac{i}{2\sqrt{6}}g_{o4}e^{i\varphi} & -\frac{1}{4\sqrt{15}}g_{o7} & -\frac{i}{\sqrt{5}}g_{o10}e^{-i\varphi} & \frac{1}{4\sqrt{15}}g_{o8}e^{-2i\varphi} & \frac{i}{2\sqrt{6}}g_{o5}e^{-3i\varphi} & -g_{o2}e^{-4i\varphi} \\ -i\sqrt{2}g_{o3}^{3i\varphi} & \frac{1}{\sqrt{3}}g_{o6}e^{2i\varphi} & -\frac{i}{\sqrt{30}}g_{o9}e^{i\varphi} & \sqrt{\frac{2}{5}}g_{o11} & \frac{i}{\sqrt{30}}g_{o9}e^{-i\varphi} & \frac{1}{\sqrt{3}}g_{o6}e^{-2i\varphi} & i\sqrt{2}g_{o3}^{-3i\varphi} \\ -g_{o2}e^{4i\varphi} & -\frac{i}{2\sqrt{6}}g_{o5}e^{3i\varphi} & \frac{1}{4\sqrt{15}}g_{o8}e^{2i\varphi} & \frac{i}{\sqrt{5}}g_{o10}e^{-i\varphi} & -\frac{1}{4\sqrt{15}}g_{o7} & -\frac{i}{2\sqrt{6}}g_{o4}e^{-i\varphi} & g_{o1}e^{-2i\varphi} \end{pmatrix} \tag{2.62}$$

The density maps of the intensity from those unit quadrupoles are displayed in figure 2.11 with similar conclusion as the ones discussed in the previous section.

$$\underline{\underline{G}}_s^{\text{oct}} = K_3 \int_0^{\theta_m} \sin\theta \cos^{\frac{3}{2}}\theta e^{ik'z} \tag{2.63}$$

$$\begin{pmatrix} (G_s^{\text{oct}})_{13}e^{2i\varphi} & (G_s^{\text{oct}})_{12}e^{i\varphi} & (G_s^{\text{oct}})_{11} & (G_s^{\text{oct}})_{10}e^{-i\varphi} & (G_s^{\text{oct}})_{1-1}e^{-2i\varphi} & (G_s^{\text{oct}})_{1-2}e^{-3i\varphi} & (G_s^{\text{oct}})_{1-3}e^{-4i\varphi} \\ 0 & 0 & 0 & 0 & 0 & 0 & 0 \\ (G_s^{\text{oct}})_{-13}e^{4i\varphi} & (G_s^{\text{oct}})_{-12}e^{3i\varphi} & (G_s^{\text{oct}})_{-11}e^{2i\varphi} & (G_s^{\text{oct}})_{-10}e^{-i\varphi} & (G_s^{\text{oct}})_{-1-1} & (G_s^{\text{oct}})_{-1-2}e^{-i\varphi} & (G_s^{\text{oct}})_{-1-3}e^{-2i\varphi} \end{pmatrix}$$

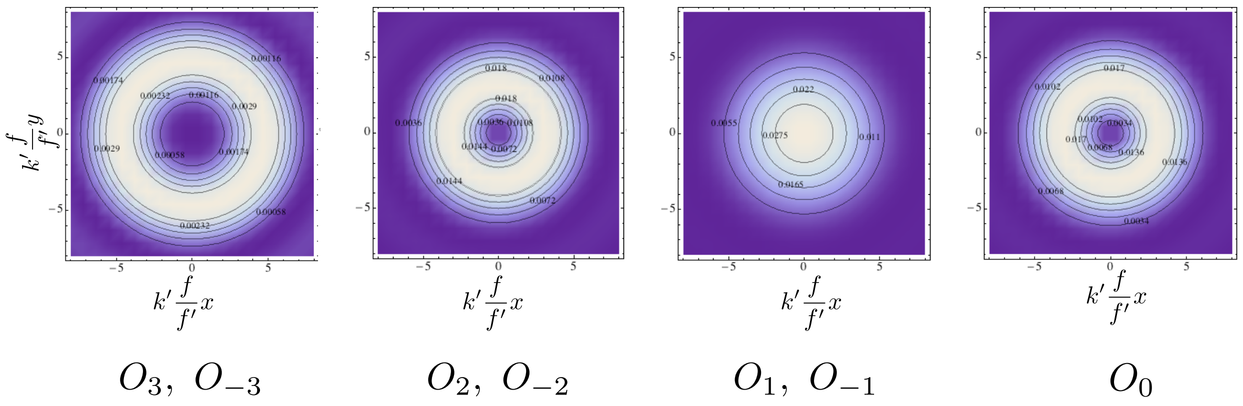

FIGURE 2.11: Contour plots of the intensity in the image plane of the field radiated by an irreducible electric octupole of components $O_{\pm3}, O_{\pm2}, O_{\pm1}$ and O_0 from left to right.

$$\begin{aligned}
(G_s^{\mathrm{oct}})_{13} &= (1+\cos\theta)\sin\theta^2 J_2 = (G_s^{\mathrm{oct}})_{-1-3} && (2.64)\\
(G_s^{\mathrm{oct}})_{-13} &= -(1-\cos\theta)\sin\theta^2 J_4 = (G_s^{\mathrm{oct}})_{1-3} && (2.65)\\
(G_s^{\mathrm{oct}})_{12} &= \frac{i}{2\sqrt{6}}(4\sin 2\theta + 3\sin 3\theta - \sin\theta)J_1 = -(G_s^{\mathrm{oct}})_{-1-2} && (2.66)\\
(G_s^{\mathrm{oct}})_{-12} &= -\frac{i}{2\sqrt{6}}(4\sin 2\theta - 3\sin 3\theta + \sin\theta)J_3 = -(G_s^{\mathrm{oct}})_{1-2} && (2.67)\\
(G_s^{\mathrm{oct}})_{11} &= -\frac{1}{4\sqrt{15}}(6+\cos\theta + 10\cos 2\theta + 15\cos 3\theta)J_0 = (G_s^{\mathrm{oct}})_{-1-1} && (2.68)\\
(G_s^{\mathrm{oct}})_{-11} &= \frac{1}{4\sqrt{15}}(6-\cos\theta + 10\cos 2\theta - 15\cos 3\theta)J_2 = (G_s^{\mathrm{oct}})_{1-1} && (2.69)\\
(G_s^{\mathrm{oct}})_{10} &= -\frac{i}{\sqrt{5}}(3+5\cos 2\theta)J_1 = -(G_s^{\mathrm{oct}})_{-10} && (2.70)
\end{aligned}$$

$$\underline{\underline{G}}_s^{\mathrm{oct}} = 2K_3\frac{ik'z}{k'r\frac{f}{f'}} \qquad (2.71)$$

$$\begin{pmatrix}
8ia^3J_3e^{2i\varphi} & -16\sqrt{\frac{2}{3}}a^2e^{i\varphi}J_2 & -\frac{32}{\sqrt{15}}iaJ_1 & \frac{32}{\sqrt{5}}a^2J_2e^{-i\varphi} & 0 & 0 & 0\\
0 & 0 & 0 & 0 & 0 & 0 & 0\\
0 & 0 & 0 & -\frac{32}{\sqrt{5}}a^2J_2e^{i\varphi} & -\frac{32}{\sqrt{15}}iaJ_1 & 16\sqrt{\frac{2}{3}}a^2e^{-i\varphi}J_2 & 8ia^3J_3e^{-2i\varphi}
\end{pmatrix}$$

2.3.3 Defocus Imaging

In this section, some contour plots of a defocused dipole are provided. Defocus imaging microscopy allows the retrieval of various informations such as orientation or crystallinity [59]. In figure 2.12, defocused contour plots of dipolar PSFs are obtained by varying z in equation 2.41. The defocus is taken at three values : $z = 0$ μm (in focus), $z = 0.47$ μm and $z = 0.95$ μm. Those values have to be compared with the density of field of the objective corresponding to the plots which is about 0.2 μm.

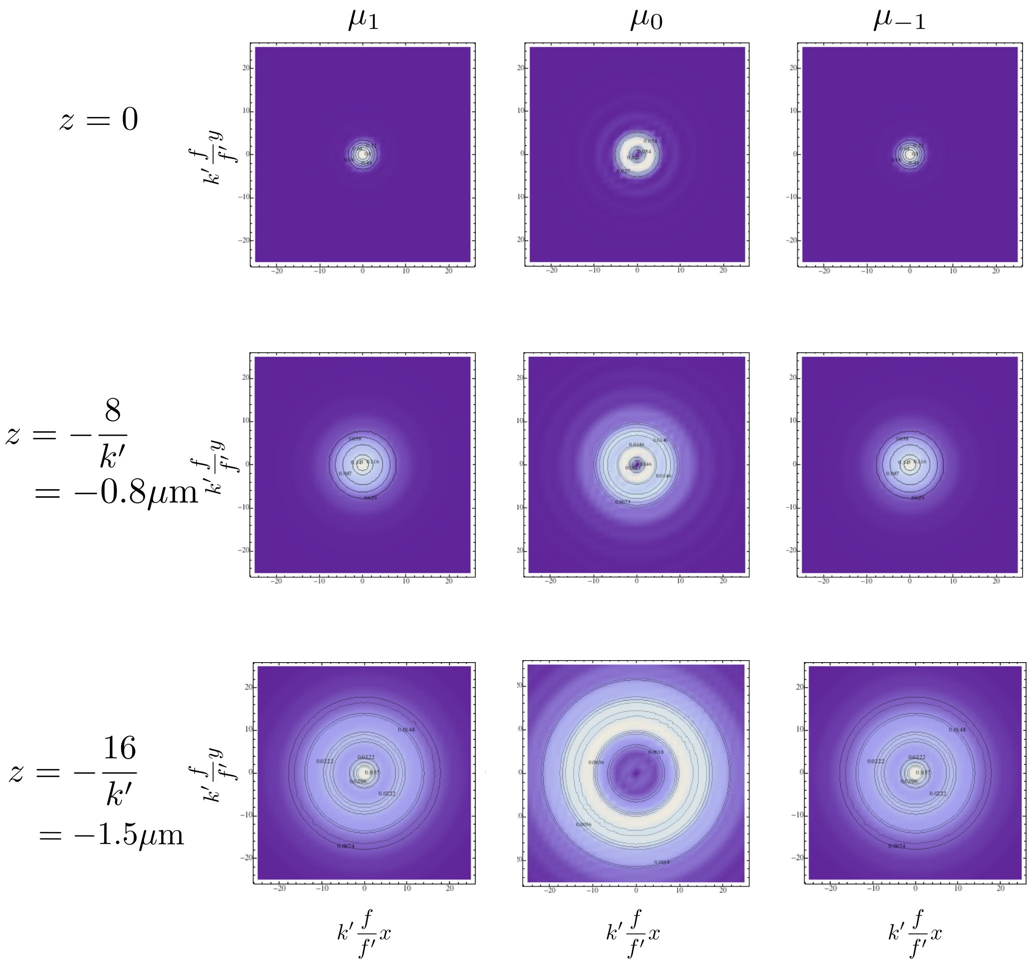

FIGURE 2.12: Defocused density plot of irreducible dipoles.

If one wants to disentangle the multipolar structure of the system being probed, it is necessary to be able to distinguish them experimentally. Unfortunately, while some PSFs are specific to one kind of multipoles, many of them have similar functions in the image plane and it is difficult to assign to which multipole they belong. Fortunately, it is possible to use defocus imaging to inspect their z behavior which provides more informations. As an example, the defocused PSFs of the components Q_{xy}, Q_{xz} and Q_{xx} of a cartesian quadrupole are displayed in the figure 2.13. The qualitative behavior is completely different with the one of the dipole and thus, one can easily distinguish them.

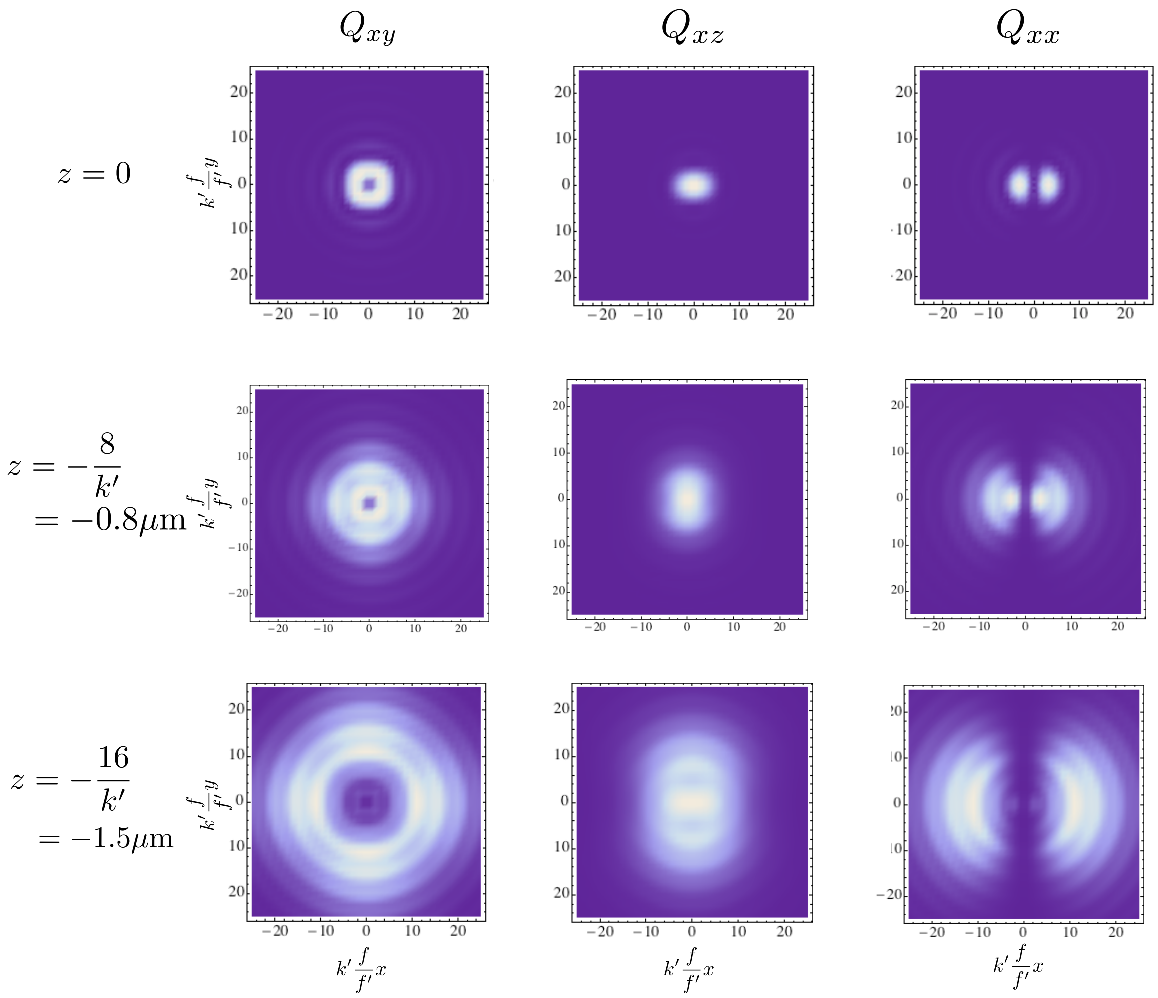

FIGURE 2.13: Defocused density plot of some components of a cartesian quadrupole.

Chapter 3

Observing multipoles in threefold gold nanostars through Second Harmonic Generation

3.1 Basic properties of threefold gold nanostars

The emergence of improved techniques of fabrication paved the way for the design of smaller objects. Among this family of new systems in nanotechnologies, nanoparticles have an important role due to their special optical properties. In particular, metallic nanoparticles have a central role to play since their plasmonic resonances fall in the visible range and have interesting properties [1, 16]. Plasmons are collective oscillationw of the free electrons cloud in metallic objects. While a surface plasmon polariton offers fascinating properties at the interface between a metal and a dielectric, metallic nanoparticles possess the so called Localized Surface Plasmon Resonance (LSPR). The collective charge motion inside the nanoparticle oscillates in phase with the incoming electric field and can enhance the electromagnetic field. The LSPR of a nanoparticle is strongly dependent on its composition, shape, symmetry and local environment. A large variety of shape has been investigated such as spheres[60, 61], shells[62, 63], rods[6], prisms[64, 65], stars[66, 67] for example. Adding the ability to put those nanoparticles in arrays[5, 68, 69] in order to have coupling effects, one can easily see that the number of possibilities is tremendous.

In figure 3.1, one can see the extinction spectra of two different systems of gold nanoparticles. On the left, spectra of nanostars organized in an hexagonal lattice are displayed. Those lattices has been made using the e-beam lithography explained in chapter 1 in the aim to produce efficient surface for SERS. Extinction spectra for lattices with a smaller

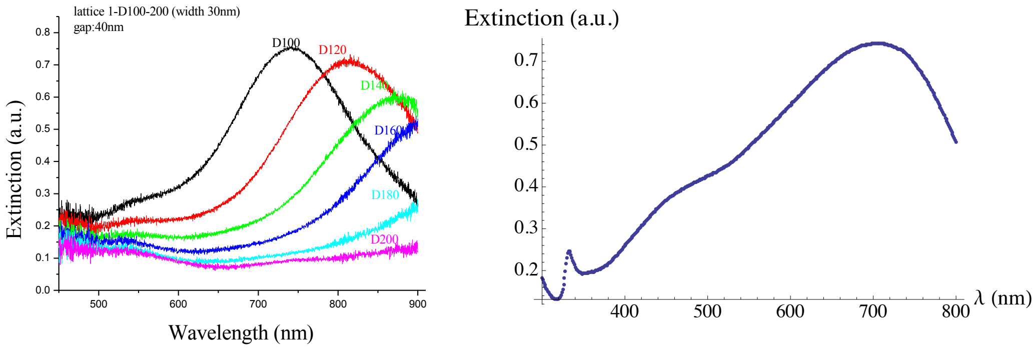

Figure 3.1: (Left) Extinction spectra of different lattices of gold nanostars as displayed in the bottom right of figure 1.7. The size of the circumscribed circle if given over the curves. (Right) Extinction spectrum of a colloidal solution of nanoprism in water.

gap are provided in appendix D. The spectrum on the right is an extinction spectrum obtained with a Cary 100 UV-Vis (Agilent) on a colloidal solution of nanoprisms according the procedure proposed by Yin [70]. One can observe two peaks in the spectrum, one at 700 nm and one at 450 nm. Within the frame of Mie theory, resonances correspond to the cancellation of the coefficients a_J/b_J and then one can assign a specific type of multipole to each resonance. Thus, the first peak is often referred as "dipolar resonance", the second one as "quadrupolar resonance" and so on. However, Mie theory is applicable only with spheres and resonances in non-spherical systems can not be assigned in such a straightforward manner. Instead of that, resonances can easily be associated with irreducible representations of the finite group of the nanoparticle. For example, in nanostars or nanoprisms, resonances can be assigned to the representations A_1, A_2 or E. Those resonant modes will themselves radiate some light that can be described using the multipolar expansion of electromagnetic fields. Nevertheless, a resonant mode can radiate various multipolar fields according to the projection of the irreducible representations of the nanoparticles over representations of SO(3).

A simple phenomenological model to understand the nonlinear response of nanostars has been constructed based on the assumption that the induced nonlinear dipole sources are located close to the tips of the star arms. Accordingly, SHG responses are generated from the nonlinear sources located at a given distance from the center of star. Consequently, these models take into account the symmetry of the particles as well as their spatial extension. A parameter describing the coherence of those dipoles radiation which is strongly dependent on the nanoparticle size is then introduced. The polar SHG responses as a function of this coherence parameter are then compared with the experimental results. Finally, in the last section, we develop some physical interpretations of this model and compare them which what is already well known with the non-linear responses of molecule. The emphases is put on the description of a non-punctual object like a nanoparticle which is of crucial importance to understand its difference with previous works on multipolar molecules.

3.2 Polarization resolved SHG measurements

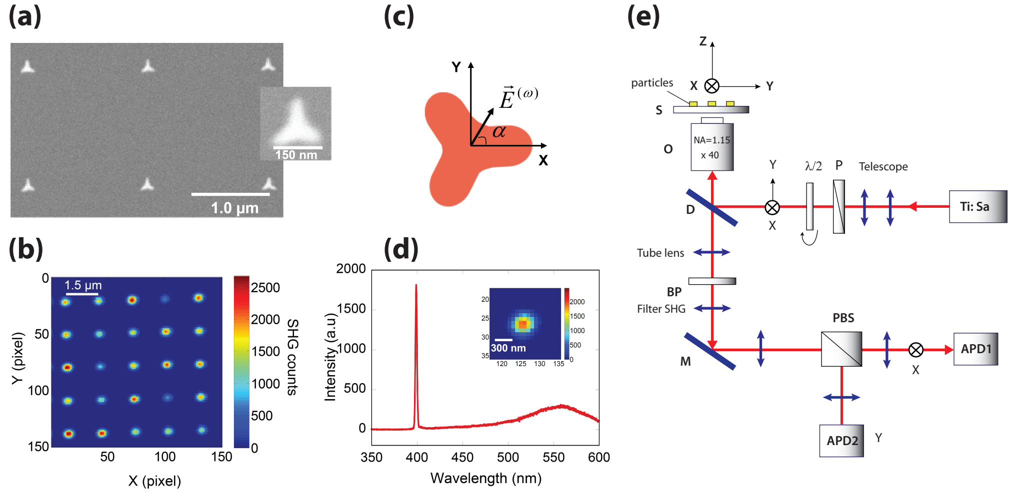

FIGURE 3.2: (a) Scanning Electron Microscopy (SEM) images of nano-stars particles. (b) SHG scanning image of an array of nano-stars. The signal scale represents the sum of the SHG signal over 32 incident polarization angles, in counts/100 μs, pixel size: 60 nm. (c) Geometry used for positioning the nanoparticles in the sample plane (X,Y) for polarization resolved and efficiency measurements. (d) Emission spectrum from a single nano-star. Integration time: 1s. (e) Schematic of the polarization resolved SHG experiment. Figure from [71].

Figure 3.2 outlines the SHG experiment conducted by N. T. Nguyen in her PhD and modeled in this chapter. The SHG signal of a single nanoparticle depicted in figure 3.2 (a) is collected using the experiment schematized in figure 3.2 (e). The nanoparticles were fabricated using the method presented in the first chapter. The signals were collected by two photodiodes, each one measuring a different polarization components thanks to a polarizing beam splitter. More details about the experimental procedure followed by N. T. Nguyen can be found in [71].

3.2.1 Description of the model

A model of polarization resolved response of nanostars is introduced in this section. We assume that the induced nonlinear dipoles follow roughly the direction of the incident polarization and are located close to the tip of the star arm. Therefore, three nonlinear sources that have the following susceptibility tensors β_1, β_2 and β_3 are modeled by positioning them at a given distance h from the center of particle as in figure 3.3. Each second harmonic induced dipole is treated like a point dipole with the hyperpolarizability β tensor consisting of 3 independent tensorial components [25, 72, 73]: $\beta_{\uparrow\uparrow\uparrow}$, $\beta_{\uparrow\perp\perp}$ and $\beta_{\perp\uparrow\perp}$ where the symbol $\uparrow$ denotes a direction along the arm the star and $\perp$ is perpendicular to its arm. With both theory and experiment, W. Hübner [74] showed that the tensorial element $\beta_{\uparrow\uparrow\uparrow}$ dominates over the elements $\beta_{\perp\uparrow\perp}$ and $\beta_{\uparrow\perp\perp}$. Each induced dipole thus possesses one single tensorial coefficient $\beta_{\uparrow\uparrow\uparrow}$ along each arm direction. The expression of polarization of each induced dipole is written :

$$\vec{\mu}_{j\uparrow} = \varepsilon_0\, \beta_{\uparrow\uparrow\uparrow} \cdot (\vec{E}^{(\omega)} \cdot \vec{e}_{j\uparrow}) \cdot (\vec{E}^{\omega} \cdot \vec{e}_{j\uparrow}) \cdot \vec{e}_{j\uparrow} \tag{3.1}$$

The three induced dipoles positioned in the focal plane, translated by a distance h from the focal point, emit a radiation that is collected by an imaging system such as the one described in chapter 2. Only the dipolar PSF needs to be used, the resulting imaged field is thus the sum of three imaged dipolar fields weighted by the strength of the dipoles β_1, β_2 and β_3.

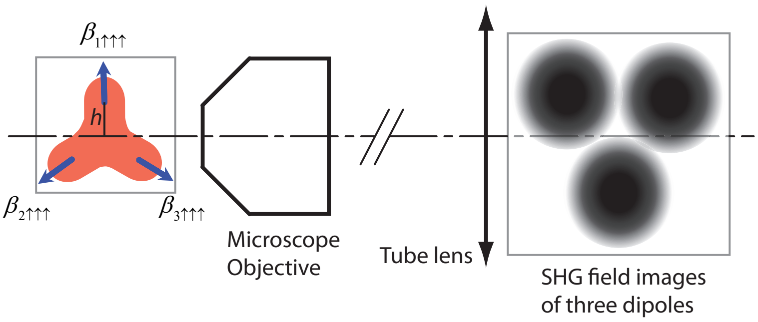

FIGURE 3.3: The radiation of three SH induced dipoles through the collection objective of microscope give rise to three SHG field images.

The total SHG signal results from the addition of the three radiations images, which contains incoherent contributions when the dipoles separation length introduces a loss of overlap in the SHG diffraction limit spots. A interference parameter c is introduced in order to weight the importance of the overlap between the dipoles radiations. Then, the parameter c is defined as a normalized overlap integral of two of the three electric fields E_i over the photodiode's surface.

$$c_{ijp} = \iint \frac{E_ip}{\sqrt{s_ip}} \frac{E_jp}{\sqrt{s_jp}} ds \tag{3.2}$$

Where p stands for X or Y to describe the detection of the X or the Y components of the imaged electric field on the photodiode. The normalizing factor s_{ip} is the integrated signal of the corresponding electric field over the photodiode. Since the star is considered to be perfectly symmetric so far, the coherence parameter is equal for every set of two dipoles and one obtained $c_{ijp} = c$.

In order to explicitly obtain an analytical expression for the total signal detected and the coherence parameter, one needs to use the exact forms of the imaged dipole electric fields. The imaged field of a radiating dipole through an aplanetic optical objective has been calculated [51, 52, 58] and we then use those results to complete the model. The total signal is given by :

$$\begin{aligned} s_{\text{total}} &= c\, s_{\text{coherent}} + (1-c)\, s_{\text{incoherent}} \\ &= c \iint \left(\sum_j E_j^{(2\,\omega)}(r,\alpha) \right)^2 ds + (1-c) \iint \sum_j \left(E_j^{(2\,\omega)}(r,\alpha) \right)^2 ds \end{aligned} \tag{3.3}$$

The coherence parameter is given as a function of the distance h of the three dipoles to the center of the star and also depends on the parameters of the optical microscope, the magnification M and the numerical aperture $NA = n \sin\theta_m$.

$$c = \frac{4}{\pi} \int_0^1 \frac{\sin(\sqrt{3}\, M\, a\, h\, \sqrt{1-v^2})}{\sqrt{3}\, M\, a\, h}\, dv \tag{3.4}$$

With $a = \frac{k\theta_m}{M}$. The derivation of the coherence parameter and the total detected signal can be found in the appendix D and its dependence on the translation length h is represented in Figure 3.4 .

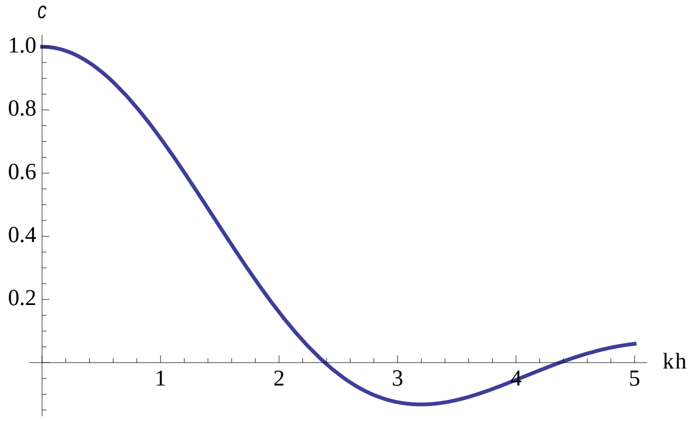

FIGURE 3.4: Evolution of the overlap parameter c as a function of the distance h of translation of the dipole from the center of the star. When $h = 0$, the 3 dipoles are on top of each other and then interfere constructively. As h increases, the overlap decreases and the dipoles start to interfere destructively.

Indeed, the total SHG signal s_{total} is independent of the polarization of the exciting field as it has been proven in previous studies [66]. However, the polarization beam splitter allows us to get the signal projected along X (s_x) and Y (s_y) axes of the sample plane. Those contributions to the signal vary strongly as a function of the polarization of $\underline{E}^{\omega}(\alpha)$, α being defined as the angle between X and $\underline{E}^{\omega}$. Then, a set of polar plots which are a signature of a nanoparticle's response is obtained for different values of c as displayed in figure 3.4.

When h is close to 0 as in figure 3.5 (a), the radiation adds up in a fully spatial coherent way and the resulting polarization dependence exhibits the characteristic lobes of threefold symmetry structures in the dipolar approximation. When h increases (see figures 3.5(b),(c),(d),(e),(f)) the overlap of the SHG images decreases, and spatial phase delay-like effects appear into the final signal build-up. As a consequence, an opening of the polarization responses lobes appears. When the SHG images do not overlap anymore, a complete incoherent addition of the responses occurs, with a loss of sensitivity to the threefold symmetry of the nanostructure. SHG polarization responses are therefore highly informative about both the symmetry of the nanoparticles and their spatial effects governed by their size.

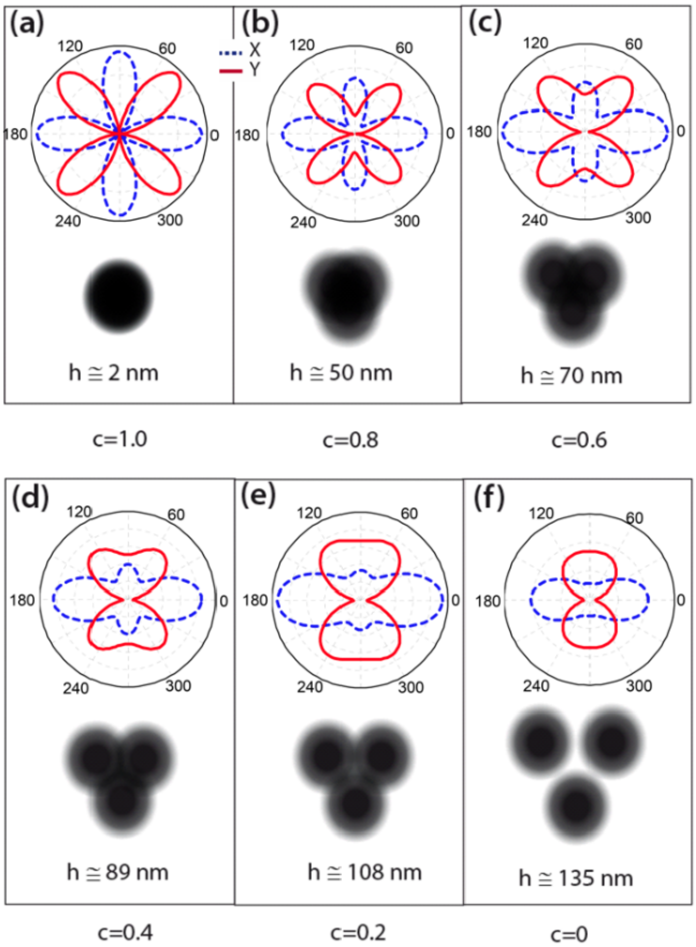

FIGURE 3.5: Those polar patterns show the SHG signal onto the photodiodes X and Y as a function of the polarization angle for various values of c corresponding to different translations h from the star center. Two lobes polar patterns are typical of a fully incoherent signal whereas four lobes polar ones are for fully coherent signals , corresponding to a threefold symmetry.

3.2.2 Comparison with experimental results

Experimental SHG polarization responses were recorded for a large quantity of single nano-stars. The incident polarization was varied continuously in the (X,Y) sample plane between 0° and 180° in 32 steps, and the emitted SHG signal was analyzed along the X and Y directions. The polarimetric SHG responses for each single particle of this array are then plotted as polar graphs by averaging the $s_X(\alpha\ )$ and $s_Y(\alpha)$ signals on an area of 10×10 pixels around the center of the nanoparticle. The polarization responses show deviations from particle to particle. About half of the whole investigated population exhibits a pure four lobe of polarization dependence for both $s_X(\alpha)$ and $s_Y(\alpha)$, while the rest of the population exhibit just two lobe polar shape. The SEM images corresponding to the measured particles show that the polarization response is strongly sensitive to the particle shape deviation. A careful check of the SEM images of recorded particles before and after SHG measurement show that shape deviations occur only during the fabrication processes. When a particle has lost its threefold symmetry even with a slight deviation, its polarization response exhibits a shape with two lobes.

Then, the model developed in the previous section is not sufficient to describe fully the imperfect nanostars and two others models have been constructed to take this into account. We finally use three models summarized in figure 3.5 to fit the experimental data :

- Model 1 (developed in section 3.1) : Ideal star with three dipoles of same strength β at $\frac{2\pi}{3}$ from each other and translated by h from the center ;
- Model 2 : An ideal star of model with a dipole added in the center. This dipole has a strength β_0 and an orientation γ ;
- Model 3 : With inequivalent dipoles of strengths β_1, β_2 and β_3 with angles ν_1 and ν_2 between the dipoles.

Moreover, an angle φ has been also included to describe an overall rotation by φ of the object in the (X,Y) plane. Fitting results show that there is a good agreement between the model 3 and the experimental data.

The fitting parameters also show that for polar plots exhibiting a pure four lobe shape, the corresponding nanostars' shapes are closer to a threefold symmetry (allowing slight angular deviation), give results in agreement with the SEM images (figure 3.6). The threefold symmetry of the nonlinear induced dipoles arrangement is seen to be slightly

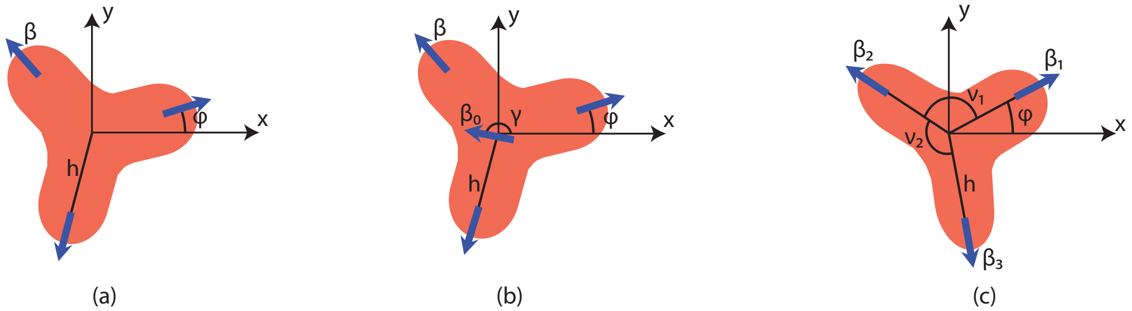

FIGURE 3.6: Schematic of the three models to fit the data. (a) Three dipoles of strength β located at a distance h from the center and separated by $\frac{2\pi}{3}$. (b) Same as (a) plus one dipole in the center of strength β_0 and angle γ. (c) Three dipoles of different strengths β_1, β_2 and β_3 and arbitrary angles ν_1 and ν_2.

modified for nanoparticles deviating from a perfect shape. In figure 3.7 (b), the nanostar has lost its three fold symmetry since one arm is visibly larger than the two other ones.

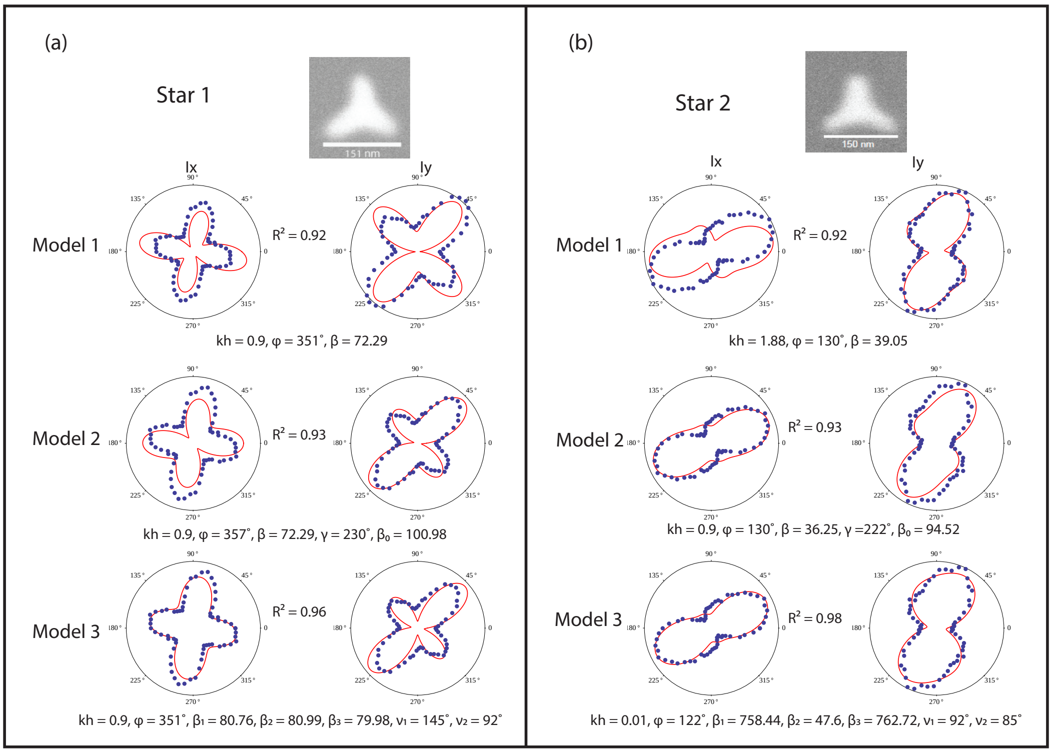

FIGURE 3.7: Fitting results obtained on the data of two typical nanostars. The fitting parameter can be obtained in table 3.2. (a) Star having an almost perfect threefold symmetry. The corresponding polar plots exhibit a characteristic four lobes shape. (b) Deformed nanostar. The model 1 that describes a perfect nanostar can not fit properly a polar response with a strong dipolar behavior.

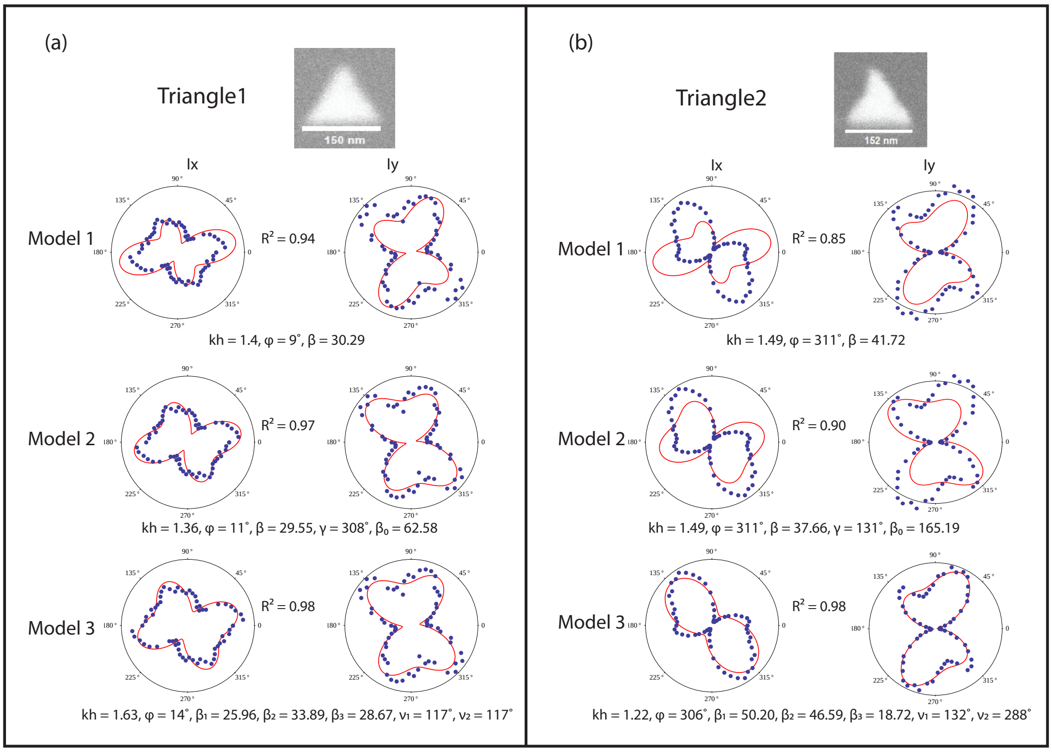

FIGURE 3.8: Fitting results on the data of two typical triangles, a perfect one (a) and a deformed one (b).

3.3 Multipolar interpretation of the data

The experimental results obtained on nanostars and nanotriangles are properly fitted using the model of the previous section. This model has permitted us to understand the high sensitivity of the response to the shape of the nanoparticle. This possibility to tune the polar response of the nonlinear emitter because of its shape is something new compared to the previous works on octupolar molecules and offer new engineering possibilities. For example, the insensitivity of the polar response is strongly due to the symmetry of the object. This is a non trivial property which depends on the nonlinear order of the interaction with the nanoparticle.

However, even if this model respects the symmetry of the nanoparticle, it does not highlight the influence of the symmetry group of the object. The nanoparticle is not treated as a whole but as a collection of dipoles. Moreover, it is possible to describe in principle any kind of shape by choosing an appropriate set of dipoles distribution but this choice would not make the physical interpretation much clearer. It is then interesting to treat the object as a whole with an unique response tensor which would include the element of symmetry of the nanoparticle.

For punctual objects, the expansion of the hyperpolarizability in its irreducible parts[34] has shown that the high nonlinear efficiency of those molecules was due to an important octupolar part of the tensor. Although multipolar elements of the tensor play an important role in the nonlinear response, the radiation of those molecules is still purely dipolar. However, a nanoparticle is an extended object and the richness of its physics is due to its spatial extension and shape. Then, one can not just simply use a local irreducible formalism to describe the nonlinear response. It can be shown that, as the size of the nanoparticle increase, higher multipolar radiations appear. To quantify those radiations, the radiated electric field is projected over the basis of the electric and magnetic vector spherical harmonics [21] defined in chapter 1 and that we recall here for convenience :

$$\begin{aligned} \underline{\Psi}_m^{JM}(r,\theta,\varphi) &= \frac{1}{\sqrt{J(J+1)}} j_J(kr) L Y_{JM}(\theta,\varphi) && (3.5) \\ \underline{\Psi}_e^{JM}(r,\theta,\varphi) &= \frac{i}{k} \nabla \wedge \underline{\Psi}_m^{JM}(r,\theta,\varphi) && (3.6) \end{aligned}$$

Where Y_{JM} is the scalar spherical harmonics, $L = \frac{1}{i}(\vec{r} \wedge \nabla)$ is the orbital angular momentum operator and j_J is the spherical Bessel function.

In this study, the multipolar coefficients are obtained by a direct projection of the current distribution in the following way :

$$J_i^{JM}(c) = \int \underline{J}(c,r) \cdot \underline{\Psi}_i^{JM} dV \tag{3.7}$$

Where i refers to m or e and $\underline{J}(c,r)$ is the current distribution generated by the three punctual dipoles according to the model of section 2. In this section, we do not use the whole apparatus of the multipolar PSF but it will be done in chapter 6 when we will be equipped with a more complete formalism. We recall that the norm of an irreducible tensor T^J is defined as [31] $\sum_M (-1)^M T^{JM} T^{J-M}$. Then, the norm of the coefficients over a whole subspace is calculated and normalized in order the measure the relative multipolar contributions.

$$J^J(c) = \frac{\sum_{iM} (-1)^M J_i^{JM}(c) J_i^{J-M}(c)}{\sum_{JiM} (-1)^M J_i^{JM}(c) J_i^{J-M}(c)} \tag{3.8}$$

The table 3.1 shows that, as the size of the nanoparticle increases the radiation has to be described using more and more multipolar orders. Indeed, when the particle has no spatial extension ($h = 0$) only a dipolar radiation is emitted as it is observed in the molecular case. Moreover, for the nanoparticle's size considered, only three orders of the multipolar expansion are necessary since the $J = 4$-pole does not appear for small

Multipolar orders $J^J(c)$	Dipole	Quadrupole	Octupole	$(J = 4)$-pole
$c = 1$ $(h = 0)$	1	0	0	0
$c = 0.8$ $(h = 50\text{nm})$	0.81	0.18	0.01	0.
$c = 0.6$ $(h = 70\text{nm})$	0.66	0.30	0.04	0.
$c = 0.4$ $(h = 89\text{nm})$	0.52	0.40	0.08	0.
$c = 0.2$ $(h = 108\text{nm})$	0.39	0.47	0.14	0.01

Table 3.1: Relative weights of the different multipole order for different values of the nanostar size.

nanoparticles. Then, nanoparticles with an high nonlinear efficiency are also the one that display a more complicated radiation including dipolar, quadrupolar and octupolar radiations.

The results in table 3.1 are obtained for the perfect star model. More extensive multipolar projection are done in table 3.2 for the different models involved using the fitting results from figure 3.7 and 3.8. The model 1 which consider 3 equivalents dipoles separated by $\frac{2\pi}{3}$ has been useful to describe an ideal star but does not provide excellent fits on the real nanostar. It comes from the deformation of the nanostar and then, model 2 and model 3 has been proposed to improve it. Model 2 adds a dipole at the center of the object while model 3 allows the dipoles to be oriented freely. Model 3 is the one giving the best fit and then the polar responses are more sensitive to deviation in the orientation of the dipoles. For the model 2 and 3, the multipolar distributions are dependent on the angle ϕ of the incoming field polarization. Then, we calculate this multipolar distribution for two angles, the one with the maximum of dipole denoted (dip) and the one with the maximum of quadrupole denoted (quad). One can observe that the star 1 possesses a much more important quadrupolar part than the star 2, especially using model 3. Then, the strong efficiency observed in the "good" stars seems to be related to their quadrupolar emission. On the other side, the multipolar distribution of triangle is quite robust to shape deformation although they don't have a great SHG efficiency.

Nanoparticles	Models	kh	φ	β_1	β_2	β_3	ν_1	ν_2	β_0	γ	R^2	Dipole	Quadrupole	Octupole
Star 1	M1	0.90	351	72.29	72.29	72.29	120	120	0	0	0.92	0.76	0.22	0.02
	M2 (dip)	0.90	357	72.29	72.29	72.29	120	120	100.98	230	0.93	0.96	0.04	0.
	M2 (quad)	”	”	”	”	”	”	”	”	”	”	0.81	0.18	0.01
	M3 (dip)	0.90	351	80.76	80.99	79.98	145	92	0	0	0.96	0.82	0.17	0.01
	M3 (quad)	”	”	”	”	”	”	”	”	”	”	0.38	0.60	0.02
Star 2	M1	1.88	130	39.05	39.05	39.05	120	120	0	0	0.92	0.31	0.49	0.18
	M2 (dip)	0.90	130	36.25	36.25	36.25	120	120	94.52	222	0.93	0.96	0.04	0.
	M2 (quad)	”	”	”	”	”	”	”	”	”	”	0.96	0.04	0.
	M3 (dip)	0.01	122	758.44	47.60	762.72	93	85	0	0	0.98	1.00	0.	0.
	M3 (quad)	”	”	”	”	”	”	”	”	”	”	0.72	0.28	0.
Triangle 1	M1	1.40	9	30.29	30.29	30.29	120	120	0	0	0.94	0.52	0.40	0.08
	M2	1.36	11	29.55	29.55	29.55	120	120	62.58	308	0.97	0.94	0.05	0.01
	M3	1.63	14	25.96	33.89	28.67	117	117	0	0	0.98	0.49	0.40	0.10
Triangle 2	M1	1.49	311	41.72	41.72	41.72	120	120	0	0	0.85	0.48	0.43	0.10
	M2	1.49	311	37.66	37.66	37.66	120	120	165.19	131	0.90	0.85	0.12	0.03
	M3	1.22	306	50.20	46.59	18.72	132	288	0	0	0.98	0.69	0.29	0.02

TABLE 3.2: This table summarizes the fitting parameters that has been calculated according the models of the previous section. Moreover, we calculate also the norm of the coefficient for the three first multipolar order through projection of the current density onto the multipolar electric vector fields. The experimental data has been taken for single nanoparticles and we provide here four typical cases. Star 2 is nanostar with some small deformation while star 1 is closer an ideal star shape. Equivalently, triangle 2 is a deformed triangle while triangle 1 has a better shape.

Part II

Development of a fully irreducible formalism

Chapter 4

A fully irreducible formalism for non-local objects

4.1 Motivation

In this chapter, a formalism which links directly the irreducible components of the incoming and outgoing fields will be developed. The irreducible response tensor constructed there is of completely different nature than the one presented in the previous parts. Those tensors were still belonging to the geometrical space related to cartesian tensors by an unitary transformation and then a reduction. Thus, the fields were just locally irreducible through the change of basis 1.35 but not globally. This is solved by using the multipolar fields introduced in the previous section and then the irreducible response tensor lies in a infinitely dimensional vector space spawned by the vector spherical harmonics (or one of their linear combination). Fortunately, in the case of metallic nanoparticles whose sizes are a bit smaller than the excitation wavelength, the multipolar expansion converges quickly and only up to the octupolar rank of the irreducible response tensor is needed.

However, it is important to emphasize that the situation discussed here describes a single nanoparticle without a high confinement of the electromagnetic fields. If such confinement were to be described, one may expect the multipolar expansion to converge slower. One the other hand, adding the diverging multipolar fields to the basis of the current density may help the description of such fields with more physical insights.

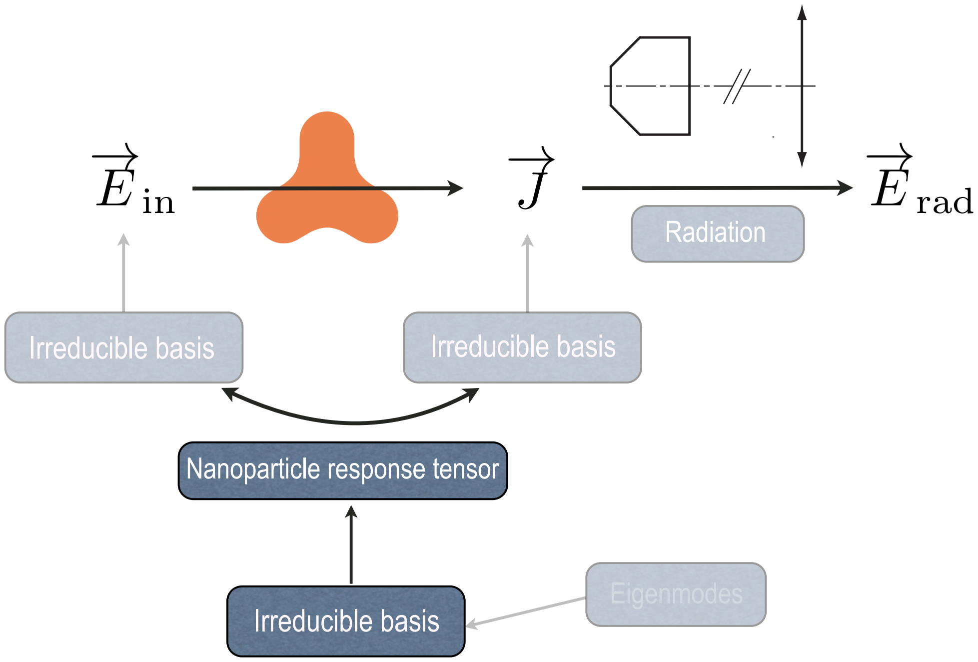

FIGURE 4.1: In this chapter, we focus on the construction of a fully irreducible response tensor that will represent how the nanoparticle connect incoming fields to radiating current density..

4.2 Derivation of the formalism

Is this section, the existence of such an irreducible response tensor is proven in two manners. The first way proceeds by identification and is quite naive but rather straightforward. The second way, which leads to much more interesting properties will necessitate to introduce more advanced mathematical tools, the bipolar vector spherical harmonics. We will then easily derive some properties of that object according to different objects. Finally, we will show how we can expand some basic beams at the vicinity of a particle in vector multipolar fields.

4.2.1 First derivation

We start from the common linear non-local response and get rid of the time dependence assuming harmonically varying fields for a while. In case of linear optics,it means that all the basis function will be used at a fixed wavenumber k. Thus, in this section the dependence on the wavenumber is considered implicit and will be most of the time omitted. The coefficients of the current density will be noted J_l^{JM} instead of J_k^{lJM}.

Then, the linear current density is obtained from the incoming electric field by the following relationship :

$$\vec{J} = \int \underline{\underline{R}}(r - r') \cdot \vec{E}_{\text{inc}}(r') d^3 r' \tag{4.1}$$

Where $\underline{\underline{R}}$ is the cartesian response tensor. In this equation, we expand the electric field into vector multipole fields. We use the regular ones since the electric field does not diverge in the vicinity of the nanoparticle. One is then left with :

$$\vec{J} = \sum_{l'J'M'} E_{l'}^{J'M'} \int j_{l'}(kr') \underline{\underline{R}}(r - r') \cdot \vec{Y}_{l'}^{J'M'}(r') d^3 r' \tag{4.2}$$

Now, using the definition of the vector spherical harmonics and writing the matrix product term by term, one is lead to the following expression :

$$\vec{J} \;=\; \sum_{l'J'M'} \sum_{\mu\sigma} E_{l'}^{J'M'} \int j_{l'}(kr') R_{\sigma\mu}(r - r') [Y_{l'}^{J'M'}(r')]^{\mu} \vec{e}_{\sigma} d^3 r' \tag{4.3}$$

One can now use the definition of the projection onto vector multipole fields to get the $l'J'M'$ components of the current density.

$$J_l^{JM} = \sum_{l'J'M'} E_{l'}^{J'M'} \sum_{\mu\sigma} \iint R_{\sigma\mu}(r - r') [\underline{\Psi}_{l'}^{J'M'}(r')]^{\mu} \underline{e}_{\sigma} \bullet \underline{\Psi}_l^{JM}(r) d^3 r d^3 r' \tag{4.4}$$

$$J_l^{JM} = \sum_{l'J'M'} E_{l'}^{J'M'} \sum_{\mu\sigma} \iint R_{\sigma\mu}(r - r') [\underline{\Psi}_{l'}^{J'M'}(r')]^{\mu} [\underline{\Psi}_l^{JM}(r)]^{\sigma} d^3 r d^3 r' \tag{4.5}$$

This can finally be summarized by introducing a response tensor R which relates components of the current density and incoming electric field.

$$J_l^{JM} = \sum_{l'J'M'} R_{lJM}^{l'J'M'} E_{l'}^{J'M'} \tag{4.6}$$

$$R_{lJM}^{l'J'M'} = \sum_{\mu\sigma} \iint R_{\sigma\mu}(r - r') [\underline{\Psi}_{l'}^{J'M'}(r')]^{\mu} [\underline{\Psi}_l^{JM}(r)]^{\sigma} d^3 r d^3 r' \tag{4.7}$$

Writing out explicitly the frequency dependence of the response tensor, one would get :

$$J_k^{lJM} = \sum_{l'J'M'} R_{lJM}^{l'J'M'}(k) E_k^{l'J'M'} \tag{4.8}$$

$$R_{lJM}^{l'J'M'}(k) = \sum_{\mu\sigma} \iint R_{\sigma\mu}(r-r')[\underline{\Psi}_{l'}^{J'M'}(k,r')]^{\mu}[\underline{\Psi}_{l}^{JM}(k,r)]^{\sigma} d^3r d^3r' \tag{4.9}$$

The response tensor links multipolar components with the same wavenumber together. Explicitly writing out the wavenumber dependence will become necessary when dealing with nonlinear optics because different wavenumbers get mixed in this case.

The equation 4.6 is very important since it shows that a formalism expressed only in terms of multipolar coefficients is possible and can be linked with the usual cartesian description. Then, one can start with the multipolar coefficients of the electric field and get those of the current. The tensor R has as uncommon nature : it relates elements of two infinite dimensional vector spaces, both being vector spaces of vector multipole fields. Moreover, the basis vectors inside the vector multipole space are vector fields rather than collections of three numbers... An infinite dimensional vector space of vector fields is very appealing despite its complexity. Its strength relies on its ability to describe extended objects with a limited number of elements and without integrating the local fields over the nanoparticle.

Another interest in describing the light matter interaction with the equation 4.6 is the possibility to easily include the symmetry properties of the nanoparticle. We will show later that symmetries reduce the number of non-vanishing components and that rotations and translations of the nanoparticle are easy to work out.

However, this first proof of existence of such a tensor does not provide a clear interpretation of the nature of the tensor R. The coefficients of E and J live in the vector space spanned respectively by $\Psi_{l'}^{J'M'}(r')$ and $\Psi_{l}^{JM}(r)$ but we need to know in which vector space the $R_{lJM}^{l'J'M'}$ are.

4.2.2 Second derivation

In this section, we offer another derivation which will lead to the same expression relating the multipolar coefficients of the incoming electric field and the current density. However, this one will make obvious the nature of this tensor which relates different vector spaces and how it can be reduced. Intuitively, one could assume that the basis of the tensor R is obtained by the direct product of the vector multipole fields. This can formally be written :

$$\underline{\underline{R}} = \sum_{l_1J_1M_1}\sum_{l_2J_2M_2} R_{l_1J_1M_1}^{l_2J_2M_2}\ \underline{\Psi}_{l_1}^{J_1M_1} \otimes \underline{\Psi}_{l_2}^{J_2M_2} \tag{4.10}$$

For the formalism developed by J. Zyss and S. Brasselet, we know that we can express the current density vector on the spherical basis.

$$\underline{J} = \sum_{\sigma} J^{\sigma} e_{\sigma} \tag{4.11}$$

Where J^{σ} is calculated from a fully contracted product with the electric field and a reading tensor.

$$J^{\sigma} = \int \underline{\underline{R}}(r, r_1) \bullet \Big(E \otimes e_{\sigma} \Big) d^3 r_1 \tag{4.12}$$

We can now expand the electric field in vector multipole fields and also project the current density onto them.

$$\begin{aligned}
J_{l_2}^{J_2 M_2} &= \sum_{\sigma} \int J^{\sigma}(r_2) \underline{e}_{\sigma} \bullet \underline{\Psi}_{l_2}^{J_2 M_2}(r_2) d^3 r_2 \\
&= \sum_{l_1 J_1 M_1} E_{l_1}^{J_1 M_1} \sum_{\sigma} \int \Big(\int \underline{\underline{R}}(r_2, r_1) \bullet \big(\underline{\Psi}_{l_1}^{J_1 M_1}(r_1) \otimes \underline{e}_{\sigma} \big) \Big[\underline{\Psi}_{l_2}^{J_2 M_2}(r_2) \Big]^{\sigma} d^3 r_1 \Big) d^3 r_2 \\
&= \sum_{l_1 J_1 M_1} E_{l_1}^{J_1 M_1} \int \Big(\int \underline{\underline{R}}(r_2, r_1) \bullet \big(\underline{\Psi}_{l_1}^{J_1 M_1}(r_1) \otimes \big(\sum_{\sigma} \Big[\underline{\Psi}_{l_2}^{J_2 M_2}(r_2) \Big]^{\sigma} \underline{e}_{\sigma} \big) \big) d^3 r_1 \Big) d^3 r_2 \\
&= \sum_{l_1 J_1 M_1} E_{l_1}^{J_1 M_1} \int \Big(\int \underline{\underline{R}}(r_2, r_1) \bullet \big(\underline{\Psi}_{l_1}^{J_1 M_1}(r_1) \otimes \underline{\Psi}_{l_2}^{J_2 M_2}(r_2) \big) d^3 r_1 \Big) d^3 r_2
\end{aligned} \tag{4.13}$$

We see from the last equation that the coefficients $J_{l_2}^{J_2 M_2}$ are obtained after a full contraction with the object $\underline{\Psi}_{l_1}^{J_1 M_1}(r_1) \otimes \underline{\Psi}_{l_2}^{J_2 M_2}(r_2)$ and an integration over all space. This operation really looks like a scalar product and suggest we can also develop $\underline{\underline{R}}(r_2, r_1)$ over the basis $\underline{\Psi}_{l_1}^{J_1 M_1}(r_1) \otimes \underline{\Psi}_{l_2}^{J_2 M_2}(r_2)$. Expanding scalar functions of two angular directions is already a well-known problem that can be tackled using the bipolar spherical harmonics, which are defined in the following way :

$$\Big\{ Y_{l_1}(\theta_1, \varphi_1) \otimes Y_{l_2}(\theta_2, \varphi_2) \Big\}^{LM} = \sum_{m_1 m_2} C_{l_1 m_1 l_2 m_2}^{LM} \; Y_{l_1 m_1}(\theta_1, \varphi_1) Y_{l_2 m_2}(\theta_2, \varphi_2) \tag{4.14}$$

The Clebsch-Gordan coefficients appear in the definition since the tensor product $Y_{l_1 m_1}(\theta_1, \varphi_1) \otimes Y_{l_2 m_2}(\theta_2, \varphi_2)$[1] is generally reducible. Then, an irreducible basis of bipolar spherical harmonics needs to be defined using the irreducible tensor product. The bipolar spherical

---

[1] Also written as $Y_{l_1 m_1}(\theta_1, \varphi_1) Y_{l_2 m_2}(\theta_2, \varphi_2)$ for shortness.

harmonics form an irreducible orthonormal basis according to the following orthogonality relation :

$$\iint \left\{Y_{l_1}(\Omega_1)\otimes Y_{l_2}(\Omega_2)\right\}^{LM}\left\{Y_{l_1'}(\Omega_1)\otimes Y_{l_2'}(\Omega_2)\right\}^{L'M'} d\Omega_1 d\Omega_2 = \delta_{l_1 l_1'}\delta_{l_2 l_2'}\delta_{LL'}\delta_{MM'} \tag{4.15}$$

In our problem, we want to describe a tensor function $\underline{\underline{R}}(r_2, r_1)$ and not a scalar one anymore. In the equation 4.13, we see that the tensor $\underline{\underline{R}}(r_2, r_1)$ is contracted with the object $\underline{\Psi}_{l_1}^{J_1M_1}(r_1)\otimes\underline{\Psi}_{l_2}^{J_2M_2}(r_2)$ and we can then deduce they are of same nature. Moreover, we know from classical tensor analysis that a tensor of rank 2 can be defined in the space constructed by the direct product of the underlining vector space and itself (or its dual). We can then define the bipolar vector spherical harmonics as an extension of the bipolar spherical harmonics to the vectorial case. Thus, we have the following definition :

$$\left\{\underline{Y}_{l_1}^{J_1}(\Omega_1)\otimes\underline{Y}_{l_2}^{J_2}(\Omega_2)\right\}^{JM} = \sum_{M_1M_2} C^{LM}_{J_1M_1J_2M_2}\,\underline{Y}_{l_1}^{J_1M_1}(\Omega_1)\underline{Y}_{l_2}^{J_2M_2}(\Omega_1) \tag{4.16}$$

Where Ω_1 is the couple of angles (θ_1, φ_1). We are now going to prove the orthogonality of the vector bipolar spherical harmonics. We start by recalling the orthogonality relationship of the vector spherical harmonics :

$$\int \underline{Y}_{l'}^{J'M'}(\Omega)\bullet\underline{Y}_{l}^{JM}(\Omega)d\Omega = \delta_{ll'}\delta_{JJ'}\delta_{MM'} \tag{4.17}$$

To prove the orthogonality of the vector bipolar spherical harmonics, we just need to take their scalar product and insert their definition in the following way :

$$\begin{aligned}\iint &\left\{\underline{Y}_{l_1}^{J_1}(\Omega_1)\otimes\underline{Y}_{l_2}^{J_2}(\Omega_2)\right\}_{JM}\bullet\left\{\underline{Y}_{l_1'}^{J_1'}(\Omega_1)\otimes\underline{Y}_{l_2'}^{J_2'}(\Omega_2)\right\}_{J'M'} d\Omega_1 d\Omega_2\\ &= \sum_{M_1M_2,M_1'M_2'} C^{JM}_{J_1M_1J_2M_2}C^{J'M'}_{J_1'M_1'J_2'M_2'}\int \underline{Y}_{l_1}^{J_1M_1}(\Omega_1)\bullet Y_{l_2}^{J_2M_2}(\Omega_1)d\Omega_1\times\\ &\qquad\int \underline{Y}_{l_1'}^{J_1'M_1'}(\Omega_2)\bullet Y_{l_2'}^{J_2'M_2'}(\Omega_2)d\Omega_2\end{aligned} \tag{4.18}$$

$$= \delta_{l_1l_1'}\delta_{l_2l_2'}\delta_{J_1J_1'}\delta_{J_2J_2'}\sum_{M_1M_2} C^{JM}_{J_1M_1J_2M_2}C^{J'M'}_{J_1M_1J_2M_2} \tag{4.19}$$

$$= \delta_{l_1l_1'}\delta_{l_2l_2'}\delta_{J_1J_1'}\delta_{J_2J_2'}\delta_{JJ'}\delta_{MM'} \tag{4.20}$$

We see that the vector bipolar spherical harmonics form an orthogonal basis for the response tensor $\underline{\underline{R}}$. We stop here in our presentation of the bipolar vector spherical harmonics and go back to equation 4.13. We expand the response tensor as direct products of vector spherical harmonics.

$$\underline{\underline{R}}(k_1;k_2) = \sum_{l_1 l_1 J_1 l_2 J_2 M_2} R^{l_2 J_2 M_2}_{l_1 J_1 M_1} \; \underline{\Psi}^{J_1 M_1}_{l_1}(k_1, r_1) \otimes \underline{\Psi}^{J_2 M_2}_{l_2}(k_2, r_2) \tag{4.21}$$

The wavenumber dependence has been kept general in this case. In the case of linear optics $k_1 = k_2 = k$ and one is left with the previous expression $\underline{\underline{R}}(k)$ or simply $\underline{\underline{R}}$ where k is implied.

However, in the previous equation, the tensor $\underline{\underline{R}}$ is not expanded on a irreducible basis which is a loss for our theory that we want to be completely irreducible. Then, one can reduce the basis using the orthogonality of the Clebsch-Gordan coefficients. This reduction is exactly the same as the one used to reduce $Y_{lm} \otimes e_\sigma$ in vector spherical harmonics and we thus only give the result here :

$$\underline{Y}^{J_1 M_1}_{l_1}(\Omega_1) \otimes \underline{Y}^{J_2 M_2}_{l_2}(\Omega_2) = \sum_{JM} C^{JM}_{J_1 M_1 J_2 M_2} \left\{ \underline{Y}^{J_1}_{l_1}(\Omega_1) \otimes \underline{Y}^{J_2}_{l_2}(\Omega_2) \right\}_{JM} \tag{4.22}$$

The response tensor can then be expanded in vector bipolar spherical harmonics in the following way :

$$\underline{\underline{R}} = \sum_{JM} \sum_{l_1 l_2 J_1 J_2} R^{JM}_{l_1 l_2 J_1 J_2} \left\{ \underline{\Psi}^{J_1}_{l_1}(r_1) \otimes \underline{\Psi}^{J_2}_{l_2}(r_2) \right\}_{JM} \tag{4.23}$$

$$R^{JM}_{l_1 l_2 J_1 J_2} = \sum_{M_1 M_2} C^{JM}_{J_1 M_1 J_1 M_2} R^{l_2 J_2 M_2}_{l_1 J_1 M_1} \tag{4.24}$$

We can finally prove in a very straightforward way the equation 4.6 we obtained in the first derivation. In the equation 4.13, we insert the expansion of the response tensor in direct product of vector spherical harmonics and simply use the orthogonality properties.

$$
\begin{aligned}
J_{l_2}^{J_2M_2} &= \sum_{l_1J_1M_1} E_{l_1}^{J_1M_1} \int \Big(\int \underline{\underline{R}}(r_2, r_1) \bullet \big(\underline{\Psi}_{l_1}^{J_1M_1}(r_1) \otimes \underline{\Psi}_{l_2}^{J_2M_2}(r_2)\big) d^3r_1 \Big) d^3r_2 \\
&= \sum_{l_1J_1M_1} \sum_{\substack{l'_2J'_2M'_2 \\ l'_1J'_1M'_1}} R_{l'_1J'_1M'_1}^{l'_2J'_2M'_2}\ E_{l_1}^{J_1M_1} \iint \Big(\underline{\Psi}_{l'_1}^{J'_1M'_1}(r_1) \otimes \underline{\Psi}_{l'_2}^{J'_2M'_2}(r_2)\Big) \bullet \\
&\qquad\qquad\qquad\qquad\qquad\qquad \Big(\underline{\Psi}_{l_1}^{J_1M_1}(r_1) \otimes \underline{\Psi}_{l_2}^{J_2M_2}(r_2)\Big) d^3r_1 d^3r_2 \\
&= \sum_{l_1J_1M_1} \sum_{\substack{l'_2J'_2M'_2 \\ l'_1J'_1M'_1}} R_{l'_1J'_1M'_1}^{l'_2J'_2M'_2}\ E_{l_1}^{J_1M_1} \delta_{(l_1J_1M_1),(l'_1J'_1M'_1)} \delta_{(l_2J_2M_2),(l'_2J'_2M'_2)} \\
&= \sum_{l_1J_1M_1} R_{l_1J_1M_1}^{l_2J_2M_2}\ E_{l_1}^{J_1M_1}
\end{aligned}
\tag{4.25}
$$

A factor $\frac{\pi}{2k^2}\delta_k(0)$ has been simplified because of the orthogonality of the Bessel function recalled here :

$$
\int_0^{+\infty} j_n(kr) j_n(k'r) r^2 dr = \frac{\pi}{2k^2}\delta(k - k') \tag{4.26}
$$

To make the equation more compact and corresponding with the result of the previous section, we can include those constant number in the definition of the response tensor and we are then left with the following simple result :

$$
J_{l_2}^{J_2M_2} = \sum_{l_1J_1M_1} R_{l_1J_1M_1}^{l_2J_2M_2}\ E_{l_1}^{J_1M_1} \tag{4.27}
$$

In those two sections, we have shown that we can define a response tensor relating the multipolar coefficients of the incoming electric field and the radiating current density. This tensor allows to describe an extended response and deals with the complete fields without carrying out an integral over all space. The infinite number of elements in that sum is not a big problem since we will want to describe the response tensors of nanoparticles. Their size is not negligible compared to the exciting wavelength and then the multipolar expansion is not reduced to its first dipolar order but those nanoparticles are still smaller than the wavelength. Thus, we know that only the first few coefficients of J will be non-negligible. As an illustration, according to the model of the previous chapter, we have hints which show that for a nanoparticle of 150 nm illuminated with a light at 800 nm (SHG at 400 nm), only the first 3 terms alone will be sufficient to describe the second order response. Moreover, a small number of coefficient $E_{l_1}^{J_1M_1}$ are needed to model with a good precision the field at the vicinity of the nanoparticle. This aspect will be developed further in the next section.

Before dealing with the multipolar expansion of common exciting electric fields, we will first derive some simple properties of the irreducible response tensor under rotation and translation, define a relationship relating multipolar coefficient using that irreducible response tensor and extend the theory to describe non-linear responses.

4.2.3 Nonlinear response tensor

So far, we have only been concerned with the linear response of a nanoparticle. We now want to extend the formalism to describe non-linear responses. In the previous sections, we have not included the frequency dependence of the response tensor but it is trivially deduced from the k dependence of the tensor by the dispersion relationship. However, in the case of a non-linear response, we have to explicitly write the frequency and allow the response tensor to mix the frequencies of the incoming electric fields as commonly seen in in non-linear optics. This extension is quite straightforward since it just implies that the coefficients of the response tensor and of the electric become frequency dependent. In the case of a linear response, we simply get :

$$J^{(1)JM}_{\;\;l}(\omega) = \sum_{l_1 J_1 M_1} R^{(1)lJM}_{\;\;l_1 J_1 M_1}(\omega)\; E^{J_1 M_1}_{l_1}(\omega) \tag{4.28}$$

The exponent (1) stands for the first order of the non-linear expansion (i.e. the linear response) following the usage in the spectroscopy field. Then, the second order non-linear current would be given by the following expression :

$$J^{(2)JM}_{\;\;l}(\omega) = \sum_{l_1 J_1 M_1 l_2 J_2 M_2} R^{(2)lJM}_{\;\;l_1 J_1 M_1 l_2 J_2 M_2}(\omega;\omega_1,\omega_2)\; E_1{}^{J_1 M_1}_{\;l_1}(\omega_1) E_2{}^{J_2 M_2}_{\;l_2}(\omega_2) \tag{4.29}$$

A generalization of this equation to the nth order is also straightforward to obtain :

$$J^{(n)JM}_{\;\;l}(\omega) = \sum_{l_1 J_1 M_1 \cdots l_n J_n M_n} R^{(n)lJM}_{\;\;l_1 J_1 M_1 \cdots l_n J_n M_n}(\omega;\omega_1,\cdots,\omega_n)\; E_1{}^{J_1 M_1}_{\;l_1}(\omega_1) \cdots E_n{}^{J_n M_n}_{\;l_n}(\omega_n) \tag{4.30}$$

The nth order non-linear response tensor is then expanded over the basis spanned by the direct product of $n+1$ vector spherical fields $\underline{\Psi}_{l_1}^{J_1 M_1}(k_1, r_1) \otimes \cdots \otimes \underline{\Psi}_{l_n}^{J_n M_n}(k_n, r_n) \otimes \underline{\Psi}_{l}^{JM}(k, r)$ that will also be written $\bigotimes_n \underline{\Psi}_{l_n}^{J_n M_n}(k_n, r_n)$ for compactness. It is clear that this $n+1$ dimensional basis can be reduced in the same way as the two-dimensional one we got when we were describing a linear response.

4.2.4 Fully reduced tensor

The response tensor of the previous sections is linking two irreducible basis. However, the response tensor itself is not fully reduced since it does not transform by rotation according to the Wigner $\mathcal{D}$ matrices. In this section, we show how this tensor can be reduced in the case of a second-order nonlinear optical process, the Second Harmonic Generation (SHG), that will be used later.

The squared exciting field will then be reduced and written as a reading field, following J. Zyss semantics [35]. In this formalism, the component of the irreducible current being read is calculated from the fully contracted product of the response tensor and the reading field in a natural way $J^{(2)} = \underline{\underline{\underline{R}}}^{(2)} \bullet \underline{\underline{\underline{F}}}$. The nonlinear response tensor expansion becomes :

$$\underline{\underline{\underline{R}}}^{(2)} = \sum_{i_1 J_1 i_2 J_2 i J M} R^{(2)\ J'M'}_{i_1 J_1 i_2 J_2 (J_{12}) i J M}(2k; k, k) \underline{\underline{\underline{\Psi}}}^{(3)\ J'M'}_{i_1 J_1 i_2 J_2 (J_{12}) i J M}(2k; k, k) \tag{4.31}$$

Where $\underline{\underline{\underline{\Psi}}}^{(3)}$ is a tripolar vector spherical harmonic defined by :

$$\underline{\underline{\underline{\Psi}}}^{(3)\ J'M'}_{i_1 J_1 i_2 J_2 (J_{12}) i J M}(2k; k, k) = \left\{ \left\{ \underline{\Psi}^{J_1}_{i_1}(k) \otimes \underline{\Psi}^{J_2}_{i_2}(k) \right\}^{J_{12}} \otimes \underline{\Psi}^{JM}_{i}(2k) \right\}^{J'M'} \tag{4.32}$$

The notation here has a small subtlety : the reading component $\underline{\Psi}^{JM}_i$ should in fact not depend on M according to the definition of the irreducible tensor product. Indeed, a sum over M is contained in the definition of the tensor product but, in order to read only one component corresponding to the desired multipolar current coefficient, we consider the vector of multipolar tensor fields with a component equal to one for $\underline{\Psi}^{JM}_i$ and zero for the others. We will also omit J_{12} in the following notation since it is not necessary in this problem. In practice, the fact that many coefficients are zero naturally forbid multiple paths of couplings.

Symmetry constraints can be applied in a straightforward manner on the fully irreducible tensor in a similar way as the one presented at the end of chapter 1 on the polarizability α. Moreover, each component of the tensor is clearly associated to an element of the symmetry group. For example, it is possible to infer which components will disappear or appear if the shape of the nanoparticle is modified or which one should be small if they belong to small defects, like rugosity.

4.3 Basic developments

4.3.1 Rotation of the nanoparticle

From now, we will call the response tensor, the response tensor expanded on the reducible basis $\underline{\Psi}_{l_1}^{J_1M_1}(r_1) \otimes \underline{\Psi}_{l_2}^{J_2M_2}(r_2)$ with coefficients $R_{l_1J_1M_1}^{l_2J_2M_2}$ and will we use the name irreducible response tensor for the one expanded on the bipolar vector spherical harmonics with coefficients $R_{l_1l_2J_1J_2}^{JM}$.

Rotating the nanoparticle has a very simple effect on the irreducible response tensor because it is by definition an irreducible tensor ! This effect is calculated using the usual Wigner D^J matrices parametrized by the Euler angles $\Omega = (\theta, \varphi, \Psi)$ in the following way :

$$R_\Omega\Big[R_{l_1l_2J_1J_2}^{JM'}\Big] = \sum_M D_{MM'}^J(\Omega)\ R_{l_1l_2J_1J_2}^{JM} \tag{4.33}$$

The rotation of the reducible response tensor is a bit more complicated. Since this tensor is not irreducible, one can not just use the Wigner matrices to perform the rotation. In order to do this operation, we can proceed in two steps : we first rotate the incoming electric field to make it incident at the angle we want on the object, then we rotate the current in the opposite direction to put everything back in the original frame of coordinate.

We can expand both fields in their multipolar coefficients and using the Wigner D matrices to operate their rotation.

$$J_l^{JM} = \sum_{l'J'M'} \sum_{M_2} R_{l'J'M'}^{lJM}\ D_{M_2M'}^{(J')}(\Omega)\ E_{l'}^{J'M_2} \tag{4.34}$$

$$\sum_{M_1} D_{MM_1}^{(J)*}(\Omega) J_l^{JM_1} = \sum_{l'J'M'} \sum_{M_2} R_{l'J'M'}^{lJM}\ D_{M_2M'}^{(J')}(\Omega)\ E_{l'}^{J'M_2} \tag{4.35}$$

$$J_l^{JM} = \sum_{l'J'M'} \sum_{M_1M_2} \Big(D_{M_1M}^{(J)}(\Omega)\ R_{l'J'M_2}^{lJM_1}\ D_{M_2M'}^{(J')}(\Omega)\Big)\ E_{l'}^{J'M'} \tag{4.36}$$

We have renamed the dummy indices to make the equation clearer. From the last equation, we see how the reducible response tensor will transform under rotation :

$$R_\Omega\big(R_{l'J'M'}^{lJM}\big) = \sum_{M_1M_2} D_{M_1M}^{(J)}(\Omega)\ R_{l'J'M_2}^{lJM_1}\ D_{M_2M'}^{(J')}(\Omega) \tag{4.37}$$

4.3.2 Translation of the nanoparticle

We now turn our attention to the translation transformation. In the equation 4.1, a translation of the object will result in an additional translation vector $\tilde{r}$. The response tensor $\underline{\underline{G}}(r-r')$ defined on the cartesian basis is thus now replaced by $\underline{\underline{G}}(r-r'-\tilde{r})$.

$$\underline{J}(r) = \int \underline{\underline{G}}(r-r'-\tilde{r})\ \underline{E}(r')d^3r' = \int \underline{\underline{G}}(r-r')\ \underline{E}(r'-\tilde{r})d^3r' \tag{4.38}$$

The coefficients of the reducible response tensor defined in equation 4.7 are almost the same, only the arguments of the vector spherical harmonics belonging to the electric field are translated by $\tilde{r}$:

$$R^{l'J'M'}_{lJM} = \sum_{\mu\sigma} \iint G_{\sigma\mu}(r-r')[\underline{\Psi}^{J'M'}_{l'}(r'-\tilde{r})]^{\mu}[\underline{\Psi}^{JM}_{l}(r)]^{\sigma} d^3r d^3r' \tag{4.39}$$

One can use the translation theorem of vector spherical harmonics defined in chapter 5 which we recall here :

$$\underline{\Psi}^{J'M'}_{l'}(r'-\tilde{r}) = \sum_{l''J''M''} T_{l''J''M'',l'J'M'}(\tilde{r})\underline{\Psi}^{J''M''}_{l''}(r') \tag{4.40}$$

Inserting this equation in the previous one, one can see that the reducible response tensor follows the rule of translation of vector multipole fields :

$$T_{\tilde{r}}\left[R^{lJM}_{l'J'M'}\right] = \sum_{l''J''M''} T_{l''J''M'',l'J'M'}\ R^{lJM}_{l''J''M''} \tag{4.41}$$

The translation behavior of the irreducible response tensor is obtained easily using the relationship linking it to the reducible one :

$$T_{\tilde{r}}\left[R^{JM}_{l_1 l_2 J_1 J_2}\right] = \sum_{M_1 M_2} C^{JM}_{J_1 M_1 J_1 M_2} T_{\tilde{r}}\left[R^{l_2 J_2 M_2}_{l_1 J_1 M_1}\right] \tag{4.42}$$

4.3.3 Dipolar order

The aim of this section is to show how the response gets simplified in the case of a local and punctual response. Before discussing the response tensor itself, we will discuss how a point dipole, a doublet, can described over the multipolar basis. For simplicity, we will consider the multipolar expansion of a doublet oriented along the z axis :

$$\underline{J} = \delta(\vec{r})\vec{e}_0 \tag{4.43}$$

To get the multipolar expansion of this doublet, one can simply project it over the basis of the multipolar vector fields :

$$\begin{aligned} J_k^{lJM} &= \int_r \delta(r)\vec{e}_0 \bullet \underline{\Psi}_l^{JM*}(k,r)d^3r && (4.44)\\ &= \left[\underline{\Psi}_l^{JM*}(k,0)\right]^0 && (4.45)\\ &= \frac{k}{\pi\sqrt{2}}\delta_{l,0}\delta_{J,1}\delta_{M,0} && (4.46) \end{aligned}$$

Where we have used the fact that the only non-vanishing multipolar vector field is $\underline{\Psi}_0^{1M}$ which take the following value :

$$\underline{\Psi}_0^{1M}(k,0) = \frac{k}{\pi\sqrt{2}}e_M \tag{4.47}$$

Using the electromagnetic multipolar basis, one would observe that only the electric multipole $\underline{\Psi}_e^{1M}$ is non-vanishing.

A doublet will then radiate a dipolar field at all wavenumbers, i.e. at all frequencies and can be expressed as :

$$\underline{J} = \delta(\vec{r})\vec{e}_0 = \int_k \frac{k}{\pi\sqrt{2}}\underline{\Psi}_0^{10}(k)dk \tag{4.48}$$

Now, we will consider what are the implication of system behaving like a doublet on the response tensor itself and link it with the standard cartesian response tensor. We will switch to an expansion in term of the electromagnetic multipole fields $\underline{\Psi}_i^{JM}$ with $i = e, m, l$ instead of the vector multipole fields because this basis has a much direct physical interpretation. The reducible response tensor can then be written on that basis without any difficulty since those two bases are simply related by a "rotation". The coefficients of the expansion on bipolar multipole fields are $R_{i'J'M'}^{iJM}$ instead of $R_{l'J'M'}^{lJM}$.

Since the multipolar expansion of a doublet leads to a dipolar radiation for all k, the response tensor takes a non-vanishing value only for $i = e$, $J = 1$. Since the response is considered local, the electric field interacts with the doublet only at the origin of the coordinate frame. Thus, only the dipolar components on the electric field interacts with the double because only those components are non-vanishing at the frame of coordinate using a similar reasoning as for the expansion of the current density.

To link the multipolar response tensor to the cartesian one, one can use the projection equation 4.7 that we recall here :

$$R_{iJM}^{i'J'M'} = \sum_{\mu\sigma} \iint R_{\sigma\mu}(r-r')[\underline{\Psi}_{l'}^{J'M'}(k,r')]^{\mu}[\underline{\Psi}_l^{JM}(k,r)]^{\sigma}d^3rd^3r' \tag{4.49}$$

In the case of a point of matter, one needs only to consider the dipolar part of the projection and the previous equation simplifies as :

$$R_{e1M}^{e1M'} = \sum_{\mu\sigma} \iint R_{\sigma\mu}(r-r')[\underline{\Psi}_e^{1M'}(k,r')]^{\mu}[\underline{\Psi}_e^{1M}(k,r)]^{\sigma} d^3r d^3r' \tag{4.50}$$

The consideration of a single point of matter implies that the spatial dependence of the cartesian response tensors is simply a Dirac that can be expanded as dipolar fields for all k :

$$R_{e1M}^{e1M'} = \sum_{\mu\sigma} \iint \iint R_{\sigma\mu} \frac{k}{\pi\sqrt{2}} j_0(kr) \frac{k'}{\pi\sqrt{2}} j_0(k'r') dk dk' [\underline{\Psi}_e^{1M'}(k,r')]^{\mu}[\underline{\Psi}_e^{1M}(k,r)]^{\sigma} d^3r d^3r' \tag{4.51}$$

To calculate the integrals over space and wavenumbers, one need the expression of the electromagnetic dipolar field at the origin :

$$\underline{\Psi}_e^{1M}(k,0) = \sqrt{\frac{2}{\pi}} \, \frac{k}{\sqrt{4\pi}} \, (\sqrt{\frac{2}{3}} \underline{e}_M) \tag{4.52}$$

Where the contribution of $\underline{\Psi}_2^{1M}$ has not been written because it is orthogonal with j_0. Inserting this definition and doing the integral over space gives :

$$\begin{aligned} R_{e1M}^{e1M'} &= \frac{1}{2\pi^2} \iint R_{MM'}(0) \; kk' \frac{k^2}{3\pi^2} \, \frac{\pi^2}{4k^4} \delta(k-k') dk dk' && (4.53) \\ R_{e1M}^{e1M'} &= \frac{1}{6} \frac{R_{MM'}(0)}{4\pi^2} && (4.54) \end{aligned}$$

Only the elements $i = i' = e$, $J = J' = 1$ of the irreducible tensor are non vanishing under those two approximations : firstly, only the dipolar component of the field interacts with the object and secondly the material radiate only a dipolar field. Thus, a single dot of interacting material is effectively corresponding to an usual dipole as one would have expected. Moreover, for a point object, the response tensor defined on the multipolar basis coincides with the standard response tensor defined over the irreducible basis (e_1, e_0, e_{-1}). Discussions on irreducibility of systems represented by this kind of tensors and their interpretations thus correspond to the classical case of Jerphagnon [34] and extensively used in nonlinear optics by Zyss and co-workers [35].

4.3.4 Zyss' writing and reading fields

Although we have defined the irreducible response tensor over the vector spherical harmonics space, we have mainly used its reducible version. In order to use the irreducible response tensor, we still need to show how this irreducible tensor can be related to the electric current which radiated the measured electric field. On their use of the irreducible tensor over the spherical basis, J. Zyss and S. Brasselet [36] developed the concept of a reading field which we are going to explain now.

In the standard cartesian picture, the linear polarization is obtained using the matrix product of the polarisability and the incoming electric field in the following way $\vec{P} = \alpha \cdot \vec{E}$. However, when using higher order tensors and an irreducible description of the matter properties, the matrix product is not clearly defined anymore. Then, to get the components of the polarization that is actually measured, Zyss has introduced an unit vector $\underline{v}$, that allows to use fully contracted product which are well defined in tensor theory.

$$\underline{P}_{\underline{v}} = \alpha \bullet \left(\underline{v} \otimes \underline{E}\right) \tag{4.55}$$

According to the previous equation, we obtain the magnitude of the electric field in the $\underline{v}$ direction using a full contraction. The tensor $\left(\underline{v} \otimes \underline{E}\right)$ is called a reading field since the tuning of a polarizer giving the direction $\underline{v}$ allows one to isolate experimentally each component of the polarisability and then "read" this tensor. In the case where $\underline{v}$ is one of the basis vectors, we then obtain the component of P along that basis vector :

$$P_i = \alpha \bullet \left(\underline{e}_i \otimes \underline{E}\right) \qquad \text{where } i = x, y, z \tag{4.56}$$

This way of obtaining the polarization allowed to expand both α and the reading field and is straightforwardly extended to non-linear orders. We now wish to prove that this kind of description is still valuable when working with a vector multipole fields basis. We start with the fully contracted products of the linear reducible response tensor with the direct product of a reading vector (the equivalent of $\underline{v}$ before) and the incoming electric field. We begin by expressing the response tensor R along its basis.

$$\underline{\underline{R}} \bullet \left(\underline{\Psi}_l^{JM} \otimes \underline{E}\right) = \sum_{\substack{l_1 J_1 M1 \\ l_2 J_2 M_2}} R^{l_2 J_2 M_2}_{l_1 J_1 M_1} \left(\underline{\Psi}_{l_1}^{J_1 M_1}(r) \otimes \underline{\Psi}_{l_2}^{J_2 M_2}(r')\right) \bullet \left(\underline{\Psi}_l^{JM}(r) \otimes \underline{E}(r')\right) \tag{4.57}$$

$$= \sum_{\substack{l_1 J_1 M1 \\ l_2 J_2 M_2}} R^{l_2 J_2 M_2}_{l_1 J_1 M_1} \left(\underline{\Psi}_{l_1}^{J_1 M_1}(r) \bullet \underline{\Psi}_l^{JM}(r)\right) \otimes \left(\underline{\Psi}_{l_2}^{J_2 M_2}(r') \bullet \underline{E}(r')\right) \tag{4.58}$$

Where we have regrouped terms belonging to the same subspace. We can now use the orthogonality condition to express those contracted products and expand the electric field over the vector spherical fields. We recall the orthogonality of the vector spherical harmonics ;

$$\iint \underline{Y}_{l'}^{J'M'}(\Omega)^* \cdot \underline{Y}_l^{JM}(\Omega) d\Omega = \delta_{ll'} \delta_{JJ'} \delta_{MM'} \tag{4.59}$$

This scalar product is used to express this contraction and one obtain :

$$R \bullet \left(\underline{\Psi}_l^{JM} \otimes E \right) = \sum_{\substack{l_1 J_1 M1 \\ l_2 J_2 M_2}} R^{l_2 J_2 M_2}_{l_1 J_1 M_1} \delta_{l_1 l} \delta_{J_1 l} \delta_{M_1 M} \sum_{l' J' M'} \delta_{l_2 l'} \delta_{J_2 J'} \delta_{M_2 M'} E_{l'}^{J' M'} \tag{4.60}$$

$$= \sum_{l' J' M'} R^{l' J' M'}_{l J M} E_{l'}^{J' M'} \tag{4.61}$$

$$= J_l^{JM} \tag{4.62}$$

From the last result, we see that the expression $R \bullet \left(\underline{\Psi}_l^{JM} \otimes E \right)$ still allows us to read one specific component of the current density. However, we now read one component of the multipolar expansion of the current density (which is directly related to the multipolar components of the radiated field) instead of one of the cartesian vectors. We can now use of the well known reduction schemes to reduce the response tensor and the reading field. Both of them will them be express over the bipolar vector spherical harmonics.

In this chapter, a fully irreducible formalism has been presented. This formalism grants us the ability to discuss the influence of the symmetry on the nonlinear response since it contains all the information about the shape in a discrete number of components having a clear geometrical behavior. It is then expected that this formalism, applied to concrete cases, could lead to a better understanding of the link between shapes and physical properties. For example, it can show which components are dominant in nanostars and nanotriangles compared to nanospheres. To do so, it is possible to make models within that formalism that will be presented in the next chapters.

Additionally, it is expected that the inclusion of elements not belonging to the symmetry group would make some components of the tensor appear. Experiments carried on nanoparticles such as EELS [75] show that the geometric eigenmodes are extremely robust and are not greatly affected by small deviations. Then, small defects and rugosity for example should not lead to major modifications on the main components of the irreducible response tensor and their influence should depends on the eigenmodes, i. e. the energy, considered. According to this, it is conjectured that the components of the response tensor can be associated with various physical properties of the object.

Chapter 5

Translational addition as a tool to describe extended objects

5.1 On the use of the translational addition theorem

In this chapter, we will see how multipoles can be spatially moved in a chosen frame of coordinates. In order to achieve this translation, the translated multipole fields are expanded over the basis of multipolar fields located at the origin of another frame of coordinates. This transformation is algebraically done by the translational addition theorem demonstrated by Cruzan [76] and by Danos and Maximon [77].

It will be shown it the next chapter how the translational addition theorem can serve as a tool to model nonlinear sources in a nanoparticles. Assuming a spatial distribution of radiating dipoles, one can gather them all at a single point and describe them as a sum of multipoles. The weight of each of those multipoles can then be measured using, for example, results of the previous chapter. Multipoles constructed in this way offer global informations about the system whereas a distribution of dipole only reflects the local environment. Thus, non-vanishing multipoles can also be inferred from group theoretical arguments and measured directly without assuming a local distribution of radiating dipoles. This approach has to be contrasted with techniques like the Discrete-Dipole Approximation (DDA) [64, 78] or the Multiple MultiPole (MMP) method [79] which are losing informations on global properties of the nanoparticles. Expressed differently, the goal of such numerical techniques is to discretize the problem efficiently while the aim here is to synthesize it.

In this chapter, we firstly introduce the translational addition theorem using a modern demonstration [80–85]. Then, we apply it to two simple cases that are useful for the understanding of the behavior of the multipolar fields under translation. We firstly introduce infinitesimal translations that have interesting algebraic properties. For example, one could expect that the sum of two infinitesimally multipole would construct multipoles of higher orders like a derivative would do but they instead create particular and simple combinations of higher and lower orders of multipoles.

5.2 Demonstration of the translational addition theorem

5.2.1 Scalar translational addition theorem

Let us start with the functions $\Psi_{lm}(r,\theta,\phi) = j_l(kr)Y_{lm}(\theta,\phi)$ which are solutions of the scalar Helmoltz equation $(\Delta + k^2)\Psi = 0$ where k^2 is a parameter corresponding to the wavevector magnitude squared of the considered wave. So, the functions Ψ_{lm} are the scalar multipole fields.

The translational addition theorem is robust by the change of the radial function. It means that everywhere in this chapter, the spherical Bessel function can be replaced by a Hankel function of the first kind. Those functions will not be discussed here but more can be find in the paper by Felderhof [82].

In order to describe two infinitely near multipoles, it is necessary to know how the Ψ_{lm} in a frame of coordinates can be translated, the result being described as a sum of multipole field in the same frame. We will write $\Psi_{lm}(\vec{r})[\vec{R}]$ the function of $\vec{r}$ corresponding to a pure multipolar field in the frame $\vec{r} + \vec{R}$. This function will usually correspond to an infinite sum of multipolar fields in the frame $\vec{r}$. The frame associated with $\vec{r}$ will be describe using the coordinates (r,θ,ϕ) while the translation vector $\vec{R}$ can be projected on this basis and has coordinates $\vec{R} = [R,\Omega,\Phi]$. At this stage, it is important to recall that great care should be taken with the difference between active and passive translation : it is equivalent to translate a function values by $\vec{R}$ or its coordinate frame by $-\vec{R}$. Because we want to work with active translations of the multipolar fields, we have to translate the coordinates by $-\vec{R}$. This discussion is represented in the adjacent picture.

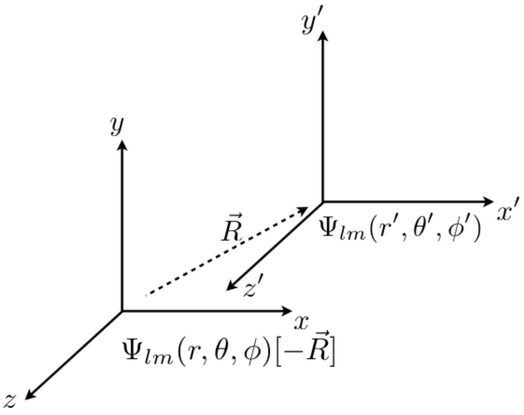

The translated multipolar field is projected of the multipolar fields basis in the original frame using coefficients $T_{l'm',lm}[R,\Omega,\Phi]$ which depends on the multipolar field under consideration and the translation applied to it :

$$\Psi_{lm}[R,\Omega,\Phi] = \sum_{l',m'} T_{l'm',lm}[R,\Omega,\Phi]\Psi_{l'm'} \tag{5.1}$$

We have omitted variables of the functions for shortness since they all depend on (r,θ,ϕ). The explicit expression of the $T_{l'm',lm}[R,\Omega,\Phi]$ coefficients can be calculated using the spherical expansion of a plane wave (Rayleigh expansion) :

$$e^{i\vec{k}\cdot\vec{r}} = 4\pi\sum_{lm} i^l j_l(kr)Y_{lm}(\theta',\varphi')Y^*_{lm}(\theta,\varphi) \tag{5.2}$$

Where r,θ,φ are the coordinates of vector $\vec{r}$ and k,θ',φ' those of vector $\vec{k}$.

One can now consider a translation $-\vec{R}$ that transforms the frame r,θ,φ in r',θ',φ'. In this case, we take the coordinates of $\vec{k}$ to be k,θ'',φ''. The plane wave $e^{i\vec{k}\cdot\vec{r}}$ can be written $e^{i\vec{k}\cdot\vec{r}'}e^{i\vec{k}\cdot\vec{R}}$. Using the Rayleigh expansion, we find :

$$\begin{aligned}\sum_{LM} 4\pi i^L j_L(kr)Y^*_{LM}(\theta'',\varphi'')Y_{LM}(\theta,\varphi) &= \left(\sum_{l'm'} 4\pi i^{l'} j_{l'}(kr')Y^*_{l'm'}(\theta'',\varphi'')Y_{l'm'}(\theta',\varphi')\right)\times \\ &\times\left(\sum_{l''m''} 4\pi i^{l''} j_{l''}(kR)Y^*_{l''m''}(\theta'',\varphi'')Y_{l''m''}(\Omega,\Phi)\right)\end{aligned} \tag{5.3}$$

To be able to use the orthogonality between the spherical harmonics on the left hand side of this equation, it is necessary to multiply each side by $Y_{lm}(\theta'',\varphi'')$ and to integrate over the whole solid angle : only the lm term survive in the sum. The right hand side is reduced is the integration of three spherical harmonics formula.

$$\begin{aligned}\int Y_{lm}(\theta,\varphi)Y_{l'm'}(\theta,\varphi)Y_{l''m''}(\theta,\varphi)d\Omega &= \sqrt{\frac{(2l+1)(2l'+1)(2l''+1)}{4\pi}}\times \\ &\begin{pmatrix} l & l' & l'' \\ 0 & 0 & 0 \end{pmatrix}\begin{pmatrix} l & l' & l'' \\ -m & m' & m'' \end{pmatrix}\end{aligned} \tag{5.4}$$

The right hand side 5.3 then becomes :

$$\sum_{l'm'}\left(\sum_{l''m''}(4\pi)^{\frac{3}{2}}i^{l'+l''}\sqrt{(2l+1)(2l'+1)(2l''+1)}\begin{pmatrix} l & l' & l'' \\ 0 & 0 & 0 \end{pmatrix}\begin{pmatrix} l & l' & l'' \\ -m & m' & m'' \end{pmatrix}\times\right.$$
$$\left.\times\, j_{l''}(kR)Y_{l''m''}(\Omega,\Phi)\right)j_{l'}(kr')Y_{l'm'}(\theta',\varphi') \quad (5.5)$$

Associating r', θ', φ' with the origin coordinate frame and comparing with equation 5.1, the $T_{l'm',lm}[R,\Omega,\Phi]$ coefficients are finally expressed in the following way :

$$T_{l'm',lm}[R,\Omega,\Phi] = \sum_{l'',m''} i^{l'+l''-l}(-1)^m\sqrt{4\pi(2l+1)(2l'+1)(2l''+1)}\times$$
$$\begin{pmatrix} l & l' & l'' \\ 0 & 0 & 0 \end{pmatrix}\times\begin{pmatrix} l & l' & l'' \\ -m & m' & m'' \end{pmatrix} j_{l''}(R)Y_{l''m''}(\Omega,\Phi) \quad (5.6)$$

In figure 5.1, we show that the construction of Ψ_{00} as a sum of other multipolar fields in another frame is possible and we remark that a big number of multipole is not necessary to achieve a satisfying reconstruction. The convergency will in fact depend on the order of the Ψ_{lm} and on the size of the translation. In figure 5.2, we show a similar result in the case of Ψ_{31}.

5.2.2 Tensor translational addition theorem

To calculate the translation coefficients of vector spherical harmonics, we will start with the result obtained for scalar multipole fields and couple each side with the spherical basis vector. We will extensively use Fano and Racah notation of irreducible tensor products that we used in equation 1.77.

$$\sum_{m'm''} C^{lm}_{l'm'l''m''}Y_{l'm'}(\theta',\varphi')\,Y_{l''m''}(\theta'',\varphi'') = \left\{Y^{l'}\otimes Y^{l''}\right\}^{lm} \quad (5.7)$$

If T is an irreducible tensor of rank J, T^J is the whole irreducible subspace spanned by T^J is $T^{J,J}$, $T^{J,J-1}$ ... $T^{J,-J}$. Using this notation, we can write the scalar multipole translation as :

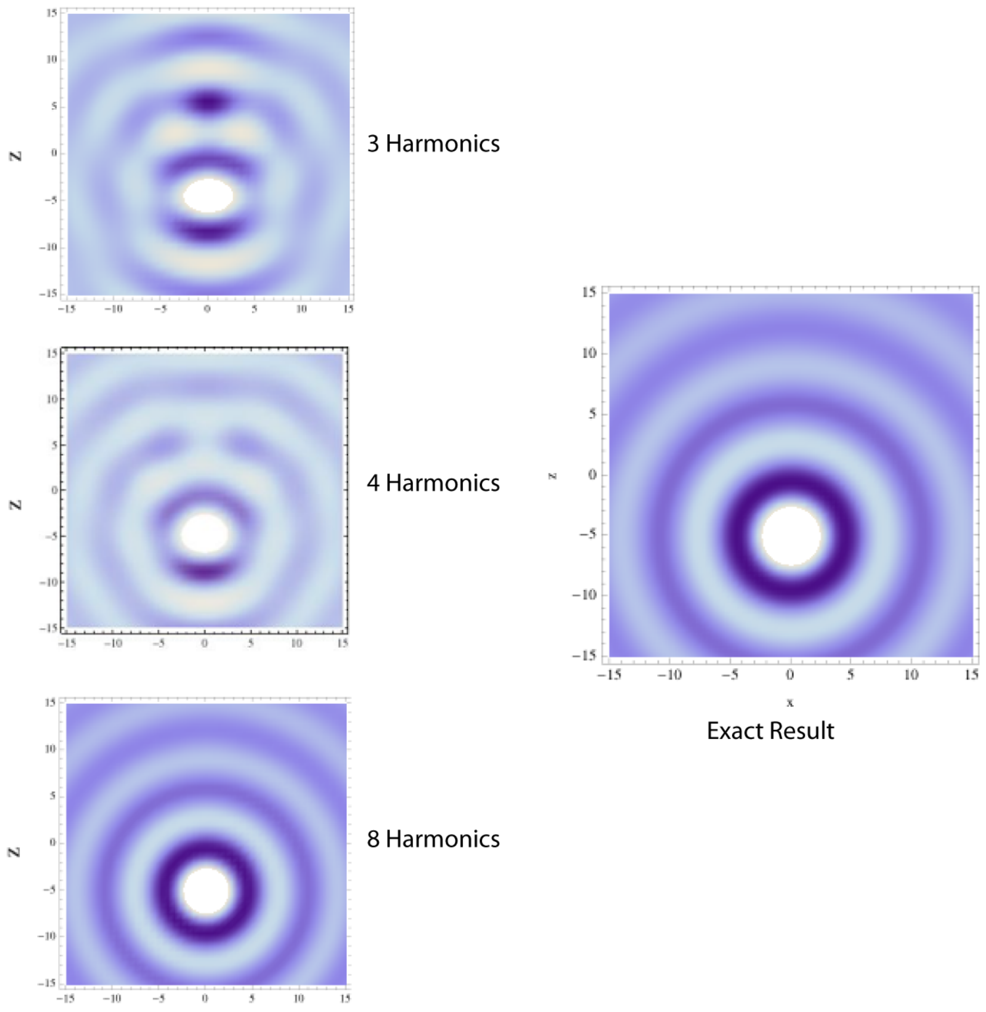

FIGURE 5.1: Translation of Ψ_{00} by 5 units along $-\vec{e}_z$. Only the function with $M=0$ are used due the specific direction of translation.

$$\Psi_{lm}[R] = \sum_{l'l''} i^{l'+l''-l}(-1)^{l'-l''}\sqrt{4\pi(2l'+1)(2l''+1)}\begin{pmatrix} l & l' & l'' \\ 0 & 0 & 0 \end{pmatrix} j_{l''}(kR)j_{l'}(kr')\left\{Y^{l'}\otimes Y^{l''}\right\}^{lm} \tag{5.8}$$

The new coefficients before the $3j$ symbol comes from the conversion of the second $3j$ symbol of equation 5.6 in a Clebsch-Gordan symbol using equation 1.28. We now couple each side with the spherical basis vector :

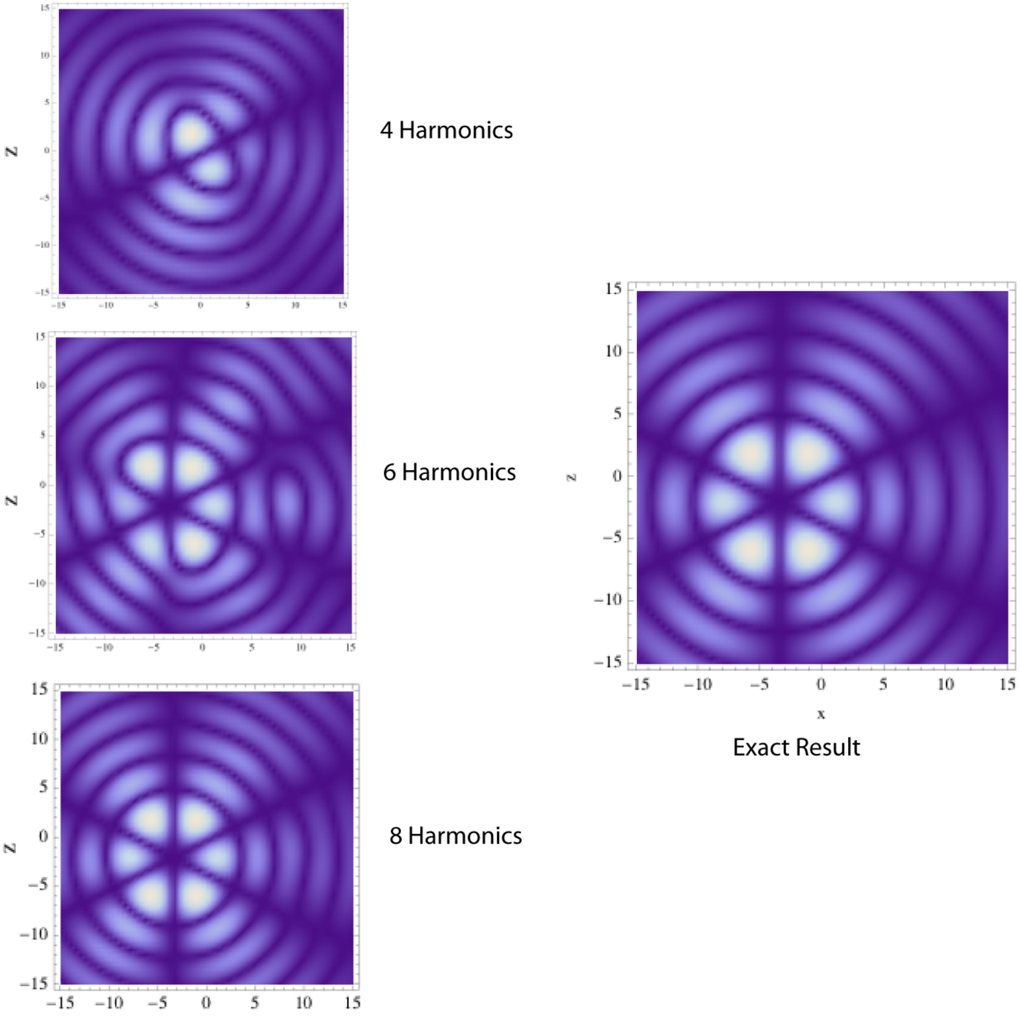

FIGURE 5.2: Translation of Ψ_{31} along the vector $[4, \frac{\pi}{3}, 0]$ (in spherical coordinates).

$$\left\{\Psi^{l}\otimes e^{s}\right\}^{JM} = \sum_{l'l''} i^{l'+l''-l}(-1)^{l'-l''}\sqrt{4\pi(2l'+1)(2l''+1)}\begin{pmatrix} l & l' & l'' \\ 0 & 0 & 0 \end{pmatrix} j_{l''}(kR)j_{l'}(kr')\times$$
$$\times\left\{\left\{Y^{l''}\otimes Y^{l'}\right\}^{l}\otimes e^{s}\right\}^{JM} \tag{5.9}$$

In this equation, three angular momenta appear : L'', L' and S. The coupling scheme which appeared naturally in the previous equation is the following $J = (L'' + L') + S = L + S$. However, we need to express the result as a sum of vector spherical harmonics and thus have to change the coupling scheme to $J = L'' + (L' + s) = L'' + J'$. This is a physically equivalent coupling and an unitary transformation relate the two schemes. Irreducible tensors recoupling formula is given in Varshalovich's book (p.69 [31]) and can be applied in our case :

$$\begin{aligned}\left\{\left\{Y^{l''}\otimes Y^{l'}\right\}^{l}\otimes e^{s}\right\}^{JM} = \sum_{J'}(-1)^{l'+l''+S+J}\sqrt{(2l+1)(2J'+1)}\begin{Bmatrix} l'' & l' & l \\ S & J & J' \end{Bmatrix}\\ \left\{Y^{l''}\otimes\left\{Y^{l'}\otimes e^{s}\right\}^{J'}\right\}^{JM}\end{aligned} \tag{5.10}$$

Using this result in equation 5.9, we find :

$$\begin{aligned}\left\{\Psi^{l}\otimes e^{s}\right\}^{JM} = \sum_{l'l''J'} i^{l'+l''-l}(-1)^{S+J}\sqrt{4\pi(2l+1)(2l'+1)(2l''+1)(2J'+1)}\begin{pmatrix} l & l' & l'' \\ 0 & 0 & 0 \end{pmatrix}\times\\ \times\begin{Bmatrix} l'' & l' & l \\ S & J & J' \end{Bmatrix} j_{l''}(kR)j_{l'}(kr')\left\{Y^{l''}\otimes\left\{Y^{l'}\otimes e^{s}\right\}^{J'M'}\right\}^{JM}\end{aligned} \tag{5.11}$$

We now use equation 5.7 to separate translation coefficient and vector multipoles :

$$\begin{aligned}\left\{\Psi^{l}\otimes e^{s}\right\}^{JM} = \sum_{l'l''J'}\sum_{m''M'} i^{l'+l''-l}(-1)^{S+J}\sqrt{4\pi(2l+1)(2l'+1)(2l''+1)(2J'+1)}\begin{pmatrix} l & l' & l'' \\ 0 & 0 & 0 \end{pmatrix}\times\\ \times\begin{Bmatrix} l'' & l' & l \\ S & J & J' \end{Bmatrix} C^{JM}_{l''m''J'M'} j_{l''}(kR)j_{l'}(kr')Y_{l''m''}(\Omega,\Phi)\left\{Y^{l'}\otimes e^{s}\right\}^{J'M'}\end{aligned} \tag{5.12}$$

Let us convert the Clebsch-Gordan symbol into a $3j$ symbol :

$$\begin{aligned}\left\{\Psi^{l}\otimes e^{s}\right\}^{JM} = \sum_{l'J'M'}\Bigg(\sum_{l''m''} i^{l'+l''-l}(-1)^{S+M}\sqrt{4\pi(2l+1)(2l'+1)(2l''+1)(2J+1)(2J'+1)}\times\\ \times\begin{pmatrix} l & l' & l'' \\ 0 & 0 & 0 \end{pmatrix}\begin{pmatrix} J & J' & l'' \\ -M & M' & m'' \end{pmatrix}\begin{Bmatrix} l'' & l' & l \\ S & J & J' \end{Bmatrix} j_{l''}(kR)Y_{l''m''}(\Omega,\Phi)\Bigg) j_{l'}(kr')\left\{Y^{l'}\otimes e^{s}\right\}^{J'M'}\end{aligned} \tag{5.13}$$

Finally, we can write vector multipolar fields translation in the simpler form :

$$\underline{\Psi}_{l}^{JM}[R,\Omega,\Phi] = \sum_{l'J'M'} T_{l'J'M',lJM}\underline{\Psi}_{l'}^{J'M'} \tag{5.14}$$

$$T_{l'J'M',lJM}[R,\Omega,\Phi] = \sum_{l''m''} i^{l'+l''-l}(-1)^{M+1}\sqrt{4\pi(2l+1)(2l'+1)(2l''+1)(2J+1)(2J'+1)}\times$$
$$\times \begin{pmatrix} l & l' & l'' \\ 0 & 0 & 0 \end{pmatrix} \begin{pmatrix} J & J' & l'' \\ -M & M' & m'' \end{pmatrix} \begin{Bmatrix} l'' & l' & l \\ 1 & J & J' \end{Bmatrix} j_{l''}(kR)Y_{l''m''}(\Omega,\Phi) \quad (5.15)$$

5.3 Application of the translational addition to simple cases

5.3.1 Infinitesimal addition of multipoles

5.3.1.1 Infinitesimal translation in the scalar case

We start with the simplest translation : the one along z. It is the simplest because the resulting sum will not mix different values of m. We consider the limit of two multipoles translated along z. So one is translated by $[\epsilon,0,0]$ while the other one is translated by $[\epsilon,\pi,0]$. In this section, we will omit the arguments of the functions Ψ_{lm} since they will all be expressed in the same coordinate system (r,θ,Φ).

$$\lim_{\epsilon\to 0}\frac{\Psi_{lm}[\epsilon,\pi,0]-\Psi_{lm}[\epsilon,0,0]}{k\epsilon} \quad (5.16)$$

We can use equation 5.1 to introduce the $T_{l'm',lm}[R,\Omega,\Phi]$ in the previous one. Since the spherical harmonics expansion converge uniformly, we can safely exchange limit and sum :

$$\lim_{\epsilon\to 0}\frac{\Psi_{lm}[\epsilon,\pi,0]-\Psi_{lm}[\epsilon,0,0]}{k\epsilon} = 2\sum_{l'm'}\lim_{\epsilon\to 0}\frac{T_{l'm',lm}[\epsilon,\pi,0]-T_{l'm',lm}[\epsilon,0,0]}{2k\epsilon}\Psi_{l'm'} \quad (5.17)$$

The factor 2 has been introduced here for convenience and the factor k to keep the denominator independent of the wave vector scale. We can now simplify the expression of the coefficients which appear in this expansion.

$$\lim_{\epsilon\to 0}\frac{T_{l'm',lm}[\epsilon,\pi,0]-T_{l'm',lm}[\epsilon,0,0]}{2k\epsilon} = \sum_{l''m''} i^{l'+l''-l}(-1)^{m}\sqrt{4\pi(2l+1)(2l'+1)(2l''+1)}\begin{pmatrix} l & l' & l'' \\ 0 & 0 & 0 \end{pmatrix}\times$$
$$\times\begin{pmatrix} l & l' & l'' \\ -m & m' & m'' \end{pmatrix}\left(\lim_{\epsilon\to 0}\frac{j_{l''}(k\epsilon)}{k\epsilon}\right)\frac{Y_{l''m''}(\pi,0)-Y_{l''m''}(0,0)}{2} \quad (5.18)$$

Using parity properties of the spherical harmonics, we can greatly reduce this expression.

$$\frac{Y_{l''m''}(\pi,0)-Y_{l''m''}(0,0)}{2}=\frac{(-1)^{l''+m''}-1}{2}Y_{l'',m''}(0,0) \tag{5.19}$$

On the other hand, the limit implying spherical Bessel function $j_{l''}$ can also be worked out. In fact, for all $l''\neq 0$, $j_{l''}(0)=0$; thus the limit can be written as a derivative. However, we need to take care of the $l''=0$ case. In this case, we have to use the spherical harmonics to remove the indetermination.

$$\lim_{\epsilon\to 0}\frac{j_0(k\epsilon)}{k\epsilon}\left(Y_{00}(\pi,0)-Y_{00}(0,0)\right)=\lim_{\epsilon\to 0}\frac{1}{2\sqrt{\pi}}\left(\frac{\sin(k\epsilon)}{k^2\epsilon^2}-\frac{\sin(k\epsilon)}{k^2\epsilon^2}\right)=0 \tag{5.20}$$

In all the other case, $l''\neq 0$ and we can derivate spherical Bessel functions :

$$j_{l''}(kr)'=\frac{k}{2l''+1}\Bigg(l''j_{l''-1}(kr)-(l''+1)j_{l''+1}(kr)\Bigg) \tag{5.21}$$

The derivative being taken as ϵ tend to zero, only $l''=1$ contributes.

$$\lim_{\epsilon\to 0}\frac{j_{l''}(k\epsilon)}{k\epsilon}=\left[\frac{d}{d(kr)}j_{l''}(kr)\right]_{r=0}=\frac{l''}{2l''+1}\delta_{l'',1} \tag{5.22}$$

The sum over l'' in equation 5.18 is thus reduced to only one term. We can also simplify the summation over m using equation 5.19 which, in the case $l''=1$, is equal to $-Y_{10}(0,0)\delta_{m'',0}$. Equation 5.18 becomes :

$$\lim_{\epsilon\to 0}\frac{T_{l'm',lm}[\epsilon,\pi,0]-T_{l'm',lm}[\epsilon,0,0]}{2k\epsilon}=-i^{l'+1-l}(-1)^m\sqrt{(2l+1)(2l'+1)}\begin{pmatrix} l & l' & 1\\ 0 & 0 & 0\end{pmatrix}\begin{pmatrix} l & l' & 1\\ -m & m' & 0\end{pmatrix} \tag{5.23}$$

Finally, two scalar multipolar fields translated along z can be expressed as :

$$\lim_{\epsilon\to 0}\frac{\Psi_{lm}[\epsilon,\pi,0]-\Psi_{lm}[\epsilon,0,0]}{k\epsilon}=-2\sum_{l'm'}i^{l'+1-l}(-1)^m\sqrt{(2l+1)(2l'+1)}\begin{pmatrix} l & l' & 1\\ 0 & 0 & 0\end{pmatrix}\times$$
$$\times\begin{pmatrix} l & l' & 1\\ -m & m' & 0\end{pmatrix}\Psi_{l'm'} \tag{5.24}$$

We will now illustrate this result with some examples from the first orders. Firstly, let us consider two monopoles translated along z. We can directly use equation 5.24 adapted to $l = 0$, $m = 0$.

$$\lim_{\epsilon\to 0}\frac{\Psi_{00}[\epsilon,\pi,0]-\Psi_{00}[\epsilon,0,0]}{k\epsilon} = -2\sum_{l'm'} i^{l'+1}\sqrt{(2l'+1)}\begin{pmatrix} 0 & l' & 1 \\ 0 & 0 & 0 \end{pmatrix}\begin{pmatrix} 0 & l' & 1 \\ 0 & m' & 0 \end{pmatrix}\Psi_{l'm'} \tag{5.25}$$

The $3j$ symbol is alway null except for $l' = 1$ and $m' = 0$. The $3j$ symbol can be obtained from any table : $\begin{pmatrix} 0 & 1 & 1 \\ 0 & 0 & 0 \end{pmatrix} = -\frac{1}{\sqrt{3}}$. The result of the infinitesimal translation is :

$$\lim_{\epsilon\to 0}\frac{\Psi_{00}[\epsilon,\pi,0]-\Psi_{00}[\epsilon,0,0]}{k\epsilon} = \frac{2}{\sqrt{3}}\Psi_{10} \tag{5.26}$$

The validity of this result is confirmed using the figure 5.3. Furthermore, the validity of the numerical coefficient in equation 5.26 is checked by comparing the values of the function.

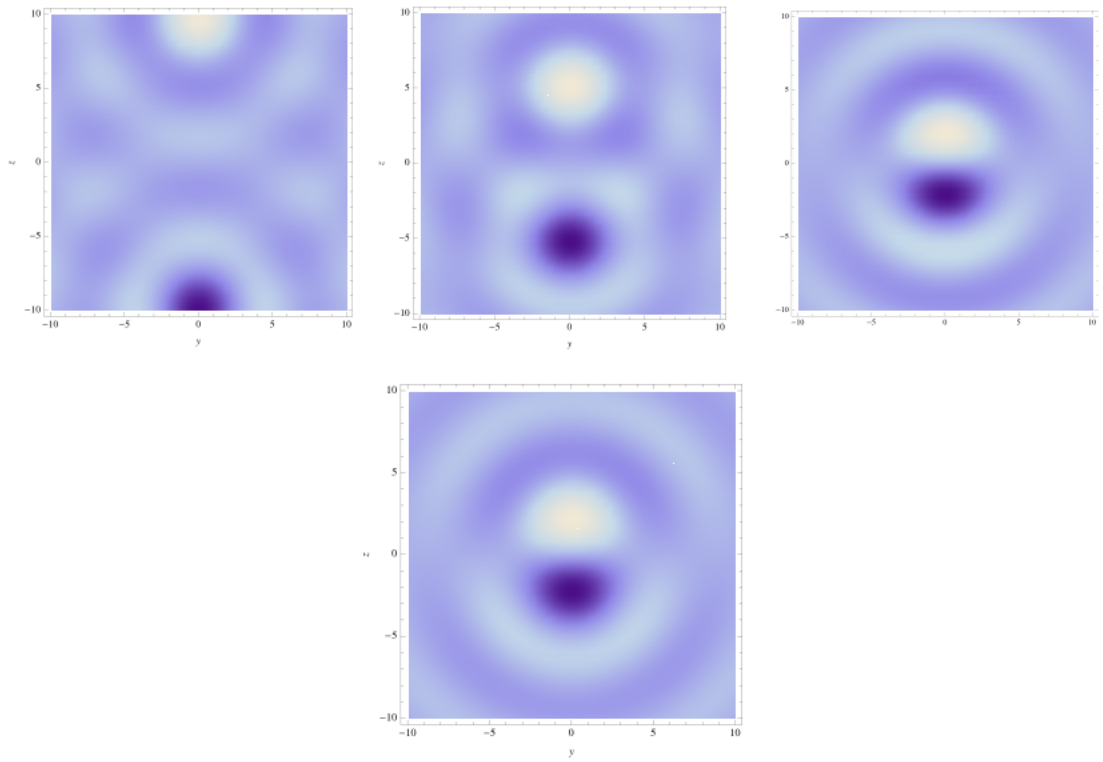

FIGURE 5.3: Upper side : we approach two monopoles Ψ_{00} as in equation 5.26. Lower side : dipole Ψ_{10}.

Let us now focus on the next term of the spherical expansion : the limit of two dipoles Ψ_{10} along z. In this case, the values $0 \leqslant l' \leqslant 2$ are authorized by the nullity condition of the $3j$ symbols. Again, we recall the explicit values of the corresponding symbols : $\begin{pmatrix} 1 & 1 & 1 \\ 0 & 0 & 0 \end{pmatrix} = 0$, $\begin{pmatrix} 1 & 2 & 1 \\ 0 & 0 & 0 \end{pmatrix} = \sqrt{\frac{2}{15}}$. The equation 5.24 gives the following result :

$$\lim_{\epsilon \to 0} \frac{\Psi_{10}[\epsilon, \pi, 0] - \Psi_{10}[\epsilon, 0, 0]}{k\epsilon} = \frac{4}{\sqrt{15}} \Psi_{20} - \frac{2}{\sqrt{3}} \Psi_{00} \tag{5.27}$$

Repeating the same steps than for the monopoles, we now display the comparison between the limit of two dipoles and a quadrupole in the figure 5.4 and check numerically the correctness of the coefficients with Mathematica. This time, we observe that the limit of two dipoles gives rise two a quadrupole but also to a monopolar term. This surprising thing is in fact the rule and the limit of two multipoles of order l will always lead to term of order $l-1$ and $l+1$.

From the multipolar expansion of radiation in electromagnetism, we know that the smallest radiating unit is the dipole and that no radiating monopole exists. However, when we will treat the vectorial case this problem will not appear since the monopolar term will cancel naturally.

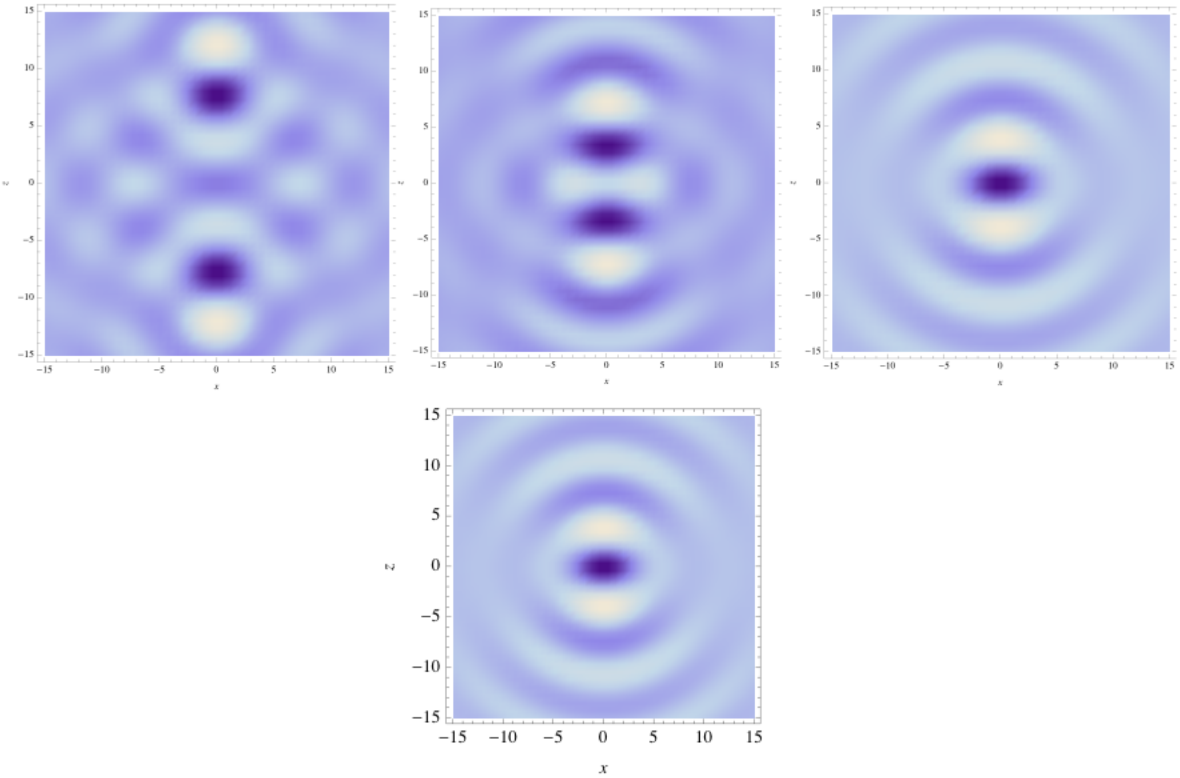

FIGURE 5.4: Upper side : we approach two monopoles Ψ_{10} as in equation 5.27. Lower side : displaying of $\frac{4}{\sqrt{15}}\Psi_{20} - \frac{2}{\sqrt{3}}\Psi_{00}$.

For reference, we give here results concerning infinitesimal translation along other directions. The calculation follows exactly the same steps and the derivation will be more succinctly presented. The y translation case results will be given at the end of the chapter.

For an x infinitesimal translation, we have to calculate the following limit :

$$\lim_{\epsilon\to 0}\frac{\Psi_{lm}[\epsilon,\frac{\pi}{2},\pi]-\Psi_{lm}[\epsilon,\frac{\pi}{2},0]}{k\epsilon} \tag{5.28}$$

The coefficients of this spherical expansion can be written as :

$$\lim_{\epsilon\to 0}\frac{T_{l'm',lm}[\epsilon,\frac{\pi}{2},\pi]-T_{l'm',lm}[\epsilon,\frac{\pi}{2},0]}{2k\epsilon} = \sum_{l''m''} i^{l'+l''-l}(-1)^m\sqrt{4\pi(2l+1)(2l'+1)(2l''+1)}\times$$
$$\times\begin{pmatrix} l & l' & l'' \\ 0 & 0 & 0 \end{pmatrix}\begin{pmatrix} l & l' & l'' \\ -m & m' & m'' \end{pmatrix}\frac{Y_{l''m''}(\frac{\pi}{2},\pi)-Y_{l''m''}(\frac{\pi}{2},0)}{2}\left(\lim_{\epsilon\to 0}\frac{j_{l''}(k\epsilon)}{k\epsilon}\right) \tag{5.29}$$

Exactly as in the previous section, derivatives over spherical Bessel functions will allow only the $l''=1$ to survive. The m'' sum is a little bit trickier to treat ; we have to use again the parity of spherical harmonics $Y_{lm}(\theta,\varphi+\pi)=(-1)^m Y_{lm}(\theta,\varphi)$ but the sum over m'' has now two non zero terms $m''=\pm 1$. We finally obtain the coefficients corresponding to the x infinitesimal translation.

$$\lim_{\epsilon\to 0}\frac{T_{l'm',lm}[\epsilon,\frac{\pi}{2},\pi]-T_{l'm',lm}[\epsilon,\frac{\pi}{2},0]}{2k\epsilon} = i^{l'+1-l}(-1)^m\sqrt{\frac{(2l+1)(2l'+1)}{2}}\begin{pmatrix} l & l' & 1 \\ 0 & 0 & 0 \end{pmatrix}\times$$
$$\times\left[\begin{pmatrix} l & l' & 1 \\ -m & m' & 1 \end{pmatrix}-\begin{pmatrix} l & l' & 1 \\ -m & m' & -1 \end{pmatrix}\right] \tag{5.30}$$

$$\lim_{\epsilon\to 0}\frac{\Psi_{lm}[\epsilon,\frac{\pi}{2},\pi]-\Psi_{lm}[\epsilon,\frac{\pi}{2},0]}{k\epsilon} = \sum_{l'm'}\left(i^{l'+1-l}(-1)^m\sqrt{2(2l+1)(2l'+1)}\begin{pmatrix} l & l' & 1 \\ 0 & 0 & 0 \end{pmatrix}\times\right.$$
$$\left.\times\left[\begin{pmatrix} l & l' & 1 \\ -m & m' & 1 \end{pmatrix}-\begin{pmatrix} l & l' & 1 \\ -m & m' & -1 \end{pmatrix}\right]\right)\Psi_{l'm'} \tag{5.31}$$

5.3.1.2 Infinitesimal translation in the vector case

The infinitesimal translations of two vector multipolar fields can be calculated in the same way than scalar multipole fields. In this case, only the results for the z direction is given without much demonstrations :

$$\begin{aligned}\lim_{\epsilon\to 0}\frac{T_{l'J'M',lJM}[\epsilon,\pi,0]-T_{l'J'M',lJM}[\epsilon,0,0]}{k\epsilon} &= \sum_{l''m''} i^{l'+l''-l}(-1)^{M+1}\sqrt{4\pi(2l+1)(2l'+1)(2l''+1)}\times \\ \sqrt{(2J+1)(2J'+1)}&\begin{pmatrix} l & l' & l'' \\ 0 & 0 & 0 \end{pmatrix}\begin{pmatrix} J & J' & l'' \\ -M & M' & m'' \end{pmatrix}\begin{Bmatrix} l'' & l' & l \\ S & J & J' \end{Bmatrix}\times \\ &\left(\lim_{\epsilon\to 0}\frac{j_{l''}(\epsilon)}{k\epsilon}\right)\frac{(-1)^{l''+m''}-1}{2}Y_{l''m''}(0,0)\end{aligned} \tag{5.32}$$

The derivative over spherical Bessel function still provides great simplification since it makes a $\delta_{l'',1}$ appearing and reduces the summation :

$$\begin{aligned}\lim_{\epsilon\to 0}\frac{\underline{\Psi}_l^{JM}[\epsilon,\pi,0]-\underline{\Psi}_l^{JM}[\epsilon,0,0]}{k\epsilon} &= 2\sum_{J'l'M'} i^{l'+1-l}(-1)^{M}\sqrt{(2l+1)(2l'+1)(2J+1)(2J'+1)}\times \\ &\times\begin{pmatrix} l & l' & 1 \\ 0 & 0 & 0 \end{pmatrix}\begin{pmatrix} J & J' & 1 \\ -M & M' & 0 \end{pmatrix}\begin{Bmatrix} 1 & l' & l \\ 1 & J & J' \end{Bmatrix}\underline{\Psi}_{l'}^{J'M'}\end{aligned} \tag{5.33}$$

5.3.2 Using translational addition to make simple models

In this section, we develop simple models that show how the multipolar sources of radiation can be engineered by playing with the position of different dipolar sources. A translated dipole will generate a sum of multipoles according to the translational addition theorem. Those multipoles are a result of the way to choose the origin and are not intrinsic to the system of sources. However, when the origin is carefully chosen, typically at the center of the nanoparticles, it is a great tool to compare different system of sources and their corresponding multipolar expansions.

To illustrate this point, the norms of different configurations of translated multipoles are given in figure 5.5 and 5.6. We recall that the norm of a multipolar order physically describe the energy of the field in this multipole. Figure 5.5 represents the norm of a simple dipole oriented and translated along the z axis. One can observe how the multipoles of higher appears one after another when the translation size increases. We also consider three configurations of sources having 2, 3 and 4 dipolar sources translated according to figure 5.6. Those three sets of dipolar sources corresponds to different symmetries and could model different kind of nanoparticles (nanorod, 3-branch nanostar, 4-branch nanostar). Using the translational addition theorem, we combine all the dipoles of a model as a sum of multipole at the origin for three different lengths of translation. For a nano-objects of typical size 100 nm and a wavelength in the visible, kR has a value roughly equal to one which is represented in the top row of the figure 5.6.

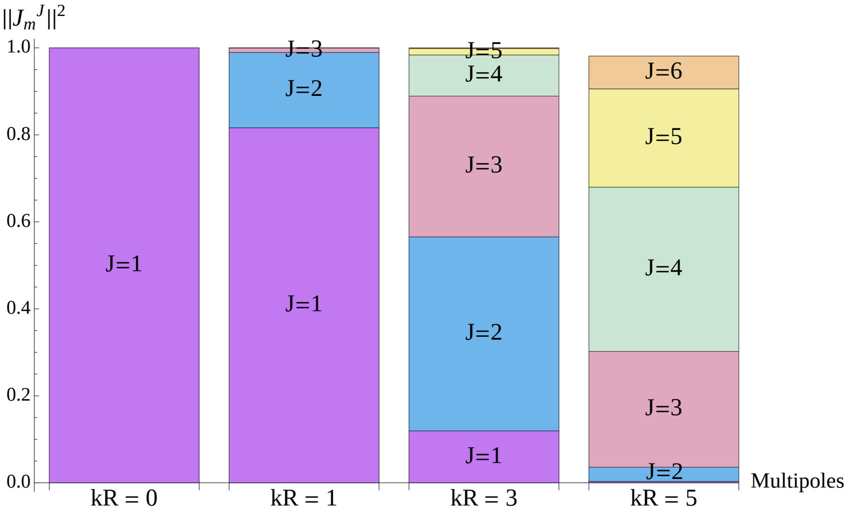

FIGURE 5.5: Histrograms representing the multipole norms of a translated dipole along z. When the dipole is not translated, only the dipolar component is present and equal to one. As the size of the translation increases, more multipoles are necessary to recover the equivalent radiation.

As can be seen from the histograms, almost only the first non-zero order is present at this value and smaller objects would then lead to a similar distribution of multipoles. Moreover, we also consider three different relative weights between the dipoles : same weight for all, weighted by a cosine function of their angular position and and weighted by a cosine squared function of their angular position. The second and third cases correspond to the projection of a linearly polarized incoming field on the dipole for linear and second order nonlinear optics.

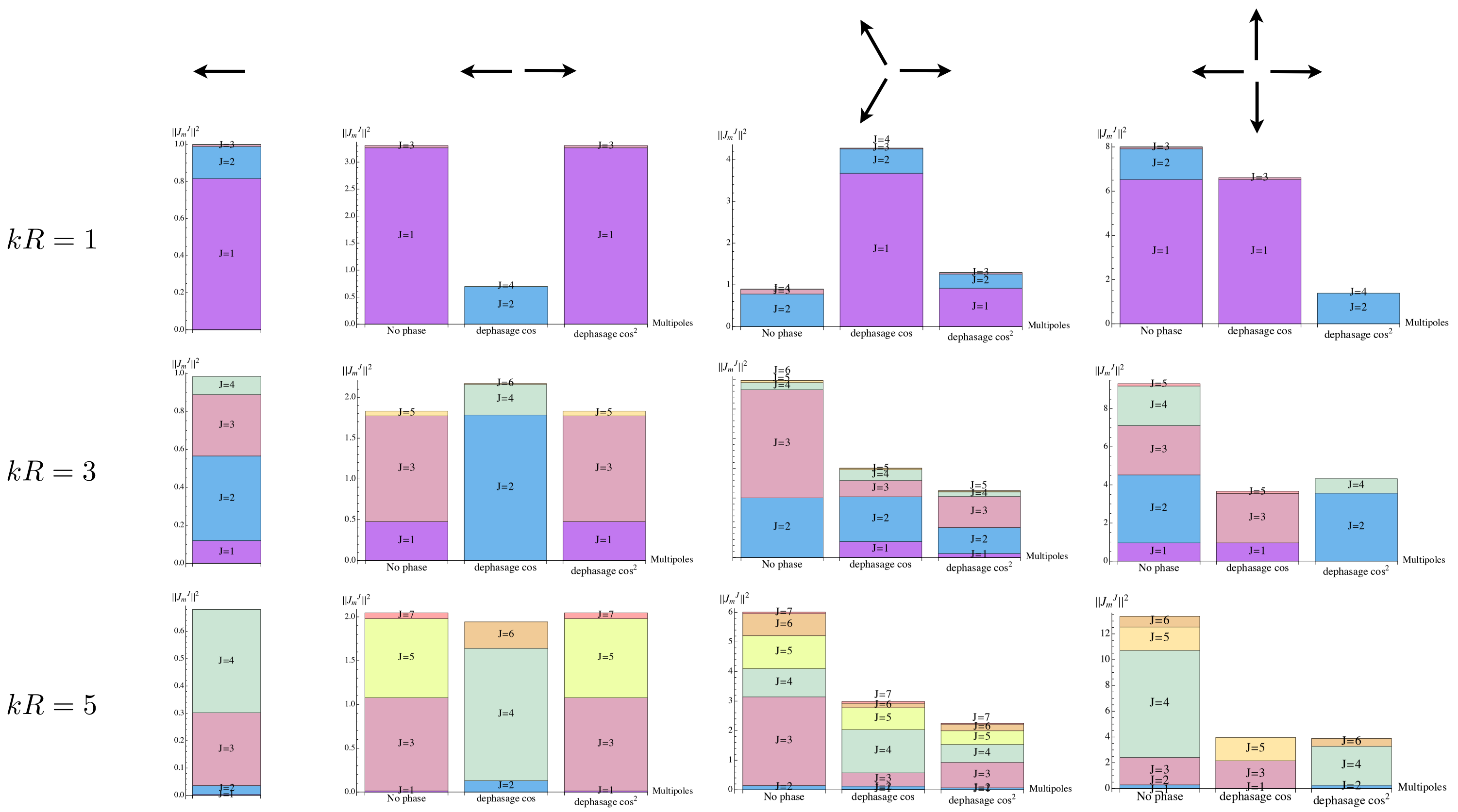

FIGURE 5.6: Histrograms representing the multipole norms for three (two, three and four dipoles) models and for different translations length ($kr = 1, kr = 3$ and $kr = 5$). For each histogram, the relative source dipoles are weighted with three different cases : no relative weight, cosine relative weight and cosine squared relative weight.

The three models exhibit very different multipolar distributions. It is interesting to look at the vanishing orders for the different models employed. The model with two dipoles keeps non-zero the odd multipole when the dipoles have the same weight and when a squared cosine is applied while only even order are kept when the projection is a cosine wave. A physical system that would be represented by such a distribution of dipoles, possibly a nanorod, would then radiate mainly like a dipole in second-order nonlinear optics and like a quadrupole in linear optics.

Interestingly, the model with 3 dipoles and the one with 4 keep all the multipolar weights nonzero except for two cases. The three dipoles model retains all orders except the dipolar one when the three dipoles are strictly equivalent. The four dipoles model keeps only even orders when a square cosine projection is applied.

If physical objects would be associated with such models, one could choose the most interesting one according to the multipolar distribution that is the most interesting for the problem considered. Choosing the shapes of the particle permits to select non vanishing orders while the size of the system control their relative weight. As expected, when the system gets bigger, higher orders in the multipolar expansion become predominant.

The model using three dipoles and a cosine squared projection will be studied with more depth in the next chapter and applied to the interpretation of the experiment presented in chapter 3.

Chapter 6

Illustration : application to threefold symmetry nanoparticles

6.1 Rigorous multipolar interpretation of the SHG experiment

6.1.1 Discretization of the current distribution

In this section, we will show how the translation of vector multipolar fields can be applied to describe the field radiated by a D_3 shaped nanoparticles. In this model, we represent a nanoparticle as three radiating dipoles located on each tip. Hence, an incoming light excites independently these dipoles which emit their own dipolar radiations. However, from a far field point of view, one can see only one object that radiates a multipolar expansion, combination of the three dipole radiations. A convenient way to tackle this problem is to express these three dipoles as a combination of multipoles located at the center of the nanoparticle. Let us start by expressing the radiated field $\underline{E}_{rad}$ in terms of an integral equation involving the Green function $G(r, r')$ and the current density $J(r', \omega)$.

$$\begin{aligned} \underline{E}_{rad} &= i\omega\mu_0 \int \underline{\underline{G}}(r, r')\ \underline{J}(r', \omega)\ d^3r' && (6.1) \\ &= \frac{\omega^2}{\epsilon_0\ c^2} \int \underline{\underline{G}}(r, r')\ \underline{P}(r', \omega)\ d^3r' && (6.2) \end{aligned}$$

This last equality is due to the relation between polarization and current density $J = i\omega P$. The polarization is calculated using the hyperpolarizabilities and the local field. At this stage, we do not pay attention to local field correction and assume that this field is equal to the incident field. For a non-localized response, the polarization can be expressed in frequency domain as :

$$
\begin{aligned}
&\underline{P}(r',\omega) = \frac{1}{2\pi}\int dr_1 d\omega_1\ \underline{\underline{\alpha}}(r';r_1,\omega)\cdot\underline{E}(r_1,\omega_1)\delta(\omega-\omega_1)\\
&+\frac{1}{(2\pi)^2}\int dr_1 dr_2 d\omega_1 d\omega_2\ \underline{\underline{\underline{\beta}}}(r';r_1,r_2,\omega_1+\omega_2,\omega_1) : \underline{E}(r_1,\omega_1)\otimes\underline{E}(r_2,\omega_2)\delta(\omega-\omega_1-\omega_2)+...
\end{aligned}
\tag{6.3}
$$

We now consider a monochromatic electric field and use the approximation that the field is constant over the object. Then, the electric field is $\underline{E}(r,\omega) = \underline{e}\ \delta(\omega-\omega_L)$ where $\underline{e}$ is a constant amplitude vector and ω_L is the frequency of the monochromatic light.

$$
\begin{aligned}
&\underline{P}(r',\omega) = \frac{\delta(\omega-)}{2\pi}\int dr_1 d\omega_1\ \underline{\underline{\alpha}}(r';r_1,\omega)\cdot\underline{E}(r_1,\omega_1)\delta(\omega-\omega_1)\\
&+\frac{1}{(2\pi)^2}\int dr_1 dr_2 d\omega_1 d\omega_2\ \underline{\underline{\underline{\beta}}}(r';r_1,r_2,\omega_1+\omega_2,\omega_1) : \underline{E}(r_1,\omega_1)\otimes\underline{E}(r_2,\omega_2)\delta(\omega-\omega_1-\omega_2)+...
\end{aligned}
\tag{6.4}
$$

At this stage, we have to choose some expression for the polarizabilities (that are phenomenological here) to model the nanoparticles. By choosing a local point response positioned at the end of each tip, the radiation corresponds to three dipoles located on each of these points. According to this approximation, the hyperpolarizabilities can be written as :

$$
\underline{\underline{\alpha}}(r';r_1,\omega_L) = \sum_i \underline{\underline{\alpha}}(r';r_1,\omega_L)\ \delta(r_1-r_i)\ \delta(r'-r_i) \tag{6.5}
$$

$$
\underline{\underline{\underline{\beta}}}(r';r_1,r_2,2\omega_L,\omega_L) = \sum_i \underline{\underline{\underline{\beta}}}(r';r_1,r_2,2\omega_L,\omega_L)\ \delta(r_1-r_i)\ \delta(r_2-r_i)\ \delta(r'-r_i) \tag{6.6}
$$

The sum over i runs over the different points where we have positioned dipoles. In this case, all the integrations disappear thanks to the Dirac δ and the polarization is simplified to :

$$
\begin{aligned}
\underline{P}(r',\omega) = &\frac{\delta(\omega-\omega_L)}{2\pi}\sum_i \underline{\underline{\alpha}}(r';r_i,\omega_L)\cdot\underline{e} + \frac{\delta(\omega-2\omega_L)}{(2\pi)^2}\sum_i \underline{\underline{\underline{\beta}}}(r';r_i,r_i,2\omega_L,\omega_L) : \underline{e}\otimes\underline{e}\\
&+...+\frac{\delta(\omega-n\omega_L)}{(2\pi)^n}\sum_i \alpha^{(n)}(r';r_i...r_i,n\omega_L...\omega_L)\odot\underline{e}\otimes....\otimes\underline{e}
\end{aligned}
\tag{6.7}
$$

We then use the integral equation 6.2 to obtain the radiated field in terms of the Green function.

$$\begin{aligned}\underline{E}_{rad}(r,\omega) = \frac{\omega^2}{\epsilon_0 c^2}\frac{\delta(\omega-\omega_L)}{2\pi}\sum_i \underline{\underline{G}}(r,r_i)\cdot(\underline{\underline{\alpha}}(r_i;r_i,\omega_L)\cdot\underline{e})+ \\ \frac{\omega^2}{\epsilon_0 c^2}\frac{\delta(\omega-2\omega_L)}{(2\pi)^2}\sum_i \underline{\underline{G}}(r,r_i)\cdot(\underline{\underline{\underline{\beta}}}(r_i;r_i,r_i,2\omega_L,\omega_L):\underline{e}\otimes\underline{e})+...\end{aligned} \tag{6.8}$$

We recall that, in free space, the field $\underline{\underline{G}}(r,r_i)\cdot\underline{p}$ corresponds to a dipole propagation. Then, by restricting the response to a local one, we are back a simple combination of dipole radiation located at the i points. The dipole moments are given by the contraction of the response tensor and the electric field amplitude. Since the non-linear terms are just different from the linear ones by the value of the dipole moment, we restrict ourselves to the linear polarizability from now without loss of generality. So far, the discussion has been quite general but we now explicitly position the dipole at the edge of the particle by giving the values of the r_i vectors.

$$r_1 = \begin{pmatrix} R \\ \frac{\pi}{2} \\ 0 \end{pmatrix} \qquad r_2 = \begin{pmatrix} R \\ \frac{\pi}{2} \\ \frac{4\pi}{3} \end{pmatrix} \qquad r_3 = \begin{pmatrix} R \\ \frac{\pi}{2} \\ \frac{2\pi}{3} \end{pmatrix} \tag{6.9}$$

Where R is the radius of the nanoparticle (distance between the center and the tip). The position of the dipoles in space is not enough to characterize them and we will need also their orientations which are expressed in terms of Euler angles :

$$r_1 : \begin{pmatrix} 0 \\ \frac{\pi}{2} \\ 0 \end{pmatrix} \qquad r_2 : \begin{pmatrix} \frac{2\pi}{3} \\ \frac{\pi}{2} \\ 0 \end{pmatrix} \qquad r_3 : \begin{pmatrix} \frac{4\pi}{3} \\ \frac{\pi}{2} \\ 0 \end{pmatrix} \tag{6.10}$$

The position and orientation of these dipole moments are given in the figure 6.1. The electric field can then be expressed in a simpler form :

$$\underline{E}_{rad}(r,\omega_L) = \frac{\omega_L^2}{2\pi\epsilon_0 c^2}\sum_i \underline{\underline{G}}(r,r_i)\cdot\underline{d}_i \tag{6.11}$$

The Green tensor can be expressed in terms of vector multipole field. The simple dipolar radiation created by the ith dipole and expressed in its local coordinate frame is :

$$\underline{E}_{rad,i}(r_i^{local}) = \frac{\omega_L^2}{\epsilon_0 c^2}\left(\underline{\Psi}_1^{11} d_1^{local,i} + \underline{\Psi}_1^{10} d_0^{local,i} + \underline{\Psi}_1^{1-1} d_{-1}^{local,i}\right) \tag{6.12}$$

Here, we have considered the multipolar expansion of the doublet over all frequencies. However, since we are only interested in the radiation associated with one specific frequency, one the projection of the doublet over the dipole having the appropriate wavenumber is taken into account in the previous equation. That is only the part of the current density associated with the wavelength 400 nm is kept for the expansion.

We choose the local coordinates with their z axis along the dipole moments. In this way, only the zero component of the local dipole moment is non-zero. The next step is to express these local radiation in the main frame of coordinates. This is made by first rotating the local frames to make the z axis parallel and then by translating the origin of the local frame to the origin of the main frame. The first step is accomplished by using Wigner $\mathcal{D}$ matrices and the second one by using finite translation operators that we described in this chapter. The dipolar fields are then :

$$\begin{aligned}
\underline{E}_{rad,1}(r) &= -\frac{\omega_L^2}{\epsilon_0 c^2}\, d_0^{local,1}\, T_{R,\frac{\pi}{2},\frac{\pi}{2}}\left[\mathcal{D}^{(1)}_{0,\frac{\pi}{2},0}\left[\underline{\Psi}_1^{10}\right]\right](r) &\quad (6.13)\\
\underline{E}_{rad,2}(r) &= -\frac{\omega_L^2}{\epsilon_0 c^2}\, d_0^{local,2}\, T_{R,\frac{\pi}{2},\frac{\pi}{2}-\frac{2\pi}{3}}\left[\mathcal{D}^{(1)}_{\frac{2\pi}{3},\frac{\pi}{2},0}\left[\underline{\Psi}_1^{10}\right]\right](r) &\quad (6.14)\\
\underline{E}_{rad,3}(r) &= -\frac{\omega_L^2}{\epsilon_0 c^2}\, d_0^{local,3}\, T_{R,\frac{\pi}{2},\frac{\pi}{2}+\frac{2\pi}{3}}\left[\mathcal{D}^{(1)}_{-\frac{2\pi}{3},\frac{\pi}{2},0}\left[\underline{\Psi}_1^{10}\right]\right](r) &\quad (6.15)
\end{aligned}$$

The minus sign appears because the Wigner $\mathcal{D}$ matrices are used in the active transformation picture. However, since we move the coordinate frames and not the values of the function itself, a minus sign as to be applied. We do not face such problems with the translation operator since the passive picture has been chosen for them.

Then, the total linear electric field radiated by this polarization is just the sum of those three electric fields.

6.1.2 Second harmonic generation by the tips

In the previous section, we have seen how we can use the multipolar expansion to get rid of the integral formulation of the electric field. Now, we will consider the second-harmonic emission from the tips of the threefold nanostar. The nanoparticle is illuminated by a plane wave with a definite polarization which will be denoted by Φ. Then, each of the non-linear dipoles is excited by the projection of the electric field on its axis. For second harmonic generation in which we are interested now, the excitation is dependent on the square of the electric field. Then, the respective weights of the three dipoles will be $\cos(\Phi)$, $\cos(\Phi - 2\pi/3)$ and $\cos(\Phi + 2\pi/3)$. The current distribution is depicted in the figure 6.1.

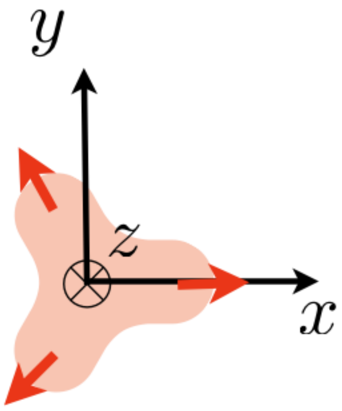

FIGURE 6.1: The red arrows represent the dipole current distribution that has been chosen to model the nanoparticle and mathematically expressed in the equation 6.16.

The calculation will be done in two steps. Firstly, we will project this non-linear current distribution on the multipolar basis keeping track carefully of the polarization dependance of each multipole. Then, we will use the multipolar PSFs of the previous chapter to obtain the electric field arriving on the photodetector. Finally, we plot the angular intensity that is the experimental response. For numerical applications, the excitation wavelength will be taken as 800 nm and then, the SHG current distribution will radiate an electric field at 400 nm.

As in the previous section, we start by the translation of the three dipoles independently but, instead of working in terms of their irreducible emitted electric fields, we use directly their current distributions which are simply related as we have shown in the chapter 1. Without polarization, the current distribution is here modeled as a sum of three radiated dipole oriented along the tips of the nanoparticle (figure 6.1).

$$\vec{J} = d\Big(T_{R,\frac{\pi}{2},0}\Big[\mathcal{D}^{(1)}_{0,\frac{\pi}{2},0}\Big[\underline{\Psi}^{10}_{m}\Big]\Big](r) + T_{R,\frac{\pi}{2},\frac{2\pi}{3}}\Big[\mathcal{D}^{(1)}_{0,\frac{\pi}{2},-\frac{2\pi}{3}}\Big[\underline{\Psi}^{10}_{m}\Big]\Big](r) + T_{R,\frac{\pi}{2},-\frac{2\pi}{3}}\Big[\mathcal{D}^{(1)}_{0,\frac{\pi}{2},\frac{2\pi}{3}}\Big[\underline{\Psi}^{10}_{m}\Big]\Big](r)\Big) \tag{6.16}$$

The coefficient d simply represent the strength of the excited dipole. Now, we explicit the form of the Wigner matrices. Then, the three dipoles can be expressed as :

$$\vec{J}_1 = -\frac{d}{\sqrt{2}}\Big(T_{R,\frac{\pi}{2},0}(\underline{\Psi}^{11}_{m} - \underline{\Psi}^{1-1}_{m})\Big) \tag{6.17}$$

$$\vec{J}_2 = -\frac{d}{\sqrt{2}}\Big(T_{R,\frac{\pi}{2},\frac{2\pi}{3}}(\underline{\Psi}^{11}_{m}e^{-\frac{2\pi}{3}} - \underline{\Psi}^{1-1}_{m}e^{\frac{2\pi}{3}})\Big) \tag{6.18}$$

$$\vec{J}_3 = -\frac{d}{\sqrt{2}}\Big(T_{R,\frac{\pi}{2},-\frac{2\pi}{3}}(\underline{\Psi}^{11}_{m}e^{\frac{2\pi}{3}} - \underline{\Psi}^{1-1}_{m}e^{-\frac{2\pi}{3}})\Big) \tag{6.19}$$

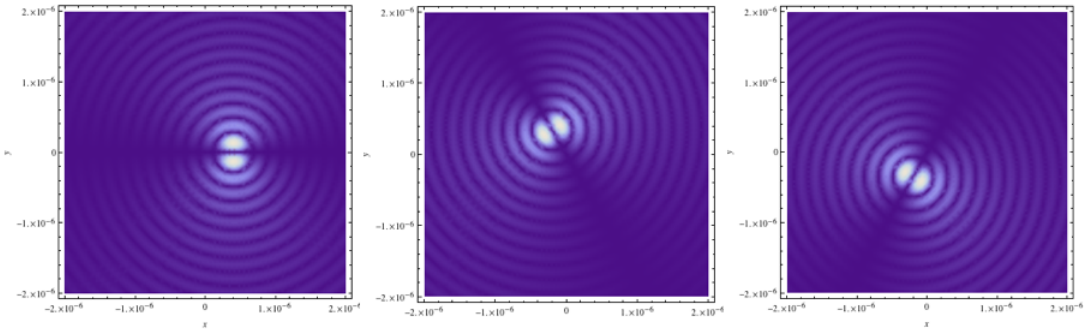

FIGURE 6.2: Those density maps represent the norm of the current density generated by the three radiating dipoles defined above. The calculation as be carried out exactly by a change of coordinates in the arguments of the dipolar EMFs.

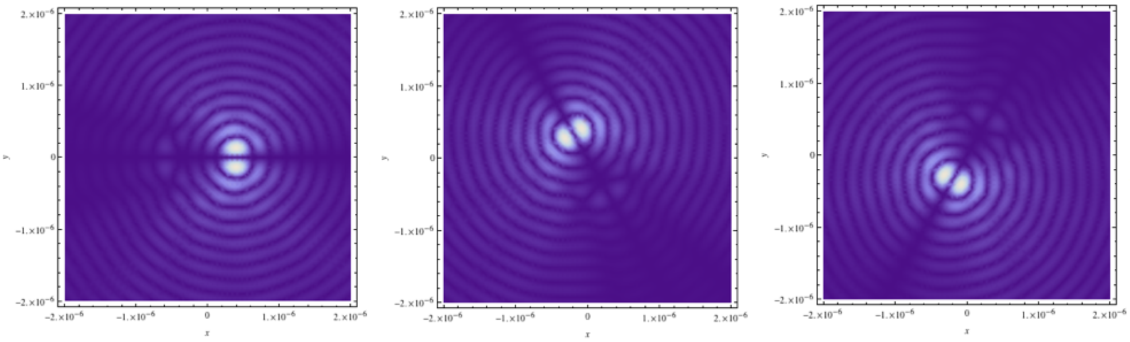

FIGURE 6.3: This density maps represent the norm of the current density generated by the three radiating dipoles defined above. This is a reconstruction of the current density of the figure 6.2 using a truncated sum of radiating multipole located of the origin.

The figure 6.2 and 6.3 represent the norm of those three current densities. One can see that the algebraic reconstruction of the current densities is faithful to the analytic one. The summation has been truncated at the seventh order to make those pictures This order is quite high but the translation length was 400 nm (R =400nm) which is a very big translation compared to the wavelength of radiation of those dipoles ($R = \lambda$!). This translation has been made that big in order to make apparent the translation to the eye on the picture. Of course, since the nanoparticle's diameter is about 100 to 200 nm the parameter R will be varying in the range 50 to 100 nm.

In the next figure (fig 6.4), we have shown the current density of the three radiating dipoles in two cases. When R = 200 nm, we see clearly the three tips corresponding to the orientation of each dipole. Again, in that case, the multipolar expansion has to be conducted to the seventh order in order to be faithful. At R = 90 nm, the three dipoles are almost on top of each other and one can not distinguish them anymore. It is interesting to point out that the multipolar has to be conducted only up to the third order now and that the two first orders almost vanish : this is almost a pure octupole ! Of course, when one takes into account the projection of the exciting electric field, the symmetry is broken and dipole and quadrupole appear. The polarization will be included only by weighting properly the three dipoles :

$$\vec{J} = \cos(\Phi)^2 \vec{J}_1 + \cos(\Phi + \frac{2\pi}{3})^2 \vec{J}_2 + \cos(\Phi - \frac{2\pi}{3})^2 \vec{J}_3 \tag{6.20}$$

So far, to show the figures, the translation operator has been used numerically but if we want to obtain analytical expressions of the weight of the different multipoles as a function of R and Φ, we need to use their expressions obtained in the previous chapter.

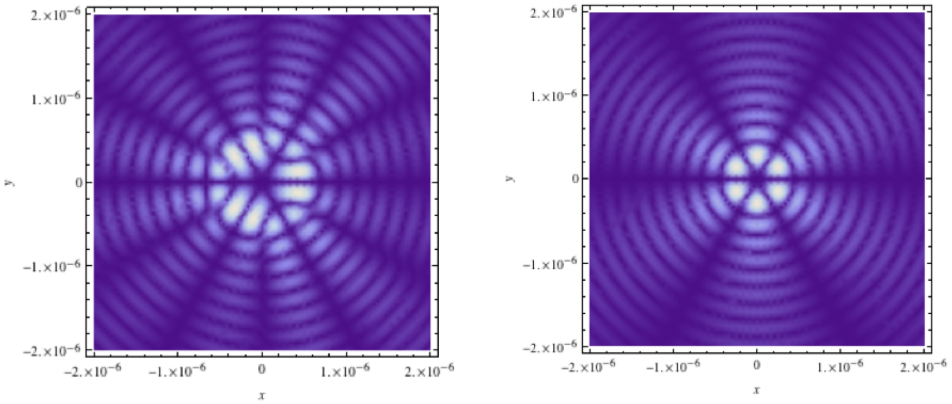

FIGURE 6.4: Those density maps represent the norm of the current density generated by the sum of the three radiating dipoles defined above. On the left, the translation R is 200 nm whereas on the right, the translation is 90 nm.

Explicitly, each dipole is now expressed as a sum of multipoles at the origin. Unfortunately, the addition-translation theorem was obtained only for the VMFs (Vector Multipole Fields) and not for the EMFs (Electric Multipole Fields). In order to translate the EMFs, we go back to the basis of VMFs, express their translations and do the reverse change of basis on the coefficients.

$$\begin{aligned}\vec{J}_1 = -\frac{d}{\sqrt{2}} \cos(\Phi)^2 \sum_{l'J'M'} \Bigg(\sum_{l"m"} i^{l'+l"} \sqrt{4\pi}\, \Pi_{l'l"J'1}\, j_{l"}(kR)\, Y_{l"m"}(\frac{\pi}{2}, 0) \\ \begin{pmatrix} 1 & l' & l" \\ 0 & 0 & 0 \end{pmatrix} \begin{Bmatrix} l" & l' & 0 \\ 1 & 1 & J' \end{Bmatrix} \Bigg[\begin{pmatrix} 1 & J' & l" \\ -1 & M' & m" \end{pmatrix} - \begin{pmatrix} 1 & J' & l" \\ 1 & M' & m" \end{pmatrix} \Bigg] \Bigg) \Psi_{l'}^{J'M'}\end{aligned} \tag{6.21}$$

$$\begin{gathered}\vec{J_2} = -\frac{d}{\sqrt{2}}\cos(\Phi+\frac{2\pi}{3})^2\sum_{l'J'M'}\left(\sum_{l"m"} i^{l'+l"}\sqrt{4\pi}\ \Pi_{l'l"J'1}\ j_{l"}(kR)\ Y_{l"m"}(\frac{\pi}{2},\frac{2\pi}{3})\right.\\ \left.\begin{pmatrix} 1 & l' & l" \\ 0 & 0 & 0 \end{pmatrix}\begin{Bmatrix} l" & l' & 0 \\ 1 & 1 & J' \end{Bmatrix}\Big[\begin{pmatrix} 1 & J' & l" \\ -1 & M' & m" \end{pmatrix} e^{-2i\frac{\pi}{3}} - \begin{pmatrix} 1 & J' & l" \\ 1 & M' & m" \end{pmatrix} e^{2i\frac{\pi}{3}}\Big]\right)\Psi_{l'}^{J'M'}\end{gathered} \tag{6.22}$$

$$\begin{gathered}\vec{J_3} = -\frac{d}{\sqrt{2}}\cos(\Phi-\frac{2\pi}{3})^2\sum_{l'J'M'}\left(\sum_{l"m"} i^{l'+l"}\sqrt{4\pi}\ \Pi_{l'l"J'1}\ j_{l"}(kR)\ Y_{l"m"}(\frac{\pi}{2},-\frac{2\pi}{3})\right.\\ \left.\begin{pmatrix} 1 & l' & l" \\ 0 & 0 & 0 \end{pmatrix}\begin{Bmatrix} l" & l' & 0 \\ 1 & 1 & J' \end{Bmatrix}\Big[\begin{pmatrix} 1 & J' & l" \\ -1 & M' & m" \end{pmatrix} e^{2i\frac{\pi}{3}} - \begin{pmatrix} 1 & J' & l" \\ 1 & M' & m" \end{pmatrix} e^{-2i\frac{\pi}{3}}\Big]\right)\Psi_{l'}^{J'M'}\end{gathered} \tag{6.23}$$

To make the expression less cumbersome, we take the sum of those three terms and make some factorizations.

$$\begin{gathered}\vec{J} = -\frac{d}{\sqrt{2}}\sum_{l'J'M'}\left(\sum_{l"m"} i^{l'+l"-1}3\sqrt{4\pi}\ \Pi_{l'l"J'}\ j_{l"}(kR)\ Y_{l"m"}(\frac{\pi}{2},0)\begin{pmatrix} 1 & l' & l" \\ 0 & 0 & 0 \end{pmatrix}\begin{Bmatrix} l" & l' & 0 \\ 1 & 1 & J' \end{Bmatrix}\right.\\ \Big[\begin{pmatrix} 1 & J' & l" \\ -1 & M' & m" \end{pmatrix}(\cos(\Phi)^2+\cos(\Phi+\frac{2\pi}{3})^2\ e^{i(m"-1)\frac{2\pi}{3}}+\cos(\Phi-\frac{2\pi}{3})^2\ e^{-i(m"-1)\frac{2\pi}{3}})\\ \left.-\begin{pmatrix} 1 & J' & l" \\ 1 & M' & m" \end{pmatrix}(\cos(\Phi)^2+\cos(\Phi+\frac{2\pi}{3})^2\ e^{i(m"+1)\frac{2\pi}{3}}+\cos(\Phi-\frac{2\pi}{3})^2\ e^{-i(m"+1)\frac{2\pi}{3}})\Big]\right)\Psi_{l'}^{J'M'}\end{gathered} \tag{6.24}$$

Finally, one can obtain the analytical expressions of the coefficient by a simple change of basis :

$$J_e^{J'M'}(R,\Phi) = \sqrt{\frac{J'+1}{2J'+1}}c_{J'-1}^{J'M'}(R,\Phi)-\sqrt{\frac{J'}{2J'+1}}c_{J'+1}^{J'M'}(R,\Phi) \tag{6.25}$$

$$J_m^{J'M'}(R,\Phi) = c_{J'}^{J'M'}(R,\Phi) \tag{6.26}$$

$$J_l^{J'M'}(R,\Phi) = \sqrt{\frac{J'}{2J'+1}}c_{J'-1}^{J'M'}(R,\Phi)+\sqrt{\frac{J'+1}{2J'+1}}c_{J'+1}^{J'M'}(R,\Phi) \tag{6.27}$$

$$J_{l'}^{J'M'}(R,\Phi) = \sum_{l"m"} i^{l'+l"-1} 3\sqrt{4\pi}\,\Pi_{l'l"J'}\, j_{l"}(kR)\, Y_{l"m"}(\frac{\pi}{2},0) \begin{pmatrix} 1 & l' & l" \\ 0 & 0 & 0 \end{pmatrix} \begin{Bmatrix} l" & l' & 0 \\ 1 & 1 & J' \end{Bmatrix}$$
$$\Big[\begin{pmatrix} 1 & J' & l" \\ -1 & M' & m" \end{pmatrix} (\cos(\Phi)^2 + \cos(\Phi+\frac{2\pi}{3})^2\ e^{i(m"-1)\frac{2\pi}{3}} + \cos(\Phi-\frac{2\pi}{3})^2\ e^{-i(m"-1)\frac{2\pi}{3}})$$
$$- \begin{pmatrix} 1 & J' & l" \\ 1 & M' & m" \end{pmatrix} (\cos(\Phi)^2 + \cos(\Phi+\frac{2\pi}{3})^2\ e^{i(m"+1)\frac{2\pi}{3}} + \cos(\Phi-\frac{2\pi}{3})^2\ e^{-i(m"+1)\frac{2\pi}{3}}) \Big] \tag{6.28}$$

We now express the multipolar coefficients up to the third order. Due to the selection rules of the $3j$ and $6j$ coefficients, only nine terms are non zero.

$$J_m^{1-1}(\Phi,R) = -\frac{3}{4}e^{2i\Phi}f_d(R) \quad c_m^{11}(\Phi,R) = \frac{3}{4}e^{-2i\Phi}f_d(R) \tag{6.29}$$

$$J_m^{2-2}(\Phi,R) = -\frac{9}{8}\sqrt{\frac{3}{5}}e^{-2i\Phi}f_q(R) \quad c_m^{20}(\Phi,R) = \frac{9}{2\sqrt{10}}f_q(R) \quad c_m^{22}(\Phi,R) = -\frac{9}{8}\sqrt{\frac{3}{5}}e^{2i\Phi}f_q(R) \tag{6.30}$$

$$J_m^{3-3}(\Phi,R) = -\frac{9}{4}\sqrt{\frac{5}{7}}f_o(R) \quad c_m^{3-1}(\Phi,R) = \frac{9}{8}\sqrt{\frac{3}{7}}e^{2i\Phi}f_o(R) \tag{6.31}$$

$$J_m^{31}(\Phi,R) = -\frac{9}{8}\sqrt{\frac{3}{7}}e^{-2i\Phi}f_o(R) \quad c_m^{33}(\Phi,R) = \frac{9}{4}\sqrt{\frac{5}{7}}f_o(R) \tag{6.32}$$

It is worth noting that the R dependance for multipoles of same J is exactly the same and that's why we have defined the functions f_d, f_q and f_o.

$$f_d(R) = j_0(kR) + j_2(kR) \tag{6.33}$$
$$f_q(R) = j_1(kR) + j_3(kR) \tag{6.34}$$
$$f_o(R) = j_2(kR) + j_4(kR) \tag{6.35}$$

We are now done with the determination of the multipolar coefficients of the current distribution we have chosen to model the threefold symmetry nanoparticle. Before moving to the second step in the next section, it is interesting to depict the evolution of those coefficients as a function of R. To do this, we take the sum of the modulus squared of the multipoles in each irreducible subspace. One can see right away that the result is independent of the polarization from the definition of the coefficients. This norm allows to see the relative contributions of each multipolar orders compared to each other as a function of the size of the nanoparticle. The result is given in figure 6.5.

On the figure 6.5, we see that for very small object (with a radius less than 20 nm), the current distribution is almost only dipolar. Then, as the size of the object increases,

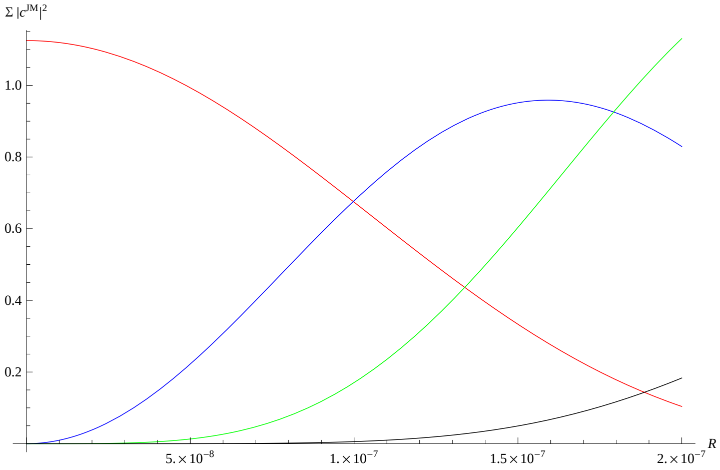

FIGURE 6.5: This curve represents the evolution of the norm of each multipolar order as a function of the translation length R. The red curve is the dipolar order, the blue one is the quadrupolar order, the green one the octupolar order and the black one is the $J = 4$ order.

the higher multipolar terms appear one after the other. The sizes we are interested in experimentally are for a radius between 50 nm and 100 nm. For those sizes, one can observe we are exactly at the scale where the dipolar order and the quadrupolar orders become comparable. The octupolar order also appears within this scale. We have plot in black the $J = 4$ order in order to show that, for a radius inferior to 100 nm, its contribution is negligible and we were safe by stopping our description at the $J = 3$ order.

6.1.3 Polar response

We now have all the elements to compute the polar responses which are measured in the experiment depicted in figure 3.2. In this experiment, the polarization of the incoming electric field ϕ is controlled by an half waveplate. Through an imaging system, the nanoparticle is excited and generates a current distribution. This current distribution is described according to the model of the previous section. This current distribution is described as a sum of a dipolar, a quadrupolar and a hexapolar multipoles. The radiation of each multipole is then propagated through the optical system thanks to the multipolar PSFs calculated in the previous chapter. The x and y components of the electric field are separated by a beam splitter and detected on the image plane with photodiodes. The experimental curves are then a polar plot of the intensity I_x and I_y as a function of the exciting field polarization ϕ.

The intensities can be written :

$$I_x(\phi, R) = \iint_{\text{image space}} \Big(\sum_{iJM} J_i^{JM}(\phi, R) G_x^{iJM} \Big) r dr d\varphi \tag{6.36}$$

$$I_y(\phi, R) = \iint_{\text{image space}} \Big(\sum_{iJM} J_i^{JM}(\phi, R) G_y^{iJM} \Big) r dr d\varphi \tag{6.37}$$

Here, we have included the elements of the mixed Green tensor. The integral is conducted numerically on the image space in cylindrical coordinates. Of course, the integration over r is truncated at a distance large enough to consider the integrand negligible. The sum over the multipolar terms is reduced to the nine terms calculated in the previous section.

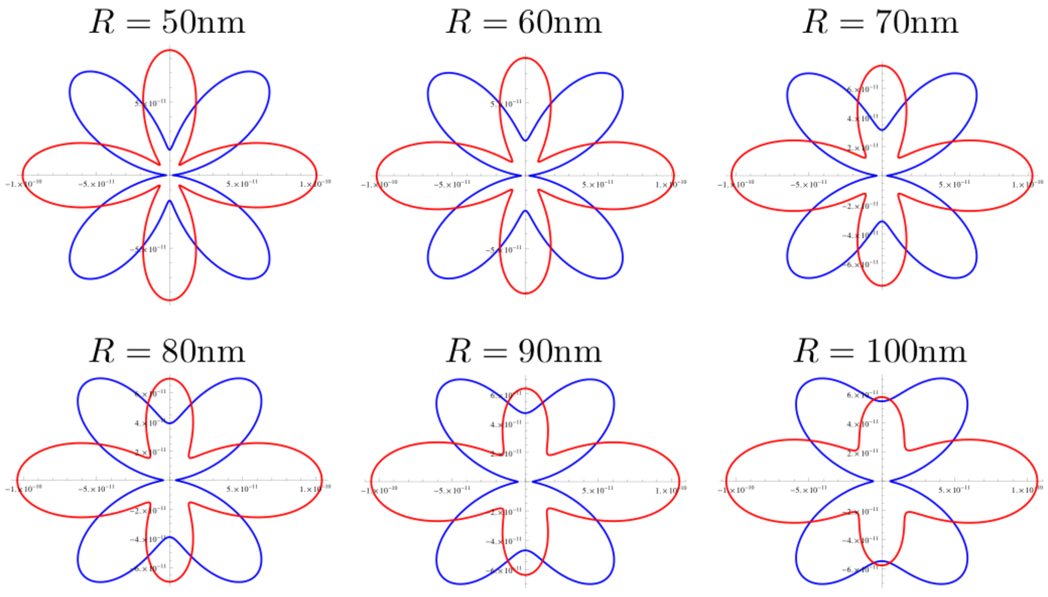

Figure 6.6: Polar response calculating according to the model described in this chapter. I_X is represented in red while I_Y is represented in blue.

6.2 Multipolar expansion of exciting fields

So far, we have been mostly concerned with the description of the response tensor itself and how it relates the coefficients of the multipolar expansion of the electric fields to those of the non-linear current densities. Now, we start to turn our attention to some real excitations cases where a nanoparticle is illuminated by a realistic electric field. The aim of this section is then to calculate the multipolar expansion of some very common electric fields like a plane wave or a gaussian beam. We will show that only a limited number of coefficients is needed to describe the field surrounding the nanoparticle accurately. We have already proven in the previous section that a punctual response will need only the first term of the electric field expansion that is the dipolar order. As the size of the object grows, more and more coefficients will be needed since the extension of the nanoparticle is bigger and it then experiences larger variations of the field. However, for sizes around 100 to 200 nm nanoparticles excited in the visible range, only a few coefficients will be necessary and that is one of the reason why a multipolar description is useful for such objects.

We start by expanding a vector plane wave in vector spherical harmonics. We use the expression of a linearly polarized plane wave but a circularly one could be treated in the same fashion. The x-polarized electric field we want to expand is then :

$$\underline{E}(r) = \underline{e}_x E_0 e^{ikz} \tag{6.38}$$

In order to express this vector field in term of vector multipole fields, one can use the well-known plane wave expansion :

$$e^{ikz} = 4\pi \sum_l i^l j_l(kr) \sum_m Y^*_{lm}(\theta,\varphi) Y_{lm}(0,0) \tag{6.39}$$

Using the expression for spherical harmonics at the origin, this equation can be reduced to :

$$e^{ikz} = \sqrt{4\pi} \sum_l \sqrt{2l+1}\; i^l \; j_l(kr) Y^*_{l0}(\theta,\varphi) \tag{6.40}$$

To express the expansion of the vector plane wave into vector spherical harmonics, one then has to use the equation we proved earlier and that we recall here for convenience :

$$Y_{l0}\; \underline{e}_\sigma = \sum_{JM} C^{JM}_{l01\sigma}\; \underline{Y}^{JM}_l \tag{6.41}$$

Then, if we plug this expression into the one of the vector plane wave linearly polarized along a spherical basis vector $\underline{e}_\sigma$, we obtain its vector spherical fields expansion :

$$e^{ikz}\; \underline{e}_\sigma = \sqrt{4\pi} \sum_{lJM} \sqrt{2l+1}\; i^l\; C^{JM}_{l01\sigma}\; j_l(kr)\; \underline{Y}^{JM}_l(\theta,\varphi) \tag{6.42}$$

For example, for an x polarized plane wave using the previous equation and the fact that $\underline{e}_x = -\frac{1}{\sqrt{2}}(\underline{e}_1 - \underline{e}_{-1})$, we get :

$$e^{ikz}\underline{e}_x = \sqrt{2\pi} \sum_{lJ} \sqrt{2l+1}\; i^l \left(C^{J1}_{l011} \underline{\Psi}^{J1}_l - C^{J-1}_{l01-1} \underline{\Psi}^{J-1}_l \right) \tag{6.43}$$

In this equation, one can see that a plane wave is the sum of vector spherical harmonics of momenta 1 and -1 which is equivalent to say that a linearly polarized plane wave is the sum of two circularly polarized ones. This simple result is quite similar to the one obtained by Jackson [21] who is using vector multipolar fields to expand a circularly polarized wave plane incident along the z axis instead :

$$\underline{E} = (\underline{e}_x \pm i\underline{e}_y)\, e^{ikz} = \sqrt{4\pi}\sum_J i^J \sqrt{2J+1}\left(\underline{\Psi}_m^{J,\pm1} \pm i\underline{\Psi}_e^{J\pm1}\right) \tag{6.44}$$

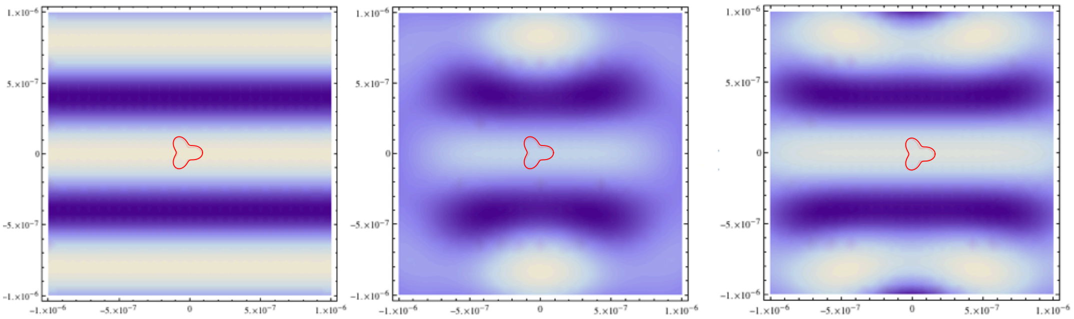

Exact **3 multipolar coefficients** **4 multipolar coefficients**

FIGURE 6.7: This figure displays the real part of the electric field of a waveplane. On the right, the exact x waveplane given by the equation 6.38 is represented with a wavelength of 800 nm. A fictitious 200 nm nanoparticle is drawn on top of the field density map to show which extension of the field it can experience. On the center and on the right, a reconstruction of that field using multipolar fields is done. Only a few coefficients are necessary to achieve a good reconstruction of the field at the vicinity of the nanoparticle.

One important thing is that we only need a few coefficients to describe the electric field at the vicinity of the nanoparticle. For example, for a nanoparticle which size is around 200 nm, only 3 coefficients are enough to achieve a realist electric field distribution and 4 of them lead to an accurate field behavior as one can see in the figure 6.7. Then, one has to use only a few coefficients to describe the electric field and the number of multipolar coefficients we need for the current density is also very limited. We have shown in the previous chapter that only 3 of them (dipolar, quadrupolar and octupolar) are needed to recover experimental response for the size of nanoparticles we have. According to those informations, only a few elements of the irreducible response are needed to describe the nanoparticle as it will be shown in the last section of this chapter.

6.3 Reconstruction of the fully irreducible response tensor

The objective of this section is to show that it is possible to access to the components of the irreducible response tensor introduced in chapter 4 using the model described in chapter 3. The methodology here is quite simple : knowing the multipolar expansion of the nonlinear current $J^{(2)}$ thanks to the analysis of experimental data along a model and the multipolar expansion of the incoming field, one can solve a set of algebraic equations to retrieve the irreducible response tensor $R^{(2)}$ defined in equation 4.29. For the sake of simplicity, we again focus on the model of a perfect star of the previous sections with which we deduced the components of the irreducible currents to be :

$$J^{(2)m1} = \begin{pmatrix} \frac{3}{4} f_d(R) e^{-2i\Phi} \\ 0 \\ -\frac{3}{4} f_d(R) e^{2i\Phi} \end{pmatrix} \qquad J^{(2)m2} = \begin{pmatrix} -\frac{9}{8}\sqrt{\frac{3}{5}} f_q(R) e^{2i\Phi} \\ 0 \\ \frac{9}{2\sqrt{10}} f_q(R) \\ 0 \\ -\frac{9}{8}\sqrt{\frac{3}{5}} f_q(R) e^{-2i\Phi} \end{pmatrix}$$

$$J^{(2)m3\ \ T} = \Big(\frac{9}{4}\sqrt{\frac{5}{7}} f_o(R)\ ,\ 0\ ,\ -\frac{9}{8}\sqrt{\frac{3}{7}} f_o(R) e^{-2i\Phi}\ ,\ 0\ ,\ \frac{9}{8}\sqrt{\frac{3}{7}} f_o(R) e^{2i\Phi}\ ,\ 0\ ,\ -\frac{9}{4}\sqrt{\frac{5}{7}} f_o(R)\Big) \tag{6.45}$$

The plane wave expansion of the previous section allows us to expand a linearly polarized waveplane as :

$$e^{ikz} \begin{pmatrix} \cos\alpha \\ \sin\alpha \\ 0 \end{pmatrix} = \sqrt{2\pi} \sum_{lJ} \sqrt{2l+1} i^l j_l(kr) \big(e^{-i\alpha} C^{J-1}_{l01-1} \underline{Y}_l^{J-1} - e^{i\alpha} C^{J1}_{l011} \underline{Y}_l^{J1}\big) \tag{6.46}$$

$$= \sum_J \sqrt{\pi(2J+1)} i^J \Big(e^{-i\alpha}(\underline{\Psi}_m^{J-1} - i\underline{\Psi}_e^{J-1}) + e^{i\alpha}(\underline{\Psi}_m^{J1} + i\underline{\Psi}_e^{J1})\Big) \tag{6.47}$$

Following again the previous section, we truncate this multipolar expansion at $J = 3$ since the field is already well reconstructed near the nanoparticle at this order. Thus, the incoming electric field is properly described by 12 terms. Fortunately, from equation 6.47, the four coefficients of each order are not independent and then the number of independent coefficients reduces to 3. The second-order nonlinear response tensor was expanded over the basis of electromagnetic multipole fields as :

$$\underline{\underline{\underline{R}}}^{(2)}(2k;k,k) = \sum_{i_1 J_1 i_2 J_2 i J} R^{(2)\ J'M'}_{i_1 J_1 i_2 J_2 (J_{12}) i J M}(2k;k,k) \Big\{ \big\{ \underline{\Psi}_{i_1}^{J_1}(k) \otimes \underline{\Psi}_{i_2}^{J_2}(k) \big\}^{J_{12}} \otimes \underline{\Psi}_i^{JM}(2k) \Big\}^{J'M'} \tag{6.48}$$

We will omit the index (2) in order to simplify the lecture. The wavenumber dependence of the response tensor will also be omitted from here. The basis of the electric fields expansions has a wavenumber k while the second-harmonic current density has a wavenumber $2k$ in the following.

This tensor links the irreducible components of the current density to the one of the exciting electric fields in the following way :

$$J_i^{JM} = R^{J'}_{i_1 J_1 i_2 J_2 (J_{12}) iJM} \bullet \left\{ \left\{ \underline{E}_{i_1}^{J_1} \otimes \underline{E}_{i_2}^{J_2} \right\}^{J_{12}} \otimes \underline{\Psi}_i^{JM} \right\}^{J'} \tag{6.49}$$

From here, a brute force calculation can be accomplished by expanding the tripolar vector spherical harmonics and solving the resulting system of linear equations. However, a great deal of simplification can be accomplished by using the knowledge about the symmetries of the response tensor :

- Using the same reasoning as in section 1.4.2, the invariance by rotation of $2\pi/3$ keeps only the components for which M' is a multiple of 3.
- The invariance by rotation of π by an axis along the tip causes $R^{J'M'}_{i_1 J_1 i_2 J_2 (J_{12}) iJM} = (-1)^{J'-M'} R^{J'-M'}_{i_1 J_1 i_2 J_2 (J_{12}) iJM}$.
- From the symmetry of the coefficients of $\underline{J}$ and $\underline{E}$, components of the irreducible response tensor obey the following constraint :

  $$R^{J'M'}_{i_1 J_1 i_2 J_2 (J_{12}) iJM} = (-1)^M \left(R^{J'M'}_{i_1 J_1 i_2 J_2 (J_{12}) iJ-M} \right)^* \tag{6.50}$$

  This relationship allows us to treat only half on the components of the irreducible current since the other can be obtained straightforwardly.
- The phase of the irreducible currents can be obtained only by a specific combination of the irreducible components of the electric fields :
  - Case $e^{-2i\phi}$ for J_m^{11} and J_m^{31} : only the product of components $E_m^{J_1 -1} E_m^{J_2 -1}$ leads to such a phase. Inserting this in the developed form of equation 6.48 leads to $M' = 3$ and thus to $J' \geqslant 3$.
  - Case $e^{2i\phi}$ for J_m^{22} : the product of components $E_m^{J_1 1} E_m^{J_2 1}$ has to be used.
  - Case 1 for J_m^{20} and $J_m 33$: the product of components $E_m^{J_1 1} E_m^{J_2 -1}$ has to be used.

The calculation can be carried in a relative simple manner by applying those informations. Great care needs to be taken when writing explicitly the components of the tripolar vector spherical harmonics. Especially, the component $\underline{\Psi}_i^{JM}$ is written here as a shortcut since the irreducible tensor product is supposed to sum over all M values.

However, since $\underline{\Psi}_i^{JM}$ is used to fully contract the tensor and get the component in this direction, it is in fact a tensor who has a zero value for all M except in the reading direction in which the component is one. Thus, we have written directly $\underline{\Psi}_i^{JM}$ as a shortcut to signify that the sum of the second irreducible product is dealt by the nature of the last tensor. Moreover, we have not emphasized so far the covariant/contravariant feature of this formalism but it is necessary to take it in account here. Since $\underline{\Psi}_i^{JM}$ has the nature of a contravariant vector in the basis of vector spherical harmonics, its components need to be inserted with the metric tensor defined in equation 1.34.

Once the calculation is fully carried out, one obtains the following non-zero components of the fully irreducible response tensor :

$$R^{33}_{m1m1(2)m11} = -\frac{j_0}{4\pi} \qquad R^{33}_{e1e1(2)m11} = \frac{j_2}{4\pi} \tag{6.51}$$

$$R^{60}_{m2m2(4)m22} = -\frac{27}{80\pi}\sqrt{\frac{77}{5}}j_1 \qquad R^{60}_{e2e2(4)m22} = \frac{27}{80\pi}\sqrt{\frac{77}{5}}j_3 \tag{6.52}$$

$$R^{60}_{m2m2(4)m20} = \frac{9}{80\pi}\sqrt{\frac{77}{5}}j_1 \qquad R^{60}_{e2e2(4)m20} = \frac{9}{80\pi}\sqrt{\frac{77}{5}}j_3 \tag{6.53}$$

$$R^{93}_{m3m3(6)m33} = -\frac{3}{28\pi}\sqrt{\frac{663}{5}}j_2 \qquad R^{93}_{e3e3(6)m33} = \frac{3}{28\pi}\sqrt{\frac{663}{5}}j_4 \tag{6.54}$$

$$R^{93}_{m3m3(6)m31} = \frac{3}{140\pi}\sqrt{\frac{663}{5}}j_2 \qquad R^{93}_{e3e3(6)m31} = -\frac{3}{140\pi}\sqrt{\frac{663}{5}}j_4 \tag{6.55}$$

Where all the spherical Bessel functions have kR as an argument, k being the wavenumber and R the size of translation of the dipoles (i. e. the nanoparticle size). It is interesting to observe that considering the limit of kR tending to zero makes all the coefficients vanishing except the one created by the component $\underline{\Psi}_m^{1\pm1}$ of the incoming electric fields. For point objects, the irreducible response tensor reduces to this components and can be straightforwardly calculated. On the other side, for extended objects, the components of the irreducible tensor linking dipolar current and electric field can be calculated easily using the limit case.

The numerical values of the components of the irreducible tensor for a nanoparticle corresponding to $R = 60$nm are given in table 6.1. This table shows that the response tensor is mainly dominated by a few components, especially $R^{60}_{m2m2(4)m22}$. Intuitively, the nature of the response has a simple shape and one thus could expect that such a response takes its origin from a limited amount of components.

Those components are calculated along the model of the previous section and are a result of this model rather than a fundamental result of the formalism. However, it shows that the formalism is complete in the sense that the fully response tensor defined for its interesting geometric properties can be calculated for specific cases allowing comparisons between different nanoparticles in terms of a limited amount of coefficients. Moreover,

$kR = 1$	$R^{33}_{i1i1(2)m11}$	$R^{60}_{i2i2(4)m22}$	$R^{60}_{i2i2(4)m20}$	$R^{93}_{i3i3(6)m33}$	$R^{93}_{i3i3(6)m31}$
$i = m$	0.067	0.13	0.042	0.024	0.0049
$i = e$	0.0049	0.0038	0.0013	4×10^{-4}	7.9×10^{-5}

Table 6.1: Value of the components of the fully irreducible tensor for $kR = 1$ ($R =$ 60nm).

this model corresponds properly to the optical response of a nanostar with a good shape. Thus, experiments can be achieved to obtain the value of R for a specific nanoparticle and the numeric value of the components are obtained accordingly.

Part III

Time-domain properties

Chapter 7

Time-domain experiments

While the purpose of this work, so far, has been to link the spatial properties of nanoparticles to the multipolar nature of their responses, this part will introduce ultrafast nonlinear spectroscopic techniques that allow to study the dynamics of the excited nanoparticles. In this first chapter, we are going to review the basics of ultrafast spectroscopy and give some of its results applied to the study of Chlorophyll *a* and LHCII. The next chapter will provide informations on how nonlinear spectroscopy can be applied to study the dynamics of nanoparticles.

7.1 General framework of ultrafast optical experiments

7.1.1 Measuring response function using ultrafast nonlinear spectroscopy

In the first chapter, nonlinear response functions have been introduced in the frequency and in the time domains. In order to remain focused on the spatial properties, the fields were considered to have an harmonic time dependence and then response functions were expressed in the frequency domain. However, when one excites a system with a time-limited pulse, it is possible to gain information about the dynamic the spectral components as well as their couplings. In this chapter, we will focus mainly on the third-order nonlinear polarization $\underline{P}^{(3)}(t)$ and will assume that the pulses are time-ordered. Then, they can be labelled as $\underline{E}_1$, $\underline{E}_2$ and $\underline{E}_3$. According to those conditions, the nonlinear polarization can be expressed as follow :

$$\underline{P}^{(3)}(t) = \int_0^{+\infty} \underline{\underline{\underline{R}}}^{(3)}(t_3, t_2, t_1) \cdot \underline{E}_3(t-t_3) \otimes \underline{E}_2(t-t_3-t_2) \otimes \underline{E}_1(t-t_3-t_2-t_1) dt_1 dt_2 dt_3 \quad (7.1)$$

In the impulsive limit, the pulses are considered short enough compared to the dynamic of the system and the time-dependence can be approximated as a Dirac function.

$$\begin{aligned} \underline{E}_3(t) &= \underline{E}_3\delta(t)e^{\pm ik_3 r} \quad (7.2)\\ \underline{E}_2(t) &= \underline{E}_2\delta(t+T_w)e^{\pm ik_2 r} \quad (7.3)\\ \underline{E}_1(t) &= \underline{E}_1\delta(t+T_w+\tau)e^{\pm ik_1 r} \quad (7.4) \end{aligned}$$

In this case, the integrals in equation 7.1 are easily calculated with the Dirac functions and a measurement of the polarization is directly a measurement of the response function $\underline{\underline{\underline{R}}}^{(3)}(t, T_w, \tau)$. While we have only been concerned so far with classical considerations, the physical processes involving photosynthetic molecules are well described in terms of a time-dependent perturbation on the density matrix. Since photosynthetic complexes are a side topic in this manuscript, the quantum theory behind nonlinear optical experiments will be described quickly and the lector is redirected to the literature for more information[86]. Quantum theory of nonlinear optics has not been used so far for nanoparticles since it is not expected to bring important corrections. However, this theory could still be applied for such systems to interpret their nonlinear responses in terms of eigenmodes. The density matrix is a powerfull tool to interpret microscopically the informations contained in the response signal and is defined by :

$$\rho(t) = |\psi(t)\rangle\langle\psi(t)| \tag{7.5}$$

Using a density matrix formalism, the expectation value of an operator is obtained by taking the trace with the density matrix. In nonlinear optics, the polarization is then calculated in the following way :

$$P(r,t) = \mathrm{Tr}(P(r)\rho(t)) \tag{7.6}$$

In order to compute the time-dependent expectation value of the polarization, it is necessary to know the time-evolution of the density matrix which is given by the Liouville-von Neumann equation :

$$\frac{\partial\rho}{\partial t} = -\frac{i}{\hbar}[H,\rho] \tag{7.7}$$

Where H is the Hamiltonian of the system. It is not possible to solve this equation in general and one has to rely on Dyson series to find the formal solution of the Liouville-von

Neumann equation using the interaction picture :

$$\rho(t) = \rho(0)\sum_{n=1}^{+\infty}\Big(-\frac{i}{\hbar}\Big)^n \int_0^t d\tau_n \int_0^{\tau_n} d\tau_{n-1}... \int_0^{\tau_2} d\tau_1$$
$$U_0(t)\big[H'(\tau_n),\big[H'(\tau_{n-1}),...\big[H'(\tau_1),\rho(0)\big]...\big]\big]U_0^\dagger(t) \quad (7.8)$$

In nonlinear optics, the interaction Hamiltonian is $-\mu E$ in the scalar approximation where μ is the dipole transition vector and E the incident electric field. The nonlinear polarization is obtained by taking the trace according to equation 7.6 :

$$P^{(n)}(t) = \Big(-\frac{i}{\hbar}\Big)^n \int_0^{+\infty} dt_n \int_0^{+\infty} dt_{n-1}... \int_0^{+\infty} dt_1 \langle\mu(t_n+...+t_1)[\mu(t_{n-1})+...t_1),...[\mu(0),\rho(0)]...]\rangle\times$$
$$\times E(t-t_n)E(t-t_n-t_{n-1})...E(t-t_n-...-t_1) \quad (7.9)$$

By identification with equation 7.1, the response function $\underline{\underline{\underline{R}}}^{(3)}(t_3,t_2,t_1)$ is :

$$\underline{\underline{\underline{R}}}^{(3)}(t_3,t_2,t_1) = \langle\mu(t_3+t_2+t_1)[\mu(t_2+t_1),[\mu(t_1),[\mu(0),\rho(0)]]]\rangle \quad (7.10)$$

Since the third-order response function is constituted of three commutators, it is composed of a sum of 8 signals, each corresponding to a different pathway of excitation. Moreover, each electric field interaction comes with a positive or a negative phase contribution and thus increases dramatically the number of possible combinations. Fortunately, multiple tricks exist to recover each part of the signal separately[86]. The first of them is time ordering that constrains the pulses to interact in a definite order. Secondly, one can use the rotating-wave approximation, which consists of eliminating the elements that have a rapid oscillatory phase term, to reduce drastically the number of relevant contributions. Finally, since each electric field carries a wavevector that will contribute positively and negatively, the signals will be emitted in all possible direction $\pm\vec{k}_1 \pm \vec{k}_2 \pm \vec{k}_3$. However, when one does not want to use a box-car geometry in order to keep an experiment close to a pump-probe geometry, it is still possible to disentangle the different contributions to the response function using phase cycling. This technique consists of sending the two first pulses collinearly through the sample with a controlled relative phase. By cycling the experiment over different phase delays, one can recover the different components of the signal by doing appropriate linear combinations of the experimental datas.

According to the previous paragraph, each element of the signal can be detected separately and thus, one can gain a lot of information about the system being probed. As an example, an element of the sum can be expressed as $\langle \mu(t_3 + t_2 + t_1)\mu(0)\rho(0)\mu(t_1)\mu(t_2 + t_1)\rangle$ and is depicted on the adjacent double-sided Feynman diagram that allows to keep track of the different patterns of interaction and to calculate easily the components of the response function. We give now a typical example of such calculation in the simple case of a two level system in the scalar approximation. The first interaction brings the system in a coherence state with a transition proportional to μ_{ab}. The system then evolves freely for a time t_1 with a factor $e^{-i\omega_{ab}t_1 - \Gamma_{ab}t_1}$ where Γ_{ab} is a phenomenological decay of the coherence. The second pulse brings the system in a population state proportionally to μ_{ab} for a time t_2 and the last pulse puts it back in a coherence state again evolving in the same way than the previous one for time t_3. Finally, the trace of the density matrix is taken in order to make the measurement and the response function is :

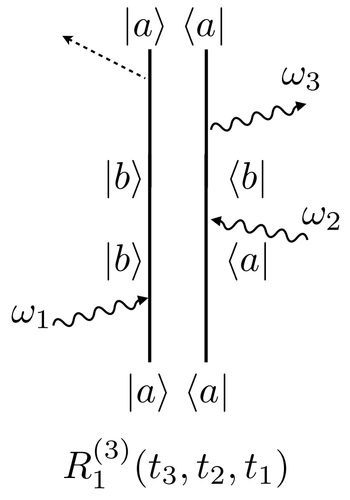

FIGURE 7.1: Non-rephasing interaction pathway.

$$\langle \mu(t_3 + t_2 + t_1)\mu(0)\rho(0)\mu(t_1)\mu(t_2 + t_1)\rangle = \mu_{ab}^4 e^{-i\omega_{ab}t_1 - \Gamma_{ab}t_1} e^{-i\omega_{ab}t_3 - \Gamma_{ab}t_3} \tag{7.11}$$

Where no population relaxation has been included during time t_2. This contribution to the signal is called non-rephasing because the first and third pulses add a phase $e^{-i\omega_{ab}t}$ in both case. This way of modeling third-order response function is the simplest possible and is in fact too simple. For example, the decoherence taken as an exponential decay corresponds to a limiting case. A more refined description can be achieved and measured using 2D electronic spectroscopy (2DES). Moreover, more complex systems like light harvesting complexes are usually multilevel systems with a complex manifold of coupled states that need more involved investigations. In the next section, measurements of the decoherence function, the lineshape function, on chlorophyll *a* is provided and is followed by measurements of 2D spectra in LHCII which contains multiple molecular excited states.

7.1.2 2D electronic spectroscopy

Two-dimensional electronic spectroscopy is the most complete technique to access to the full third-order nonlinear optical response $\underline{\underline{\underline{R}}}^{(3)}(t, T_w, \tau)$. Schematically, the experiment is represented in figure 7.2

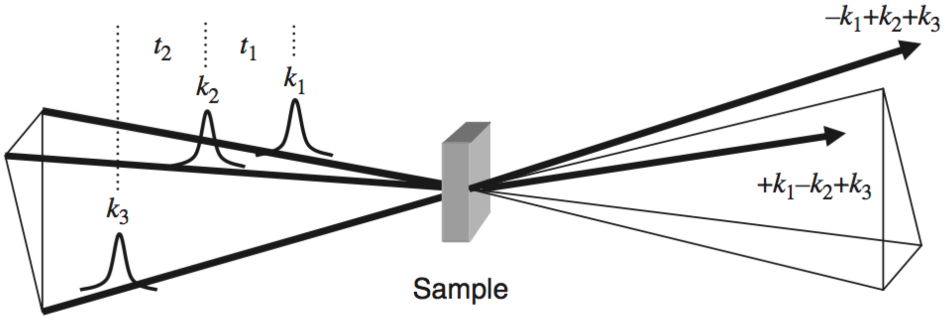

FIGURE 7.2: Figure from [86]. Three pulses hit the sample with wave vector $\vec{k}_1, \vec{k}_2$ and $\vec{k}_3$ pass through the sample and generate signals in the directions $\pm\vec{k}_1 + \pm\vec{k}_2 \pm \vec{k}_3$ which correspond to different interaction pathways (different Feynman diagrams). Those components of the full response are acquired by placing the detector in the proper direction.

The experiment in the lab uses a regenerative amplifier laser system (Legend Elite, Coherent) that provides pulses centered at 800 nm (0.8 W, 1 kHz, 40 fs). The beam is then split in two as one can see in figure 7.3, one for the pump path and one for the probe path.

On the pump-path, the pulses are used to pump a home-built, two-stage optical parametric amplifier (OPA) to generate near-infrared wavelengths that are doubled to fall in the visible. The obtained pulses are centered around 665 nm to be resonant with the Q_y band of chlorophyll *a* or 650 to excite LHCII. This beam is then passed through a commercially available acousto-optic programmable dispersive filter (Dazzler, Fastlite) to shape the pulses. The shaping permits to create two pulses from an incoming one with a controlled delay and relative phase between them in order to achieve a 1×2 phase cycling scheme[87, 88]. The Dazzler is also used to reference the shaped pulses to a carrier frequency of 419 THz to use a partial rotating frame and to attenuate the energy of the two pulses down to 300 nJ per two pulses. Finally, the pulse shaper is also used to compress the pulses to 45 fs FWHM (<1.3 times transform limited) using the feedback from an intensity autocorrelator.

The pulse in the probe path is used to generate a white light continuum by focusing the 800 nm light in a 2 mm sapphire window. The arrival time of the white light on the sample is controlled by a corner cube on a motorized delay stage. The white light is delayed in order to be the last interaction with a controlled waiting time T_w with the first two pulses. It also acts as the local oscillator to heterodyne detect the signal. The shaped pump pulse and the white light continuum are overlapped in the sample sample cell and the white light is then sent to a spectrometer (Acton SP2300, Princeton Instruments) equipped with a CCD detector (PIXIS 100B, Princeton Instruments)

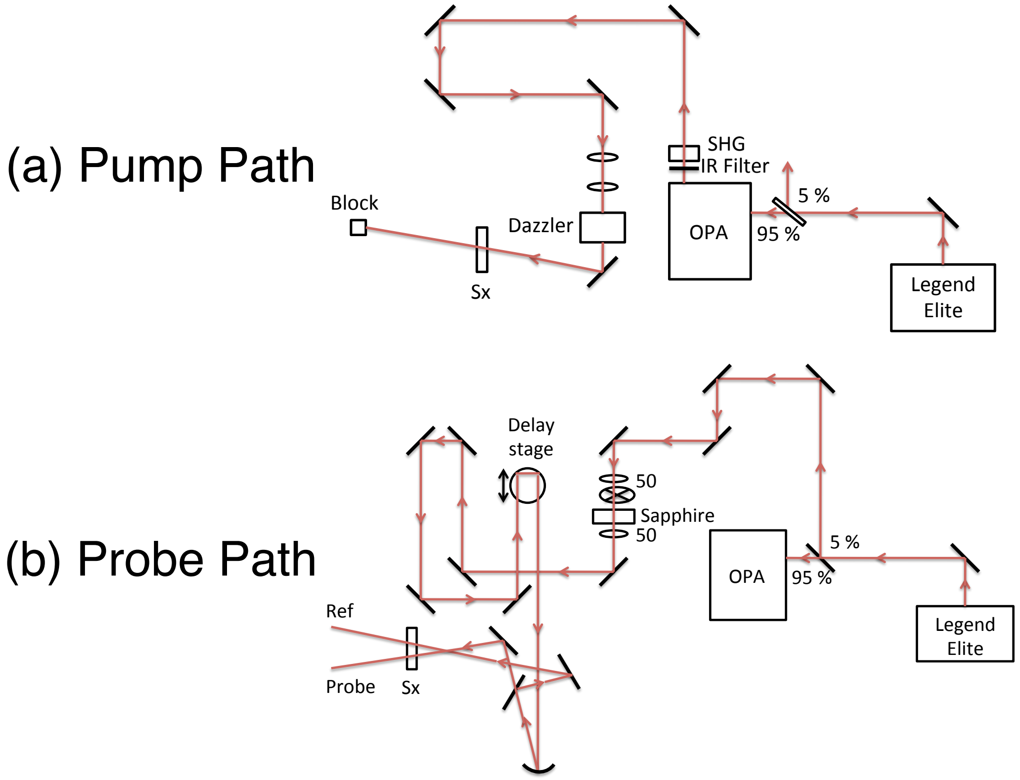

FIGURE 7.3: Experimental setup. (a) 95% of the pulses are driven toward an OPA that permits to tune the wavelength of the exciting pump between 550 nm and 700nm after the SHG crystal. Then, the light passes through a Dazzler which shapes the pulses : from one single pulse coming from the OPA, two pulses with controlled delay and relative phase emerge from the pulse shaper and are directed toward the sample Sx. (b) The 5 other percents are sent through a sapphire window that generates a white light continuum and then delayed by a translation stage. This probe pulse is split in two parts, one that crosses the pump called the probe and one reference.

7.2 Application of 2D spectroscopy to study Chlorophyll *a* and LHCII

Before being able to use the experimental setup on nanoparticles, the author participated in measurements conducted on Chlorophyll *a* and Light Harvesting Complex II (LHCII) that are respectively represented in figure 7.4 (a) and (b). LHCII is one of the major photosynthetic complex in plants and it responds to various necessities. It acts as antenna to gather energy from the sunlight and then transfer it toward the reaction center. LHCII is composed of 14 chlorophyll molecules (8 Chl a and 6 Chl b) and thus has a very intricate manifold of states. The side results obtained in this topic are briefly presented in this section.

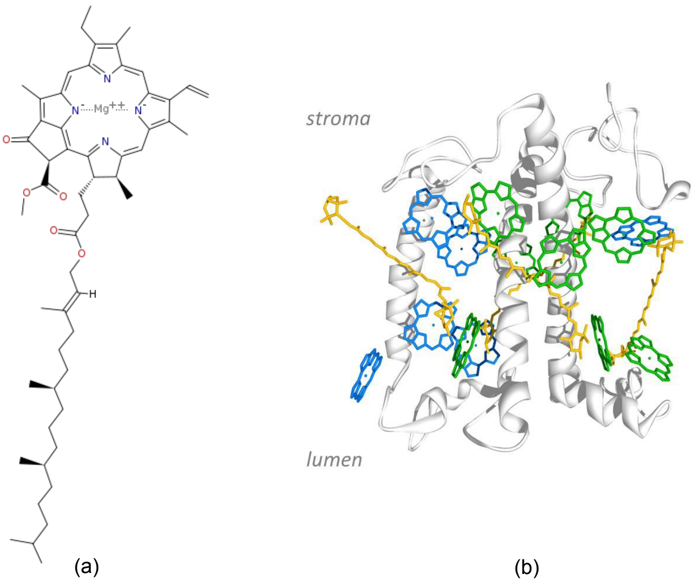

(a) (b)

FIGURE 7.4: Schematic representation of a Chlorophyll a molecule (a) and of a Light Harvesting Complex II (b).

7.2.1 Lineshape analysis

So far, only a phenomenological decay was used to describe the dephasing by introducing an exponential decay of the amplitude during the coherences time. However, dephasing could be included more naturally by discussing the influence of the bath surrounding the system. It is done by considering that the fluctuation of the bath slightly modifies the dipole transition moment by interacting with the system. Then, instead of having an harmonic oscillation $e^{i\omega_{10}t}$ during the coherences, one now obtains the time-dependent dipole transition moment with the following equation :

$$\dot{\mu}_{10}(t) = -i\omega_{10}(t)\mu_{01}(t) \tag{7.12}$$

Which is formally solved in the following way :

$$\mu_{10}(t) = \mu_{10}(0)e^{-i\int_0^t \omega_{10}(\tau)d\tau} \tag{7.13}$$

Assuming that the fluctuations are small, it is reasonable to express the transition frequency $\omega_{10}(t)$ as a sum of its average $\langle\omega_{10}(t)\rangle = \omega_{10}$ and of a small time varying part $\delta\omega_{10}(t)$. Using a truncated cumulant expansion to calculate the mean value of equation 7.13, the linear response function can be calculated in term of a lineshape function $g(t)$:

$$\langle\mu_{10}(t)\mu_{10}\rho_{00}\rangle = \mu_{10}^2 e^{-i\omega_{10}t}e^{-g(t)} \tag{7.14}$$

Where the lineshape function can be expressed with the frequency-frequency correlation function $\delta\omega_{10}(\tau')\delta_{10}(\tau'')$:

$$g(t) = \frac{1}{2}\int_0^t\int_0^t \delta\omega_{10}(\tau')\delta\omega_{10}(\tau'')d\tau'd\tau'' \tag{7.15}$$

The frequency-frequency correlation function (FFCF) measures the ensemble averaged frequency fluctuation of a transition over time and is sensitive to changes in the solvation environment. In third-order nonlinear optical experiments, $g(t)$ also describes the lineshape of the multidimensional spectra. As an example, the non-rephasing contribution calculated in the previous section now becomes :

$$\langle\mu(t_3+t_2+t_1)\mu(0)\rho(0)\mu(t_1)\mu(t_2+t_1)\rangle = \mu_{ab}^4 e^{-i\omega_{ab}(t_1+t_3)}e^{-g(t_1)-g(t_2)-g(t_3)+g(t_1+t_2)+g(t_2+t_3)-g(t_1+t_2+t_3)} \tag{7.16}$$

7.2.2 Measuring the frequency-frequency correlation function

7.2.2.1 Experimental methodology

In this section, we investigate and quantify the spectral diffusion dynamics of the Q_y band of chlorophyll *a* in methanol, by observing the evolution of the time-dependent portion of the FFCF utilizing partially collinear, pump-probe geometry 2D electronic spectroscopy as described in the previous section. In order to measure the FFCF, the center-line slope method (CLS) devised by Fayer [89] was utilized. This method enables a simplified extraction of the FFCF.

Adding information obtained by fitting the linear spectrum, it is possible to recover the FFCF from the experimental data. Such a strategy has also been used recently by Marcus [90] in his study of exciton-coupled porphyrin dimers. However, it seems that the use of the CLS method has not been used in electronic spectroscopy so far and was restrained to vibrational systems. Here, the CLS method is used to measure directly the normalized FFCF of the chromophores from 2D spectra.

All measurements were conducted at ambient temperatures of approximately 298 K. Chlorophyll *a* (Sigma Aldrich) was dissolved in methanol to provide a sample OD of 0.22 in a 1 mm sample cell (1 mm sapphire windows).

For each 2D electronic spectra (2DES) collected, the delay between the first two interaction pulses covers a total time range of 180 fs in 3 fs steps, while the T_w time remains constant. Due to the observation of a coherent artifact which is spectrally overlapped with the desired signal, collection of 2DES was only permissible at a shortest T_w of 250 fs. This is not a significant limitation, as the CLS method used to recover the normalized FFCF only applies for waiting time much longer than the free induction decay (FID) time scale. In this instance, the FID is approximately 70 fs. 2DES were collected at T_w values extending to 400 ps, to ensure that the evolution of the 2DES over time scales pertinent to the time-dependent portion of the FFCF was fully observed.

7.2.2.2 Results

Figure 7.5 shows the linear spectrum of Chl *a* in methanol. The main peak is assigned to the Q_y transition, within the plane of the porphyrin ring[91]. The peak is centered at 665 nm (451 THz) with a bandwidth of 20 nm (14 THz). The other peaks blue-shifted from the main peak are generally assigned to a vibronic progression from the Q_y band[92].

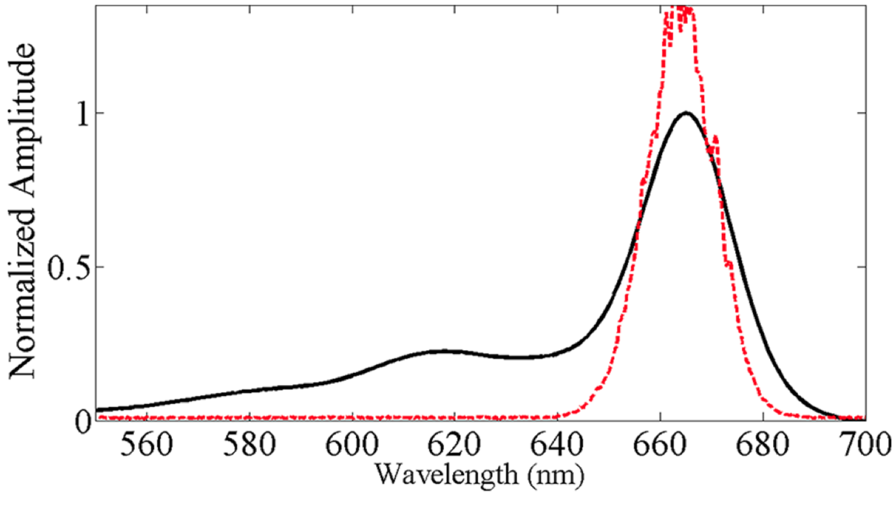

Figure 7.5: Linear absorption spectra of Chl a in methanol (black), with typical spectrum of the frequency doubled OPA output overlaid (red dashed).

Figure 7.6 shows the evolution of the 2DES line shape of the Q_y band of Chl a in methanol as T_w is increased, with the corresponding CLS fits overlaid which are subsequently discussed. These 2DES are typical examples of the observed 2DES at these T_w values.

The use of a continuum probe has been demonstrated to cause frequency dependent distortions to the antidiagonal 2DES line width[93]. The limited minimum T_w value of 250 fs, combined with the long time scales of the processes measured here compared to the chirp of the probe over the bandwidth of the Q_y transition means no such distortions are easily discernible here. It is however anticipated that at short T_w values, and in cases where the time scales of the measured processes and probe chirp are comparable, corrective procedures such as those suggested by Ogilvie[93] will become necessary..

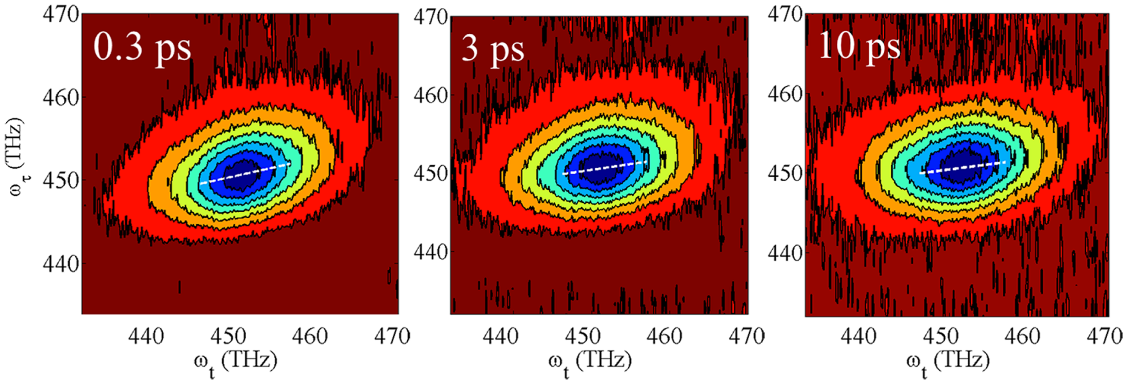

Figure 7.6: 2DES of the Q_y band of Chl a in methanol shown at T_w values of 0.3, 3, and 10 ps (top to bottom) with corresponding CLS fits overlaid (white dashed lines).

In recent years, efforts have been made to simplify the extraction of the FFCF from experimental 2D data, with the ellipticity method suggested by Tokmakoff[94] and the CLS method of Fayer [89] being the most straightforward to implement. In the CLS method, one fits a line through the maxima of the slice of the 2D spectrum at each detection frequency. Fayer have shown analytically that, under the short time approximation where the coherence time is short compared to T_w, the gradient of this line equates the normalized FFCF as a function of T_w :

$$S(T_w) = \mathrm{CLS}(T_w) = \frac{\langle \delta\omega(T_w)\delta\omega(0)}{\langle \delta\omega(0)\delta\omega(0)} \tag{7.17}$$

In this work, a band of about 10 THz corresponding to the highest signal intensity (to reduce the influence of noise at the edges of the peak) was fitted with a Gaussian function at each value of ω_t and linear regression of the determined maxima were performed through a least-squared method to yield the CLS values. Figure 7.7 depicts the CLS progression as T_w increases. Figure 7.7 depicts the measured CLS versus T_w. These data points were fitted with a biexponential decay with amplitude A_1 and A_2 and decay constant of τ_1 and τ_2 as well as a baseline offset (A_3) corresponding to a process with a time scale larger than the observation window of these measurements ($\gg$ 500 ps). The determined fit parameters are displayed in Table 1. The optimal values of the two amplitudes are similar, with $A_1 \approx 0.07$ and $A_2 \approx 0.06$, and have time constants of $\tau_1 \approx 0.5$ ps and $\tau_2 \approx 7$ ps, respectively. Supplementary to these 2DES, pump-probe scans of the transient spectra of Chl *a* in methanol were also measured (not presented here) and the Q_y excited-state lifetime was found to be 110 ± 15 ps. High temporal resolution pump-probe scans at pump-probe delay times < 1ps do not show any discernible oscillations.

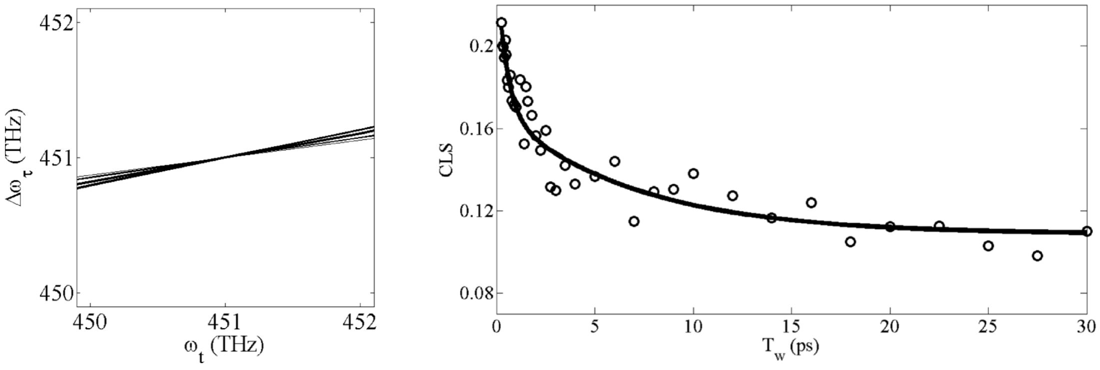

(a)

(b)

FIGURE 7.7: (a) CLS fits of 2DES at T_w values of 0.5, 1.4, 6, and 10 ps (progressing from thickest line to thinnest respectively). (b) 2DES of the Q_y band of Chl a in methanol shown at T_w values of 0.3, 3, and 10 ps (top to bottom) with corresponding CLS fits overlaid (white dashed lines).

The FFCF can be phenomenologically modeled with a generalized Kubo line shape, using a series of exponential decays, where each term may represent a certain dynamical process :

$$C(t) = \sum_i \Delta_i^2 e^{-\frac{t}{\tau_i}} \tag{7.18}$$

where Δ_i and τ_i are the amplitude and the correlation time of the frequency fluctuation of the ith component, respectively. No discernible oscillation is observed in the CLS data presented in Figure 7.7, as well as in the pump-probe traces. This leads us to conclude that there is no underdamped oscillating component in the FFCF of equation 7.18 in this instance. $C(t)$ is related to the line shape function $g(t)$

$$g(t) = \int_0^t dt_1 \int_0^{t_1} C(t_2) dt_2 \tag{7.19}$$

which is in turn related to the linear optical response $R^{(1)}(t_1)$ and the third-order non-linear optical response $R^{(3)}(t_1, t_2, t_3)$

In the case where $\Delta_i \tau_i \ll 1$, the line-shape function can be expressed as $g(t) = \delta(t)/T_2$ and is said to be motionally narrowed (where T_2 is the homogeneous dephasing constant), and the observed linear spectrum line shape is Lorentzian in nature. Conversely, when $\Delta_i \tau_i \gg 1$, it simplifies to give $g(t) = (\Delta_i/2)t^2$ and can be approximated as a constant, corresponding to the inhomogeneous limit, and a Gaussian line shape is observed. In many condensed phase systems, $\Delta_i \tau_i \approx 1$ and are classified as being in the spectral diffusion regime. From a purely absorptive 2D spectrum, the CLS gives the normalized FFCF as shown in equation 7.17. Comparing equations 7.17 and 7.18, the experimental amplitudes of the exponential decay used to fit the CLS can therefore be recognized as $A_i = \Delta_i^2 / \sum \Delta_i^2$. By definition, $S(T_w = 0) = 1$. The three amplitudes in table 7.1 sum to only 0.239. The experimental data points only begin at $T_w = 250$ fs. It is therefore clear that at least one fast process is occurring within the first 250 fs that is not directly observed in these measurements. We therefore assign an additional exponential decay with quantities Δ_0 and τ_0 to account for this short process which makes up for the shortfall of 0.761. From Table 7.1, we know the values of τ_1 and τ_2, while the time scale for the baseline component, τ_3 (corresponding to A_3), is assigned as >1 ns. This leaves only the value of τ_0 and the total sum of the square of the fluctuation amplitude, $\sum \Delta_i^2$, to be determined. In order to obtain these values, we make use of the linear spectrum. The linear spectrum is related to the FFCF via the line-shape function $g(t)$, as shown in equation 7.20.

$$I(\omega) = \mathrm{Re}\Big[FT\big(e^{-g(t)}\big)\Big] \tag{7.20}$$

A_1	τ_1 (fs)	A_2	τ_2 (ps)	A_3
0.070 ± 0.022	500 ± 299	0.060 ± 0.012	6.9± 3.5	0.109± 0.007

Table 7.1: Fitting parameters of measured biexponential decays of the normalized FFCF

Using this relationship, we can obtain values for $\sum \Delta_i^2$ and τ_0 by fitting to the experimental linear spectrum. In the fit optimization performed here, the relative amplitudes between Δ_i^2 are constrained according to values in Table 7.1. This means that the relative normalized amplitude, Δ_0, of the extremely fast component, is set to be 0.761. The total of the square of the fluctuation amplitudes $\sum \Delta_i^2$ and τ_0 were allowed to vary to obtain the best fit to the experimental linear spectra, while the transition frequency was allowed to vary over tight bounds around the experimentally observed transition maxima. For the experimental linear spectrum to be fitted, it is imperative that only the band of the Q_y transition of Chl *a* is used. However, the experimental linear spectrum consists of vibronic progressions on the blue side of the main Q_y transition peak.

An excellent fit to the linear spectrum is obtained. The optimized fit value for the short time constant $\tau_0 = 65\pm\ 10$ fs while that for the total of the square of the fluctuation amplitudes $\sum \Delta_i^2 = 42.4$ THz. Despite the large errors associated with the fit to the CLS, the recovered τ_0 and $\sum \Delta_i^2$ values are extremely robust since the relative amplitude of the unknown component is large (0.761) compared to the sum of the other components

(0.239). In cases where the relative amplitude of the unknown component is small, the propagation of error will result in greater uncertainty in the recovered values for the unknown component. Table 2 summarizes the values recovered from both the fit and experiment.

Numerous experiments such as 3PEPS (3 Pulse Photon Echo Peak Shift) have been performed on dye molecules. One common feature is the presence of a fast component that is attributed to the inertial component of solvation. In the present study, the time constant τ_0 of 65± 10 fs is consistent with values recorded for other species elsewhere in the literature.This fast component with $\Delta_0\tau_0 = 2.36$ is not in the motionally narrowed regime that gives rise to homogeneous line-width contributions to the spectrum. This is also obvious from observing the linear line shape, as there is no discernible Lorentzian component, typified by a gentle slope at the spectral wings of the Voigt profile making up the spectrum. The relative proportion of the fast component is also consistent with these other studies. Sub-10 fs time scale components have been observed in studies of IR144 and attributed to the rapid dephasing of the initially prepared vibronic wavepacket. In the measurements presented here, these extremely fast components are not observed. If there is indeed a very fast sub-10 fs component, it does not significantly contribute to the line shape, as it may well be in the motionally narrowed regime ($\Delta\tau \ll 1$), and the resultant Lorentzian line shape would be too narrow to contribute to the final line shape, as discussed above.

A more exact value of the long time component of τ_3 cannot be determined due to the limited scanning range of this experimental setup, as well as limitations in achieving reasonable signal-to-noise ratios as the signal decays. It is therefore assigned as $\tau_3 > 1$ ns. This long time component is not due to the lifetime of the excited state. The reason is that the FFCF measured here is not the intensity of the signal as a function of T_w but that of the slope of the peak. This long time component is a measure of the inhomogeneity of the chromophore and has a value of 13.97 THz.

As a conclusion, the full FFCF occurs over four time scales, with each represented by an exponential decay. The shortest time scale whose amplitude accounts for approximately 75% of the FFCF decay has a time constant of 65 fs and is attributed to the inertial component of solvation. The next components are attributed to spectral diffusion, τ_1 with a time scale of ≈500 fs and τ_2, a picosecond component, of ≈7 ps, assigned to solvent rearrangement. The long time (>1 ns) is attributed to inhomogeneity and could be intramolecular in origin.

7.2.3 2D spectroscopy of LHCII trimers

In this section, we follow a supermolecule approach[95] to interpret the multidimensional optical signal from LHCII trimers.

As stated in the beginning of this section, LHCII molecules have a complex dynamics due to the high number of couple excitonic (molecular) eigenstates. In this section, 2D spectroscopies done on LHCII trimers are interpreted using a multilevel approach and allowing population transfer during the population time. To do so, a superoperator in Liouville space is introduced in order to model population transfer by a master equation :

$$\dot{\rho}_{ee}(t) = -\sum_{e'} K_{ee,e'e'}\ \rho_{e'e'}(t) \tag{7.21}$$

The solution of this differential equation can be formally be obtained using a population Green function G : $\rho_{e'e'}(t) = \sum_e G_{e'e',ee}(t)\rho_{ee}(0)$. The Green function is expressed as :

$$G_{e'e',ee}(t) = \left[e^{-Kt}\right]_{e'e',ee} \tag{7.22}$$

The time-evolution of the coherences $\rho_{e'e}(t) = e^{-i\omega_{e'e}t-\Gamma_{e'e}t}\rho_{e'e}(0)$ is also included in the Green's function which final components are :

$$G_{e_4e_3,e_2e_1}(t) = \delta_{e_4e_3}\delta_{e_2e_1}\theta(t)\left[e^{-Kt}\right]_{e_4e_4,e_2e_2} + (1-\delta_{e_4e_2})\delta_{e_3e_1}\theta(t)e^{-i\omega_{e_4e_3}t-\Gamma_{e_4e_3}t} \tag{7.23}$$

Contrary to equation 7.11, we also need to add a sum over states since we consider a multilevel system. Indeed, LHCII has complex set of eigenstates and the richness of its physics comes from the great number of couplings between them. As an example, the Feynman diagram corresponding to the equation 7.11 is modified accordingly and the element of the response function is now :

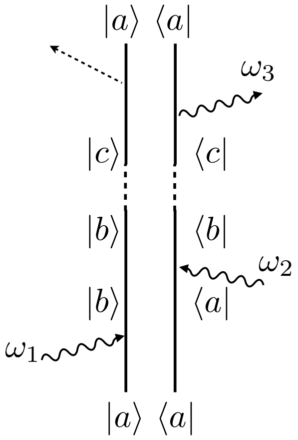

FIGURE 7.8: Feynman diagram equivalent to 7.1 with population transfer added.

$$R^{\rm nr} = \sum_{e_4e_3e_2e_1} \mu_{ge_4}\mu_{e_3g}\mu_{ge_1}\mu_{e_2g}\ e^{-i\omega_{e_4g}t_1-\Gamma_{e_4g}t_1}e^{-i\omega_{e_2g}t_3-\Gamma_{e_2g}t_3}G_{e_4e_3,e_2e_1}(t_2) \tag{7.24}$$

Experiments were conducted on LHCII trimers extracted from spinach thylakoid membranes. The trimers were placed in the experiment previously described in figure 7.3 and their 2D spectra were measured by tuning the OPA at 650 nm with a FWHM of 14 nm to be resonant with the Q_y transition of Chl b. The pulse from the OPA was then sent in the Dazzler as previously mentioned and the resulting two pulses were compressed down to 55 fs.

The measured non-rephasing, rephasing and purely absorptive pathways are displayed on the 2D Electronic spectra in figure 7.9. The first significant 2D spectra are measured at T_w = 250 fs because the coherent artifact is present at shorter times. The purely absorptive spectra all exhibit a diagonal resonance corresponding to molecular states of the Chlorophyll b which vanish along time. For the longer time displayed here (1 ps), the diagonal peak is already very weak and completely disappear around 5 ps. Those molecular states get their energy transferred to the Chlorophyll a molecular states as can be observed on the crosspeak that appears around (15 400 cm^{-1} , 14800 cm^{-1}). This cross peak finally decays for longer waiting time (>10 ps) when the system relaxes to the ground state.

The fitting procedure uses a mix between global and target analysis as a strategy [96]. Since individual states can not be resolved, we use target analysis to recover the number of necessary states to recover the experimental data. Those states are those of a compartmental model in which states having close resonances and lifetimes can not be distinguished. This approach permits to find the number of separable states of the system accessible by the experiment.

In this case, we first use a spectral model in which all 2D spectra are fitted using lorentzian lineshapes while the T_w time dependence is adjusted by a linear coefficient :

$$\text{Fit} = \sum_{T_i} a_i S(\omega_\tau, T_i, \omega_t) \tag{7.25}$$

Where $S(\omega_\tau, T_i, \omega_t)$ is a sum over states of 2D lorenzian. Using this model, we can distinguish 4 four main compartmental states corresponding to Chlorophyll b high (15408 cm^{-1}) and low (15256 cm^{-1}) and to Chlorophyll a high (14910 cm^{-1}) and low (14700 cm^{-1}) molecular eigenstates. The lineshapes of those four states are also defined by the following decoherence of the population : $\Gamma_{hb,ha} = 249\text{cm}^{-1}, \Gamma_{lb,la} = 263\text{cm}^{-1}$, and $\Gamma_{ha,la} = 354\text{cm}^{-1}$ where h and l stands for high and low and a and b stands for the two kind of chlorophyll a and b.

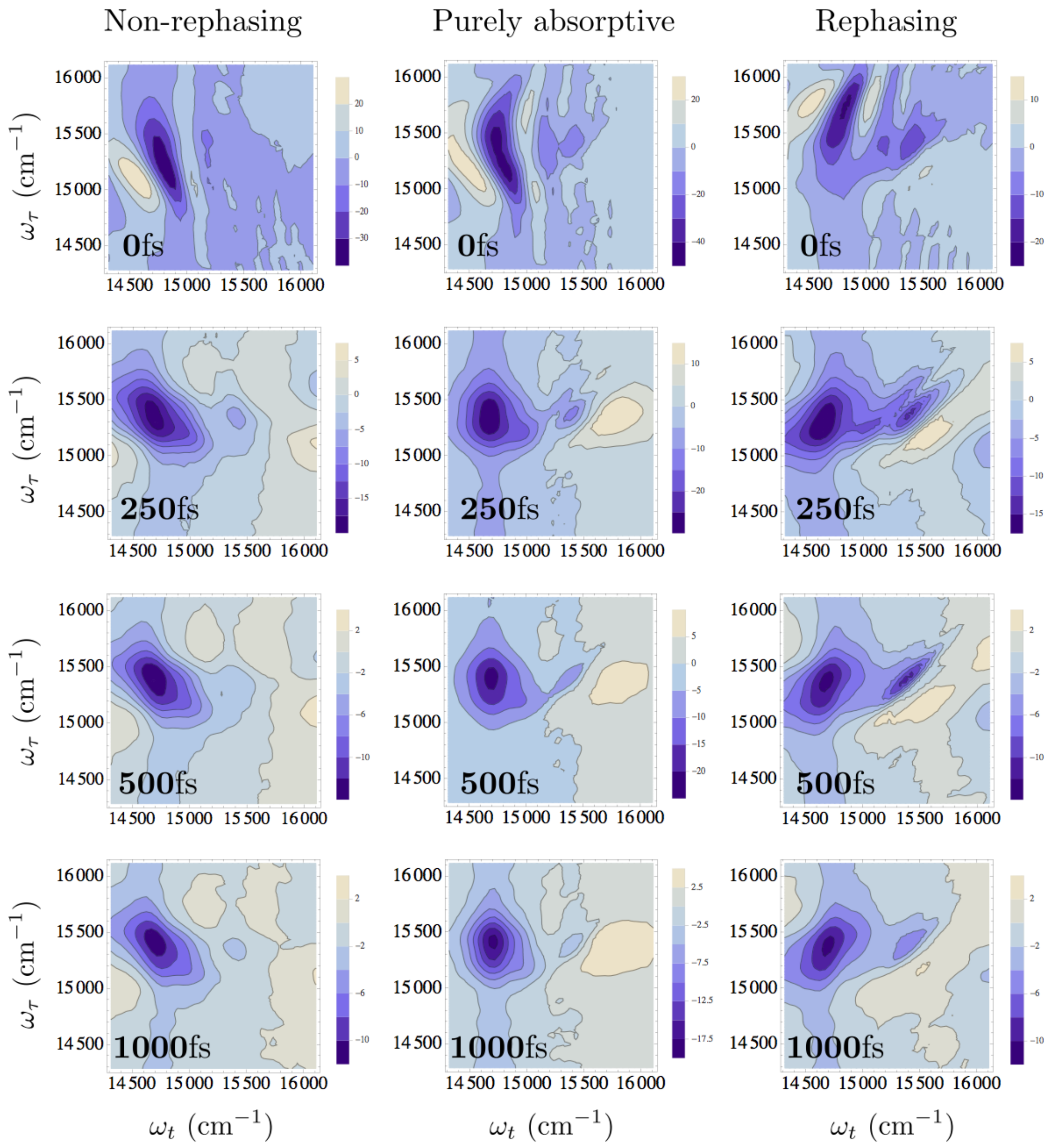

FIGURE 7.9: Experimental 2D electronic spectra measured on LHCII trimers. From left to right, the columns represent the time evolution of the non-rephasing, of the purely absorptive and of the rephasing spectra. At $T_w = 0$, the interesting signal is hidden by the coherent artifact and the shortest viable data are measured at $T_w = 250$ fs.

Once the distinguishable states are obtained by fitting the data, the linear time coefficient are trashed and a spectral model is proposed. This model requires to conjecture a specific time dependence, i.e a form of the master equation rate matrix, in order to be numerically tractable. This choice can be assisted using kinetic models and decay associated spectra[97]. The rate matrix chosen is the following :

$$K = \begin{pmatrix} \gamma_{la,la} & 0 & 0 & 0 \\ -\gamma_{ha,la} & \gamma_{ha,ha} & 0 & 0 \\ -\gamma_{lb,la} & 0 & \gamma_{lb,lb} & 0 \\ 0 & -\gamma_{hb,ha} & -\gamma_{hb,lb} & \gamma_{hb,hb} \end{pmatrix} \tag{7.26}$$

To make the model simpler, we have not included the possibility for the excitation energy transfer to move from low energy states to higher ones. If those coefficients were to be included, they are not independent and can be calculated using the detailed-balance[95]. Moreover, the off-diagonal components are not independent with the diagonal ones because of the probability conservation : $\sum_e K_{ee,e'e'} = 0$.

The fitting procedure thus uses the coefficients of the rate matrix as fitting parameters while the resonance positions and the lineshapes parameters are given from the previous fitting. One obtains $\gamma_{hb,hb} = 6590\text{fs}^{-1}$, $\gamma_{hb,lb} = 106\text{fs}^{-1}$, $\gamma_{hb,ha} > 1\text{ps}^{-1}$, $\gamma_{lb,la} = 782\text{fs}^{-1}$ and $\gamma_{ha,hb} < 1ps$. Results from the fitting model are shown in figure 7.10 to show the acceptable agreement between it and the data.

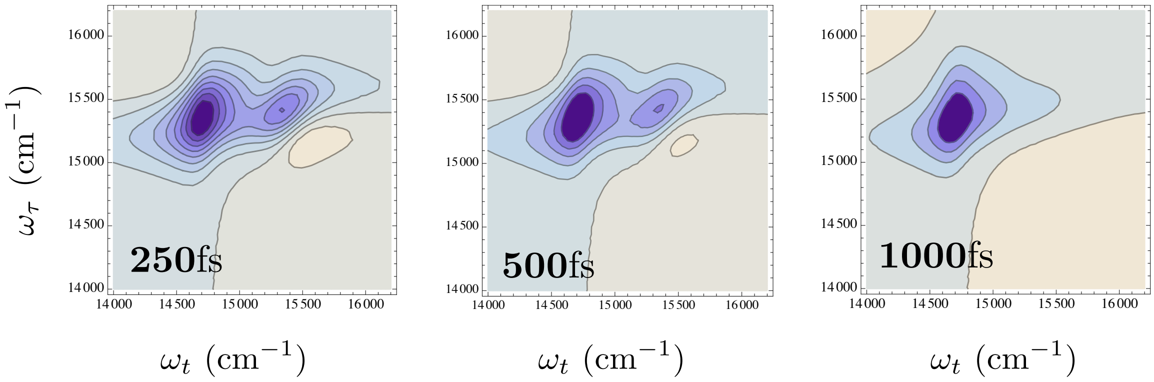

FIGURE 7.10: Display of some 2D rephasing spectra using the parameter obtained by the fitting procedure described in this section.

Those results can be compared with the one obtained by K. Wells [97] whose analysis suggested the following :

- A fast energy transfer ($\leqslant$ 300 fs) from high chlorophyll *b* (15400-15500 cm^{-1}) to low chlorophyll *a*.
- An other fast energy transfer from intermediate chlorophyll *b* (15200-15300 cm^{-1}) to low ones (15000-15100 cm^{-1}).
- A picoseconds energy transfer from chlorophyll *b* to chlorophyll *a*.
- A slow relaxation ($\gg$ 10 ps) of the high energy chlorophyll *a* to its lower levels.

As a conclusion of this short digression, the excitation energy transfer has been investigated using a supermolecule approach. The data collected using 2DES allowed to obtained a lot informations on the energy pathways even if the technique does not produce fully resolved spectra. More investigations are still required to disentangle further the complicated energy transfer relaxation pathways in LHCII.

Chapter 8

Pump-Probe on nanoparticles

8.1 Eigenmodes in nanoparticles

The goal of this chapter is to introduce preliminary works on the dynamical properties of gold nanoparticles in the visible range. While the formalism of ultrafast spectroscopy makes a great use of quantum mechanics when molecules are investigated, nanoparticles are described in a classical fashion and the modes probed by a spectroscopic technique need to be clarified. Once the modes of the global electromagnetic motion are well understood, it is possible to use them to calculate time-domain response function. Moreover, since each mode belongs to irreducible representations of the symmetry group of the nanoparticle, they fit completely in the irreducible formalism developed in the previous part.

Those modes were firstly postulated at the beginning of this work as eigenmodes of the electron cloud depending only on the shape and the symmetry of the nanoparticle which acts only as a support for the modes. In the end, the exact value of measured quantity will be calculated using the materials properties but a great deal of informations can be obtained without that. It appears that the use of the Local Density Of States (LDOS) concept can introduce naturally eigenmodes under some constraints [75, 98–100]. In this section, we first present how geometric eigenmodes can be introduced in the electrostatic limit as proposed by Boudarham and Kociak [75]. Then, we present simple calculation of geometric eigenmodes using conformal mapping that can retrospectively be explained using geometric eigenmodes.

8.1.1 Notion of geometric eigenmodes

In this section, we present briefly the notion of geometric eigenmodes recently introduced by Kociak[75]. The Maxwell equation $\nabla \cdot \epsilon \underline{E} = 4\pi\rho_f$, where ϵ is the permittivity of the material under consideration and ρ_f the free charges, can be expressed in term of potentials :

$$\nabla \cdot \Big(\epsilon(-\nabla\Phi - \frac{\partial \underline{A}}{\partial t})\Big) = 4\pi\rho_f \tag{8.1}$$

In the static limit, one then just obtains a Poisson equation for the scalar potential :

$$\nabla \cdot \big(\epsilon\nabla\Phi\big) = -4\pi\rho_f \tag{8.2}$$

Equation 8.2 can be written in an integral form separating contribution from the homogeneous part of the material and from the inhomogeneity of the permittivity :

$$\begin{aligned}
\Phi(r,\omega) &= \Phi^{\infty}(r,\omega) + \Phi^{b}(r,\omega) && (8.3)\\
\Phi^{\infty}(r,\omega) &= \int \frac{\rho^{\text{ext}}(r';\omega)}{\epsilon(r',\omega)|r-r'|} dr' && (8.4)\\
\Phi^{b}(r,\omega) &= \frac{1}{4\pi}\int \frac{\nabla\Phi(r',\omega)\cdot\nabla\epsilon(r',\omega)}{\epsilon(r',\omega)|r-r'|} dr' && (8.5)
\end{aligned}$$

In our case, where we consider the material inside the nanoparticles homogeneous, the second term reduce to the surface contribution and can be recast in a surface equation :

$$\Phi^{b}(r,\omega) = \int \frac{\sigma(s,\omega}{|\vec{r}-\vec{s}|} ds \tag{8.6}$$

Where σ is the induced boundary charge. Following reference [99], the expression of the surface charge σ can be written as an eigenvalue problem with source :

$$2\pi\lambda(\omega)\sigma(s,\omega) = \vec{n}_s \cdot \nabla\phi^{\infty}(s,\omega) + \int F(s,s')\sigma(s',\omega) \tag{8.7}$$

Where $\vec{n}_s$ is the normal vector at the boundary s. The normal derivative $F(s,s')$ of the Green function in equation 8.6 and $\lambda(\omega)$ are defined by :

$$F(s,s') = -\frac{\vec{n}_s \cdot (\vec{s}-\vec{s'})}{|s-s'|^3} = \partial_{n_s}\frac{1}{|s-s'|} \tag{8.8}$$

$$\lambda(\omega) = \frac{\epsilon_2(\omega)+\epsilon_1(\omega)}{\epsilon_2(\omega)-\epsilon_1(\omega)} \tag{8.9}$$

Putting the source-term to zero, one calculate the eignemodes σ^i of the system :

$$2\pi\lambda_i\sigma^i(s) = \int F(s,s')\sigma^i(s')ds' \tag{8.10}$$

In the paper written by Ouyang and Isaacson [98], it is proven that the eigenvalues λ_i are real due to algebraic properties of the operator appearing in equation 8.10 and defined by :

$$C = \int \partial_{n_s}\frac{1}{|s-s'|} \quad \bullet\, ds' \tag{8.11}$$

In fact, C is not symmetric but shares its spectrum with a self-adjoint operator and thus the λ_i are real. Moreover, the eigenmodes $\sigma^i(s)$ form a basis having the following orthogonality relationship :

$$\int \frac{\sigma^i(s)\sigma^j(s')^*}{|s-s'|}dsds' = \delta_{ij} \tag{8.12}$$

For objects having sharp shapes, i. e. the surface S of the nanoparticle is not smooth, $\sigma^i(s)$ may be singular are the irregular points of S and it is then more convenient to solve the equation of the adjoint operator to C. The eigenmodes of the adjoint operator C^* to C are denoted $\tau^i(s)$ and verify :

$$2\pi\lambda_i\tau^i(s) = \int F(s',s)\tau^i(s')ds' \tag{8.13}$$

The introduction of the basis $\tau^i(s)$ is equivalent to construct a reciprocal basis to the basis of $\sigma^i(s)$. Physically, the modes $\tau^i(s)$ can be interpreted as a distribution of dipoles over the surface. As a reciprocal basis, they naturally have a simple orthogonality relationship with the original basis [101] :

$$\int \sigma^i(s)\tau^j(s)ds = \delta_{ij} \tag{8.14}$$

At this stage already, in equation 8.10, one can notice that the eigenproblem is scale invariant. Thus, the eigenmodes is just a property of the shape of the objects. The size and the material properties will appear when one will move from the eigenmodes σ^i/τ^i to the corresponding scalar potential $\phi^{b,i}/\tilde{\phi}^{b,i}$ respectively using equation 8.6. Being equipped with the basis σ^i and its reciprocal basis τ^i, one can use spectral theory [102] to expand the Green function of equation 8.10 on its eigenstates. We define the operator $\mathcal{L}$ as :

$$\mathcal{L}\bullet = \int F(s,s')\bullet ds' \tag{8.15}$$

The Green function $g(s, s'', \lambda)$ of $\mathcal{L}$ is defined by :

$$\big(\mathcal{L} - 2\pi\lambda\big) g(s, s'', \lambda) = \delta(s - s'') \tag{8.16}$$

Where

$$g(s, s'', \lambda) = \frac{1}{2\pi} \sum_i \frac{\sigma^i(s)\tau^i(s'')}{\lambda - \lambda_i} \tag{8.17}$$

The scalar Green function of the scalar potential $G^b(r, r', \omega)$, the dyadic Green $\underline{\underline{G}}(r, r', \omega)$ function of the corresponding electric field and the LDOS $\underline{\underline{\rho}}$ that can be obtained from $\underline{\underline{G}}(r, r', \omega)$ can all be deduced from $g(s, s'', \lambda)$. This interesting feature makes $g(s, s'', \lambda)$ a fundamental quantity which contains essential information about the shape of the nanoparticles. However, the use of the Poisson equation as start and thus of the quasi-static limit is a crude approximation in our case since the size of the nanoparticle is non-negligible compared to the excitation wavelength. This procedure is strictly valid for small nanoparticles and discrepancies will appear for bigger ones as retardation effects will become larger. One can still argue that the nanoparticles under study in this thesis are still small enough ($\approx \lambda/3$) to make the approximation acceptable. Moreover, further investigations using the spectral theory of operators could allow to find eigenmodes of the time-dependent problem rather than in the quasi-static limit.

8.1.2 Obtention of modes through conformal mapping

According to the previous section, the existence of eigenmodes that contains informations about the symmetry is acquired. Before knowing the work in reference [75], the author postulated the existence of eigenmodes based only on geometrical considerations. In this case, no clear equation that permits to calculate rigorously the eigenmodes are available but, as discussed before, any physical integral equation giving the electric field from sources, whether it is a Poisson or a wave equation, should lead to qualitatively similar modes since they are strongly constrained by group theory.

Two different candidates of eigenmodes were then created for the nanostars D_3 starting from well-known eigenstates of rotationally invariant problems. Those circular eigenstates are then transformed in eigenstates of D_3 using conformal mapping and group theoretical considerations are used to assign unambiguously each eigenstates to each irreducible representations in D_3.

Those eigenmodes should not be mingled with the irreducible current densities discussed in the previous parts of this thesis. The irreducible currents were belonging to irreducible representation of SO(3) while those eigenmodes are related to the irreducible representation of the point group D_3. The link between the eigenmodes of the nanoparticle and the irreducible currents can be achieved by inspecting how the representations of D_3 are projected into the representation of SO(3). Thus, each eigenmode will generate a finite and predictable number of irreducible currents. The analytical calculation of the corresponding irreducible currents can be achieved using an appropriate Green function. Finally, irreducible current densities obtained in such way does not depend on the incoming electric field and are rather adapted to the shape of the system. Thus, they are related to the components of the irreducible tensor and offer a basis of irreducible currents more adapted to the point group under consideration than the full irreducible basis in SO(3).

8.1.2.1 Harmonic oscillator modes

The first candidate is the well-known Hermite polynomials basis defined by :

$$\psi_{n_x}(x) = \left(\frac{1}{\pi}\right)^{\frac{1}{4}} \frac{1}{\sqrt{2^m m!}} H_m(x) e^{-\frac{1}{2}x^2} \tag{8.18}$$

Where $H_n(x)$ is the Hermite polynomial of order n. The function $\psi_{n_x}(x)$ are the solution of the eigenproblem for a harmonic oscillator. This configuration is chosen due to the broad range of validity of the harmonic oscillator which describes the behavior of any dynamic close to its equilibrium. The eigenmodes of the 2D circular harmonic oscillator are just the direct product of the one of the 1D oscillator. The eigenstates are then $\psi_{n_x n_y}(x, y) = \psi_{n_x}(x)\psi_{n_y}(y)$. The basis $\psi_{n_x n_y}$ are the eigenvectors of the operator :

$$\mathcal{L} \bullet = -\frac{1}{2}\Delta \ \bullet + \frac{1}{2} k r^2 \bullet \tag{8.19}$$

Where k describes the oscillator's shape. For a circular oscillator, $k = 1$ while "nanostars-shaped" can be constructed using $k = a + b\cos(3\theta)$ with a and b are parameters leading to various shapes of stars. The eigenvalues corresponding to the eigenvectors are :

$$\lambda_{n_x n_y} = (n_x + n_y + 1) \tag{8.20}$$

It is interesting to observe that, although the symmetry group of the circular harmonic oscillator is SO(2) which contains only one-dimensional irreducible representation, each level $n = n_x + n_y$ is degenerated $n + 1$ times. Extra degeneracies can appear in two fashions : either by coincidence when a parameter of the system has been fine tuned to make accidental degeneracies or when some hidden symmetries have not been taken into account. In the case of the 2D harmonic oscillator, we fall in the second case. According to Noether theorem, the construction of an invariant operator will correspond to a extra symmetry called dynamic symmetry. Following reference [103], it is possible to construct the following operator A that will commute with $\mathcal{L}$:

$$A_{ij} = \frac{1}{2}(\nabla_i \nabla_j + x_i x_j) \tag{8.21}$$

From this operator, we can define three more invariants by :

$$S_1 = \frac{A_{12} + A_{21}}{2} \tag{8.22}$$

$$S_2 = \frac{A_{22} + A_{11}}{2} \tag{8.23}$$

$$S_3 = \frac{L_z}{2} \tag{8.24}$$

The explicit calculation of the commutators leads to the following relationship :

$$[S_i, S_j] = \epsilon_{ijk} S_k \tag{8.25}$$

As seen in chapter 1, this is the Lie algebra of the rotation group SO(3). The 2D harmonic oscillator possesses a dynamical symmetry that explains the degeneracies of the level n. However, the degeneracy of the level n is $2n+1$ in SO(3) and not $n+1$ as in this case. This comes from the fact that SO(3) authorizes only integer values of J while the harmonic oscillator needs instead half-integer ones. Finally, the symmetry group of the 2D harmonic oscillator is SU(2) which is homomorphic to SO(3).

Using conformal mapping, the eigenstates in SU(2) will be transformed in eigenstates of the subgroup D_3. However, if one wants to keep track of the association of each eigenstates to each irreducible representation, it is first necessary to know how each representation of SU(2) will be projected over D_3. Since D_3 is a subgroup of SO(3), it corresponds to integer values of $J = n/2$ and can not take into account the fact that a rotation by 2π is not the identity in SU(2). Thus, an extended group D_3' is introduced instead. In this group, the identity E is a rotation by 4π around z while a new symmetry operation R is introduced and is a rotation by 2π around z. Using the character table of D_3 and orthogonality relationships between characters, it is possible to construct the character table of D_3' :

D_3'	E	R	$2C_3$	$2RC_3$	$3C_2'$	$3RC_2'$
A_1	1	1	1	1	1	1
A_2	1	1	1	1	−1	−1
E	2	2	−1	−1	0	0
A_1'	1	−1	−1	1	1	−1
A_2'	1	−1	−1	1	−1	1
E'	2	−2	1	−1	0	0

(8.26)

It is then easy to calculate the values of the characters of the irreducible representation of SU(2) for the operations of symmetry in D_3' that we give in the following table :

D_3'	E	R	$2C_3$	$2RC_3$	$3C_2'$	$3RC_2'$
D_0	1	1	1	1	1	1
$D_{1/2}$	2	−2	1	−1	0	0
D_1	3	3	0	0	−1	−1
$D_{3/2}$	4	−4	−1	1	0	0
⋮	⋮	⋮	⋮	⋮	⋮	⋮

(8.27)

The next step is to use this table to project the reducible representation of the irreducible ones using :

$$a_j = \frac{1}{g}\sum_k N_k \chi^{(j)}(\mathrm{C_k})\chi(\mathrm{C_k}) \tag{8.28}$$

The result of the projection gives how irreducible representations of SU(2) will be written as a linear combination of the one of D_3' :

$$\begin{aligned} D_0 &= A_1 && (8.29)\\ D_{1/2} &= E' && (8.30)\\ D_1 &= A_2 + E && (8.31)\\ D_{3/2} &= A_1' + A_2' + E' && (8.32) \end{aligned}$$

As one could expect, the integer representation of SU(2) are projected over the representations of D_3 while the half-integer ones require the introduction of the representations of D_3'. It will now be possible to label each eigenstates of D_3' according to their irreducible representations since we know from which representations in SU(2) they are made from.

Since our problem is essentially two-dimensional, one can use conformal mapping. The mapping that we will use is represented in figure 8.1 and the holomorphic function used is :

$$z \leftarrow z + \frac{1}{4} z^4 \tag{8.33}$$

This mapping can be translated for the variables x and y of the plane as :

$$\begin{cases} x \leftarrow x + \frac{1}{4}(x^4 + y^4) - \frac{3}{2}(xy)^2 \\ \qquad y \leftarrow y + x^3 y - xy^3 \end{cases} \tag{8.34}$$

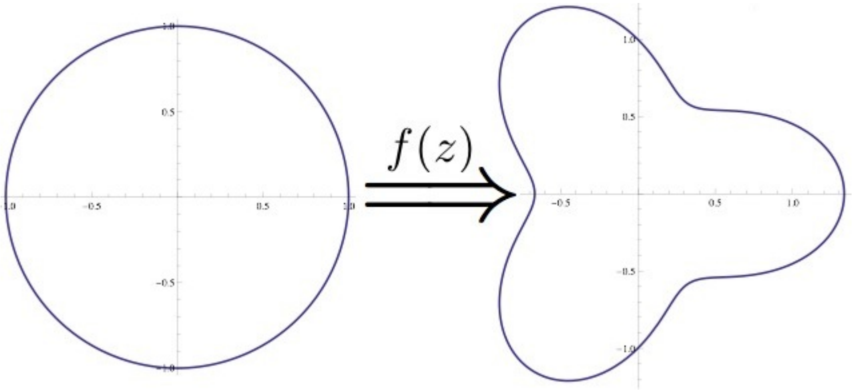

Figure 8.1: Schematic description of the conformal mapping.

The applications of the conformal mapping on the fundamental mode and the first doubly-degenerated higher state is displayed in figure 8.2. Those eigenstates can be associated easily to representations A_1 or E' respectively and behave under transforms according to the character table 8.26.

The next level $n = 2$ is triply degenerated in SU(2) and the conformal mapping of those functions is represented in figure 8.3. Those three eigenstates were degenerated in the circular geometry and the conformal mapping has projected them on A_2 and E.

However, it is not obvious from the aspect of the modes if they subtend irreducible representation or if they all have a mixture between eigenmodes of A_2 and E. Group theory provides tools to inspect the belonging of a eigenstate to an irreducible representation like the generalized Unsöld theorem[27, 104] or an automatic procedure to make projector. The Unsöld theorem states that the sum of the square modulus of spherical harmonics over a whole subspace is invariant by rotation : $\sum_m |Y_{lm}(\theta, \varphi)|^2 = (2l+1)/4\pi$. The generalized version of the theorem applies on any group of symmetry and affirms that the sum of the squared eigenstates is an invariant of the group :

$$P_R \sum_{\kappa} |\varphi_{\kappa}^{(j)}|^2 = \sum_{\kappa} |\varphi_{\kappa}^{(j)}|^2 \tag{8.35}$$

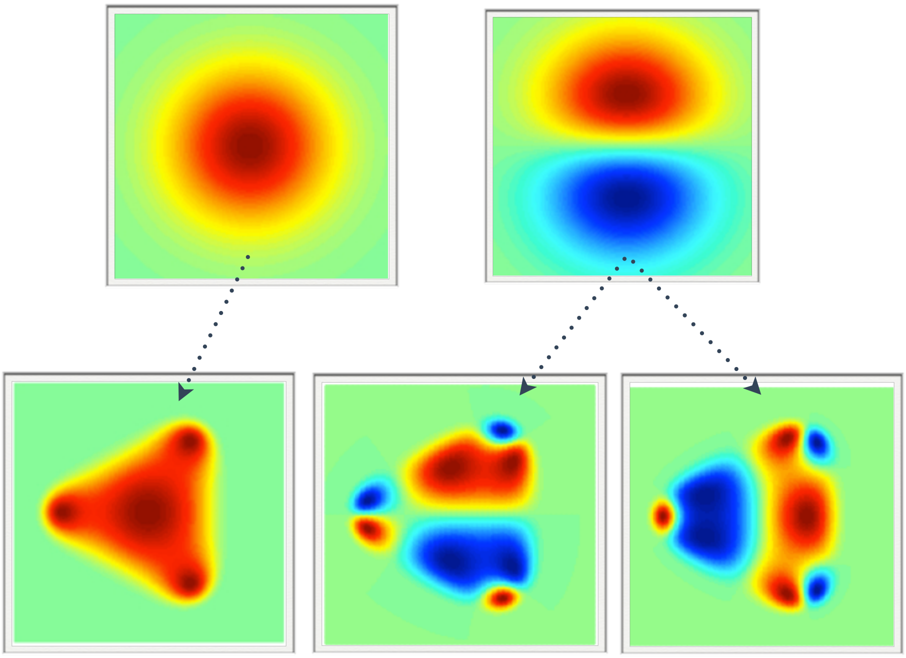

FIGURE 8.2: Obtention of the three first eigenmodes using conformal mapping. The eigenmodes of the cylindrical symmetry are mapped toward the modes of D_3'. The first excited mode is doubly degenerated and this degeneracy is preserved through the mapping toward the two-dimensional representation E' of D_3'.

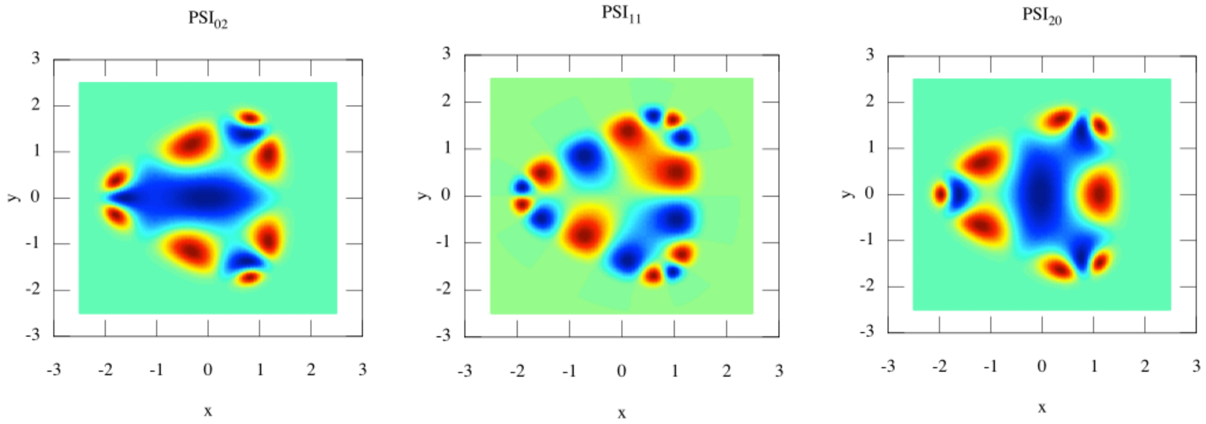

FIGURE 8.3: Representation of the eigenmodes obtained from the one of the irreducible representation D_1 of SU(2).

Figure 8.4 displays this sum for the $n = 2$ level of SU(2) and shows that the Unsöld theorem is followed by the eigenmodes obtained through conformal mapping.

Thanks to the Unsöld theorem, we know that the eigenmodes still form complete subspace but we can not disambiguate between the one of A_2 and E.

$$\mathcal{P}_\kappa^{(j)} = \frac{l_j}{g} \sum_R \Gamma^{(j)}_{\kappa\kappa}(R)^* P_R \tag{8.36}$$

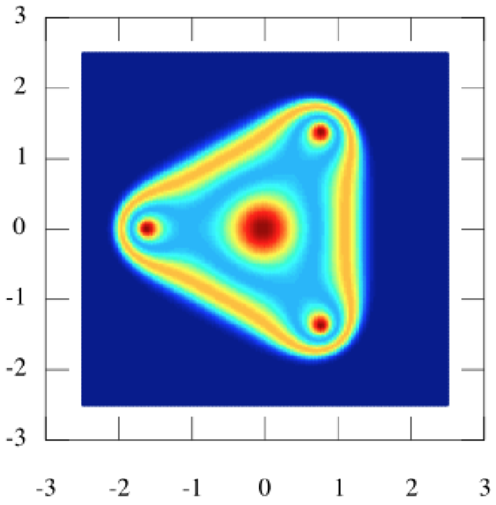

FIGURE 8.4: Sum of the squared moduli of the eigenfunction ψ_{20}, ψ_{11} and ψ_{02}. One can observe that the function obtained is invariant by the operation of the D_3' according to the generalized Unsöld theorem.

With g the order of the symmetry group, l_j the dimension of the j-th irreducible representation and R a group operation according to the notation of chapter 1. For D_3', all the representations, except E and E', are one dimensional and the projector are easily obtained using the character table 8.26.

$$\mathcal{P}_{A_1} = \frac{1}{6}\Big(P_E + P_{C_3} + P_{C_{-3}} + P_{C_2'(1)} + P_{C_2'(2)} + P_{C_2'(3)}\Big) \tag{8.37}$$

$$\mathcal{P}_{A_2} = \frac{1}{6}\Big(P_E + P_{C_3} + P_{C_{-3}} - P_{C_2'(1)} - P_{C_2'(2)} - P_{C_2'(3)}\Big) \tag{8.38}$$

Where we have not included the primed operations of the group since we are interested in the projection of D_1 over A_2 and E. It is again an interesting feature of the double group D_3' that integer representation of SU(2) are projected and affected only by the unprimed representation of D_3' and that the half-integer ones follow the primed ones.

In order to connect this section with experiments, figure 8.5 shows measurements on aluminum nanotriangles using Electron Energy Loss Spectroscopy (EELS) made by J. Martin [105] in the LNIO. This technique accesses to maps tightly connected to the LDOS projected along the z axis. By varying the beam energy, various modes appears having shapes clearly belonging to irreducible representation of D_3. As can be seen, the shape of the intensity maps obtained by this technique strongly suggests that the eigenmodes of the nanotriangles behave like irreducible representation of the group D_3.

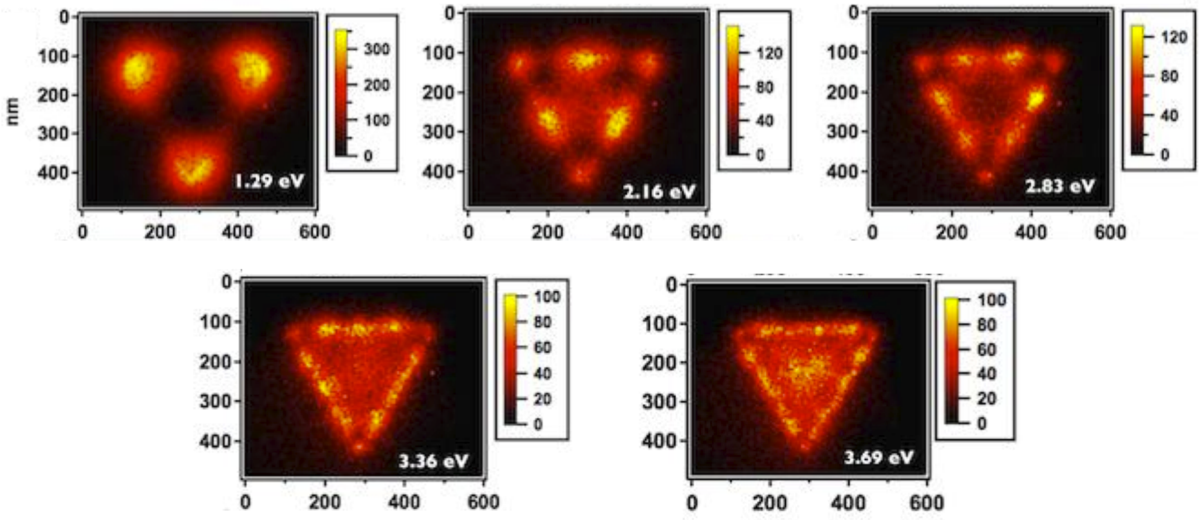

FIGURE 8.5: EELS intensity maps obtained on aluminium nanotriangles by J. Martin[105].

8.2 Preliminary results on nanoparticles

In this section, preliminary results of time domain experiments on nanoparticles with symmetry D_3 are presented.

8.2.1 Experiment

The experimental setup used in this experiment is the one displayed in figure 7.3. However, this setup is well suited for solutions and the use of lithographed nanoparticles as a sample is not possible with this configuration. Thus, chemical synthesis were used to obtained nanoprisms following straightforwardly the protocol published by Yin's group [70]. In this protocol, 24.24 mL of distilled water was mixed and stirred with a solution of silver nitrate (0.05M, 50 μL), disodium citramalate (75 mM, 0.5 mL), PVP ($M_w \approx$ 25000g/mol, 17.5 mM, 0.1 mL) and hydrogen peroxide (10 wt. %, 60 μL) at room temperature. Sodium borohydride (100mM, 50 μL) was then injected in the mixture and the nanoprisms where obtained after letting the growth occurring.

Moreover, other colloidal solutions of nanoprisms, with less size-dispersion, were also provided by the Xue Can's group (NTU - MSE) following their pH-switchable fabrication protocol to produce nano-prisms [106]

Pump-probe spectroscopy were achieved on the colloidal solution of nanoprism synthesized by the author and by Xue Can's group with no major variations. The reader is referred to the previous chapter for detailed informations on the setup. The OPA was tuned in order to deliver an excitation centered at 650 nm. One can see that the center of the main peak is positioned at 700 nm rather than 650 nm but the choice of an excitation has been chosen for convenience. The lineshape of the peak is broad enough to be excited in a large spectral band and, since LHCII requires an excitation wavelength centered at 650 nm, both sets of experiment can be done with minor modifications of the setup. The Dazzler was not taken out of the beam but was simply programmed to block pulses, acting as a simple chopper for the pump-light. Both pump and probe light were polarized parallel to the optical table.

8.2.2 Results

The pump-probe signal acquired is displayed in figure 8.6 for every probing wavelength λ. One can observe that, although the excitation wavelength is 650 nm (bandwidth of $\approx$14 nm), a pump-probe signal is obtained for a large bandwidth, all over the spectral range of the probe light.

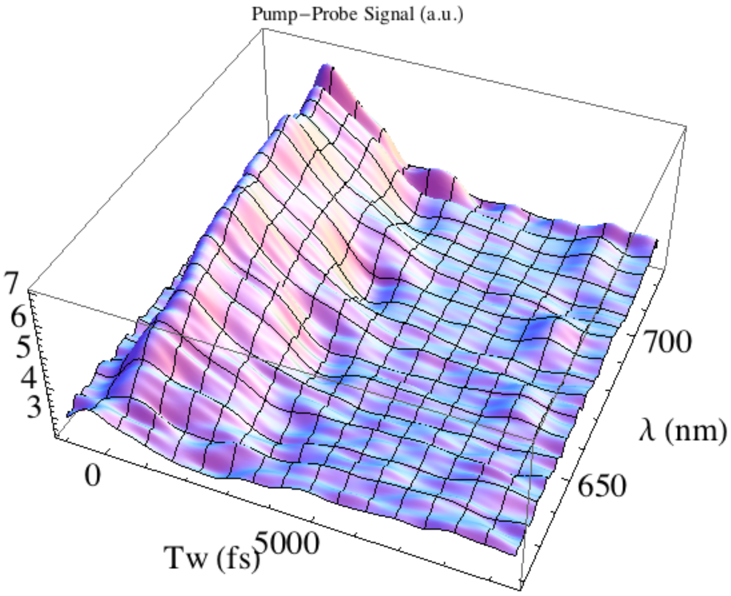

FIGURE 8.6: Pump-Probe signal of a colloidal solution of nanoprisms. The pump is centered around 650 nm and has a duration of 55 fs (1.15 Fourier-transform limited) and the probe is a broadband white light.

A specific pump-probe trace corresponding to $\lambda_{\text{pump}} = 650$ nm and $\lambda_{\text{probe}} = 650$ nm is displayed in figure 8.7. A simple decaying exponential fit has been used on the data giving a lifetime of 2 017 fs (95 % confidence interval : 1708 - 2326 fs).

The coherent oscillation inside the nanoparticle is driven by the excitation provided by the ultrashort pulse which duration is about 50 fs. After the pump is gone, the plasmon starts to dephase quickly with a much faster lifetime than the one measured here. As an example Utikal [107, 108] obtains a decay time of 10 fs due to electron-electron scattering. The microscopic mechanisms underlying this decay are still under

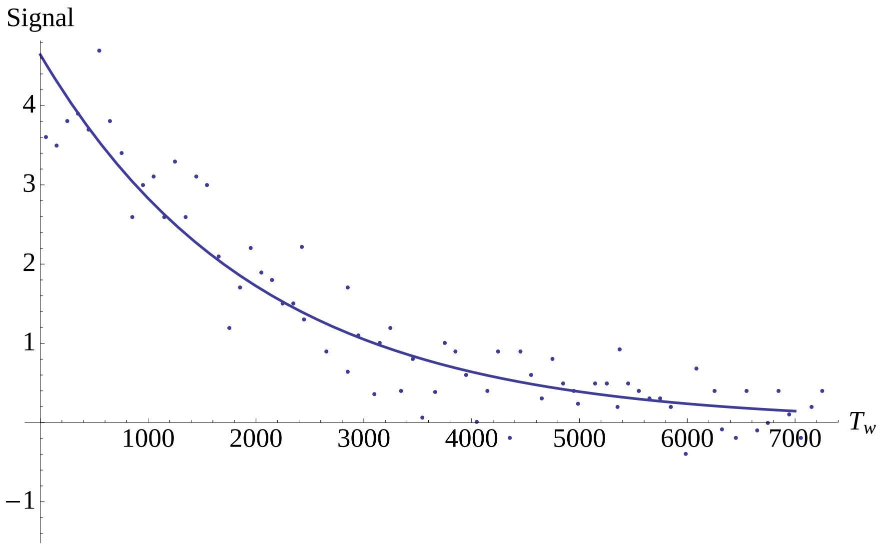

FIGURE 8.7: Extraction of pump-probe trace at 650 nm. The decaying pump-probe signal is fitted by a simple exponential decay, giving a lifetime of 2 ps.

investigation and depend in many parameters like the shape, the size, the material and the surrounding environment. The plasmon could decay by pure dephasing[109] due to local inhomogeneities in the nanoparticle or a loss of the collective mode because of the various phase velocities. It could also be due to an energy transfer to an electron-hole pair. This coherent oscillation is inaccessible in this experiment due to its very short timescale and would then require much shorter pulses.

The physical phenomena corresponding to a lifetime of ≈ 2 ps and measured in this experiment has been assigned to the relaxation of nonthermalized "hot" electrons[110]. However, this time dependence is also highly shape-dependent and the inhomogeneous broadening present in the experiment inevitably blurry the informations for the pump-probe in figure 8.7. To solve this problem, Spatial Modulation Spectroscopy (SMS) has been proposed in the literature [111, 112] to detect the signal from single nanoparticle by modulating its position in the focal point of the excitation light. Combined with the pump-probe setup used in this thesis, it could be used to study relaxation of the electron cloud. Although the state oscillating coherently with the incoming field has been lost at this stage, the "hot" electron cloud is most likely in a geometrical eigenmode according to previous discussions. Thus, 2DES could provide a way to inspect this conjecture and study the behavior of those modes.

By combining knowledge of the spectral features and of the geometric eigenmodes, it would be greatly fruitful to end in the construction of some kind of spectroscopic table relating the eigenmodes and their properties (energy, lifetime...) to their irreducible representations in the finite group.

Conclusion

Metallic nanoparticles offer a wide range of promising fundamental and applied developments. As the collective excitation of the electron cloud generating LSPR can be easily excited in the visible range for such particles, their optical properties are of great interests. Moreover, those properties can be finely tuned using different shapes and materials. Adding the ability to couple those elementary bricks together or with various other structures, one is virtually left with an infinite number of possible structures. However, a deep understanding of the behavior of the nanoparticles under linear and nonlinear excitations is still required. While a great effort has already been realized by the community, this work had for objective to highlight the importance of the nanoparticles' symmetries and to obtain as much information as possible from it.

The most natural way to introduce symmetry considerations in nonlinear optics is through group theory and particularly irreducible representation theory. The use of irreducible tensors allows one to rewrite nonlinear optics with a fully irreducible formalism which is the main result of this work. This formalism permits to greatly simplify the description of the nonlinear polarization of a nanoparticle by gathering all the spatial dependence of the response tensor in a finite number of coefficients. Indeed, instead of taking into account the value of the exciting fields and the resulting current at each point of space, those fields are expanded in discrete number of multipolar fields. The link between the irreducible currents and the irreducible components of the exciting field is the irreducible response tensor. This approach should not be mistaken for a T-matrix one that is deeply a numerical method by essence while the irreducible tensor formalism is rooted in analytical development and the creation of models within it.

To demonstrate the viability of the formalism, it has been applied to the description of nonlinear optical experiments, especially polarization-resolved SHG experiments done on threefold symmetry gold nanoparticles. The high susceptibilities of those nanoparticles has been linked to the emergence of higher multipolar current densities as the size of the nanoparticles increase. Nanoparticles need to be big enough in order to have non-negligible multipolar contributions and still small enough so the plasmonic resonance still falls in the visible range. The model chosen within the fully irreducible formalism is a simple one that describes correctly only almost perfect stars. Within the irreducible formalism, it would then be interesting to introduce imperfections like the ones used in the fitting models in chapter 3 or like rugosity. Vanishing elements of the response tensor in the perfect case would no longer be zero and linking them with the shape of the stars under consideration could permit to quantify deviations acceptable from perfection that conserve the strong nonlinear resonances of nanostars. The modeling procedure presented in this work could also be greatly improved by introducing a more realistic description of the incident electromagnetic field like a gaussian beam and its associated multipolar expansion.

The use of more complex beam shapes could in fact lead to a better ability to separately address the components of the irreducible response tensor. Higher order modes, like Laguerre-Gauss modes, carry a specific angular momentum and would allow to address specific irreducible components of the response tensor, whereas the plane wave used in this thesis to reconstruct the response tensor is not sufficient to distinguish those components without using an already stringent model. However, a polarization-resolved experiment already permitted to extract useful information.

This polarization-resolved experiment could fruitfully be extended to the time-domain, as proposed in chapter 8, by looking at the polarization dependence of the pump-probe signal. However, two main drawbacks have to be addressed in order to pursue work in that direction. The pump-probe experiment has to be able to collect the signal from a single nanoparticle, rather than an ensemble in solution, that requires to include a microscope setup. Otherwise, the signal is averaged over the different directions that the nanoparticles have in the colloidal solution and it is necessary to include the possible reorientation of the particles during the waiting time. This microscope system would make the non collinear crossing between the pump and the probe difficult to achieve in the experiment and then a fully collinear pump-probe should be done. This brings the second difficulty of extracting the pump-probe signal in a collinear setup since the powerful pump beam will be on top of it. An appropriate phase-cycling scheme or a spatial modulation method could perhaps be proposed to reach that goal. Two-dimensional electronic spectroscopy is also a good candidate to study spectral properties of nanoparticles and disentangle the possible couplings between the eigenmodes.

The ultimate goal of the spectral and spatial approaches is to make them converge toward an unified treatment. Then, one could expect to be able to obtain information about the spectral properties from the spatial ones. The components of the irreducible response tensors have so far been obtained by linking the measured current density to the known incoming electric fields. This current density can also be viewed as a consequence of the oscillation of the plasmon modes inside the nanoparticle. Computing those modes could be simplified by using symmetry properties and their eigenvalues would give spectral information. Then, since those modes belong to irreducible representations of the finite group of the nanoparticle, they can be projected onto the representations of SO(3) , e. g. the multipolar fields.

Appendix A

Useful relationships

This appendix recapitulates the main formulae used in this work obtained from the literature[31, 113].

A.1 Special functions

A.1.1 Bessel functions

- Definition of the Bessel and Hankel functions

$$\begin{aligned} J_n(z) &= \Big(\frac{1}{2}z\Big)^n \sum_k \frac{\big(-\frac{1}{4}z^2\big)^k}{k!\ \Gamma(n+k+1)} && \text{(A.1)} \\ Y_n(z) &= \frac{J_n(z)\cos n\pi - J_{-n}(z)}{\sin n\pi} && \text{(A.2)} \\ H_n^{(1)}(z) &= J_n(z) + iY_n(z) && \text{(A.3)} \\ H_n^{(2)}(z) &= J_n(z) - iY_n(z) && \text{(A.4)} \end{aligned}$$

- Definition of the spherical Bessel and Hankel functions

$$\begin{aligned} j_n(z) &= \sqrt{\frac{\pi}{2z}} J_{n+\frac{1}{2}}(z) && \text{(A.5)} \\ y_n(z) &= \sqrt{\frac{\pi}{2z}} Y_{n+\frac{1}{2}}(z) && \text{(A.6)} \\ h_n^{(1)}(z) &= j_n(z) + iy_n(z) && \text{(A.7)} \\ h_n^{(2)}(z) &= j_n(z) - iy_n(z) && \text{(A.8)} \end{aligned}$$

- Integral definition :

$$J_n(z) \;=\; \frac{i^{-n}}{\pi}\int_0^{\pi} e^{iz\cos\theta}\cos n\theta d\theta \tag{A.9}$$

- Limits :

$$j_n(z) \;\underset{z\ll 1}{\longrightarrow}\; \frac{z^n}{(2n+1)!!} \tag{A.10}$$

$$h_n^{(1)}(z) \;\underset{z\gg n}{\longrightarrow}\; (-i)^{n+1}\frac{e^{iz}}{z} \tag{A.11}$$

A.2 Angular momentum

A.2.1 Spherical harmonics

- Explicit form :

$$Y_{lm}(\theta,\varphi) = \sqrt{\frac{2l+1}{4\pi}\frac{(l-m)!}{(l+m)!}}\; P_l^m(\cos\theta)\; e^{im\varphi} \tag{A.12}$$

- Angular momentum operators :

$$[L_\mu,\; Y_{lm}] \;=\; \sqrt{l(l+1)}C_{lm1\mu}^{lm+\mu}Y_{lm+\mu} \tag{A.13}$$

$$L^2Y_{lm} \;=\; l(l+1)\; Y_{lm} \tag{A.14}$$

- Condon and Shortley phase choice :

$$Y_{l0}(0,0) = \sqrt{\frac{2l+1}{4\pi}} \Longrightarrow Y_{lm}^{*} = (-1)^m Y_{l-m} \tag{A.15}$$

- Rotation :

$$R(\theta,\varphi,\psi)\; Y_{lm} = \sum_{m'=-l}^{l} D_{m'm}^{(l)}(\theta,\varphi,\psi)\; Y_{lm'} \tag{A.16}$$

A.2.2 Vector spherical harmonics and multipolar fields

- Definition of the vector spherical harmonics :

$$\underline{Y}_l^{JM} = \{Y^l \otimes e^{S=1}\}^{JM} = \sum_{m\sigma} C_{lm1\sigma}^{JM} Y_{lm}\; e_\sigma \tag{A.17}$$

$$\underline{\Psi}_l^{JM} = j_l\; \underline{Y}_l^{JM} \tag{A.18}$$

- Equivalent definition :

$$\underline{Y}_J^{JM} = \frac{\vec{L}\,Y_{JM}}{\sqrt{J(J+1)}} \tag{A.19}$$

$$\underline{Y}_{J-1}^{JM} = -\frac{1}{\sqrt{J(2J+1)}}(-J\vec{n} + i\vec{n} \wedge \vec{L})Y_{JM} \tag{A.20}$$

$$\underline{Y}_{J+1}^{JM} = -\frac{1}{\sqrt{(J+1)(2J+1)}}((J+1)\vec{n} + i\vec{n} \wedge \vec{L})Y_{JM} \tag{A.21}$$

- Definition of the vector multipolar fields :

$$\underline{\Psi}_m^{JM} = \underline{\Psi}_J^{JM} \tag{A.22}$$

$$\underline{\Psi}_e^{JM} = \sqrt{\frac{J+1}{2J+1}}\underline{\Psi}_{J-1}^{JM} - \sqrt{\frac{J}{2J+1}}\underline{\Psi}_{J+1}^{JM} \tag{A.23}$$

$$\underline{\Psi}_l^{JM} = \sqrt{\frac{J}{2J+1}}\underline{\Psi}_{J-1}^{JM} + \sqrt{\frac{J+1}{2J+1}}\underline{\Psi}_{J+1}^{JM} \tag{A.24}$$

- Curl and divergence of the vector multipolar fields :

$$\nabla \wedge \underline{\Psi}_e^{JM} = -ik\underline{\Psi}_m^{JM} \qquad \nabla \cdot \underline{\Psi}_e^{JM} = 0 \tag{A.25}$$

$$\nabla \wedge \underline{\Psi}_m^{JM} = ik\underline{\Psi}_e^{JM} \qquad \nabla \cdot \underline{\Psi}_m^{JM} = 0 \tag{A.26}$$

$$\nabla \wedge \underline{\Psi}_l^{JM} = 0 \qquad \nabla \cdot \underline{\Psi}_l^{JM} = -k\Psi_{JM} \tag{A.27}$$

Appendix B

Links between different notations

In this appendix, vector spherical harmonics defined by others authors are presented with their link to the ones defined in this work.

- Blatt and Weisskopf[114], Rose [115] :

$$\mathbf{T}_{J1}^{M} = (-1)^{J}\underline{Y}_{e}^{JM} \tag{B.1}$$

$$\mathbf{T}_{J0}^{M} = (-1)^{J-1}\underline{Y}_{m}^{JM} \tag{B.2}$$

$$\mathbf{T}_{J-1}^{M} = (-1)^{J}\underline{Y}_{l}^{JM} \tag{B.3}$$

- Jackson [21] :

$$\mathbf{X}_{JM} = \underline{Y}_{J}^{JM} \tag{B.4}$$

- Mie theory :

$$\underline{M}_{JM} = i(-1)^{M}\sqrt{4\pi\frac{J(J+1)}{2J+1}\frac{(J+M)!}{(J-M)!}}\, f_l\ \underline{Y}_{J}^{JM} \tag{B.5}$$

$$\underline{M}_{JM}^{*} = i\sqrt{4\pi\frac{J(J+1)}{2J+1}\frac{(J+M)!}{(J-M)!}}\, f_l\ \underline{Y}_{J}^{J-M} \tag{B.6}$$

Appendix C

Multipolar PSF functions

C.1 Dipolar PSF functions

$$g_{d1}\left(r,\,z\right) = \int_0^{\theta_m}\left(\frac{\cos\theta}{\cos\theta'}\right)^{\frac{3}{2}}\left(1+\cos\theta\cos\theta'\right)\mathrm{J}_0\;e^{ik'z\cos\theta'}\sin\theta d\theta \tag{C.1}$$

$$g_{d2}\left(r,\,z\right) = \int_0^{\theta_m}\left(\frac{\cos\theta}{\cos\theta'}\right)^{\frac{3}{2}}\sin\theta\cos\theta'\,\mathrm{J}_1\;e^{ik'z\cos\theta'}\sin\theta d\theta \tag{C.2}$$

$$g_{d3}\left(r,\,z\right) = \int_0^{\theta_m}\left(\frac{\cos\theta}{\cos\theta'}\right)^{\frac{3}{2}}\left(1-\cos\theta\cos\theta'\right)\mathrm{J}_2\;e^{ik'z\cos\theta'}\sin\theta d\theta \tag{C.3}$$

$$g_{d4}\left(r,\,z\right) = \int_0^{\theta_m}\left(\frac{\cos\theta}{\cos\theta'}\right)^{\frac{3}{2}}\cos\theta\sin\theta'\,\mathrm{J}_1\;e^{ik'z\cos\theta'}\sin\theta d\theta \tag{C.4}$$

$$g_{d5}\left(r,\,z\right) = \int_0^{\theta_m}\left(\frac{\cos\theta}{\cos\theta'}\right)^{\frac{3}{2}}\sin\theta\sin\theta'\,\mathrm{J}_0\;e^{ik'z\cos\theta'}\;\sin\theta d\theta \tag{C.5}$$

C.2 Quadrupolar PSF functions

$$g_{q1}(r,z) = \int_0^{\theta_m}\left(\frac{\cos\theta}{\cos\theta'}\right)^{\frac{3}{2}}(1+\cos\theta\cos\theta')\sin\theta J_1e^{ik'z\cos\theta'}\sin\theta d\theta \tag{C.6}$$

$$g_{q2}(r,z) = \int_0^{\theta_m}\left(\frac{\cos\theta}{\cos\theta'}\right)^{\frac{3}{2}}(1-\cos\theta\cos\theta')\sin\theta J_3e^{ik'z\cos\theta'}\sin\theta d\theta \tag{C.7}$$

$$g_{q3}(r,z) = \int_0^{\theta_m}\left(\frac{\cos\theta}{\cos\theta'}\right)^{\frac{3}{2}}\sin 2\theta\sin\theta' J_2e^{ik'z\cos\theta'}\sin\theta d\theta \tag{C.8}$$

$$g_{q4}(r,z) = \int_0^{\theta_m}\left(\frac{\cos\theta}{\cos\theta'}\right)^{\frac{3}{2}}(\cos\theta+\cos 2\theta\cos\theta')J_0e^{ik'z\cos\theta'}\sin\theta d\theta \tag{C.9}$$

$$g_{q5}(r,z) = \int_0^{\theta_m} \left(\frac{\cos\theta}{\cos\theta'}\right)^{\frac{3}{2}} (\cos\theta - \cos 2\theta\cos\theta') J_2 e^{ik'z\cos\theta'} \sin\theta d\theta \tag{C.10}$$

$$g_{q6}(r,z) = \int_0^{\theta_m} \left(\frac{\cos\theta}{\cos\theta'}\right)^{\frac{3}{2}} \cos 2\theta \sin\theta' J_1 e^{ik'z\cos\theta'} \sin\theta d\theta \tag{C.11}$$

$$g_{q7}(r,z) = \int_0^{\theta_m} \left(\frac{\cos\theta}{\cos\theta'}\right)^{\frac{3}{2}} \sin 2\theta \cos\theta' J_1 e^{ik'z\cos\theta'} \sin\theta d\theta \tag{C.12}$$

$$g_{q8}(r,z) = \int_0^{\theta_m} \left(\frac{\cos\theta}{\cos\theta'}\right)^{\frac{3}{2}} \sin 2\theta \sin\theta' J_0 e^{ik'z\cos\theta'} \sin\theta d\theta \tag{C.13}$$

C.3 Octupolar PSF functions

$$g_{o1}(r,z) = \int_0^{\theta_m} \left(\frac{\cos\theta}{\cos\theta'}\right)^{\frac{3}{2}} (1 + \cos\theta\cos\theta') \sin\theta J_2 \sin\theta^2 e^{ik'z\cos\theta'} \sin\theta d\theta \tag{C.14}$$

$$g_{o2}(r,z) = \int_0^{\theta_m} \left(\frac{\cos\theta}{\cos\theta'}\right)^{\frac{3}{2}} (1 - \cos\theta\cos\theta') \sin\theta J_4 \sin\theta^2 e^{ik'z\cos\theta'} \sin\theta d\theta \tag{C.15}$$

$$g_{o3}(r,z) = \int_0^{\theta_m} \left(\frac{\cos\theta}{\cos\theta'}\right)^{\frac{3}{2}} \cos\theta \sin\theta' J_3 \sin\theta^2 e^{ik'z\cos\theta'} \sin\theta d\theta \tag{C.16}$$

$$g_{o4}(r,z) = \int_0^{\theta_m} \left(\frac{\cos\theta}{\cos\theta'}\right)^{\frac{3}{2}} (4\sin 2\theta - \cos\theta'(\sin\theta - 3\sin 3\theta)) J_1 e^{ik'z\cos\theta'} \sin\theta d\theta \tag{C.17}$$

$$g_{o5}(r,z) = \int_0^{\theta_m} \left(\frac{\cos\theta}{\cos\theta'}\right)^{\frac{3}{2}} (4\sin 2\theta + \cos\theta'(\sin\theta - 3\sin 3\theta)) J_3 e^{ik'z\cos\theta'} \sin\theta d\theta \tag{C.18}$$

$$g_{o6}(r,z) = \int_0^{\theta_m} \left(\frac{\cos\theta}{\cos\theta'}\right)^{\frac{3}{2}} (1 + 3\cos 2\theta) \sin\theta \sin\theta' J_2 e^{ik'z\cos\theta'} \sin\theta d\theta \tag{C.19}$$

$$g_{o7}(r,z) = \int_0^{\theta_m} \left(\frac{\cos\theta}{\cos\theta'}\right)^{\frac{3}{2}} (6 + 10\cos 2\theta + \cos\theta'(\cos\theta + 15\cos 3\theta)) J_0 e^{ik'z\cos\theta'} \sin\theta d\theta \tag{C.20}$$

$$g_{o8}(r,z) = \int_0^{\theta_m} \left(\frac{\cos\theta}{\cos\theta'}\right)^{\frac{3}{2}} (6 + 10\cos 2\theta - \cos\theta'(\cos\theta + 15\cos 3\theta)) J_2 e^{ik'z\cos\theta'} \sin\theta d\theta \tag{C.21}$$

$$g_{o9}(r,z) = \int_0^{\theta_m} \left(\frac{\cos\theta}{\cos\theta'}\right)^{\frac{3}{2}} (7 - 15\cos 2\theta)\cos\theta \sin\theta' J_1 e^{ik'z\cos\theta'} \sin\theta d\theta \quad \text{(C.22)}$$

$$g_{o10}(r,z) = \int_0^{\theta_m} \left(\frac{\cos\theta}{\cos\theta'}\right)^{\frac{3}{2}} (3 + 5\cos 2\theta)\cos\theta' \sin\theta J_1 e^{ik'z\cos\theta'} \sin\theta d\theta \quad \text{(C.23)}$$

$$g_{o11}(r,z) = \int_0^{\theta_m} \left(\frac{\cos\theta}{\cos\theta'}\right)^{\frac{3}{2}} (3 + 5\cos 2\theta)\sin\theta' \sin\theta J_0 e^{ik'z\cos\theta'} \sin\theta d\theta \quad \text{(C.24)}$$

Appendix D

Coupled systems of nanoparticles for SERS and SEIRA

The goal of this appendix is to propose a first step in the design of a nanostructured surface that can be used in SERS and SEIRA. To achieve this, the bidimensional metal lattice has to be resonant in both infrared and visible. In this part, we use a simple model to show the feasibility of such structure : we will assume that the surface absorption around a wavelength is proportional to the eigenvalue number and we will use a scalar model.

D.1 Nanowire

In this section, we present a simple model to expression the limitation induced by nanowires used as nanoantenna. We use a scalar model to describe electromagnetic resonance for simplification purpose. Each nanowire is assumed to be coupled with its two nearest neighbor. This one dimensional is represented in figure D.1.

Figure D.1: Nanowires chain. Each wire resonate at ω and the coupling factor between two wires is Ω.

Thus, a matrix describing the resonance of nanowires could be written as :

$$\begin{pmatrix} \omega & \Omega & 0 & 0 & 0 \\ \Omega & \omega & \Omega & 0 & 0 \\ 0 & \ddots & \ddots & \ddots & 0 \\ 0 & 0 & \Omega & \omega & \Omega \\ 0 & 0 & 0 & \Omega & \omega \end{pmatrix} \tag{D.1}$$

If one would consider an infinite chain of nanowire, it is possible to loop the first and the last element of this matrix.

This matrix eigenmodes correspond to resonance wavelength. For exemple, for a matrix describing 1000 nanowires, the list of eigenvalues obtained is plotted on figure D.2. We have chosen $\omega = 2$ eV and $\Omega = 0.5$ eV.

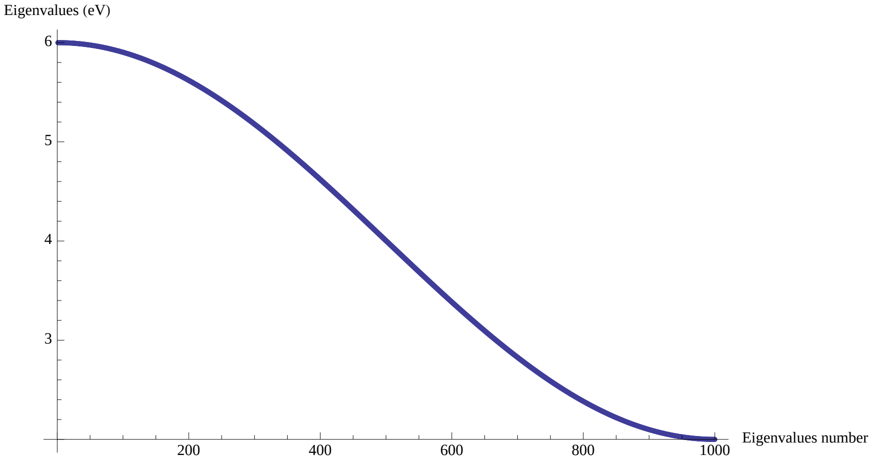

Figure D.2: Nanowires chain eigenvalues.

The curve D.2 is rather smooth : this does not allow high resonances. Because we consider the resonance to be proportional to the eigenvalues density, it gives clearer informations to plot the eigenvalues number against frequencies intervals as in figure D.3. The resonance seems very flat except on the edges of the graph : an important number of modes are localized at the extremal frequencies. These modes corresponds to non-physical ones since a very low gaussian noise ($\omega\pm$ noise, $\Omega\pm$ noise) removes them. This means that these modes correspond to perfectly collective behavior of the nanowires assembly and can not exist in a real system.

When a gaussian noise is added, two pikes still appear but the curve is too flat to obtain interesting resonance. This very simple example showed that nanowires does not seem to be suitable for multi-wavelength resonator.

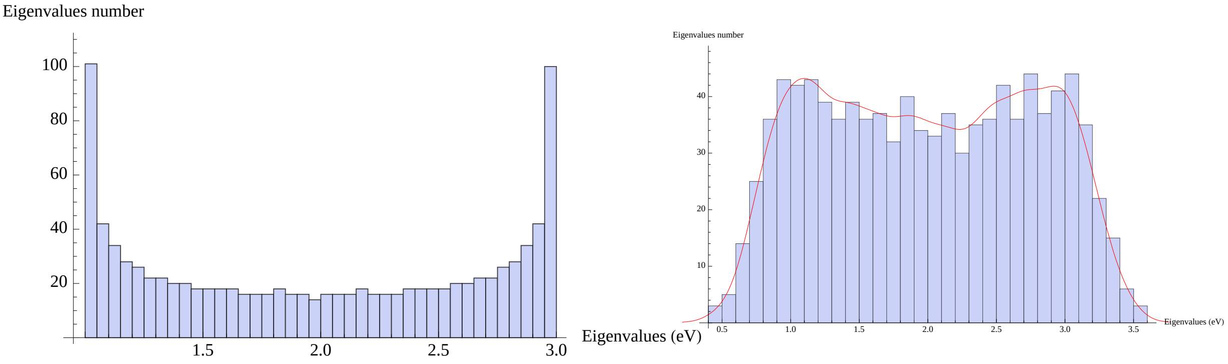

FIGURE D.3: Nanowires chain eigenvalues number density. $\omega = 2$ eV, $\Omega = 0.5$ eV. Left : 1000 nanowires with no gaussian. Right : 1000 nanowires with a low gaussian noise. noise $\sim 1/10\ \Omega$.

D.2 Array of nanostars

D.2.1 Objectives

We are now going to apply the same procedure to a gold nanostar lattice. We want to show that these objects offer a peculiar behavior in linear and non-linear optics. One of these nanoparticles is represented in figure D.4. Thanks to their shape, it is possible to construct an hexagonal lattice which is a two dimensional lattice. We want to show that an array of these particles exhibits two distinct resonances and so are suitable to design IR-visible resonator.

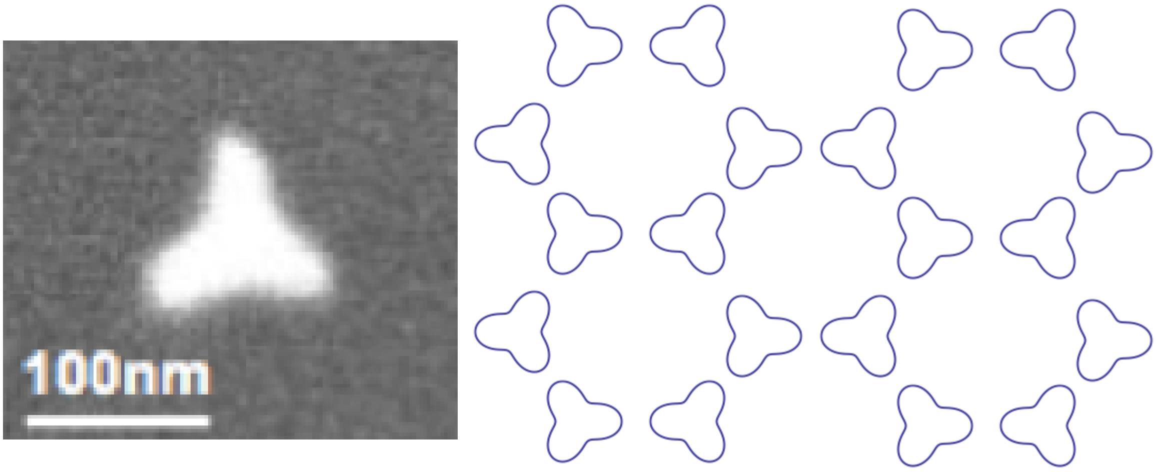

FIGURE D.4: Left : Gold nanostar. Right : hexagonal lattice made form nanostar.

D.2.2 Scalar Model : matrix formulation

We are interested in the eigenvalues density for the nanoparticles hexagonal lattice. The hexagonal lattice's unit cell is depicted in figure D.5 and is used to fill the whole plane. Each nanoparticle is linked with three neighbors by a coupling factor Ω (less than one eV). We can consider a finite assembly of nanoparticles as represented in the right part of figure D.5. Like in the previous section, we are looking for the eigenvalues of such a coupling matrix. Alternatively, an infinite lattice can be modeled with a finite matrix by coupling the edges with a dephasing factor. This is similar to Bloch functions dephasing in a periodic lattice. In that case, the coupling matrix is no longer real but hermitian.

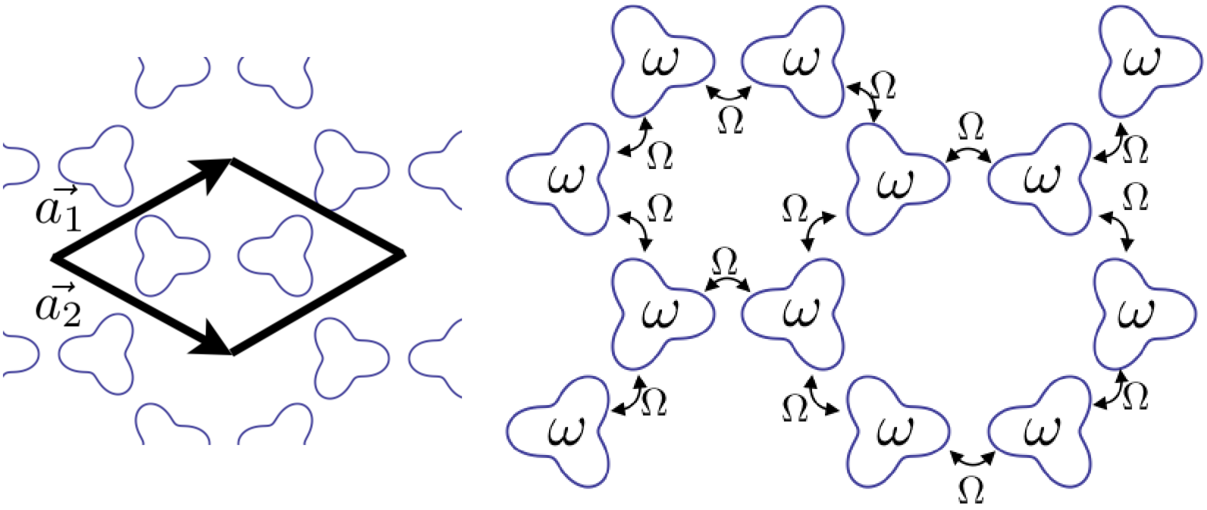

FIGURE D.5: Construction of the periodic lattice of gold nanoparticles. Left : Unit cell in a graphen like lattice. Right : Coupling occuring for 12 nanoparticles : each particle is coupled with its three neighbors.

The code to write the coupling matrix for an arbitrary number of nanoparticles is given in appendix.

D.2.3 Results

The coupling matrix eigenvalue problem is solved numerically and the frequency dependent eigenvalues density is plotted. We will consider different values for Ω, ω, ϕ and Ψ.. A new behavior appears with nanostars eigenvalues plot : a "forbidden band" appears near ω. This phenomena leads to two pikes at $\omega + \Omega$ and $\omega - \Omega$ and, thus, to a multi-wavelength resonator.

The figure D.6 corresponds to $\phi = \frac{2\pi}{3}$ and $\Psi = \frac{4\pi}{3}$. The values of ω and Ω are $\omega = 1.2$ eV, $\Omega = 0.4$ eV in order to obtain resonances in visible and infrared (775 nm and 1551 nm). If one increases Ω, it will appear negative eigenvalues : resonances can not be further appart than $\omega - \frac{\omega}{3}$ and $\omega + \frac{\omega}{3}$.

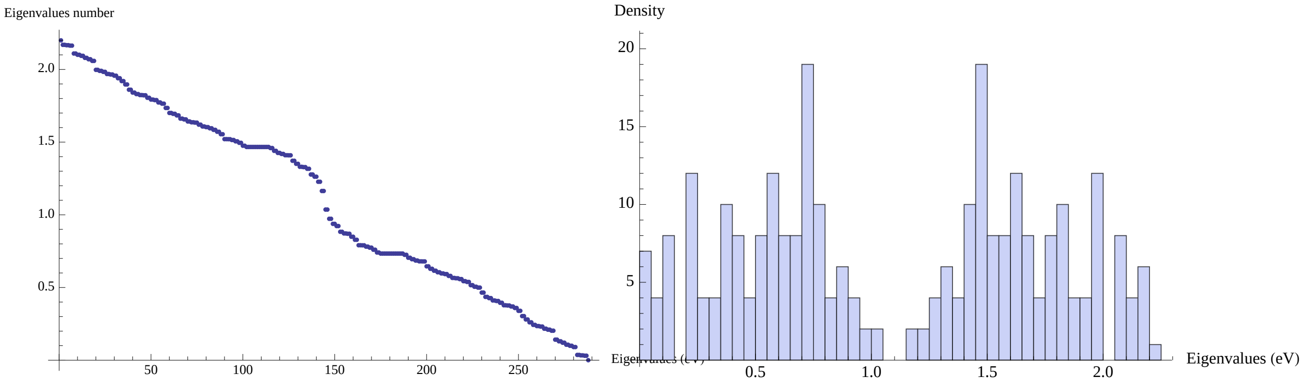

FIGURE D.6: Left : Nanostars lattice eigenvalues. Right : Nanostars lattice eigenvalues number density. Two resonances are observed at 0.8 eV and 1.6 eV.

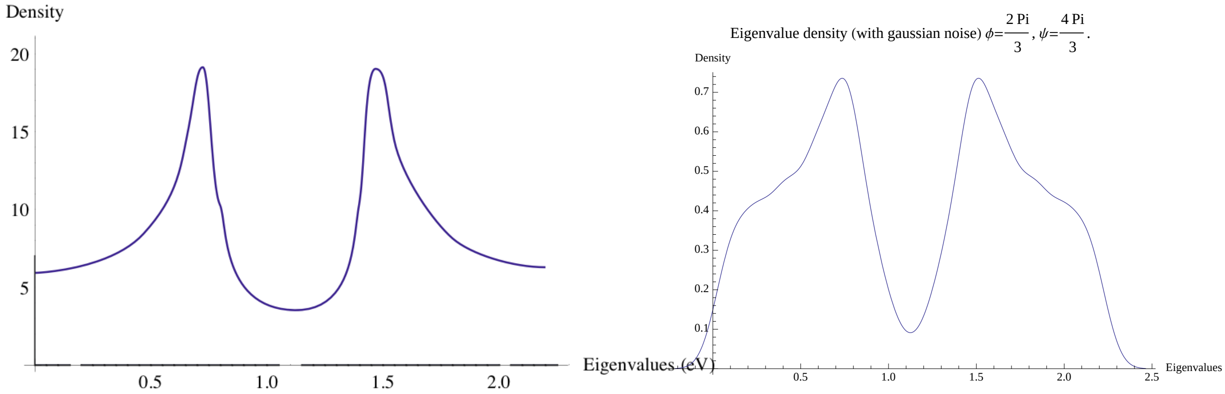

FIGURE D.7: Left : Eigenvalues density without noise. Right : Eigenvalues density with a gaussian noise. The resonance peaks are still important and are not translated.

We want our model to be robust : when a gaussian noise is included, the behavior of the response is almost the same. The normalized eigenvalue density is plotted in figure The right part of the graph has been made using five random noise iterations and taking the average over them.

We are also interested to see how the eigenmodes are represented on the lattice. For a better understanding, we represent the eigenvectors components on the lattice. A disk is represented on each nanoparticle with a radius and color corresponding respectively to the amplitude and the phase. The figure D.8 gives the first eigenmode for a 288 nanoparticles cell on an infinite lattice. One can see that the components of an eigenvector have all the same value. This is consistent with the fact all the particles are the same in an infinite lattice.

Because the lattice is infinite, the modes have to be periodic and we can observe it by juxtaposing lattice cell as the left part of figure D.8 and taking account of the dephasing factor we have chosen to calculate the eigenmodes. Indeed, figure D.8 also shows this periodicity of the modes on the lattice.

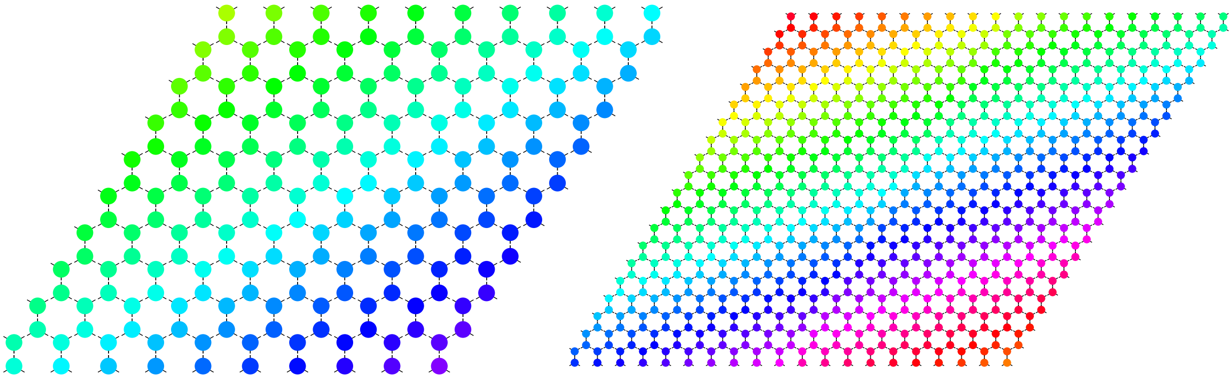

FIGURE D.8: Left : First eigenvector on a nanoparticle's hexagonal lattice ($\phi = \frac{\pi}{3}$, and $\psi = \frac{\pi}{4}$). Right :Same eigenvector on a bigger part of the lattice.

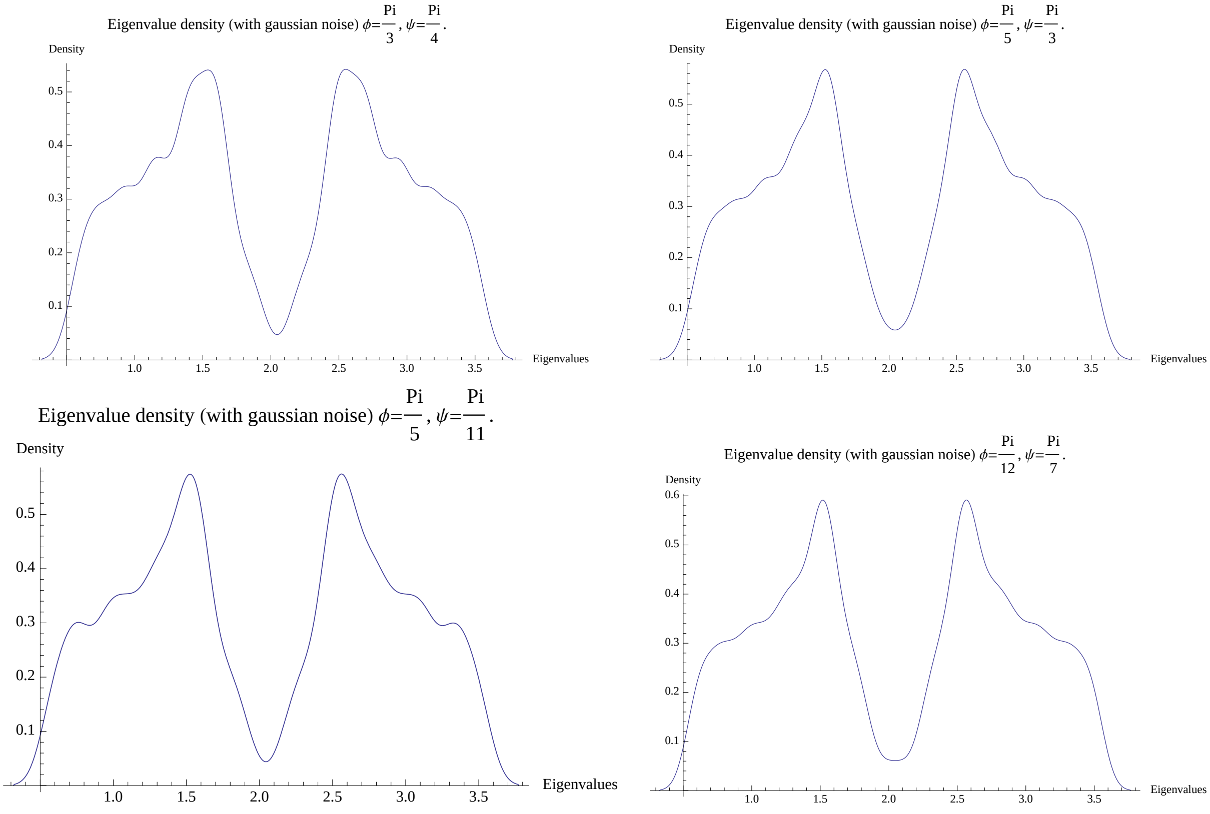

TABLE D.1: Eigenvalues density with gaussian noise for different dephasing angles values.

The Table D.1 shows the dependance in dephasing angles. Here ω and Ω has been chosen to ensure there is no negative eigenvalues, $\omega = 2$ eV and $\Omega = 0.5$ eV. The figures in Table D.1 show that the gap position does not depend on ϕ and Ψ. As ϕ and Ψ decrease, the resonances seem to be slightly sharper.

This model is a highly simplified representation of coupled systems. However, coupling is a very general feature in physical phenomena and deep understanding is not always necessary to have an overview of it. For example, in the present case, both the resonances of single units and the coupling strengths between them is taken as a given value and adjusted to correspond to data measured. In fact, the resonance of a single nanoparticle is a complicated function of its shape and its material while the coupling strength depends on the gap size chosen.

To investigate the hypothesis of this appendix, lattices as the one displayed in figure D.9 has been made by e-beam lithography and sent to Paris in the group of M. Lamy de la Chapelle where extinction measurements has been carried out. Even if those results have to be taken cautiously, the lattices seem to exhibit two resonances in the IR and in the visible as desired. Unfortunately, e-beam lithography is a money and time consuming fabrication process that does not fit with the applied goal of such systems. Thus, a PhD thesis by J. Ibrahim focuses on the development of an efficient fabrication process using interferometric lithography and will achieve a new step in the achievement of multi wavelength SERS substrate.

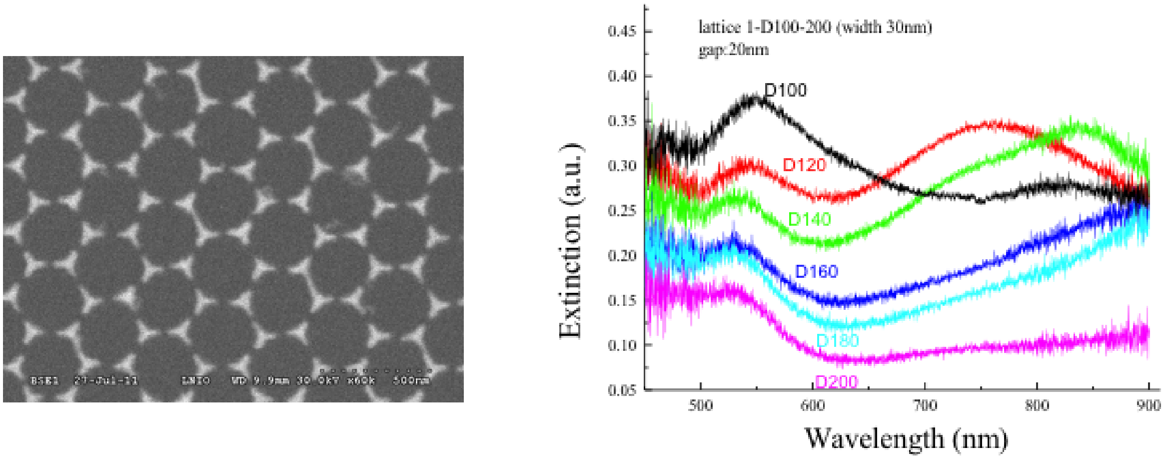

FIGURE D.9: Left : One of the hexagonal lattices used for the preliminary measurement. Right : Extinction measurement of corresponding nano-antenna lattice. The size of the nanostars is varied from 100 nm to 200 nm while the gap between them is kept constant at 20 nm.

Appendix E

Algebraic properties of translation operators

Infinitesimal translations of vector multipole fields possess a specific algebraic nature that can be related to the operators of the Lie algebra of SO(3). Having an operator point of view on the combined application of rotation and translation can lead to simplified computation and to a better understanding of the behavior of the infinitesimal translation operators.

The definition of the translation operators and the form of their coefficients lead us to define a linear combination of the translation operators similar to the one ue for spherical basis vectors.

$$\begin{aligned} T^+ &= -\frac{1}{2\sqrt{2}}(T_x + iT_y) && \text{(E.1)} \\ T^0 &= \frac{T_z}{2} && \text{(E.2)} \\ T^- &= \frac{1}{2\sqrt{2}}(T_x - iT_y) && \text{(E.3)} \end{aligned}$$

We thus define the coefficients $a^i_{l'm',lm}$ and $a^i_{l'J'M',lJM}$ with $i = 1, -1, 0$ with are easily obtained from cartesian definitions.

$$T^i_{l'm',lm} = i^{l'+1-l}(-1)^m \sqrt{(2l+1)(2l'+1)} \begin{pmatrix} l' & l & 1 \\ 0 & 0 & 0 \end{pmatrix} \begin{pmatrix} l' & l & 1 \\ m' & -m & -i \end{pmatrix} \tag{E.4}$$

$$T^{i}_{l'J'M',lJM} = i^{l'+1-l}(-1)^{M}\sqrt{(2l+1)(2l'+1)(2J+1)(2J'+1)}\begin{pmatrix} l' & l & 1 \\ 0 & 0 & 0 \end{pmatrix} \times \begin{pmatrix} J & J' & 1 \\ -M & M' & -i \end{pmatrix}\begin{Bmatrix} 1 & J' & J \\ 1 & l & l' \end{Bmatrix} \tag{E.5}$$

These T^i operators commute. This comes from the fact that infinitesimal translations can be expressed as a derivative. A well known property of multivariate analysis states that partial derivatives ordering can be changed if all partial derivatives exists and are continuous. The Ψ_{lm} and $\underline{\Psi}_l^{JM}$ satisfy this property since they are all continuous in 0 and we can thus safely say that translation operators commute.

$$[T^i, T^j] = 0 \tag{E.6}$$

Then, translation operators form an abelian Lie algebra and are generators of a commutative Lie group. From the coefficients definition, we can also easily calculate adjoint operators :

$$(T^+)^\dagger = T^- \qquad (T^-)^\dagger = T^+ \qquad (T^0)^\dagger = -T^0 \tag{E.7}$$

All these properties are stated for scalar and vector translation operators. The infinitesimal translation operator is in fact highly related to the gradient operator. For example, the application of the irreducible gradient ∇_μ on a vector multipole field can be expressed as :

$$\nabla_\mu \underline{\Psi}_l^{JM} = (-1)^{J+l}\sqrt{(2J+1)(l+1)}\sum_{J'}\begin{Bmatrix} J & J' & 1 \\ l+1 & l & 1 \end{Bmatrix} C^{J'M+\mu}_{JM1\mu}\underline{\Psi}_{l+1}^{J'M+\mu} + (-1)^{J+l}\sqrt{(2J+1)l}\sum_{J'}\begin{Bmatrix} J & J' & 1 \\ l-1 & l & 1 \end{Bmatrix} C^{J'M+\mu}_{JM1\mu}\underline{\Psi}_{l-1}^{J'M+\mu} \tag{E.8}$$

This expression can recasted in a form similar to the one in equation E.5 up to a normalization factor by switching to $3j$ symbols and including the sum over l'.

To complete the algebraic structure of the operation on the multipole fields, it is possible to mix rotation and translation to study the link between the two. We will now turn to their relationship with angular momentum operators. We recall here angular momentum commutators and adoints :

$$[J^\mu, J^\nu] = -\sqrt{2}\, C^{1\lambda}_{1\mu,1\nu}\, J^\lambda \qquad (J^+)^\dagger = J^- \qquad (J^-)^\dagger = J^+ \qquad (J^0)^\dagger = J^0 \tag{E.9}$$

Orbital angular momentum acting on a spherical harmonic gives :

$$\mathcal{L}^\mu Y_{lm} = (-1)^{l+m+\mu}\sqrt{l(l+1)(2l+1)}\begin{pmatrix} l & 1 & l \\ -m & -\mu & m+\mu \end{pmatrix} Y_{l\ m+\mu} \tag{E.10}$$

Using this relationship, we can calculate directly $\mathcal{L}^\mu T^i$:

$$\begin{aligned}\mathcal{L}^\mu T^i \Psi_{lm} &= (-1)^{l+\mu+i}(2l-1)\sqrt{l(l-1)(2l+1)}\begin{pmatrix} l-1 & l & 1 \\ 0 & 0 & 0 \end{pmatrix}\begin{pmatrix} l-1 & l & 1 \\ m+i & -m & -i \end{pmatrix}\times \\ &\times\begin{pmatrix} l-1 & 1 & l-1 \\ -m-i & -\mu & m+i+\mu \end{pmatrix}\Psi_{l-1,m+\mu+i} - (-1)^{l+\mu+i}(2l+3)\sqrt{(l+1)(l+2)(2l+1)}\begin{pmatrix} l+1 & l & 1 \\ 0 & 0 & 0 \end{pmatrix} \\ &\times\begin{pmatrix} l+1 & l & 1 \\ m+i & -m & -i \end{pmatrix}\begin{pmatrix} l+1 & 1 & l+1 \\ -m-i & -\mu & m+i+\mu \end{pmatrix}\Psi_{l+1,m+\mu+i}\end{aligned} \tag{E.11}$$

We can calculate also $T^i\mathcal{L}^\mu$ and then deduce the commutators. Even if calculation is tedious, the commutators are extremely simple :

$$\begin{array}{lll} [T^+,\mathcal{L}^-] = T^0 & [T^+,\mathcal{L}^0] = -T^+ & [T^0,\mathcal{L}^0] = 0 \\ [T^-,\mathcal{L}^+] = T^0 & [T^-,\mathcal{L}^0] = T^- & \end{array}$$

In the vector case, we can not directly calculate each term of the commutator. However, it is possible to calculate directly the whole commutator. As a example, we study the commutator between T^+ and J^-.

$$\begin{aligned}[T^+,J^-]\Psi_l^{JM} &= \sum_{l'J'M'}\sqrt{\frac{J(J+1)-M(M-1)}{2}}\, i^{l'+1-l}(-1)^{M-1}\Pi_{ll'JJ'}\begin{pmatrix} l & l' & 1 \\ 0 & 0 & 0 \end{pmatrix}\times \\ &\times\begin{pmatrix} J & J' & 1 \\ -M+1 & M' & -1 \end{pmatrix}\begin{Bmatrix} 1 & J' & J \\ 1 & l & l' \end{Bmatrix}\Psi'^{J'M'}_{l} \\ &- \sum_{l'J'M'}\sqrt{\frac{J'(J'+1)-M'(M-'1)}{2}}\, i^{l'+1-l}(-1)^{M}\Pi_{ll'JJ'}\begin{pmatrix} l & l' & 1 \\ 0 & 0 & 0 \end{pmatrix}\times \\ &\begin{pmatrix} J & J' & 1 \\ -M & M' & -1 \end{pmatrix}\begin{Bmatrix} 1 & J' & J \\ 1 & l & l' \end{Bmatrix}\Psi'^{J',M'-1}_{l}\end{aligned} \tag{E.12}$$

At this stage, we use the definition $\Pi_{a...d} = \sqrt{(2a+1)...(2d+1)}$ to make the equations better looking. Using cancelation properties of $3j$ symbols, we can simplify the sum over

M'.

$$[T^+, J^-]\Psi_l^{JM} = -\frac{1}{\sqrt{2}}\sum_{l'J'}\Big[\sqrt{J(J+1)-M(M-1)}\begin{pmatrix} J & J' & 1 \\ -M+1 & M & -1 \end{pmatrix}$$
$$+\sqrt{J'(J'+1)-M(M+1)}\begin{pmatrix} J & J' & 1 \\ -M & M+1 & -1 \end{pmatrix}\Big]\times$$
$$\times\, i^{l'+1-l}(-1)^M \Pi_{ll'JJ'}\begin{pmatrix} l & l' & 1 \\ 0 & 0 & 0 \end{pmatrix}\times\begin{Bmatrix} 1 & J' & J \\ 1 & l & l' \end{Bmatrix}\Psi_l'^{J'M} \quad \text{(E.13)}$$

To continue, we need to use the following relationship between $3j$ symbols :

$$\begin{pmatrix} J & J' & 1 \\ -M & M & 0 \end{pmatrix} = -\frac{1}{\sqrt{2}}\Big[\sqrt{J(J+1)-M(M-1)}\begin{pmatrix} J & J' & 1 \\ -M+1 & M & -1 \end{pmatrix}+$$
$$\sqrt{J'(J'+1)-M(M+1)}\times\begin{pmatrix} J & J' & 1 \\ -M & M+1 & -1 \end{pmatrix}\Big] \quad \text{(E.14)}$$

Inserting this result in the previous equation, we can make the T^0 coefficients appear and obtain the commutators $[T^+, J^-] = T^0$. All the commutators can be calculated in a similar fashion. The result are identical with those obtain in the scalar case except that we have here a composite angular momentum J instead of the orbital angular momentum L.

$$[T^+, J^-] = T^0 \qquad [T^+, J^0] = -T^+ \qquad [T^0, J^0] = 0$$
$$[T^-, J^+] = T^0 \qquad [T^-, J^0] = T^- \quad \text{(E.15)}$$

Finally, one can see that the algebraic properties of the operators of translation and rotation keep the simplicity they usually have when applied on simpler basis. The use of these properties can offer a great deal of simplification when carrying out specific calculations. Moreover, it is expected that more investigations on the structure of this specific representation of the Lie algebra of rotation and translation in 3D space could lead to an improved understanding of the one in the corresponding Lie group.

Appendix F

Résumé de la thèse en français

F.1 Introduction

Ce résumé en français contient les idées clefs développées dans chacun des chapitres de ce manuscrit. Cette thèse prolonge des travaux sur les relations entre la symétrie et les propriétés optiques non-linéaires de nanoparticules métalliques commencés de longue date par J. Jerphagnon [34] puis par J. Zyss [35] dans des cas différents.

Le premier s'est intéressé à l'implémentation d'un formalisme irréductible afin de simplifier l'écriture et la compréhension des propriétés des tenseurs qui décrivent le comportement de la matière condensée dans des domaines aussi divers que l'optique ou la mécanique. L'utilisation de l'irréductibilité, au sens de la théorie des groupes, afin de décrire les propriétés physiques de la matière a puisé son origine dans les avancées fondamentales effectuées par E. Wigner [28] et par Fano et Racah dans le cadre de la physique atomique.

L'étape suivante, franchie par J. Zyss, a été de s'intéresser à l'irréductibilité de tenseurs "ponctuels" au sens où ils décrivent les propriétés d'un objet qui a une extension spatiale négligeable. Ainsi, J. Zyss et S. Brasselet ont pu optimiser les tenseurs d'hyperpolarisabilités non-linéaires afin que les polarisabilités associées aient une grande amplitude. Dans ce but de créer des émetteurs non-linéaires performants, ils ont ainsi été en mesure de constater que les molécules ayant un comportement satisfaisant puisaient l'efficacité de leur réponse dans les composantes irréductibles d'ordres supérieurs. En effet, un tenseur T décrivant des propriétés physiques pourra toujours s'exprimer comme une somme de tenseurs irréductibles T^J :

$$T = \sum_{\oplus J} T^J \tag{F.1}$$

Cette écriture consiste à décomposer le tenseur initial en une somme de tenseurs dont la rotation s'effectue à l'aide des représentations irréductibles du groupe des rotations SO(3). Un point de vue équivalent consiste à affirmer que les tenseurs irréductibles forment une base de décomposition pour les tenseurs isomorphe aux harmoniques sphériques. Revenant aux molécules, la composante octupolaire $J = 3$ a permis d'apporter de nouvelles possibilités d'ingénierie et donc de sélectionner une nouvelle classe de molécules, les molécules octupolaires, comme de bonnes candidates pour une hyperpolarisabilité β importante. Ces molécules possèdent idéalement des composantes dipolaires $J = 1$ et quadrupolaires $J = 2$ nulles et leur hyperpolarisabilité totale est donc seulement contenue dans la composante octupolaire $\beta^{J=3}$.

L'objet de la présente étude est d'étendre ces travaux aux nanoparticules métalliques. Les nanoparticules métalliques ont l'avantage par rapport aux molécules de pouvoir être utilisées à résonance avec un endommagement limitée ainsi que de pouvoir être organisées spatialement afin d'ajouter un effet de réseau à l'efficacité d'une nanoparticule unique. Cependant, le fait de s'intéresser à des objets qui ne sont plus négligeables devant la longueur d'onde amène de nouvelles difficultés théoriques fondamentales qui constituent le noyau de cette thèse "**Propriétés optiques non-linéaires de nanoparticules métalliques**". Ces éléments seront développés dans les sections de ce résumé mais l'on peut d'ors et déjà indiquer que la nécessité de prendre en compte les possibles variations du champ dans le volume de la nanoparticule imposerait l'utilisation d'un champ de tenseurs irréductibles si l'on voulait se contenter de réduire la partie vectorielle des champs et donc spinorielle du tenseurs. Ainsi, une description qui conserve l'esprit des précédents études, c'est à dire réduire la réponse en un nombre fini de composantes qui prennent en compte la globalité de l'objet afin de contenir sa symétrie, doit non seulement réduire les parties spinorielles et orbitales. Les termes "spinoriels" et "orbitaux" ne doivent pas être interprétés dans le cadre de la théorie du moment angulaire en mécanique quantique mais bien dans celui de la physique classique. En effet, la composante spinorielle du champ décrit sa partie vectorielle dans l'espace $\underline{e}_1, \underline{e}_0$ et $\underline{e}_{-1}$ alors la composante orbitale s'intéresse aux fonctions qui dépendent des variables de l'espace. Chacune de ces composantes peut être réduite séparément mais les propriétés d'irréductibilité sont alors perdues car un produit direct de tenseurs irréductibles n'en est pas un. Il est alors nécessaire d'introduire la notion de produit tensoriel irréductible afin de résoudre ce problème et de donner aux formalismes les propriétés algébriques souhaitées.

Ce résumé va donc reprendre chacune des parties de cette thèse en se concentrant sur les résultats obtenus. La première section est un résumé succinct des éléments théoriques nécessaires et des bases choisies dans la suite de l'étude. La section suivante présente les résultats préliminaires qui ont motivé l'introduction d'un formalisme totalement irréductible. La troisième section développe ce formalisme et l'applique à l'expérience présentée dans la section d'avant. La quatrième et dernière section présente les travaux préliminaires effectués dans le domaine temporel.

F.2 Cadre de l'étude

F.2.1 Tenseurs irréductibles et champs multipolaires

Afin de décrire le comportement optique non-linéaire d'objets ayant des symétries élevées, l'utilisation des tenseurs irréductibles s'impose naturellement. Dans ce formalisme, un tenseur T de rang n est décomposé en une somme directe de parties irréductibles comme indiqué à l'équation F.1. Chaque tenseur irréductible $T^{(\tau)J}$ se transforme par rotation selon les représentations irréductibles de SO(3), c'est-à-dire en leur appliquant les matrices de Wigner. Un tenseur cartésien peut se décomposer en plusieurs tenseurs irréductibles du même ordre J et l'indice de séniorité τ sert alors à les distinguer.

Le champ électromagnétique peut lui même être décomposée en une somme de tenseurs irréductibles qui sont solutions de l'équation de Helmholtz sphérique. Leurs parties angulaires sont les harmoniques sphériques vectorielles $\underline{Y}_l^{JM}(\theta,\phi)$ issues du produit direct irréductible entre les harmoniques sphériques scalaires et un spineur $S=1$. La partie radiale f_l est quant à elle une fonction de Bessel sphérique ou une des fonctions qui y sont associées :

$$\underline{\Psi}_l^{JM}(r,\theta,\phi) = f_l(kr)\underline{Y}_l^{JM}(\theta,\phi) \tag{F.2}$$

Une autre base issue d'une combinaison linéaire de la précédente et dû à Hansen permet un traitement algébrique plus adapté à l'électromagnétisme :

$$\underline{\Psi}_m^{JM} = \underline{\Psi}_J^{JM} \tag{F.3}$$

$$\underline{\Psi}_e^{JM} = \sqrt{\frac{J+1}{2J+1}}\underline{\Psi}_{J-1}^{JM} - \sqrt{\frac{J}{2J+1}}\underline{\Psi}_{J+1}^{JM} \tag{F.4}$$

$$\underline{\Psi}_l^{JM} = \sqrt{\frac{J}{2J+1}}\underline{\Psi}_{J-1}^{JM} + \sqrt{\frac{J+1}{2J+1}}\underline{\Psi}_{J+1}^{JM} \tag{F.5}$$

En effet, $\underline{\Psi}_m^{JM}$ et $\underline{\Psi}_e^{JM}$ sont de divergences nulles et permettent de décomposer naturellement les champs de radiation sur cette base.

F.2.2 Fabrication et description des échantillons

Afin d'effectuer des mesures optiques sur les nanoparticules, ces dernières ont été fabriquées en utilisant un procédé de lithographie électronique dont les étapes sont résumées à la figure F.1. Les étapes de fabrications principales sont les suivantes :

- Sur un substrat de verre nettoyé, une couche de PMMA est déposée par tournette afin d'obtenir une épaisseur de 150 nm. Par évaporation, une couche de quelques nanomètres d'argent est à son tour déposée afin d'assurer une bonne conductivité pour la lithographie électronique ;
- Le faisceau électronique d'un MEB (Microscope Electronique à Balayage) est utilisé pour insoler la résine. Il s'agit d'une résine positive et les zones insolées sont donc celles où sera déposé de l'or;
- Après avoir enlevé la couche d'aluminium à l'aide d'une solution de KOH, du MIBK est utilisé pour l'étape de révélation en enlevant le PMMA insolé;
- De l'or est déposé sur l'échantillon par évaporation. Le reste de résine est finalement enlevèe par lift-off.

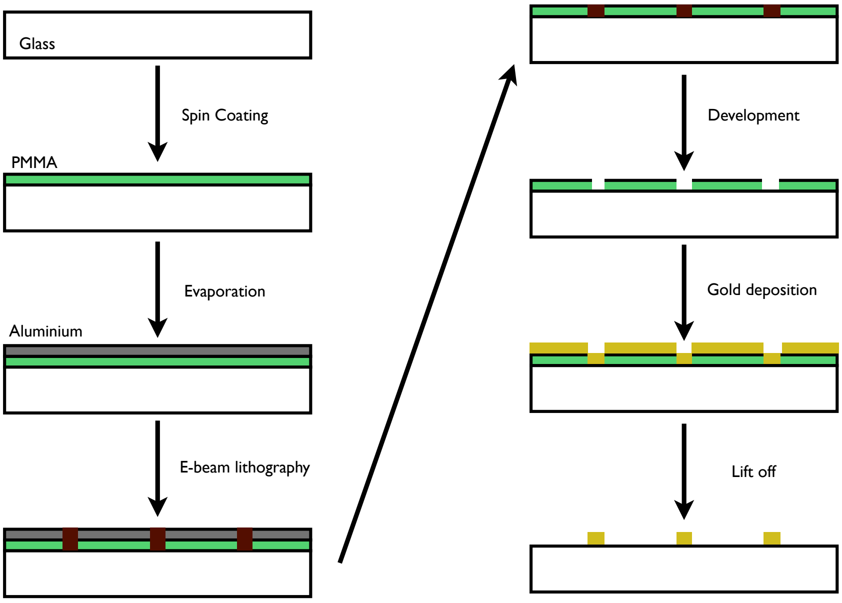

FIGURE F.1: Résumé des différentes étapes nécessaires à la conception d'un échantillon par lithographie électronique.

Par cette méthode, de nombreux échantillons ont été fabriqués. Quelques réalisations sont présentées à la figure F.2. Bien que la majeure partie de cette thèse soit concentrée sur les propriétés de nanoparticules uniques, les couplages entre nanoparticules constituent une étape supplémentaire qui a aussi été considérée (voire l'appendice D). Les nanoparticules sont suffisamment éloignées de façon à négliger les interactions entre elles.

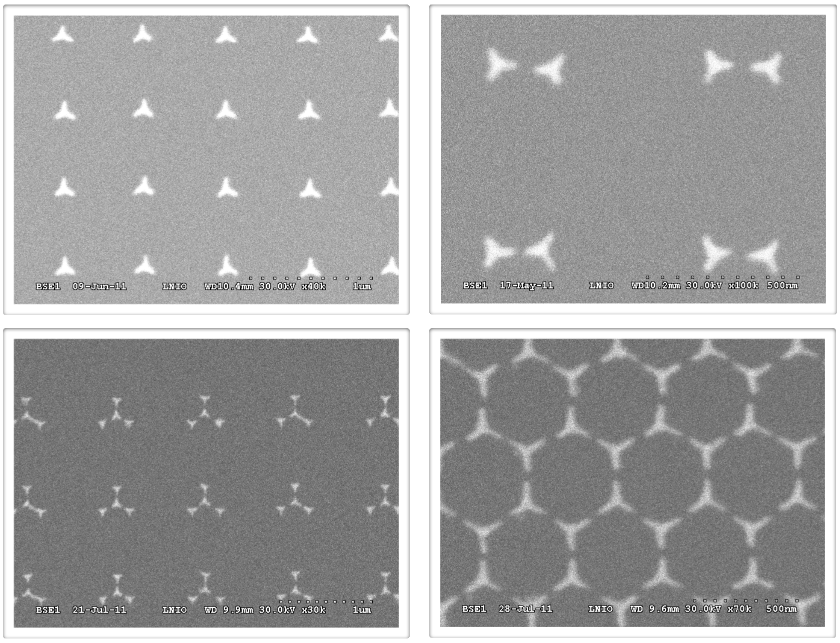

Figure F.2: Différents types de réseaux obtenus par lithographie électronique.

F.3 Génération de seconde harmonique pour les nano-étoiles

F.3.1 Description de l'expérience

Les nanoparticules d'or en forme de nanoétoiles possèdent une susceptibilité non-linéaires du second ordre élevée (44 pm/V). Ainsi, cette dernière est plus importante que celle du KTP (34 pm/V) qui est déjà un cristal non-linéaire de qualité. Afin d'étudier cette réponse non-linéaire, l'expérience schématisée à la figure F.3 (e) à été conduite préalablement à ce travail de thèse. Les nanoparticules sont excitées par un faisceau issu d'un laser titane- saphir et de longueur d'onde centrale égale à 800 nm. La polarisation de l'onde incidente est contrôlée par une lame $\lambda/2$. Un objectif de microscope sert à focaliser l'excitation sur une nanoparticule. La mesure effectuée par les deux photodiodes (voir légende) permet d'obtenir les intensités $I_x(\phi)$ et $I_y(\phi)$ des composantes E_x et E_y du champ de seconde harmonique rayonné par la nanoétoile.

Une des premières étapes de cette thèse fut de décrire et d'interpréter les résultats expérimentaux de cette expérience. La nécessité de décrire correctement la propagation du champ électrique à travers le système optique a conduit à prolongé des calculs

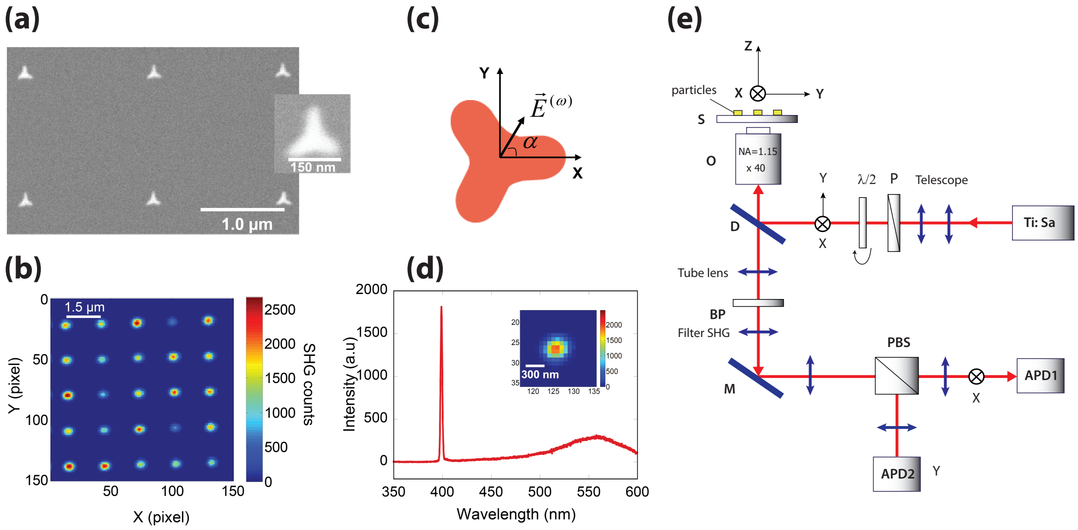

FIGURE F.3: Cette figure résume les différentes étapes expérimentales réalisées afin d'obtenir la SHG de nanoparticules uniques. L'expérience représentée en (e) permet d'exciter des nanoparticules uniques telle que celles visible en (a) tout en contrôlant la polarisation du champ incident grâce à la lame $\lambda/2$. L'intensité du signal SHG est alors détectée par deux photodiodes permettant de mesurer séparément les amplitudes carrées selon x et selon y. Les signaux obtenus sur une assemblée de nanoparticules est représentée en (b). On peut y voir que la réponse est très différente selon les nanoparticules considérées et il est alors nécessaire de corréler les réponses mesurées optiquement aux observations des étoiles par microscopie électronique. Le spectre d'une nanoparticule particulière est représenté en (d). On peut y voir une résonance très piquée à 400 nm correspondant au signal de seconde harmonique. Finalement, un schéma de la nanoparticule avec le champ incident l'excitant est représenté en (c).

effectués par Enderlein afin de calculer les PSFs (Point Spread Function) d'un dipôle rayonnant puis celle de multipôles. Pour cela, la géométrie présentée en figure F.4 est utilisée afin de conduire les calculs. Cette configuration permet d'utiliser la propagation du spectre angulaire afin de conduire le calcul :

$$\underline{E}(\vec{r}) = -2ik' \frac{e^{ik'f'}}{4\pi f'} \iint_S e^{ik' r \cos\epsilon} \underline{E}_S \sin\theta' d\theta' d\phi \tag{F.6}$$

Finalement, les calculs permettent d'obtenir une fonction de Green G^J qui est une matrice $3 \times (2J+1)$ et qui permet d'obtenir le champ $E(\vec{r})$ dans l'espace image d'un multipole rayonnant M^J de rang J situé au point focal de l'espace objet :

$$\underline{E}(\vec{r}) = K_J G^J \cdot M^J \tag{F.7}$$

Les figures F.5 et F.6 représentent les intensités de dipôles cartésiens et sphériques respectivement. La PSF d'un dipôle cartésien est similaire à celle déjà obtenue dans des

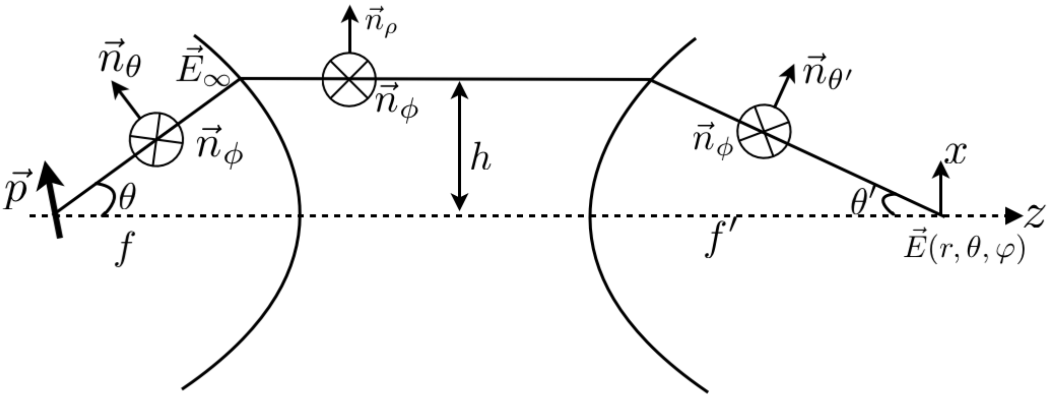

Figure F.4: Représentation schématique de l'imagerie d'un dipôle. Le choix des vecteurs de base pour projeter le champ entre les repères sphériques et cylindriques est représenté sur le schéma.

travaux précédents à celui-ci. Cependant, alors que l'ouverture numérique augmente, les PSFs obtenues deviennent différentes car les auteurs considèrent généralement que l'approximation paraxiale est valable au-delà de son domaine de validité. La PSF dipolaire sphérique de la figure suivante présente un aspect similaire mais l'ellipticité des PSFs orientées selon $\vec{e}_x$ et $\vec{e}_y$ disparait pour les PSFs orientées selon $\vec{e}_{-1}$ et $\vec{e}_1$. Cela provient simplement du fait que la base sphérique est une base plus respectueuse de la symétrie cylindrique du problème considéré.

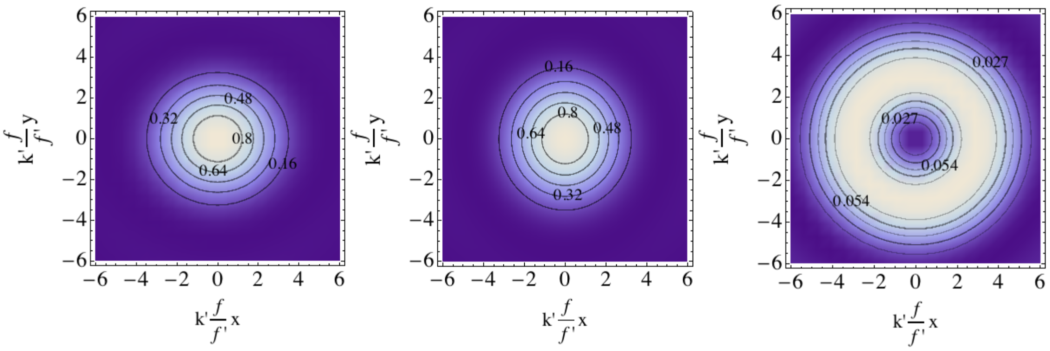

Figure F.5: Intensité du champ électrique dans le plan image des différentes composantes d'un dipôle cartésien. De gauche à droite, le dipôle source est respectivement orienté selon $\vec{e}_x, \vec{e}_y$ et $\vec{e}_z$. L'ellipticité des champs pour les dipôles μ_x et μ_y est liée à la réductibilité de la base cartésienne.

F.3.2 Une première interprétation multipolaire

Fort de la capacité de pouvoir décrire analytiquement la propagation des multipôles à travers le système optique, il est alors possible de modéliser la nanoparticule excitée comme une assemblée de dipôles rayonnants et de calculer le champ correspondant dans

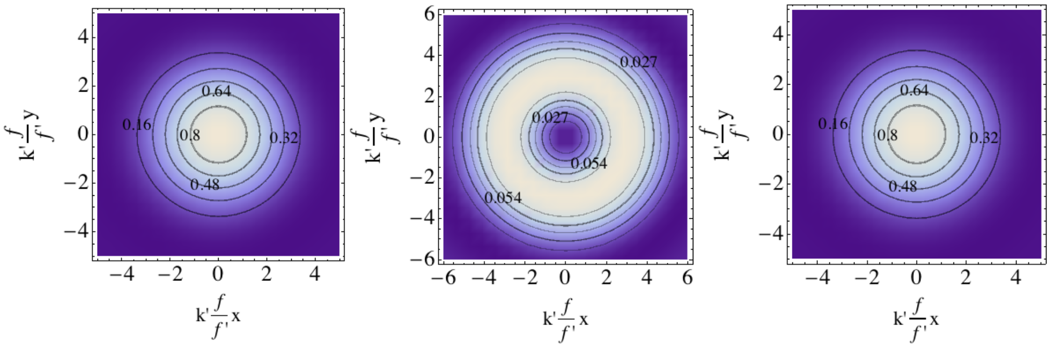

FIGURE F.6: Intensité du champ électrique dans le plan image des différentes composantes d'un dipôle irréductible. De gauche à droite, le dipôle source est respectivement orienté selon $\vec{e}_1, \vec{e}_0$ et $\vec{e}_{-1}$.

l'espace image, c'est-à-dire celui mesuré sur les photodiodes. Les modèles utilisés afin de représenter la nanoparticule sont illustrés à la figure F.7 et considèrent que l'essentiel de l'émission non-linéaire est issue de dipôles positionnés le long des bras. Ce modèle simple permet de conserver les propriétés de symétrie de l'objet et dépend de peu de paramètres (distance h des trois dipôles par rapport au centre et force des trois dipôles β). Il s'avère représenter de façon acceptable la variation polaire des intensités I_x et I_y lorsque les nanoparticules considérées sont proches de la perfection mais pas quand elles sont déformées. Les modèles (b) et (c) de la figure F.7 ont dont été introduits afin de modéliser les imperfections.

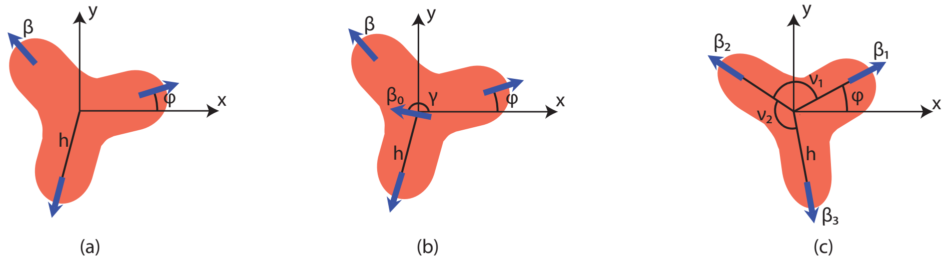

FIGURE F.7: Représentation graphique des différents modèles utilisés afin de représenter les données expérimentales. L'étoile représentée en (a) est une étoile parfaite conservant les propriétés de symétrie du groupe D_3 de la nanoparticules. Cependant, la réponse optique non-linéaire étant très sensible aux variations de forme et aux écarts à la symétrie parfaite, il a été nécessaire d'introduire deux autres modèles prenant en compte ces imperfections. Le modèle (b) rajoute un dipôle au centre de la nanoparticule alors que le modèle (c) libère les angles des trois dipôles aux pointes et leur autorise d'avoir une amplitude différente.

Les résultats des ajustements de courbe sont donnés à la figure F.8 dans le cas d'une nanoparticules proche de la perfection en (a) et d'une avec des défauts en (b). Ces résultats correspondent à une distribution de courant (3 dipôles paramètrés) qui peut alors être projetée sur la base multipolaire. Cette projection indique la nanoparticule de bonne qualité rayonne une composante quadrupolaire non-négligeable et même dominante selon la polarisation choisie alors que le rayonnement de la nanoparticule imparfaite est très nettement dominé par sa composante dipolaire.

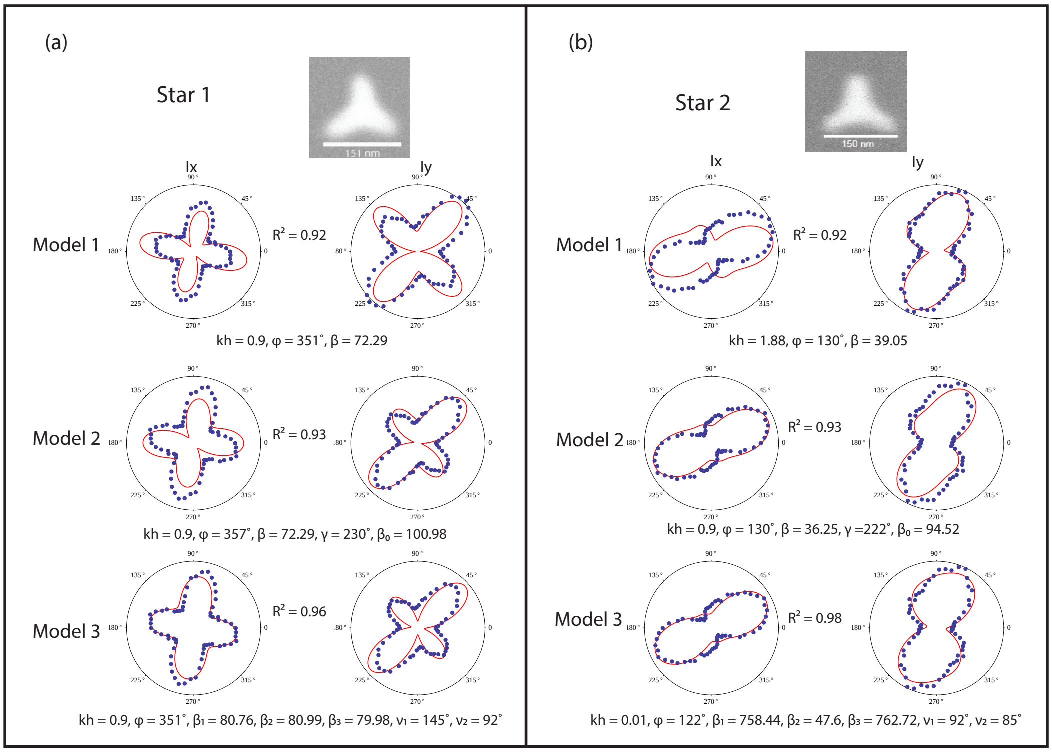

FIGURE F.8: Résultats des fits effectués selon les modèles de la figure **??**. La colonne de gauche correspond à une nanoparticule ayant une forme de bonne qualité alors que celle de droite correspondant à une nanoparticule de moins bonne qualité. On peut ainsi observer que dès le modèle 1, le fit est convenable dans le cas de la bonne nanoparticule alors que ce n'est pas du tout le cas pour celle ayant une mauvaise forme.

F.4 Développent et application d'un formalisme complètement irréductible

F.4.1 Exposition du formalisme

Les résultats de la section indiquent l'importance des éléments multipolaires d'ordre supérieurs aux dipôles dans l'interprétation de la réponse non-linéaire. Cependant, à la différence du cas moléculaire où seul le tenseur de réponse était décomposé en tenseurs irréductibles, l'extension de la nanoparticule nécessite de décomposer aussi les champs sur une base multipolaire. Dans ces conditions, le tenseur de réponse dépend alors de l'espace et la réduction de ses composantes sur une base irréductible est insuffisante et il convient décomposer aussi sa dépendance spatiale. Ceci permet ainsi d'obtenir un tenseur qui prend en compte la globalité de la nanoparticule et qui comporte donc des informations sur sa symétrie que ne pourrait pas contenir un tenseur local. Qui plus est, le tenseur est décrit par un nombre discret de composantes dans cette base convergeant rapidement et localisées en un point unique de l'espace pris pour origine. En pratique, quelques valeurs permettront donc de décrire un objet tel que ceux considérés dans cette thèse (dont la taille est environ $\approx \lambda/3$).

On peut démontrer que le tenseur de réponse linéaire $\underline{\underline{R}}$ peut s'écrire sur la base des produits directs d'harmoniques sphériques vectorielles :

$$\underline{\underline{R}} = \sum_{l_1 J_1 M_1} \sum_{l_2 J_2 M_2} R^{l_2 J_2 M_2}_{l_1 J_1 M_1} \; \underline{\Psi}^{J_1 M_1}_{l_1} \otimes \underline{\Psi}^{J_2 M_2}_{l_2} \tag{F.8}$$

Ce tenseur de réponse permet d'obtenir les composantes irréductibles de la densité de courant $J^{J_2 M_2}_{l_2}$ induite par le champ incident :

$$J^{J_2 M_2}_{l_2} = \sum_{l_1 J_1 M_1} R^{l_2 J_2 M_2}_{l_1 J_1 M_1} \; E^{J_1 M_1}_{l_1} \tag{F.9}$$

L'homologue non-linéaire de cette équation peut être obtenu de façon directe :

$$J^{(n)JM}_{\;\;\;\;l}(\omega) = \sum_{l_1 J_1 M_1 \cdots l_n J_n M_n} R^{(n)lJM}_{\;\;\;\;l_1 J_1 M_1 \cdots l_n J_n M_n}(\omega; \omega_1, \cdots, \omega_n)\, E_1{}^{J_1 M_1}_{\;\;l_1}(\omega_1) \cdots E_n{}^{J_n M_n}_{\;\;l_n}(\omega_n) \tag{F.10}$$

Où l'on a ajouté explicitement les fréquences ω_n car elles ne sont alors plus toutes égales à la même valeur ω. La base choisie jusqu'alors est issue du produit direct de tenseurs irréductibles et peut elle-même être réduite, conduisant à la définition des harmoniques sphériques vectorielles bipolaires dans le cas linéaire :

$$\Big\{ Y_{l_1}(\theta_1, \varphi_1) \otimes Y_{l_2}(\theta_2, \varphi_2) \Big\}_{LM} = \sum_{m_1 m_2} C^{LM}_{l_1 m_1 l_2 m_2} \; Y_{l_1 m_1}(\theta_1, \varphi_1) Y_{l_2 m_2}(\theta_2, \varphi_2) \tag{F.11}$$

Dans le cas non-linéaire, la base irréductible sera obtenue par produit irréductible successifs d'harmoniques sphériques vectorielles. Ces bases sont complètement irréductible et permettent de décomposer le tenseur de réponse de façon efficace en prenant en compte la symétrie de la nanoparticule. Dans le cas linéaire, le tenseur de réponse s'écrit alors :

$$\underline{\underline{R}} = \sum_{l_1 J_1 l_2 J_2 JM} R^{JM}_{l_1 J_1 l_2 J_2} \; \Big\{ \underline{\Psi}^{J_1}_{l_1} \otimes \underline{\Psi}^{J_2}_{l_2} \Big\}^{JM} \tag{F.12}$$

Des expressions analogues existent en utilisent les harmoniques sphériques multipolaires $\underline{\Psi}_m^{JM}$ et $\underline{\Psi}_e^{JM}$ plutôt que les $\underline{\Psi}_l^{JM}$. L'utilisation d'une base ou d'un autre, totalement réduite ou pas, s'effectue en fonction du problème considéré, les calculs et les interprétations s'avérant plus simple dans un formalisme ou dans un autre en fonction des cas.

Afin de traiter des problèmes concrets avec ce formalisme, il est nécessaire de pouvoir développer des modèles avec. Typiquement, une mesure de la réponse optique non-linéaire permet d'accéder indirectement à la densité de courante émettrice en utilisant un modèle approprié comme à la section précédente. Connaissant le champ excitateur envoyé et sa décomposition multipolaire, il est possible de déduire les composantes irréductibles du tenseur de réponse les reliant. Cette tâche est en général peu aisée car une mesure complète de la densité de courante est souvent inaccessible. Dans cette situation, il est important d'utiliser les propriétés de symétrie du tenseur afin d'éliminer les termes non autorisés par la géométrie de l'objet.

F.4.2 Application à la description du comportement non-linéaire de nano-étoiles

En utilisant la théorie précédente, il est possible de décrire plus précisément les résultats de l'expérience de la figure F.8. On considère le cas du modèle (a) de la figure F.7 et donc d'une étoile parfaite ayant la symétrie D_3. La distribution de courant correspondante, trois dipôles positionnés dans les bras de la nanoparticule, est simplifiée en l'écrivant comme une somme de multipôles à l'origine. Pour cela, le théorème d'addition translationnelle permettant d'exprimer une harmonique sphérique vectorielle translatée en une somme de ces objets à l'origine est utilisé :

$$\Psi_l^{JM}[R,\Omega,\Phi] = \sum_{l'J'M'} T_{l'J'M',lJM}\Psi_{l'}^{J'M'} \tag{F.13}$$

Où les composantes de l'opérateur de translation T sont définit par :

$$\begin{aligned} T_{l'J'M',lJM}[R,\Omega,\Phi] = \sum_{l''m''} & i^{l'+l''-l}(-1)^{M+1}\sqrt{4\pi(2l+1)(2l'+1)(2l''+1)(2J+1)(2J'+1)}\times \\ & \times \begin{pmatrix} l & l' & l'' \\ 0 & 0 & 0 \end{pmatrix} \begin{pmatrix} J & J' & l'' \\ -M & M' & m'' \end{pmatrix} \begin{Bmatrix} l'' & l' & l \\ 1 & J & J' \end{Bmatrix} j_{l''}(kR)Y_{l''m''}(\Omega,\Phi) \end{aligned} \tag{F.14}$$

La distribution de courant de la nanoparticule s'obtient en translatant et en orientant de façon appropriée les trois champs dipolaires placés sur chacun des bras :

$$\vec{J} = \mu\Big(T_{R,\frac{\pi}{2},0}\Big[\mathcal{D}^{(1)}_{0,\frac{\pi}{2},0}\Big[\underline{\Psi}^{10}_{m}\Big]\Big](r)+T_{R,\frac{\pi}{2},\frac{2\pi}{3}}\Big[\mathcal{D}^{(1)}_{0,\frac{\pi}{2},-\frac{2\pi}{3}}\Big[\underline{\Psi}^{10}_{m}\Big]\Big](r)+T_{R,\frac{\pi}{2},-\frac{2\pi}{3}}\Big[\mathcal{D}^{(1)}_{0,\frac{\pi}{2},\frac{2\pi}{3}}\Big[\underline{\Psi}^{10}_{m}\Big]\Big](r)\Big) \tag{F.15}$$

Les projections effectuées précédemment nous indiquent que seuls les trois premiers ordres multipolaires sont nécessaires pour reconstruire une distribution de courante fidèle. Après calcul, les composantes multipolaires non nulles de la densité de courant sont :

$$J^{1-1}_{m}(\Phi,R) = -\frac{3}{4}e^{2i\Phi}f_d(R) \quad c^{11}_{m}(\Phi,R) = \frac{3}{4}e^{-2i\Phi}f_d(R) \tag{F.16}$$

$$J^{2-2}_{m}(\Phi,R) = -\frac{9}{8}\sqrt{\frac{3}{5}}e^{-2i\Phi}f_q(R) \;\; c^{20}_{m}(\Phi,R) = \frac{9}{2\sqrt{10}}f_q(R) \;\; c^{22}_{m}(\Phi,R) = -\frac{9}{8}\sqrt{\frac{3}{5}}e^{2i\Phi}f_q(R) \tag{F.17}$$

$$J^{3-3}_{m}(\Phi,R) = -\frac{9}{4}\sqrt{\frac{5}{7}}f_o(R) \;\; c^{3-1}_{m}(\Phi,R) = \frac{9}{8}\sqrt{\frac{3}{7}}e^{2i\Phi}f_o(R) \tag{F.18}$$

$$J^{31}_{m}(\Phi,R) = -\frac{9}{8}\sqrt{\frac{3}{7}}e^{-2i\Phi}f_o(R) \;\; c^{33}_{m}(\Phi,R) = \frac{9}{4}\sqrt{\frac{5}{7}}f_o(R) \tag{F.19}$$

Avec :

$$f_d(R) = j_0(kR) + j_2(kR) \tag{F.20}$$

$$f_q(R) = j_1(kR) + j_3(kR) \tag{F.21}$$

$$f_o(R) = j_2(kR) + j_4(kR) \tag{F.22}$$

Les poids relatifs des multipôles entrant en jeu dans le développement de la distribution de courant sont représentés à la figure F.9. On peut y observer que pour les tailles des nanoparticules étudiées (R = 50 nm à R = 100 nm), les composantes dipolaires (en rouge) et quadrupolaires (en bleu) sont celles qui prédominent largement.

Les données mesurées expérimentalement peuvent être reconstruites en utilisant les PSFs multipolaires précédemment calculées pour propager les rayonnements correspondants à cette décomposition multipolaire :

$$I_x(\phi,R) = \iint_{\text{image space}}\Big(\sum_{JM} J^{JM}_{m}(\phi,R)G^{mJM}_{x}\Big)rdrd\varphi \tag{F.23}$$

$$I_y(\phi,R) = \iint_{\text{image space}}\Big(\sum_{JM} J^{JM}_{m}(\phi,R)G^{mJM}_{y}\Big)rdrd\varphi \tag{F.24}$$

On obtient alors des courbes similaires à celles affichées à la figure F.8 pour une étoile parfaite. Cette étape permet de relier l'expérience au modèle et donc de déduire les

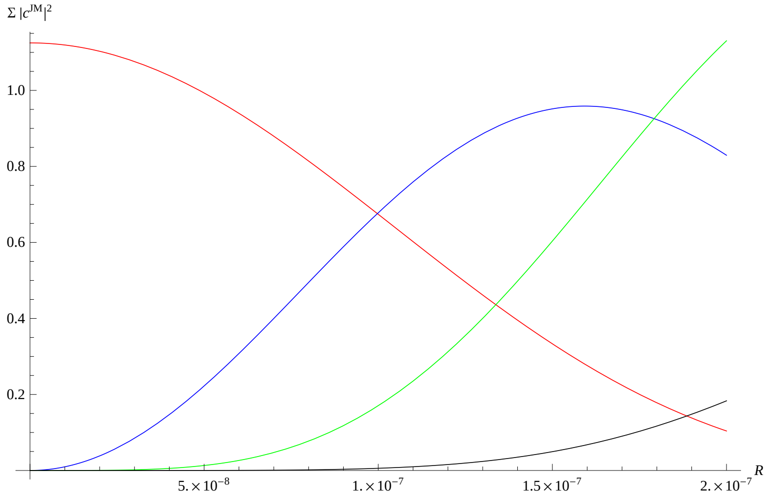

FIGURE F.9: Variation des poids multipolaires à mesure que la distance entre les dipôles, et donc la taille de l'étoile, augmente. La composante dipolaire en rouge est l'unique présente en $R = 0$ conformément au fait que la somme de trois dipôles en un point redonne un dipôle pur. Lorsque la taille de l'étoile augmente, les composantes multipolaires d'ordre supérieur apparaissent l'une après l'autre. Ainsi, une nanoparticles de 150 nm de diamètre circonscrit (soit $R = 75$ nm) correspond environ au moment le quadrupole en bleu devient dominant devant le dipôle et où l'octupole commence à apparaitre.

multipôles décrivant l'objet ainsi que leur dépendance en fonction de la polarisation du champ incident. Ensuite, le champ incident est à sont tour décomposé sur une base multipolaire de la façon suivante :

$$e^{ikz}\begin{pmatrix}\cos\alpha\\ \sin\alpha\\ 0\end{pmatrix} = \sum_J \sqrt{\pi(2J+1)}\,i^J\Big(e^{-i\alpha}(\underline{\Psi}_m^{J-1} - i\underline{\Psi}_e^{J-1}) + e^{i\alpha}(\underline{\Psi}_m^{J1} + i\underline{\Psi}_e^{J1})\Big) \tag{F.25}$$

Pour préserver la simplicité des calculs, le champ incident a été modélisé par une onde plane mais il est bien sur possible d'utiliser la décomposition multipolaire de faisceaux plus réalistes tel que des faisceaux gaussiens et la famille de leurs modes d'ordres supérieurs (Laguerre-Gauss, Hermite). Cette décomposition peut s'avérer nécessaire dans le cas d'objet grand par rapport à la taille du col ("waist") du faisceau. De plus, un choix judicieux de faisceaux différents permettrait d'adresser différemment les différentes composantes du tenseur de réponse et donc d'obtenir des informations différentes. La figure F.10 représente la reconstruction de l'onde plane en utilisant l'équation F.25. La nanoparticule est représentée en rouge par dessus le champ. Encore une fois, le nombre de composantes nécessaires à une reconstruction acceptable du champ est très limité et seul un nombre restreint d'ordre est nécessaire.

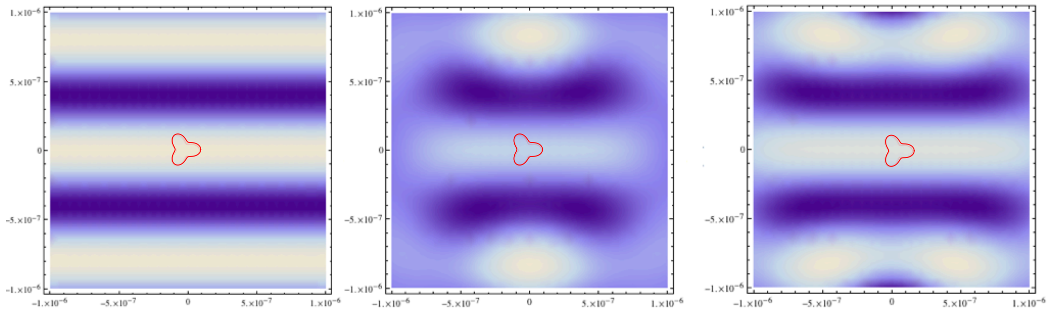

Exact

3 multipolar coefficients

4 multipolar coefficients

FIGURE F.10: Reconstruction du champ électromagnétique à proximité de la nanoparticule. Une nanoparticule de 150 nm de diamètre circonscrit est représentée en rouge au centre du champ. Il est possible d'observer que seuls quelques ordres sont nécessaires afin de reproduire le champ de façon convenable.

Dans un formalisme totalement réduit, le tenseur de réponse est développé sur une base d'harmoniques sphériques tripolaires :

$$\underline{\underline{R}}^{(2)} = \sum_{i_1 J_1 i_2 J_2 i J} R^{(2)\ J'M'}_{i_1 J_1 i_2 J_2 (J_{12}) i J} \underline{\underline{\Psi}}^{(3)\ J'M'}_{i_1 J_1 i_2 J_2 (J_{12}) i J M} \tag{F.26}$$

Cette expression permet d'utiliser simplement l'invariance par rotation de $2\pi/3$ du système afin d'obtenir les composantes du tenseur.

F.5 Etude du comportement non-linéaires dans le domaine temporel

F.5.1 Etude des mécanismes de photosynthèse

Dans le cadre de cette thèse, le montage expérimental utilisé pour mesurer des signaux de pompe-sonde sur des solutions colloïdales de nanoparticules l'a aussi été pour étudier le comportement optique de complexes moléculaires en charge de la captation et du transfert de l'énergie dans le cadre de la photosynthèse. Le complexe étudié, LHCII (Light Harvesting Complex II), est l'un des complexes photosynthétiques majeurs présents dans la nature et est constitué d'un nombre important de chromophores. Ces chromophores sont essentiellement des molécules de chlorophylle *a* et *b* couplées entre elles. Deux études ont donc été menées, l'une se concentrant sur la fonction de fluctuation responsable de la décohérence de la chlorophylle *a* alors que l'autre étudie le transfert d'énergie entre niveau d'énergie moléculaire dans LHCII.

Les informations obtenues l'ont été grâce à la mise en place d'une expérience de spectroscopie bidimensionnelle représentée à la figure F.11. La spectroscopie bidimensionnelle est l'expérience la plus complete afin d'accéder au tenseur de réponse non-linéaire du troisième ordre. En ajustant la position du détecteur et en contrôlant de façon adéquate les délais entre les pulses ainsi que leur phase relative, il est possible d'accéder indépendamment à différents éléments du tenseur de réponse correspondant à des diagrammes de Feynmann différents, c'est-à-dire à des chemins d'interactions différents.

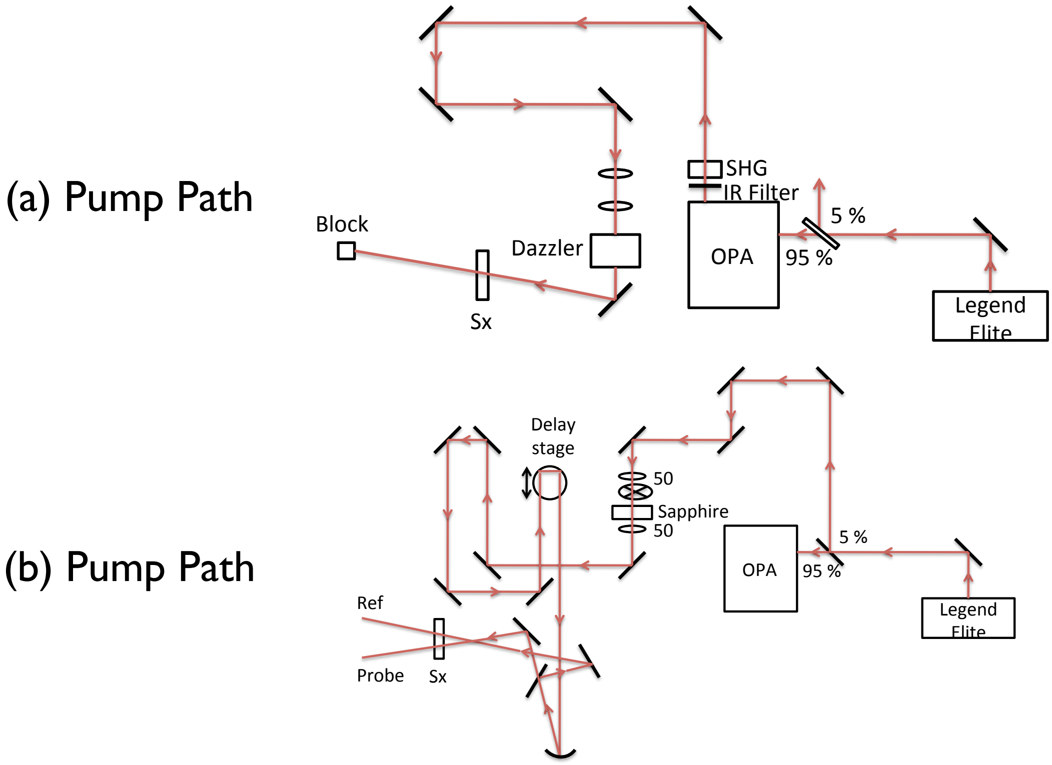

FIGURE F.11: Représentation schématique de l'expérience de spectroscopie électronique bidimensionnelle. La partie supérieure (a) représente le chemin emprunté par la pompe. Après avoir traversé un OPA qui permet de choisir une longueur d'onde centrale entre 550 et 700 nm, la pompe est dirigée dans un Dazzler. Ce façonneur de pulse est utilisé afin de générer deux pulses de pompes avec une phase relative et une distance temporelle entre eux contrôlées précisément. La sonde décrite dans la partie (b) traverse un cristal de saphir afin de générer une lumière blanche qui va permettre de sonder sur une large bande spectrale. Son arrivé sur l'échantillon est contrôlée par un miroir disposé sur une ligne à retard. La sonde est ensuite séparée en deux afin de créer une référence et la véritable sonde qui va se superposer à la zone traversée par la pompe.

La fonction de corrélation des fluctuations (FFCF pour Frequency-Frequency Correlation Function) de la Chlorophylle a a été mesurée en utilisant la pente de la résonance du niveau Q_y. En effet, il a été montré que la pente de l'ellipse de l'élément diagonal correspondant à cette résonance est reliée à la FFCF normalisée :

$$S(T_w) = \mathrm{CLS}(T_w) = \frac{\langle \delta\omega(T_w)\delta\omega(0)}{\langle \delta\omega(0)\delta\omega(0)} \tag{F.27}$$

L'ajustement de la courbe par un modèle bi-exponentiel a permis d'observer une décroissance des corrélations sur deux durées : une durée courte $\tau_1 \approx 500$ fs et une durée plus longue $\tau_2 \approx 7$ ps. Par ailleurs, une décroissance sur un temps nettement plus long (> 1 ns) a aussi été mesurée dans la littérature et, ne pouvant être sondé sur l'expérience présentée ici, est représentée par une ligne de base. De même, les premières valeurs mesurables de la fonction CLS sont inférieures à 1, ce qui indique qu'il existe aussi un temps de décroissance < 250 fs ne pouvant être mesuré dans cette expérience. Les deux durées de décroissances intermédiaires ont pu être sondées et être assignées au réarrangement du solvant suite à l'excitation de la molécule.

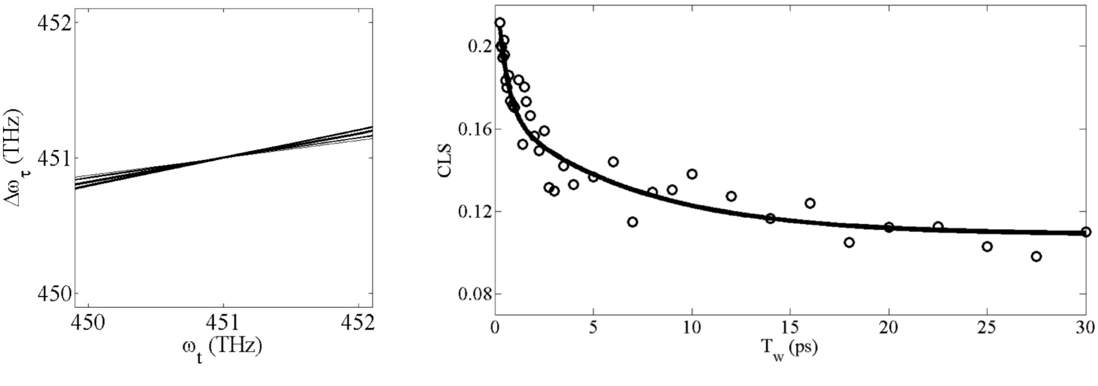

(a) (b)

FIGURE F.12: Illustration de la méthode de la pente centrale (Center Line Slope) afin d'obtenir la fonction de corrélation des fluctuations (Frequency-Frequency Correlation Function). (a) Evolution de la pente de la résonance diagonale du spectre 2D. (b) FFCF normalisée correspondante.

L'expérience de spectroscopie bidimensionnelle a aussi été conduite sur des solutions de complexes LHCII afin d'étudier le transfert d'énergie de l'excitation (EET, Excitation Energy Transfer) entre les niveaux moléculaires. Pour cela, les données expérimentales ont été reconstruites à l'aide d'un modèle autorisant le transfert d'énergie entre populations via une équation maitresse :

$$\dot{\rho}_{ee}(t) = -\sum_{e'} K_{ee,e'e'}\ \rho_{e'e'}(t) \tag{F.28}$$

La fonction de Green de l'équation a aussi été modifié pour inclure les oscillations et les relaxations durant les temps de cohérence :

$$G_{e_4e_3,e_2e_1}(t) = \delta_{e_4e_3}\delta_{e_2e_1}\theta(t)\left[e^{-Kt}\right]_{e_4e_4,e_2e_2} + (1-\delta_{e_4e_2})\delta_{e_3e_1}\theta(t)e^{-i\omega_{e_4e_3}t-\Gamma_{e_4e_3}t} \tag{F.29}$$

En utilisant cette évolution temporelle pour les cohérences et les populations, l'ajustement de ce modèle sur les données expérimentales a permis d'accéder aux paramètres de l'équation maitresse et de reconstruire les données expérimentales dont le fit est représenté à la figure F.13.

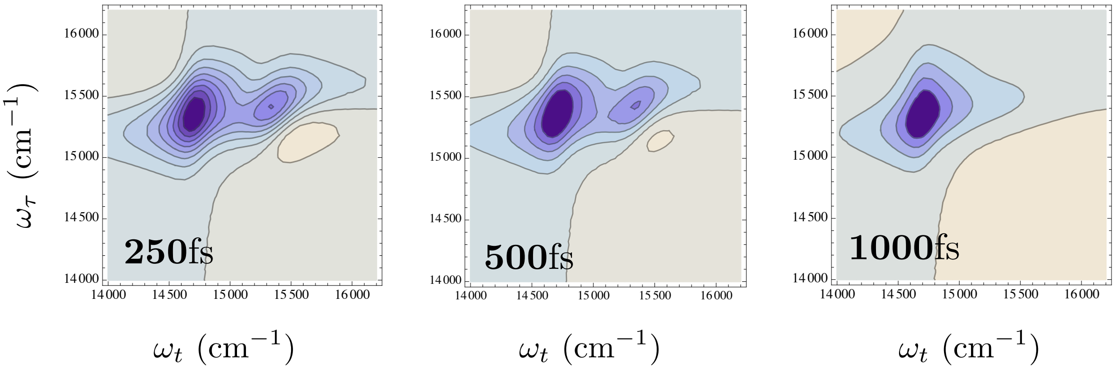

FIGURE F.13: Ajustement du modèlle présenté dans le texte sur les données expérimentales de spectroscopies bidimensionnelles effectuées sur des solutions de LHCII..

F.5.2 Résultats préliminaires sur les nanoparticules

Le développement du formalisme multipolaire a permis de comprendre le lien entre forme et comportement multipolaire de la nanoparticule. Ce faisant, il est alors possible d'associer l'efficacité de la réponse optique non linéaire des nano-étoiles à leur comportement multipolaire différent de celui des nanobatonnets. Cependant, une compréhension complète du comportement optique nécessite d'étudier les modes propres de ces systèmes ainsi que leur comportement fréquentiel afin de pouvoir interpréter chaque résonance en fonction d'un phénomène physique particulier.

En effet, la base multipolaire est très puissante pour les problèmes de rayonnement étant donnée l'isotropie de l'espace et constitue donc une base privilégiée pour une multitude de nanoparticules. Il est ainsi intéressant de décomposer les courants rayonnés sur la base multipolaire puisque ce sont les éléments de cette base qui seront mesurés en champ lointain. Par contre, les densités de courant dans la nanoparticule sont constitués d'éléments qui eux appartiennent à son groupe fini. Chacun de ces éléments constituent une base plus naturelle adaptée à chaque nanoparticule et peuvent être décomposés en somme de multipoles rayonnant. Ces éléments constituent une base de mode propre et fournissent un lien entre le comportement spatial et le comportement fréquentiel.

Ces modes peuvent être obtenus à partir d'une équation aux valeurs propres ne dépendant que de la géométrie de la nanoparticules. Cette équation a été obtenue dans le cadre de l'électrostatique par M. Kociak[75] et il est très envisageable qu'une similaire existe dans le cadre de l'électrodynamique. Comme ces modes propres ne dépendent que de la géométrie de la nanoparticule, l'utilisation de la théorie des groupes permet de les construire de façon raisonnable. Ainsi, les modes obtenus par des considérations géométriques seules ont nécessairement un comportement qualitatif acceptable et l'utilisation de l'équation aux valeurs propres pour le calcul exact n'est supposée qu'apporter des corrections mineures.

Dans le but d'obtenir des modes réalistes, une transformation conforme permettant de passer de la géométrie circulaire à celle d'une nano-étoile a été appliquée sur les modes de l'oscillateur harmonique circulaire. Les modes propres de ce dernier sont les produits direct de polynômes d'Hermite $\psi_{n_x}(x) = \left(\frac{1}{\pi}\right)^{\frac{1}{4}} \frac{1}{\sqrt{2^m m!}} H_m(x) e^{-\frac{1}{2}x^2}$. La transformation conforme utilisée est la suivante :

$$z \leftarrow z + \frac{1}{4} z^4 \tag{F.30}$$

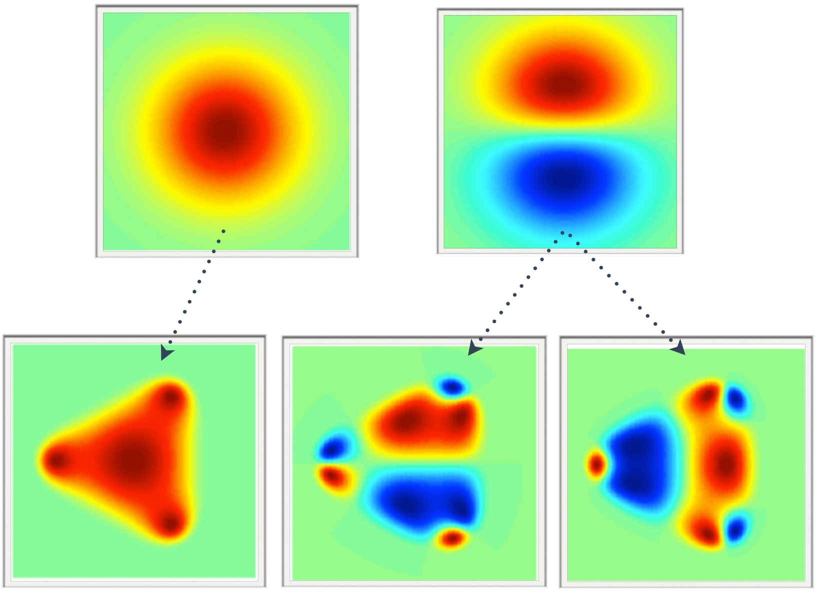

FIGURE F.14: Obtention des trois premiers modes propres d'une nano-étoile en utilisant la transformation conforme de l'équation F.30. Le mode en bas à gauche est le mode fondamental alors que les deux suivants constituent le premier mode excité doublement dégénéré et correspondant à la représentation E' du groupe D_3'.

Chaque mode propre de SO(3) est alors transformé en modes de D_3' comme le montre la figure F.14. L'association entre ces modes issues des transformations conformes et les représentations irréductibles de D_3' est réalisée en utilisant des projecteurs sur ces dernières. L'utilisation explicite de l'opérateur de l'équation aux valeurs propres permettrait d'obtenir la valeur propre du mode. Ensuite, chaque mode peut finalement être développé sur la base multipolaire. La finalité de cette démarche est de connaitre l'énergie d'excitation de chaque mode afin d'interpréter les spectres expérimentaux. Associé à la connaissance du tenseur de réponse irréductible à une fréquence donnée, ceci pourrait permettre de développer le tenseur de réponse irréductible sur une base de modes propres et donc combiner les connaissances spatiales et spectrales sur les nanoparticules.

Afin d'étudier le comportement spectral des nanoparticules de forme D_3', des expériences de pompe-sonde ont été réalisées sur celles-ci. Devant la difficulté de réaliser ces mesures sur un montage initialement destiné à l'étude de molécules, des solutions colloïsales de nanoprismes d'argent ont été réalisées par voie chimique. Ceci permet d'obtenir un signal plus important et donc mesurable sur ce système bien que le contrôle de la position des nanoparticules soit perdu et que l'élargissement inhomogène soit plus conséquent. La figure F.15 présente un résultat de pompe-sonde obtenu sur ces nanoprismes pour une pompe et une sonde centrées à 650 nm. Cette mesure a permis d'obtenir le temps de vie du système à cette énergie qui est de 2 017 fs.

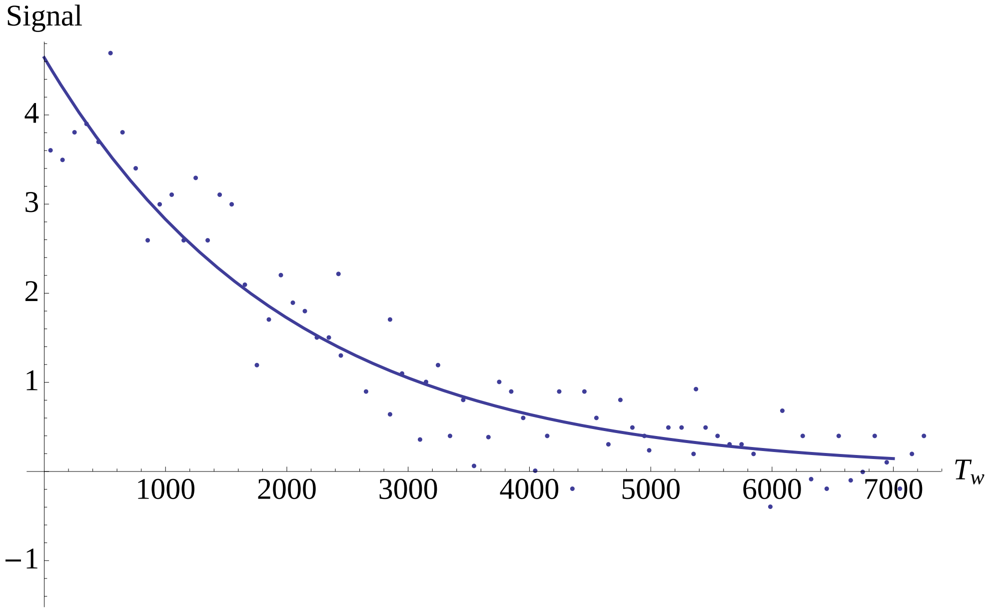

Figure F.15: Pompe-sonde dont la pompe et la sonde sont centrées à 650 nm. La décroissance du signal peut être modélisée par une simple décroissance exponentielle ayant un temps de vie de 2017 fs.

F.5.3 Conclusion

Les nanoparticules métalliques possèdent une grand nombre d'applications fondamentales et appliquées. En particulier, l'exploitation des propriétés de la résonance plasmonique ouvre la voie à l'exploration de nouveaux comportements optiques. La grande sensibilité de la résonance plasmon à la taille et au forme des nanoparticules utilisées nécessite l'élaboration d'un formalisme qui prend en compte ces différents éléments afin de concevoir des objets qui possèdent le comportement désiré. Cette thèse a eu pour objectif de montrer que l'utilisation d'un formalisme totalement irréductible, c'est-à-dire en décomposant aussi bien les champs incidents et émis que le tenseur de réponse lui-même sur une base multipolaire, permet une interprétation d'expériences d'optique linéaire et non-linéaire en associant des comportements physiques spécifiques à des éléments irréductibles particuliers.

L'utilisation du formalisme totalement irréductible combiné à une modélisation utilisant le théorème d'addition translationnelle a pu mettre en lumière l'importance des éléments quadripolaires dans le rayonnement de seconde harmonique des nano-étoiles d'or. Ce formalisme peut être étendu de nombreuses façon afin d'inclure les couplages dans des assemblées de nanoparticules ou pour compléter l'association entre propriétés spectrales et géométriques.

Bibliography

[1] Y. Wang, E. W. Plummer, and K. Kempa. Foundations of plasmonics. *Advances in Physics*, 60(5), 2001.

[2] F. Le, D. W. Brandl, Y. A. Urzhumov, H. Wang, J. Kundu, N. J. Halas, J. Aizpurua, and P. Nordlander. Metallic nanoparticle arrays : A common substrate for both surface-enhanced raman scattering and surface-enhanced infrared absorption. *ACS Nano*, 2(4), 2008.

[3] X. M. Hua and J. I. Gersten. Theory of second-harmonic generation by small metal spheres. *Phys. Rev. B*, 33:3756, 1986.

[4] V. Lozovski. Electrodynamical interactions inside a system of nano-particles. *Physica E*, 19, 2003.

[5] T. R. Jensen, M. D. Malinsky, C. L. Haynes, and R. P. van Duyne. Nanosphere lithography: Tunable localized surface plasmon resonance spectra of silver nanosphere lithography: Tunable localized surface plasmon resonance spectra of silver nanosphere lithography: Tunable localized surface plasmon resonance spectra of silver nanoparticles. *J. Phys. Chem. B*, 104, 2000.

[6] C. Hubert, L. Billot, P.-M. Adam, R. Bachelot, P. Royer, J. Grand, D. Gindre, K. D. Dorkenoo, and A. Fort. Role of surface plasmon in second harmonic generation from gold nanorods. *Appl. Phys. Lett*, 90:181105, 2007.

[7] E. Hutter and J. H. Fendler. Exploitation of localized surface plasmon resonance. *Adv. Mater*, 16:1685, 2004.

[8] C. L. Nehl, H. Liao, and J. H. Hafner. Optical properties of star-shaped gold nanoparticles. *Nano Lett*, 6:683, 2006.

[9] Sami Kujala, Brian K. Canfield, Martti Kauranen, Yuri Svirko, and Jari Turunen. Multipolar analysis of shg from gold nanoparticles. *Optics Express*, 16(22):17196, 2008.

[10] V Svorcik, Z. Kolska, T. Luxbacher, and J. Mistrik. Properties of au nanolayer sputtered on polyethyleneterephthalate. *Materials Letters*, 64(5), 2010.

[11] C. Burda, X. Chen, R. Narayanan, and M. A. El-Sayed. Chemistry and properties of nanocrystals of different shapes. *Chem. Rev.*, 105, 2005.

[12] J. Y. Suh and T. W. Odom. Nonlinear properties of nanoscale antennas. *Nano Today*, 8, 2013.

[13] A. N. Shipway, E. Katz, and I Willner. Nanoparticle arrays on surfaces for electronic, optical, and sensor applications. *Chem. Phys. Chem.*, 1, 2000.

[14] K. A. Willets and R. P. Van Duyne. Localized surface plasmon resonance spectroscopy and sensing. *Annual Review of physical chemistry*, 58, 2007.

[15] E. Stratakis and E. Kymakis. Nanoparticle-based plasmonic organic photovoltaic devices. *Materials Today*, 16(4), 2013.

[16] N. G. Khlebtsov and L. A. Dykman. Optical properties and biomedical applications of plasmonic nanoparticles. *Journal of quantitative spectroscopy and radiative transfer*, 111, 2010.

[17] C. J. Murphy, T. K. Sau, A. M. Gole, C. J. Orendoff, J. Gao, L. Gou, S. E. Hunyadi, and T. Li. Anisotropic metal nanoparticles : synthesis, assembly and optical applications. *J. Phys. Chem. B*, 109, 2005.

[18] Gustav Mie. Contributions on the optics of turbid media, particularly colloidal metal solutions - translation. *Annalen der Physik*, 25(3), 1908.

[19] M. I. Mischenko, L. D. Travis, and D. W. Mackowski. T-matrix computations of light scattering by nonspherical particles : a review. *J. of Quantitative Spectroscopy & Radiative Transfer*, 55(5), 1996.

[20] T. N. Nguyen. *Second harmonic generation of three-fold symmetry gold nanoparticles : measurements and modelling.* PhD thesis, Universite de Technologie de Troyes, 2013.

[21] John David Jackson. *Classical Electrodynamics.* Wiley, 1998.

[22] R. G. Brown. Classical electrodynamics part ii, 2007.

[23] Shaul Mukamel. *Principles of Non-Linear Optical Spectroscopy.* Oxford, 1995.

[24] Robert W. Boyd. *Nonlinear Optics, Third Edition.* Elsevier, 2008.

[25] Y. R. Shen. *The principles of Nonlinear optics.* John Wiley and Sons, Inc, Hoboken, USA, 2003.

[26] M. Joffre. Optique non-linéaire en régimes continu et femtoseconde. http://www.enseignement.polytechnique.fr/profs/physique/manuel.joffre/onl/index.htm, 2009.

[27] Michael Tinkham. *Group Theory and Quantum Mechanics.* Dover, 1964.

[28] Eugene Wigner. *Group Theory and its Application to the Quantum Mechanics of Atomic Spectra.* Academic Press, 1959.

[29] Morton Hamermesh. *Group Theory and its Application to Physical Problems.* Dover, 1989.

[30] Robert Gilmore. *Lie Groups, Lie Algebras, and Some of Their Applications.* Dover, 2005.

[31] D.A. Varshalovich, A.N. Moskalev, and V.K. Khersonskii. *Quantum Theory of Angular Momentum.* World Scientific Pub Co Inc, 1988.

[32] F. W. Strauch. Euler angles : http://demonstrations.wolfram.com/eulerangles/, 2011.

[33] Jean Jerphagnon. Invariants of the third-rank cartesian tensor : Optical nonlinear susceptibilities. *Physical Review B*, 1970.

[34] Jean Jerphagnon, Daniel Chemla, and R. Bonneville. The description of the physical properties of condensed matter using irreducible tensors. *Advances in Physics*, 1978.

[35] Joseph Zyss. Molecular engineering implications of rotational invariance in quadratique nonlinear optics : From dipole to octupolar molecules and materials. *J. Chem. Phys.*, 98(9), 1993.

[36] Sophie Brasselet and Joseph Zyss. Multipolar molecules and multipolar fields : probing and controlling the tensorial nature of nonlinear molecular media. *J. Opt. Soc. Am. B*, 1997.

[37] I. Ledoux and Joseph Zyss. Multipolar engineering of molecules and materials for quadratic nonlinear optics. *C. R. Physique*, 3, 2002.

[38] L. Lorenz. *Oeuvres scientifiques de L. Lorenz. Sur la lumière réfléchie et réfractée par une sphère (surface) transparente.* Lehmann and Stage, 1898.

[39] Craig F. Bohren and Donald R. Huffman. *Absorption and Scattering of Light by Small Particles.* Wiley, 1983.

[40] A. Vial, Anne-Sophie Grimault, D. Macias, D. Barchiesi, and M. Lamy de la Chapelle. Improved analytical fit of gold dispersion : Application to the modeling of extinction spectra with a finite-difference time-domain method. *Phys. Rev B*, 71, 2005.

[41] C. J. Bouwkamp. Diffraction theory. *Reports in Progress in Physics*, 17(35), 1954.

[42] S. Orlov, U. Peschel, T. Bauer, and P. Banzer. Analytical expansion of highly focused vector beams into vector spherical harmonics and its application to mie scattering. *Physical Review A*, 85, 2012.

[43] H. Xu. Calculation of the near field of aggregates of arbitrary spheres. *J. Opt. Soc. Am. A*, 21(5), 2004.

[44] J. H. Bruning and Y. T. Lo. Multiple scattering of em waves by spheres. part i - multipole expansion and ray-optical solutions. *IEE Transactions on Antennas and Propagation*, 19(3), 1971.

[45] J. H. Bruning and Y. T. Lo. Multiple scattering of em waves by spheres. part ii - numerical and experimental results. *IEE Transactions on Antennas and Propagation*, 19(3), 1971.

[46] Kirk A Fuller and George W Kattawar. Consummate solution to the problem of classical electromagnetic scattering by an ensemble of spheres. i: Linear chains. *Optics letters*, 13(2):90–92, 1988.

[47] Kirk A Fuller and George W Kattawar. Consummate solution to the problem of classical electromagnetic scattering by an ensemble of spheres. ii: Clusters of arbitrary configuration. *Optics letters*, 13(12):1063–1065, 1988.

[48] T. Wriedt. *The Mie Theory, chap : Mie theory: A review.* Springer, 2012.

[49] M. Stepanova and S. Dew. *Nanofabrication, Techniques and Principles.* Springer, 2012.

[50] E. Wolf. Electromagnetic diffraction in optical systems. i. an integral representation of the image field. *Proc. R. Soc. Lond. A*, 253(1274), 1959.

[51] B. Richards and E. Wolf. Electromagnetic diffraction in optical systems. ii. structure of the image field in an aplanatic system. *Proc. R. Soc. Lond. A*, 253(1274): 358–379, 1959.

[52] J. Enderlein. Theoretical study of detection of a dipole emitter through an objective with high numerical aperture. *Optics Letters*, 2000.

[53] J. A. Stratton and L. J. Chu. Diffraction theory of electromagnetic waves. *Physical Review*, 56, 1939.

[54] T. D. Visser and H. Wiersma. Diffraction of converging electromagnetic waves. *J. Opt. Soc. Am. A*, 9(11), 1992.

[55] T. D. Visser and S. H. Wiersma. Spherical aberration and the electromagnetic field in high-apertures systems. *J. Opt. Soc. Am. A*, 8(9), 1991.

[56] T. D. Visser and S. H. Wiersma. Electromagnetic description of image formation in confocal fluorescence microscopy. *J. Opt. Soc. Am. A*, 11(2), 1994.

[57] C. J. R. Sheppard. Validity of the debye approximation. *Optics Letters*, 25(22), 2000.

[58] L. Novotny and B. Hecht. *Principles of Nano-Optics*. Cambridge, 2006.

[59] N. Sandeau, L. Le Xuan, D. Chauvat, C. Zhou, J.-F. Roch, and S. Brasselet. Defocused imaging of second harmonic generation from a single nanocrystal. *Opt. Express*, 15(24), 2007.

[60] D.Östling ans P. Stampfli and K.H. Bennemann. Theory of nonlinear optical properties of small metallic spheres. *Z. Phys. D*, 28:169, 1993.

[61] G. Bachelier, I. R. Antoine, E. Benichou, C. Jonin, and P. F. Brevet. Multipolar second-harmonic generation in noble metal nanoparticles. *Phys. Rev*, 25:955, 2008.

[62] J. P. Abid, J. Nappa, H. H. Girault, and P. F. Brevet. Pure surface plasmon resonance enhancement of the first hyperpolarizability of gold core-silver shell nanoparticles. *J. Chem. Phys*, 121:12577, 2004.

[63] A. M. Brito-Silva, R. G. Sobral-Filho, R. Barbosa-Silva, C. B. de Araujo, A. Galembeck, and A. G. Brolo. Improved synthesis of gold and silver nanoshells. *Langmuir*, 29, 2013.

[64] K. L. Shuford, M. A. Ratner, and G. C. Schatz. Multipolar excitation in triangular nanoprisms. *J. Chem. Phys.*, 123, 2005.

[65] F. K. Guedje, M. Giloan, M. Potara, M. N. Hounkonnou, and S. Astilean. Optical properties of single silver triangular nanoprism. *Phys. Scr.*, 86, 2012.

[66] Hong Shen, Jérémy Rouxel, Nicolas Guillot, M. Lamy de la Chapelle, and Timothée Toury. Light polarization properties of three fold symmetry gold nanoparticles : Model and experiments. *C. R. Physique*, 2012.

[67] H. Shen, N. Guillot, J. Rouxel, M. Lamy de la Chapelle, and T. Toury. Optimized plasmonic nanostructures for improved sensing activities. *Optics Express*, 20(19), 2012.

[68] D. D. Evanoff Jr. and G. Chumanov. Synthesis and optical properties of silver nanoparticles and arrays. *Chem. Phys. Chem*, 6:1221, 2005.

[69] J. Martorell and R. Scattering of second harmonic light from small spherical particles ordered in a crystalline lattice. *Chem. Phys. Lett*, 429:533, 2006.

[70] Q. Zhang, N. Li, J. Goebl, Z. Lu, and Y. Yin. A systematic study of the synthesis of silver nanoplates : is citrate a "magic" reagent ? *J. Am. Chem. Soc.*, 133, 2011.

[71] J. Rouxel, T. N. Nguyen, S. Hong, S. Brasselet, and T. Toury. Contour induced second harmonic generation of three fold symmetry gold nanostars. *To be submitted*, 2014.

[72] J. I. Dadap, J. Shan, and T. F. Heinz. Theory of optical second-harmonic generation from a sphere of centrosymmetric material: small-particle limit. *J. Opt. Soc. Am. B*, 21:1328, 2004.

[73] C. I. Valencia and E. R. Méndez. Second-harmonic generation in the scattering of light by two-dimensional particles. *J. Opt. Soc. Am. B*, 20:2150, 2003.

[74] W. Hübner, K. H. Bennemann, and K. Böhmer. Theory for the nonlinear optical response of transition metals: Polarization dependence as a fingerprint of the electronic structure at surfaces and interfaces. *Phys. Rev B*, 50:17597, 1994.

[75] G. Boudarham and M. Kociak. Modal decompositions of the local electromagnetic density of states and spatially resolved electron energy loss probability in terms of geometric modes. *Phys. Rev. B*, 85, 2012.

[76] O. R. Cruzan. Translational addition theorems for spherical vector wave functions. *Q. Appl. Math.*, 20, 1962.

[77] M. Danos and L. C. Maximon. Multipole matrix elements of the translation operator. *J. Math. Phys.*, 6(5), 1965.

[78] B. T. Draine and P. J. Flatau. Discrete-dipole approximation for scattering calculations. *J. Opt. Soc. Am. A*, 11(4), 1994.

[79] N. Kuster. Multiple multipole method for simulating em problems involving biological studies. *IEEE Transactions on Biomedical Engineering*, 40(7), 1993.

[80] W. C. Chew. Vector addition theorem and its diagonalization. *Communications in Computational Physics*, 3(2), 2008.

[81] W.Z. Yan, H. Wu, Y. Du, Q. W. Xiao, D. W. Liu, and J. A. Kong. On the convergency properties of translational addition theorems. *Progress in Electromagnetics Resarch Symposium, Beijing, China*, March 2009.

[82] B. U. Felderhof and R. B. Jones. Addition theorems for spherical wave solutions of the vector helmholtz equation. *J. Math. Phys.*, 28(4), 1987.

[83] T. J. Dufva, J. Sarvas, and J. C.-E. Sten. Unified derivation of the translational addition theorems for the spherical scalar and vector wave functions. *Progress in Electromagnetics Research B*, 4, 2008.

[84] K. T. Kim. The translation formula for vector multipole fields and the recurrence relations of the translation coefficients of scalar and vector multipole fields. *IEE Transactions on Antennas and Propagation*, 44(11), 1996.

[85] R. C. Wittmann. Spherical wave operators and the translation formulas. *IEE Transactions on Antennas and Propagation*, 36(8), 1988.

[86] P. Hamm and M. Zanni. *Concepts and Methods of 2D Infrared Spectroscopy.* Cambridge, 2011.

[87] S. X. Yan and H.-S. Tan. Phase cycling schemes for two-dimensional optical spectroscopy with a pump-probe beam geometry. *Chem. Phys*, 360, 2009.

[88] Z. Zhang, K. L. Wells, E. W. J. Hyland, and H.-S. Tan. Phase-cycling schemes for pump-probe beam geometry two-dimensional electronic spectroscopy. *Chem. Phys. Lett.*, 550, 2012.

[89] Kyungwon Kwak, Sungnam Park, Ilya J. Finkelstein, and M. D. Fayer. Frequency-frequency correlation functions and apodization in two-dimensional infrared vibrational echo spectroscopy : a new approach. *J. Chem. Phys.*, 127, 2007.

[90] A. Perdomo-Ortiz, J. R. Widom, G. A Lott, A. Aspuru-Guzik, and A. H. Marcus. Conformation and electronic population transfer in membrane-supported self-assembled porphyrin dimers by 2d fluorescence spectroscopy. *J. Phys. Chem. B*, 116, 2012.

[91] L. L. Shipman, T. M. Cotton, J. R. Norris, and J. J. Katz. An analysis of the visible absorption spectrum of chlorophyll a monomer, dimer, and oligomers in solution. *J. Am. Chem. Soc.*, 98, 1976.

[92] D. Sundholm. Density functional theory calculations of the visible spectrum of chlorophyll a. *Chem. Phys. Lett.*, 302, 1999.

[93] P. A. Tekavec, K. L. Lewis, F. D. Fuller, J. A. Myers, and J. P. Ogilvie. Toward broad bandwidth 2-d electronic spectroscopy : correction of chirp from a continuum probe. *IEEE J. Sel. Top. Quantum Electron.*, 18, 2012.

[94] S. T. Roberts, J. J. Loparo, and A. Tokmakoff. Characterization of spectral diffusion in two-dimensional line shapes. *J. Chem. Phys.*, 125, 2006.

[95] D. Abramavicius, B. Palmieri, D. V. Voronine, F. Sanda, and S. Mukamel. Coherent multidimensional optical spectroscopy of excitons in molecular aggregates; quasiparticle versus supermolecule perspectives. *Chem. Rev.*, 109, 2009.

[96] I. H. M. van Stokkum, D. S. Larsen, and R. van Grondelle. Global and target analysis of time-resolved spectra. *Biochimica et Biophysica acta*, 1657, 2004.

[97] K. L. Wells, P. H. Lambrev, Z. Zhang, G. Garab, and H-S. Tang. Pathways of energy transfer in lhcii revealed by room-temperature 2d elcetronic spectroscopy. *Phys. Chem. Chem. Phys.*, 16, 2014.

[98] F. Ouyang and M. Isaacson. Surface plasmon excitation of objects with arbitrary shape and dielectric constant. *Phil. Mag. B*, 60(4), 1989.

[99] F. J. Garcia de Abajo"AND J. Aizpurua. Numerical simulation of electron energy loss near inhomogeneous dielectrics. *Phys. Rev. B.*, 54(24), 1997.

[100] I. D. Mayergoyz, D. R. Fredkin, and Z. Zhang. Electrostatic (plasmon) resonances in nanoparticles. *Phys. Rev. B*, 72, 2005.

[101] R. Aris. *Vectors, Tensors, and the basic equations of fluid mechanics.* Dover, 1989.

[102] M. Baker and S. Sutlief. *Green's functions in Physics.* REprints, 2003.

[103] Herbert Goldstein. *Classical Mechanics 2nd edition.* Addison Wesley, 1980.

[104] B. C. Carlson and G. S. Rushbrooke. On the expansion of a coulomb potential in spherical harmonics. *Mathematical Proceedings of the Cambridge Philosophical Society*, 46:626–633, 1950.

[105] J. Martin, M. Kociak, Z. Mahfoud, J. Proust, D. Gerard, and J. Plain. High-resolution imaging and spectroscopy of multipolar plasmonic resonances in aluminium nanoantennas (accepted). *Nano. Lett.*, 2014.

[106] C. Xue and C. A. Mirkin. ph-switchable silver nanoprism growth pathways. *Angew. Chem. Int. Ed.*, 46, 2007.

[107] T. Utikal. *Ultrafast Nonlinear spectroscopy of hybrid plasmonic systems.* PhD thesis, Physikalisches Institut der Universistat Stuttgart, 2011.

[108] T. Utikal, T. Zentgraf, T. Paul, C. Rockstuhl, F. Lederer, M. Lippitz, and H. Giessen. Towards the origin of the nonlinear response in hybrid plasmonic systems. *Phys. Rev. Lett.*, 106, 2011.

[109] M. Scharte, R. Porath, T. Ohms, and M. Aeschlimann. Lifetime and dephasing of plasmons in ag-nanoparticles. *Proc. SPIE*, 4456, 2001.

[110] T. Itoh, T. Asahi, and H. Masuhara. Femtosecond light scattering spectroscopy of single gold nanoparticles. *Appl. Phys. Lett.*, 79, 2001.

[111] H. Baida, D. Christofilos, P. Maioli, A. Crut, N. Del Fatti, and F. Vallee. Ultrafast nonlinear spectroscopy of a single silver nanoparticle. *J. of Raman Spectroscopy*, 42, 2011.

[112] H. Baida, D. Mongin, D. Christofilos, G. Bachelier, A. Crut, P. Maioli, N. Del Fatti, and F. Vallee. Ultrafast nonlinear optical response of a single gold nanorod near its surface plasmon resonance. *Phys. Rev. Lett.*, 107, 2011.

[113] M. Abramowitz and I. A. Stegun. *Handbook of mathematical functions, tenth printing.* National bureau of standards, 1972.

[114] J. M. Blatt and V. F. Weisskopf. *Theoretical nuclear physics.* McGraw-Hill, 1952.

[115] Morris Edgar Rose. *Elementary Theory of Angular Momentum.* Dover, 1957.

Jérémy ROUXEL
Doctorat : Optique et Nanotechnologies
Année 2015

Construction d’un cadre rigoureux pour la description multipolaire des propriétés optiques de nanoparticules

Les propriétés optiques linéaires et non-linéaires de nanoparticules métalliques de tailles non-négligeables comparées à celles des longueurs d’onde excitatrices sont étudiées dans cette thèse. Les informations issues de la symétrie sont mises en avant afin de décrire des nanoparticules appartenant à des groupes ponctuels. Pour cela, un formalisme totalement irréductible est mis en place afin de prendre en compte l’extension spatiale des objets étudiés. Dans ce formalisme, le tenseur de réponse non-linéaire possède un nombre fini de valeurs significatives reliant les composantes multipolaires des champs incidents et sortants. Ce formalisme est alors appliqué analytiquement à l’étude de la réponse non- linéaire du second ordre de nano-étoiles d’or en interprétant des mesures de SHG résolue en polarisation. Finalement, des expériences de spectroscopies multidimensionnelles sont utilisées dans le but de connecter les propriétés spatiales et les propriétés spectrales de ces objets. L’introduction de modes propres définis par la symétrie des objets permet encore une fois de donner un sens physique aux comportements électroniques mis en jeu.

Mots clés : optique non-linéaire - symétries - nanoparticules - spectroscopie résolue en temps.

A Rigorous Multipolar Framework for Nanoparticles Optical Properties Description: Theory and Experiments

Using metallic nanoparticles with a threefold symmetry thorough the study, the impact of the symmetry on the nonlinear properties is investigated. Interpretations of polarization-resolved SHG experiments indicate the importance of multipolar resonances, in particular quadrupole and octupole, to explain the strong values of the nonlinear susceptibilities in such systems. A fully irreducible formalism is then developed to treat extended objects like nanoparticles. In this formalism, the nonlinear response tensor is a discrete set of values easily constrained by symmetries instead of a field. This formalism permits to describe simply linear and nonlinear optical response from nanoparticles. Finally, time-domain experiments are conducted with the aim to connect spatial and spectral properties. These experiments allow to interpret the spectra in terms of eigenmodes.

Keywords: nonlinear optics - symmetries - nanoparticles - time-resolved spectroscopy.

Thèse réalisée en partenariat entre :

NANYANG TECHNOLOGICAL UNIVERSITY

utt
université de technologie
Troyes

Ecole Doctorale "Sciences et Technologies"